

Experimental Study and Surface Deposition Modelling of
Amended Oil Sands Tailings Products

by

Shabnam Mizani

A thesis submitted to the Faculty of Graduate and Postdoctoral
Affairs in partial fulfillment of the requirements for the degree of

Doctor of Philosophy

in

Civil and Environmental Engineering

Carleton University
Ottawa, Ontario

©2016, Shabnam Mizani

Abstract

Recent pilots on emerging oil sands tailings technologies have confirmed that deposit thickness is an important parameter controlling tailings dewatering, and a key parameter governing cost. Controlling or managing deposit thickness continues to be an important challenge for full-scale implementation of tailings technologies that exhibit a yield stress. From the perspective of deterministic modelling of such deposits, there are many challenges, including measurement of the relevant rheological parameters, and how to handle time-variant rheology when modelling.

This research characterizes the rheology of a mineral slurry with relatively high clay content, which is treated with a high molecular weight anionic polymer to induce flocculation. Rheometry results showed that while flocs break down under high shear, flocs reform at lower shear rates. Breakdown and recovery of flocs was confirmed by measuring the shear modulus under dynamic loading and a set of microstructural analysis. Moreover, it was shown that the tailings manifest viscosity bifurcation behaviour similar to pure clay, including shear history dependent apparent yield stress. The measured rheology was then modeled using a previously published viscosity bifurcation model that accounts for hysteresis in the apparent yield stress.

The rheology results are used semi-quantitatively to explain deposition rate dependent behaviour seen in flume tests. The geometry of tailings in flume tests with relatively slow deposition is affected by the behaviour of earliest deposited tailings, which appear to have

recovered structure sufficiently to manifest a large yield stress. This yield stress is much larger than the yield stress exhibited by tailings when they initially come to rest. This full recovery of the yield stress seems to be particularly important to managing surface deposition, as zones of tailings that have stopped moving substantially steepen the slope of deposits near the deposition point.

Finally, and using the rheological models obtained, an attempt was made to model such flows at bench and pilot scales using 3D/2D numerical simulations. The flume test and field deposition conducted were simulated using CFX. It is found that using the lower limit yield stress value and by conducting simulation in several stages (to account for ageing behaviour), more realistic results could be obtained.

Dedication

To my wonderful parents, Shayesteh and Nasser, for their constant support, love and encouragement.

Acknowledgements

First and foremost I would like express my deep gratitude and sincere thanks to my supervisor, Professor Paul Simms, for his immense guidance, support, and encouragement during the course of my studies. Thanks to him I learned the skills necessary to conduct research in a professional manner. This work would not have been possible without his continuous direction and feedback.

A special thanks to Stanley Conley, Jason Arnott and Pierre Trudel, Dr. Marie Tudoret and other technical staff in department of Civil and Environmental Engineering for their technical support and help.

I would also like to acknowledge Shell Canada for providing MFT and polymer samples and Oil sand Tailings Research Facility (OSTRF). Financial support by the Canadian Oil Sands Innovation Alliance (COSIA) and the Natural Science and Engineering Research Council of Canada (NSERC) is greatly appreciated.

I would like to give my special thanks to Dr. Jianqun Wang (Carleton University), Professor David F. James (University of Toronto), Dr. Alebachew Demoz (Canmet Energy) and Professor Ward Wilson for their helpful comments, suggestions and help. I am also grateful to Professors Rayhani, Sivathayalan, Rennie, Vanapalli whom I have taken courses with during my graduate studies.

Finally, I would like to express sincere appreciation to my family for their constant encouragement and support which have allowed me to reach this stage of my life.

Table of Contents

Abstract.....	ii
Acknowledgements.....	v
Table of Contents	vi
List of Tables	xiii
List of Illustrations	xiv
List of Abbreviations	xxix
1 Chapter: Introduction	1
1.1 Background.....	1
1.2 Objective of the Study and scope of the research program	6
1.3 Novelty	7
1.4 Outline of the dissertation.....	8
1.5 Publications related to dissertation.....	9
2 Chapter: Literature Review	11
2.1 Alberta's Oil Sands.....	11
2.2 Basic properties of Tailings and Bitumen Extraction Process	14
2.2.1 Mature Fine Tailings	16
2.3 Challenges Associated with Oil Sands Tailings.....	17
2.3.1 Tailings Regulation	18
2.3.2 Tailings Dewatering.....	19
2.3.3 Flocculation	21
2.3.4 Characteristics of Flocculated MFT	23

2.3.5	Sub-aerial Deposition and Dewaterability	23
2.4	Role of Rheology in Tailings Management	24
2.4.1	Effects of Micro-structure on Rheological Behaviour	25
2.4.1.1	Particle Association	27
2.4.1.2	Deformation	28
2.4.1.3	Amplitude sweep test.....	29
2.4.2	Fabric of Clay Material under Shear.....	31
2.4.3	Thixotropy.....	33
2.4.3.1	Thixotropy Models	35
2.4.3.2	Effects of Consolidation on Thixotropic Strength.....	36
2.5	Methods to Estimate Beach Slope Employed in Practice	37
2.5.1	Mephail Stream Power	37
2.5.2	Fitton Method	40
2.5.3	Lubrication Theory	42
2.6	Atmospheric Fines Drying (AFD) - Pilot scale Deposition of In-line Thickened Tailings	43
2.6.1	Velocity Measurements in Test Cells.....	46
2.6.2	Rheological Characterization of Deposited Material	48
2.6.3	Slopes of Deposits.....	50
2.6.4	Slopes of Deposits at Field Scale.....	53
2.7	Numerical Modelling of Non-Newtonian Fluids	55
2.7.1	Finite Volume	56
2.7.2	Finite Element.....	56
2.7.3	Smoothed Particle Hydrodynamics.....	57
2.7.4	Governing Equation.....	58

3	Chapter: Materials and Methods	60
3.1	Mature Fine Tailings	60
3.2	Property Test.....	62
3.2.1	Solids Content (Cs).....	62
3.2.2	Water Content.....	63
3.2.3	Bitumen Content.....	63
3.2.4	Shrinkage Limit	63
3.2.5	Void Ratio	64
3.3	Water Chemistry	64
3.3.1	Results	65
3.4	X-Ray Fluorescence (XRF) Analysis.....	66
3.4.1	Results	67
3.5	Mineralogical Composition. X-Ray Diffraction Analysis.....	69
3.5.1	Results	70
3.6	Methylene Blue Index Tests	73
3.6.1	Method	73
3.6.2	Results	74
3.7	Dean Stark Analysis	75
3.7.1	Results	76
3.8	Polymer solution	76
3.9	Procedure for Preparation of Flocculated MFT	78
3.10	Soil Water Characteristic Curve (SWCC).....	86
4	Chapter: Rheological Properties	89
4.1	Slump Test.....	90
4.1.1	Experimental Procedure.....	90

4.1.2	Analysis	91
4.1.3	Results	92
4.2	Rheology and Test Procedure on Laboratory-Prepared Polymer-Amended MFT	93
4.2.1	Wall Slip	95
4.2.2	Flow Curve	97
4.2.3	Stress Relaxation	98
4.2.4	Stress Growth	99
4.2.5	Controlled Stress Rheometry	102
4.3	Theoretical Background on Rheometry	107
4.3.1	Oscillatory shear	107
4.3.2	Oscillatory Tests for Determination of Elastic Response Zone	107
4.4	Mathematical Model for Viscoelastic Response	110
4.4.1	Maxwell's Model	110
4.4.2	Kelvin-Voigt model	112
4.4.3	Amplitude Sweep test	114
4.5	Thixotropic Behaviour of Flocculated MFT	117
4.5.1	Effects of Aging and Shearing on Tailings Structure	123
4.6	Comparison of Thixotropic Models to Rheological Data	127
4.6.1	Coussot Thixotropy Model	127
4.6.1.1	Experimental Data	131
4.6.1.2	Comparison with Controlled Shear Rate Data	135
4.6.2	Hewitt Thixotropy Model	136
4.6.2.1	Fitting model to experimental data	139
4.6.3	Modified Hewitt Thixotropy Model	140
4.6.4	Discussion on the Proposed Thixotropy Models	142

5	Chapter: Microstructure and Rheological changes over time.....	145
5.1	Introduction.....	145
5.2	Scanning electron microscopy (SEM).....	146
5.2.1	Image J analysis.....	148
5.2.2	Objective of Microstructural Study.....	148
5.2.3	Testing Procedure.....	149
5.2.4	Microstructural Analysis.....	149
5.3	Changes in Elastic Modulus at Rest.....	154
5.4	PSD Analysis of ESEM Images from Thixotropic Tests.....	163
5.4.1	Elastic Modulus versus Yield Stress.....	177
5.5	Microstructural Analysis Under Shear.....	180
5.6	Mechanical Behavior of Flocculated MFT using Rheology.....	189
6	Chapter: Laboratory Flume Tests	191
6.1	Objectives of the Flume Tests.....	191
6.2	Small Scale Flume Tests Setup.....	192
6.2.1	Testing Procedure.....	192
6.2.2	Test Results.....	193
6.3	Pilot Scale testing at OSTRF.....	194
6.3.1	Pilot Scale Flume Tests Setup.....	196
6.3.2	Experiment Setup.....	200
6.3.3	Mixture Quality.....	202
6.3.4	Flume test Results.....	204
6.3.4.1	Fast Pour.....	204
6.3.4.2	Slow Pour.....	209
6.4	Discussion on flume test results.....	216

7	Chapter: Numerical Simulation of Tailings Flow.....	219
7.1	ANSYS.....	219
7.1.1	Basic definitions.....	219
7.1.2	Euler-Lagrangian.....	221
7.1.3	Euler-Euler.....	222
7.1.4	Volume of Fluid.....	223
7.2	Coupled Versus Segregated Solvers.....	225
7.3	Advection and Transient Scheme.....	226
7.4	Free Surface Flow.....	226
7.4.1	Volume of fluid with interface compression.....	228
7.5	Methodology.....	229
7.5.1	Boundary Conditions.....	230
7.5.2	Computational Setup.....	230
7.5.3	Bingham Model.....	231
7.5.4	2D Simulation using Thixotropic Models.....	231
7.5.5	2D Simulation Results.....	234
7.5.5.1	Comparison with an analytical solution.....	234
7.5.5.2	2D Simulation Results of various Thixotropy Models.....	237
7.6	CFD Simulation of Flume Test on Flocculated MFT.....	242
7.6.1	Model Set-Up (Bench scale).....	243
7.6.2	Boundary conditions.....	244
7.6.3	3D Simulation Results (Bench scale).....	245
7.6.3.1	Validation.....	245
7.6.3.2	Results.....	246
7.6.4	Model Set-Up (pilot scale flume tests).....	252

7.7	Simulation of Deposits at Field Scale	259
7.7.1	Deposition Cell	260
7.8	Discussion.....	265
8	Chapter: Discussion and Conclusion	268
8.1	Summary of the work.....	268
8.2	Implications for the Industry.....	277
8.3	Recommendations.....	278
	REFERENCES	279
	APPENDICES	295
	Appendix A Diffraction patterns of bulk samples	296
	Appendix B Diffraction patterns of the < 2 μm size fraction.....	301
	Appendix C Centrifuge Cake Rheological Data.....	308

List of Tables

Table 2.6-1 Yield stress and slump heights as measured in on site laboratory.....	50
Table 3.1-1 Geotechnical properties of raw MFT.....	61
Table 3.3-1 Water chemistry of pond water.....	65
Table 3.4-1: Elemental composition of raw MFT.....	68
Table 3.5-1 Mineral amount in bulk samples (wt%)	72
Table 3.5-2 Clay minerals identified in the <2 µm size fraction and their semi- quantitative amounts	72
Table 3.6-1 MBI Data	75
Table 3.7-1 Dean Stark Data	76
Table 4.2-1 Maximum stress versus rotational speed at 850gr/tonne.....	102
Table 6.3-1 Vane Spindle Ranges	202
Table 7.6-1 Summary of Flume Tests.....	243
Table 7.6-2 Yield stress obtained from flume test, predicted Eq. 2.5-11 and using cfx (Bingham model).....	252
Table 7.7-1 Cell 4 timeline	261
Table C-1 Centrifuge cake sample identification and geotechnical properties	309

List of Illustrations

Figure 2.1-1 Three major oil sands areas (Modified from EUB, 2004).	12
Figure 2.1-2 Steam-assisted gravity drainage (SAGD) technique used in oil sands industry in deep deposits (Modified from Government of Alberta, Canada, 2009).	13
Figure 2.2-1 Schematic of HWP bitumen extraction (Chalaturnyk et al. 2002).	16
Figure 2.3-1 Schematic of flocculation process.	22
Figure 2.4-1 Various structures at rest and in flow (Modified from Chhabra and Richardson, 2008).	26
Figure 2.4-2 Dependency of clay particle aggregation on the pH-value (Jasmund and Lagaly, 1993).	28
Figure 2.4-3 Amplitude sweep test at a constant frequency and variable deformation. G' is the storage modulus (elastic behaviour) and G'' is the loss modulus (viscous behaviour) (Markgraf 2006).	30
Figure 2.4-4 Four zones of deformation as defined by Jardine, (1992): Zone A, plastic strain ($d\epsilon^p$) is 0, zone B the region of true and non-linear elasticity, zone C or the full plastic region where $d\epsilon^p$ equals total strain ($d\epsilon^t$).	31
Figure 2.4-5 Thixotropic Material (Modified Mitchell and Soga 2005).	34
Figure 2.6-1 Generalized AFD Process (Modified from Barr Engineering report, 2012)	44
Figure 2.6-2 Schematics of deposition scheme for 2012-2013 depositions.	45
Figure 2.6-3 Spill box and discharge piping configuration in Test Cell.	46
Figure 2.6-4 Velocity measurement during the 6th layer deposition in Multi-lift cell Thin.	47

Figure 2.6-5 Velocity measurement during the 3rd layer deposition in Multi-lift cell Thick.	48
Figure 2.6-6 Collection of sample from upstream and downstream during deposition	49
Figure 2.6-7 Thin Multilift cell profile after deposition of 7 layers in September 2013 ...	51
Figure 2.6-8 Thick Multilift cell profile after deposition of 3 layers in September 2013.	52
Figure 2.6-9 Tailings profile measured at Shell Atmospheric Fine Drying (AFD) operation at cell 4 during 2010 campaign.....	53
Figure 2.6-10 Yield stress measurement and dynamic scanning of Thin Multi Lift (Layer 6) from Barr Engineering.....	54
Figure 3.1-1 Particle size distributions of raw MFT from hydrometer and sieve analyses with and without using 4% sodium hexa-metaphosphate (NaPO ₃)	61
Figure 3.5-1 Schematic representation of Braggès law.	69
Figure 3.8-1 Structure of anionic PAM (http://www.snfcanda.com/product- literature.php)	77
Figure 3.8-2 Flow curve for A3338 polymer prepared at concentration of 0.4% w/w (left), viscosity profile with shear rate (right).....	78
Figure 3.9-1 Effects of mixing speed on yield stress values of flocculant MFT at 850g/tonne.	79
Figure 3.9-2 Mixing of flocculant with MFT.	80
Figure 3.9-3 Effect of mixing time at 250rpm on rate of water release for tailings prepared at 725g/tonne.....	81
Figure 3.9-4 Comparison between yield stress values measured in laboratory and deposition in Muskeg River Mines tailings site during Aug-Oct 2012.	82

Figure 3.9-5 Settling column setup.....	83
Figure 3.9-6 Water content as a function of flocculant dosage and time for column height of (a)50 and (b)30 cm and (c)10cm respectively.	85
Figure 3.9-7 Total solid concentrations in released water as a function of flocculant dosage.	86
Figure 3.10-1 Flocculated MFT before transferring sample to total suction machine.	87
Figure 3.10-2 SWCC for Flocculated and raw MFT.	88
Figure 4.1-1 Graphical illustration of slump test.	90
Figure 4.1-2 Dimensionless slump height versus polymer dose in g/tonne after 30minutes upon mixing.	92
Figure 4.1-3 Yield stress and density values versus polymer dose in g/tonne after 30minutes upon mixing.	93
Figure 4.2-1 An Anton Paar Physica Rheometer.	94
Figure 4.2-2 Stress growth test on type I Portland cement and deionized water at water to cement ratios of 0.30.	96
Figure 4.2-3 Flow curves on raw and flocculated MFT.	97
Figure 4.2-4 Flow curves on raw MFT at various measuring point duration.	98
Figure 4.2-5 Stress relaxation test on raw and flocculated MFT at 850 g/tonne dose.....	99
Figure 4.2-6 Stress growth test on flocculated MFT at 850 g/tonne dose at various rotational speed.....	100
Figure 4.2-7 Strain-stress plots of MFT dosed at 850 g/tonne for various rotational speeds.....	101
Figure 4.2-8 Variation of viscosity with stress (Coussot et al. 2002b).	102

Figure 4.2-9 Variation of viscosity with time under various shear stress rates.	103
Figure 4.2-10 Variation of viscosity with time under various shear stress levels.....	104
Figure 4.2-11 Viscosity variation over 45s for a sample prepared at 850 g/tonne. Stress was decreased in steps from 800 Pa to 5 Pa.	106
Figure 4.2-12 Viscosity variation over 50min for a sample prepared at 850 g/tonne. Stress was decreased in steps from 250 Pa to 5 Pa.	106
Figure 4.3-1 Sinusoidal applied strain and corresponding sinusoidal stress response (Macosko, 1994).....	108
Figure 4.3-2 Schematic illustration of complex shear modulus (Markgraf, 2006).....	110
Figure 4.4-1 Maxwell Model.....	111
Figure 4.4-2 Kelvin-Voigt model (Chhabra and Richardson, 2008).	112
Figure 4.4-3 Stress response (b) to a step input of 5% strain (a).	114
Figure 4.4-4 Response to strain sweeps showing the linear viscoelastic region at three different frequency.....	115
Figure 4.4-5 Stress versus strain plots for material prepared at 850 g/tonne under constant shear rate of 0.1 s^{-1}	116
Figure 4.4-6 Response to strain sweeps showing the linear viscoelastic region at 10 rad/s for raw MFT.	117
Figure 4.5-1 Samples prepared for thixotropy testing	120
Figure 4.5-2 Solid content measurement of flocculated MFT for three different samples at various times.....	120
Figure 4.5-3 Strength measurement for flocculated MFT dosed at 850g/tonne for different solid contents over time.....	121

Figure 4.5-4 Thixotropic ratio for flocculated MFT dosed at 850g/tonne for different solid contents over time.	121
Figure 4.5-5 Interpolated thixotropic strength at 39.4% and 43.3% solid content using the procedure in Miller, 2004.	122
Figure 4.5-6 Thixotropic ratio in different clay type and raw MFT (Jeeravipoolvarn, 2005).	122
Figure 4.5-7 Three-interval thixotropy scheme.....	124
Figure 4.5-8 Postshear recovery for samples prepared at 850 g/tonne after applying a shear stress of 500 Pa for different times (90s and 300s).	125
Figure 4.5-9 Post shear recovery for samples prepared at 850 g/tonne under constant decreasing shear stresses.....	126
Figure 4.6-1 Dimensionless viscosity versus dimensionless time for various dimensionless stresses (using $n=2, \alpha=1$ and $\lambda_0=1$).....	130
Figure 4.6-2 Viscosity (a) and shear rate (b) versus time for flocculated MFT dosed at 850g/tonne exposed to different levels of stress over a period of 120 seconds.	132
Figure 4.6-3 Predictions of Coussot thixotropy model (continuous lines) and measured experimental data (symbols) at different imposed (dimensionless) stresses (Roussel et al. 2004).	133
Figure 4.6-4 Viscosity versus dimensionless time as predicted by the Coussot model and as measured by the rheometer, for $T=0.01$ and $\mu_0=1$	134
Figure 4.6-5 Measured and predicted values of the viscosity at five shear rates, using Eq. 4.6-11 for $n=1.075$, $\alpha=0.36$ and $\mu_0=1\text{Pa.s}$	136

Figure 4.6-6 Variation of λ with time and under various stress level ($\beta=0.97$ and $\alpha T/\mu=0.077$).....	138
Figure 4.6-7 Creep tests modeled using thixotropy model ($\mu_0 = 1.5$ Pa.s, $T = 10$, $\alpha=0.01275$).....	139
Figure 4.6-8 Stress growth test under various shear rate and as predicted by the proposed thixotropy Model.....	140
Figure 4.6-9 Viscosity variation for flocculated MFT at 850 g/tonne dose for different times of rest.	142
Figure 5.2-1 Schematic of an ESEM (Danilatos, 1993).	147
Figure 5.2-2 ESEM micrograph of A3338 polymer used to prepare flocculated MFT (magnification: 500x).....	150
Figure 5.2-3 Backscattered environmental scanning electron of mature fine tailings for a magnification - 1000 x, scale - 20 μm , view field - 150 μm	151
Figure 5.2-4 Backscattered environmental scanning electron of polymer amended MFT at a dose of 650g/tonne for a magnification - 2000 x, scale - 20 μm , view field - 75 μm	151
Figure 5.2-5 Backscattered environmental scanning electron of polymer amended MFT at a dose of 725g/tonne for a magnification - 1000 x, scale - 50 μm , view field - 150 μm	152
Figure 5.2-6 Backscattered environmental scanning electron of polymer amended MFT at a dose of 1000g/tonne for a magnification - 1000 x, scale - 20 μm , view field - 150 μm	152

Figure 5.2-7 Backscattered environmental scanning electron of polymer amended MFT at a dose of 1200gr/tonne for a magnification - 1000 x, scale - 20 μm , view field - 150 μm	153
Figure 5.3-1 Elastic modulus values measured over a course of 35days at (a) 650g/tonne, (b) 850g/tonne and 1000g/tonne and for three individual samples.	155
Figure 5.3-2 Elastic modulus values measured over a course of 35days at various floc dosages for sample#1.	156
Figure 5.3-3 Yield stress values measured over 13days for polymer dosages of 650g/tonne.	156
Figure 5.3-4 Yield stress values measured over 16 days for polymer dosages of 850g/tonne.	157
Figure 5.3-5 Yield stress values measured over 13 days for polymer dosages of 1000g/tonne.	157
Figure 5.3-6 Yield stress measurement over a course of 16 days at various floc dosages for sample#3.	158
Figure 5.3-7 Moisture content measured for various floc dosages of samples in Figure 5.3-1.	159
Figure 5.3-8 Moisture content versus thixotropy ratio (τ_y/τ_{y0}) for various floc dosages.	160
Figure 5.3-9 Moisture content versus (G'/G'_0) for various floc dosages (subscript ‘‘0’’ denotes initial value).	161
Figure 5.3-10 Moisture content versus G' and/or τ_y for various floc dosages of sample#3.	162

Figure 5.3-11 Moisture content versus (G'/G'_0) and τ_y/τ_{y0} for various floc dosages of sample#3.....	163
Figure 5.4-1 Scanning electron micrographs of polymer amended oil sands tailings for polymer dose of 650g/tonne a) – two hour after polymer mixing; b)– 96 hours after polymer mixing (sample#1).....	164
Figure 5.4-2 Scanning electron micrographs of polymer amended oil sands tailings for polymer dose of 650g/tonne a) –four hour after polymer mixing; b)– 96 hours after polymer mixing; c)-14 days after polymer mixing (sample#2)	166
Figure 5.4-3 Scanning electron micrographs of polymer amended oil sands tailings for polymer dose of 1000g/tonne a) – two hour after polymer mixing; b)– 72 hours after polymer mixing (sample#1).....	167
Figure 5.4-4 Scanning electron micrographs of polymer amended oil sands tailings for polymer dose of 1000g/tonne a) – four hour after polymer mixing; b)– 96 hours after polymer mixing; c)– 14 days after polymer mixing((sample#2).	169
Figure 5.4-5 Gray pixel analysis of polymer amended tailings at 650g/tonne after 2 hours upon polymer mixing at three different locations of P1, P2 and P4.	170
Figure 5.4-6 Optimum threshold for sample#1 and 2 prepared at 650g/tonne over time.	171
Figure 5.4-7 Gray pixel analysis of polymer amended tailings at 650g/tonne over a period of 14days after polymer mixing for (a) sample#1 -Figure 5.4-1 and (b) sample#2-Figure 5.4-2.	172
Figure 5.4-8 Optimum threshold for sample#1 and 2 prepared at 1000g/tonne over time.	173

Figure 5.4-9 Gray pixel analysis of polymer amended tailings at 1000g/tonne over a period of 14days after polymer mixing (a) sample#1-Figure 5.4-3 and (b) sample#2-Figure 5.4-4.	174
Figure 5.4-10 Scanning electron micrographs of polymer amended oil sands tailings for polymer dose of 1000g/tonne (14 days after polymer mixing (sample#2)) and associated segmented image . Here the dark and light gray represent solids and blue represents pores.....	175
Figure 5.4-11 Yield stress vs elastic modulus for various floc dosage at different resting time as indicated in Figure 5.3-3 to Figure 5.3-5.....	178
Figure 5.4-12 Typical stress-time response curve for the vane illustrating the slope of linear elastic region (Nguyen et al. 2006).....	179
Figure 5.4-13 Yield stress vs slope of linear zone for various floc dosage at different resting time as indicated in Figure 5.3-3 to Figure 5.3-5.....	179
Figure 5.5-1 Backscattered environmental scanning electron of polymer amended MFT at a dose of 850g/tonne for a magnification - 1000 x, scale - 20 μm , view field - 150 μm - before shearing.	181
Figure 5.5-2 Backscattered environmental scanning electron of polymer amended MFT at a dose of 850g/tonne for a magnification - 1000 x, scale - 20 μm , view field - 150 μm - after shearing.	182
Figure 5.5-3 Backscattered environmental scanning electron of polymer amended MFT at a dose of 850g/tonne for a magnification - 1000 x, scale - 20 μm , view field - 150 μm - after 50 min of resting upon shearing.	183

Figure 5.5-4 Gray pixel analysis of polymer amended tailings at 850g/tonne before, after and recovery upon shearing at 1RPM.	184
Figure 5.5-5 Elastic modulus values measured at dosage of 850g/tonne before and after shearing.	184
Figure 5.5-6 Elastic modulus values measured at dosage of 850g/tonne before and after (0min, 20min and 45min) shearing at 50RPM for 4 minutes.	185
Figure 5.5-7 Backscattered environmental scanning electron of polymer amended MFT at a dose of 850g/tonne for a magnification - 1000 x, scale - 20 μm , view field - 150 μm - (a) before shearing, (b) after shearing at RPM of 50 for 4 minutes and (c) after 45minutes upon shearing at RPM of 50 for 4 minutes.	187
Figure 5.5-8 Gray pixel analysis of polymer amended tailings at 850g/tonne before, after shearing at 50RPM and after 45minutes upon resting.	188
Figure 5.5-9 Mechanical behavior of clay particles under oscillatory stress.	189
Figure 5.6-1 Phase angle versus strain as a function of soil texture (Markgraf et al. 2012).	190
Figure 5.6-2 $\tan \delta$ as a function of strain for raw and flocculated MFT.	190
Figure 6.2-1 Dimensions of the flume used (small scale).	192
Figure 6.2-2 Flume test.	193
Figure 6.2-3 A single layer flow at various floc dosages.	194
Figure 6.3-1 KMS static mixer.	195
Figure 6.3-2 Flume apparatus used in OSTRF and dimensions.	197
Figure 6.3-3 Pump mixing in totes.	199
Figure 6.3-4 Tailings transportation into CT tank.	199

Figure 6.3-5 Particle size distributions of raw MFT used for flume test from hydrometer and sieve analysis.	200
Figure 6.3-6 Illustration of the setup for small pilot scale flume test at OSTRF.	201
Figure 6.3-7 Yield stress values for various setup (please refer to Figure 6.3-9 for pump calibrations)	202
Figure 6.3-8 a) Over sheared material-poor mixing (at highest flow rate using 3 static mixers) (b) Well flocculated material at same speed using 2 static mixers.	203
Figure 6.3-9 Flume test operational pump speed for various floc dosages (the following conversions were used: Floc pump speed (L/min) = $32.465x-3.1371$ and MFT Pump speed (L/min)= $0.4261x+1.2594$, where x is percent pump speed).	204
Figure 6.3-10 Pressure drop across static mixers during fast pour.	205
Figure 6.3-11 Transient profile in the flume for a single layer, at floc dosage of 850g/tonne (MFT pump speed of 75% and Floc pump speed of 98%).	205
Figure 6.3-12 Photos corresponding to transient profile in the flume for a single layer, at floc dosage of 850g/tonne (fast pour).	208
Figure 6.3-13 Yield stress values measured at the end of the flume test (t =25minutes) at surface of the deposit and at 0 and 6m from deposition point.	209
Figure 6.3-14 Pressure drop across static mixers during slow pour.	210
Figure 6.3-15 Transient profile in the flume for a single layer, at floc dosage of 850g/tonne (MFT pump speed of 20% and Floc pump speed of 26%)	210
Figure 6.3-16 Photos corresponding to transient profile in the flume for a single layer, at floc dosage of 850g/tonne (slow pour).	214

Figure 6.3-17 Yield stress values measured at the end of the flume test (t=65minutes) at surface of the deposit and at 0, 2.5 and 5.2m from deposition point.	215
Figure 6.3-18 Mixing energy density of static mixers for fast and slow pour	215
Figure 6.4-1 Flume deposition of 850gr/tonne tailings in a long flume (0.65 m wide) at 36 L/ min, fitted using 1D lubrication theory, yield stress of 60 Pa.	217
Figure 6.4-2 Flume deposition of 850 g/tonne tailings in a long flume (0.65 m wide) at 10 L/ min, the 45 minute profile fitted with 1D lubrication theory using yield stress of 400 Pa.	218
Figure 7.1-1 Volume of Fluid for an arc over a structured grid (ANSYS CFX 2015 Multiphse flow workshop).....	220
Figure 7.1-2 Schematic illustration of volume fraction for two phase flow.	224
Figure 7.5-1 Schematic of initial position of tailings for 2D simulations.	229
Figure 7.5-2 2D simulation: Effect of height of initial configuration on shape of final profile for a 100 Pa yield stress material.	235
Figure 7.5-3 Comparison between simulated and 2D analytical solution of Balmforth et al. 2007 using a Bingham number of 0.1. Here lines show the results for analytical solution and dotes are obtained from numerical simulation.....	235
Figure 7.5-4 2D simulation: Effect of yield stress on shape of final profile of flocculated MFT at a viscosity of 0.5Pa.s where x and y=0.15m.....	236
Figure 7.5-5 2D simulation: Effect of various rheological models on shape of final profile for dam break problem (0.15m by 0.15m).....	238
Figure 7.5-6 2D simulation: Effect of initial geometry and $\dot{\gamma}_c$ on shape of final profile using the Hewitt model.	239

Figure 7.5-7 2D simulation: Effect ageing term on shape of final profile using the Hewitt Model.....	240
Figure 7.5-8 2D simulation: Effect shearing term on shape of final profile using the Hewitt Model.....	240
Figure 7.5-9 Variation of structure term with space for case#1 and 2 presented in Figure 7.5-8.	242
Figure 7.6-1 Medium mesh used for simulation of flume tests.	245
Figure 7.6-2 Final geometry for different mesh sizing for deposition velocity of 0.026kg/s and at t=400s employing a yield stress value of 60Pa and viscosity of 0.5Pa.s.....	246
Figure 7.6-3 3D Numerical-experimental comparison of deposition of 5.7 kg of flocculated MFT (650g/tonne) into the flume using a yield stress value of 40Pa (Flume Test #1).	247
Figure 7.6-4 Tailings deposition simulation at t=50s, and 200 s, employing a yield stress of 40 Pa and viscosity of 0.5 Pa.s (Flume Test #1).....	248
Figure 7.6-5 3D Numerical-experimental comparison of deposition of 5.8 kg of flocculated MFT(850g/tonne) into the flume using a yield stress value of 60Pa (Flume Test #2).	248
Figure 7.6-6 Tailings deposition simulation at t=110s, and 400 s, employing a yield stress of 60 Pa and viscosity of 0.5 Pa.s (Flume Test #2).....	249
Figure 7.6-7 3D Numerical-experimental comparison of deposition of 5.88 kg of flocculated MFT(1000gr/ton) into the flume using a yield stress value of 70Pa (Flume Test #3).	250

Figure 7.6-8 Tailings deposition simulation at t=170s, and 400 s, employing a yield stress of 70 Pa and viscosity of 0.5 Pa.s (Flume Test #3).....	251
Figure 7.6-9 Mesh used for simulation of pilot scale testing at OSTRF.	253
Figure 7.6-10 Tailings deposition simulation at t=10min, 15min and end of simulation, employing a yield stress of 40 Pa and viscosity of 0.5 Pa.s (Flume Test #6).	255
Figure 7.6-11 3D Numerical-experimental comparison of pilot scale flume test using Bingham model.	256
Figure 7.6-12 2D Numerical-experimental comparison of slow pour (~ 60 minute test) where the measured tailings profile at 30 minutes was used as the new topography. Figure (a) illustrates the profile in the Hewitt model at the time when channel flow was first observed in the experiment (~49 minutes using thixotropy model and 42min using Bingham model).....	257
Figure 7.6-13 Snapshots of 3D simulation of tailings on inclined plane at 38%.....	259
Figure 7.7-1 Schematic plan of cell 4 deposition cell.....	260
Figure 7.7-2 Measured and predicted beach profiles for Cell 4.....	263
Figure 7.7-3 Measured and predicted beach profiles for Cell 4 conducted in 2 steps.....	263
Figure 7.7-4 Measured and predicted beach profiles for Cell 4 using deposition periods as indicated in Table 7.7-1 employing yield stress of 50 Pa.....	264
Figure 7.7-5 Measured and predicted beach profiles for Cell 4 using deposition periods as indicated in Table 7.7-1 employing thixoropy model.....	264
Figure A-1 Bulk Sample Diffraction Pattern 2013a.	297
Figure A-2 Bulk Sample Diffraction Pattern 2013b.	298
Figure A-3 Bulk Sample Diffraction Pattern 2014a.	299

Figure A-4 Bulk Sample Diffraction Pattern 2014b.	300
Figure B-5 XRD - Clay speciation (Air Dry) -2013a.	302
Figure B-6 XRD - Clay speciation (Glycolated) -2013a.	302
Figure B-7 XRD - Clay speciation Superimpositions -2013a	303
Figure B-8 XRD - Clay speciation (Air Dry) -2013b	303
Figure B-9 XRD - Clay speciation (Glycolated) -2013b.....	304
Figure B-10 XRD - Clay speciation Superimpositions -2013b.....	304
Figure B-11 XRD - Clay speciation (Air Dry) -2014a.	305
Figure B-12 XRD - Clay speciation (Glycolated) -2014a.	305
Figure B-13 XRD - Clay speciation Superimpositions -2014a.....	306
Figure B-14 XRD - Clay speciation (Air Dry) -2014b.	306
Figure B-15 XRD - Clay speciation (Glycolated) -2014b.....	307
Figure B-16 XRD - Clay speciation Superimpositions -2014b.....	307
Figure C-17 Response to strain sweeps (0.01%-300%) for centrifuge cake (sample#7) showing the linear viscoelastic region of around 250Pa.	310
Figure C-18 Postshear recovery for sample #7 after applying a shear stress of 500 Pa and 700Pa for 240s.....	311
Figure C-19 Post shear recovery for sample #9&10 under constant decreasing shear stresses	312

List of Abbreviations

C_s	Solid concentration
d	Depth of flow
D	Shear rate tensor
S_u	Undrained shear strength
G^*	Complex modulus
G'	Elastic modulus
G''	Loss modulus
τ	Shear stress
σ	Normal stress
τ_y	Yield stress
μ	Viscosity
γ	Shear strain
P	Pressure
P_x	Stream power
Q	Flow rate
ρ	Density
R_H	Hydraulic radius
Re	Reynolds number
Fr	Froude number
f	Average friction factor
ν	Kinematic viscosity

K	Consistency coefficient
w	Gravimetric water content
e	Void ratio
S'	Dimensionless slump
τ'_y	Dimensionless yield stress
T_m	Measured torque
ω	Frequency
$\dot{\gamma}$	Shear rate
δ	Phase lag
λ	Structure term
Λ	Wavelength
$\dot{\gamma}_c$	Critical shear rate
τ_c	Critical shear stress
ψ	Dimensionless stress
Γ	Dimensionless shear rate
t^*	Dimensionless time
T	Characteristic time of restructuring
E	Energy density
∇	Gradient operator
\cdot	Dot product
\otimes	Tensor product
α_i	Volume of fraction of the i^{th} phase

S	Source term
U	Velocity vector
u_c	Artificial velocity
ξ	Energy density

1 Chapter: Introduction

1.1 Background

The oil sands industry is an integral component of Canadian economy. The Canadian Energy Research Institute (CERI) estimates oil sands will create \$350 billion in royalties and \$122 billion in tax revenue across Canada over the next 25 years (<http://oilsands.alberta.ca/economicinvestment.html>). Some forecasts predict production to rise up to 3.4 million bpd by 2020 (Calgary Herald, 2015). However, the oil sands industry has unfavorable impacts on the environment, including water consumption by tailings generation, and the technical difficulties associated with reclaiming large tailings impoundments. For instance, fluid tailings held behind containment dams has made Northern Alberta tailings facilities one of the very few man-made structures visible from the space. The total land occupied by oil sands tailings ponds and associated structures (such as dykes) was estimated to be 220 square kilometers in 2013 (Alberta Energy, 2016; <http://www.energy.alberta.ca/oilsands/791.asp>).

Oil sands tailings, the residue from mining and bitumen extraction, comprise coarse solids (sands, fines (clay and silts)), water, and unrecovered bitumen. Upon deposition of

tailings into ponds, sands will settle out, trapping a portion of the fine particles. The remaining fines form a suspension that settles to a solid content (C_s , mass of solids over total mass) of around 30-40%. At this point the suspension is referred to as Mature Fine Tailings (MFT), and the rate of settling past this point is minimal. At this solids content approximately 84% of the volume in the tailings pond is water, and the tailings have very low bearing capacity, far below that needed to support foot traffic (< 1 kPa). Hence these deposits are not reclaimable.

The settling and consolidation properties of MFT are influenced by both the innate characteristics of the ore body, (residual bitumen, clay minerals), and the bitumen extraction process. Bitumen is extracted using different variants of the Clark hot water process (Masliya et al. 2004; Xu and Hamza, 2003) which includes the addition of NaOH to promote beneficial surface chemistry for bitumen separation. However, the addition of NaOH also increases inter-particle repulsion between clay particles, therefore promoting a highly dispersed fabric. As a result of clay particle dispersion, MFT exhibits slower settling rates, lower permeability and thus substantial volumes of water to be remained tied up in dammed impoundments. Moreover, thixotropic strength gain resulting in apparent preconsolidation pressure is thought to impede consolidation (Scott et al. 2013).

The poor consolidation leaves operators with enormous volumes of tailings remaining in a soft condition for decades to centuries. According to Houlihan and Haneef (2008), the volume of fluid tailings will likely reach two billion cubic meters by 2034 if no change is made to the way tailings are managed. This poses significant challenges to the ultimate goal of land reclamation and expands the physical footprint of mine waste facilities. Many of the mines in the Northern Alberta are limited to certain area for their waste deposits.

Therefore, overburden dumps, lean ore deposits, drying cells and external tailings pond need to be situated in a constrained area.

The government of Alberta released new plan: Tailings Management Framework for Mineable Athabasca Oil Sands (TMF), in 2015 for management of fluid tailings, setting higher penalties for failures in achieving reclaimable deposits (Alberta Energy Regulator (AER), 2015). Previously, in 2009, Energy Resource Conservation Board (ERCB) introduced regulations - Directive 074: Tailings Performance Criteria and Requirements for Oil Sands Mining Schemes. This regulation was introduced with the aim to make affected area trafficable (minimum undrained shear strength of 10 kPa) and thus ready for reclamation in future. Directive 074 requires tailings to gain shear strength of 5 kPa within a year and 10 kPa after 5 years upon stopping active deposition. Any material not reaching the required strength must be removed or remediated (Energy Resources Conservation Board, 2009). Directive 074 has been recently rescinded (July 2016), and AER released a new Directive 085: Fluid Tailings Management for Oil Sands Mining Projects. This new requirement along with TMF target the volume of the fine tailings (rather than the strength of MFT), requiring performance reporting and ensuring tailings treatment and reclamation through the life of the projects.

In response to practical needs and to new regulations, operators have accelerated large-scale trials of different technologies to accelerate dewatering of fine tailings. These include: composite tailings, centrifugation, conventional thickening, in-line thickening, and/or the combination of these techniques.

In-line flocculation involves in-line mixing of polymer into fresh fluid fine tailings or reclaimed MFT to promote clay flocculation, which has the benefits of improving

dewatering, to the point where the generated material exhibits a yield stress and will stack. Stack-ability allows for placement in lifts, which can facilitate further dewatering through surface processes such as evaporation or freeze-thaw. In-line flocculation has been implemented at the commercial scale (Wells et al. 2011; Matthews et al. 2011; Dunmola et al. 2013).

Not just limited to inline flocculation, most if not all of these technologies, rely on post-deposition dewatering (i.e. desiccation, consolidation) for further strength gain in order to meet Directive 085 requirements. The application of these technologies usually dewater tailings to the extent they being to resemble non-Newtonian fluids (Yogurt, toothpaste) and manifest a yield stress during deposition. However, as the behaviour of non-Newtonian materials can be quite complex, managing the deposition of the dewatered tailings can be challenging; and successful management of tailings geometry requires knowledge of the rheology.

Layer thickness is an important parameter in tailings deposition technologies that maximize evaporation and freeze-thaw contributions to dewatering. Thin layered deposits mainly rely on initial dewatering and subsequent long term dewatering through both evaporation and freeze-thaw. On the other hand, long term dewatering of deep lift deposition is mainly due to self-weight consolidation and creep. Irrespective of deposition scheme, the geometry of deposition plays a significant role in the dewatering process. Thus, to optimize dewatering process, tailings deposit geometry should be controlled. Predicting or managing the slope and the evolution of the geometry of thickened tailing deposits has long been an important issue in mine waste management (Simms et al. 2011). As of yet, there exists no definitive method to correctly predict how stack geometry evolves.

A common issue encountered in yield stress fluids (fluids that deform indefinitely when they are subjected to stress levels above some critical value) is variability in the results when different techniques are employed. Variation in the results are often associated with the time scale of the technique, definition of yield stress and the principle inherited in each method (Cheng, 1986; Nguyen and Boger, 1992; Nguyen et al. 2006). Previous studies (Mizani et al. 2013a; Mizani and Simms, 2016a) have shown that yield stress that best describes the material behavior during flow stoppage can be much different than the yield stress that characterizes when the tailings start flowing. Coussot et al. (2002a,b) and Roussel et al. (2004), showed that in pure clay suspensions, which exhibited both thixotropic effects and hysteresis, the apparent yield stress depends on the stress history of the material. This behaviour is often simulated using a Non-Newtonian variable viscosity in literature, where the viscosity decreases rapidly upon shearing and increases slowly when left at rest or under lower stress levels (Coussot et al. 2002; Hewitt and Balmforth 2013; Hewitt 2012). Variable yield stress, hysteresis, jamming and avalanche of various non-Newtonian fluid are believed to originate from this type of rheology (Alexandrou et al. 2009; Bonn et al. 2004; Moller et al. 2009; Hewitt and Balmforth 2013). While a wide range of thixotropic models have been proposed, yet the confounding effects of thixotropy behavior is often ignored in most problems involving gravity currents in particular tailings stacks geometries.

In addition, sensitivity of the flocs created by polymer mixing to shear, is another concern for operators of in-line flocculation. Flocs could be destroyed by shear during transport and shear during deposition, which would reduce both the yield stress and the

dewatering potential of the tailings. However, little quantitative information on the rheology of polymer amended mature fine tailings is available.

1.2 Objective of the Study and scope of the research program

The goal of this study is to improve the capacity of engineers to predict the evolving geometry of deposited polymer amended MFT. A necessary secondary goal is to describe the rheology of the same material. This is done through both laboratory experiments/field testing and numerical modellings. The following scope of work was pursued:

- ✓ Imaging flocculated MFT deposition in progress using video cameras and height sensors, and measuring final deposition geometry profiles using lasers and scanners both in the field and laboratory flume test as a function of operational terms and pour quality. This includes pilot scale flume test (using available 8m long flume at Oil Sands Tailings Research Facility (OSTRF), in Devon, Alberta). Generated data to serve for calibration and validation of model development.
- ✓ Measuring rheological properties of tailing (using Anton Paar Physics Rheometer and slump tests). Rheometry include both controlled stress and controlled strain tests, with the aim to find the most appropriate technique to determine yield stress from deposition point of view.
- ✓ Microstructure investigation to confirm rheological findings and evaluate structural changes due to ageing and shearing
- ✓ Modelling aspects of tailings flow using ANSYS CFX, a commercial finite volume based software. Numerical model was used to develop relationships between final

geometry and deposition parameters such as flowrate and the properties of the material (i.e., floc dose).

1.3 Novelty

In this study it was shown that the rheology of polymer amended tailings is dependent not only on shear thinning behaviour but on ageing or thixotropic behavior. Through the larger scale tests it became apparent that the ageing/density effects of the material plays a more dominant role. In order to incorporate both these effects a biviscosity model (constitutive model) was calibrated with material rheology and consequently used in the numerical modelling. It was also shown that the recovery and de-structuration of flocculated MFT can be accurately determined through oscillatory rheometry test.

Although there exists extensive work on rheological measurement and modelling on thixotropic fluids in the literature, only a limited number of studies have incorporated these models into actual and full scale depositions. Aside from computational works reported by Coussot et al. 2005 and Hewitt and Balmfoth 2013, involving finite volume of thixotropy material released from rest, there has been no attempt to model the spatial and temporal changes of thixotropic material following deposition during continuous pumping.

At the outset of the research program, no other work on the rheology and deposition modelling of any tailings with this level of sophistication has been conducted. Since the onset of the program and the reporting of initial results in conference papers, some contract work sponsored by oil sands companies using similar principles has been launched.

1.4 Outline of the dissertation

The outline of the thesis is presented as follow:

Chapter II: This chapter consists of a brief background on the research topic and includes the following:

- a) An overview of common tailings deposition methods in the oil sands industry.
- b) A review of previous theories on predicting the geometry of tailings deposits and techniques on how to measure the rheological properties and discussion on various numerical methods applied to non-Newtonian fluids.
- c) Explaining the details of a field pilot program at Shell AFD (Air Fines Drying), Muskeg River Mine (MRM) initiated in 2012. This test program includes various deposition schemes such as (thin multiple lifts, thick multiple lifts, and deep stacking).

Chapter III: Provides a description of the methods employed throughout the course of this study and the materials utilized for both rheological testing and flume tests.

Chapter IV: A detailed description of rheometry test results will be presented and applicability of thixotropic models will be discussed. The data presented includes stress growth tests on samples after different rest periods, controlled shear tests to simulate stress histories likely encountered during deposition, and measurement of elastic shear modulus using oscillatory rheology, to track destruction and recovery of structure during shear. The results are explained using a viscosity bifurcation model of Hewitt, (2012).

Chapter V: This chapter focuses on microstructural studies and ESEM analysis on amended oil sands tailings over different resting times and shearing conditions.

Chapter VI: This chapter is allocated to large pilot scale flume test (8m long flume) at Oil Sands Tailings Research Facility (OSTRF), where the relevance of the rheology to surface

deposition is explored by analyzing two relatively large flume deposition tests conducted at two different deposition rates.

Chapter VII: This chapter will describe the theory of the numerical modeling approach, and how it is implemented in the commercial software used in the thesis. Results of the numerical modelling of bench scale tests along with modification for larger scale problems (field scale) will be presented.

Chapter VIII: presents a summary and discussion of the experimental results, significant findings and conclusion.

1.5 Publications related to dissertation

The following section presents a summary of publications that have been submitted to various journals and conferences related to the research carried out for this thesis.

Mizani, S., Soleimani, S., and Simms, P. (2013b). Effects of polymer dosage on dewaterability, rheology, and spreadability of polymer-amended MFT. In Proceedings 16th International Seminar on Paste and Thickened Tailings. Belo Horizonte, Brazil. This paper is presented as part of this Ph.D. thesis in Chapter 2 and 3.

Mizani, S., and Simms, P. (2014a). Geometry of polymer-amended fine tailings deposits: yield stress measurement and numerical modelling. International Conference on Oil Sands Tailings, Lake Louis, AB. This paper is presented as part of this Ph.D. thesis in Chapter 4 and 7.

Mizani, S., and Simms, P. (2014b). Rheology for surface deposition of polymer-amended fine tailings. In Proceedings of the 17th International Conference on Paste and Thickened Tailings, Vancouver, BC. This paper is presented as part of this Ph.D. thesis in Chapter 4.

Mizani, S., and Simms, P. (2016a). Method-dependent variation of yield stress in a thickened gold tailings explained using a structure based viscosity model. Minerals Engineering. (98):40–48- This work is not part of this thesis but includes thixotropic rheology and modelling of hard rock tailings.

Mizani, S., and Simms, P. (2016b) .Rheology for deposition control of polymer amended oil sands tailings. Submitted to Journal of Rheologica Acta. Recommended for publishing pending revision, December 2016. This paper is presented as part of this Ph.D. thesis in Chapter 4 and 7.

Mizani, S., Simms, P, Wilson, W, and Beier, N (2016c). Thixotropic effects on the rheology of polymer amended mature fine tailings: Implication for surface deposition control and dewatering. International Oil Sands Tailings Conference, Lake Louis, AB. This paper is presented as part of this Ph.D. thesis in Chapter 4 and 7.

Mizani S, and Simms P (2016d). Deposition Modelling of Amended Oil Sands Tailings Accounting for Thixotropy. In Proceedings 19th International Seminar on Paste and Thickened Tailings, Santiago, Chile. This paper is presented as part of this Ph.D. thesis in Chapter 4 and 7.

2 Chapter: Literature Review

2.1 Alberta's Oil Sands

The world's increasing demand for crude oil, fossil fuel and energy has brought Northern Alberta's oil sands deposits in production, turning oil sands to a major industry in Alberta. The oil sands reserves of Northern Alberta are comparable to those of Saudi Arabia (larger than the reserves of Iran, Iraq or Russia), estimated to contain 1.7 trillion barrels of bitumen (Government of Alberta, Canada, 2009). It is also estimated that 170 billion barrels may be recovered with the existing technology.

The following figure illustrates the three major areas in which the oils sands are contained: Athabasca, Cold Lake and Peace River (covering an area of approximately 142,200 km²). To produce 1 barrel of oil, approximately two tones of oil sands must be dug up.



Figure 2.1-1 Three major oil sands areas (Modified from EUB, 2004).

While 20% of oil sands are recoverable through surface mining the remaining 80%, can be recovered through in situ techniques (Government of Alberta, Canada, 2009). For deeper deposits (greater than 400m) extraction techniques similar to those used in conventional oil productions are utilized. One of the popular methods utilized in the oil sands industry today is the steam-assisted gravity drainage (SAGD) through the use of two parallel wells. While steam is injected in one (helping in release and flow of bitumen), the lower well is used for collecting and returning the released bitumen. Figure 2.1-2 illustrates the three stage of SAGD process.

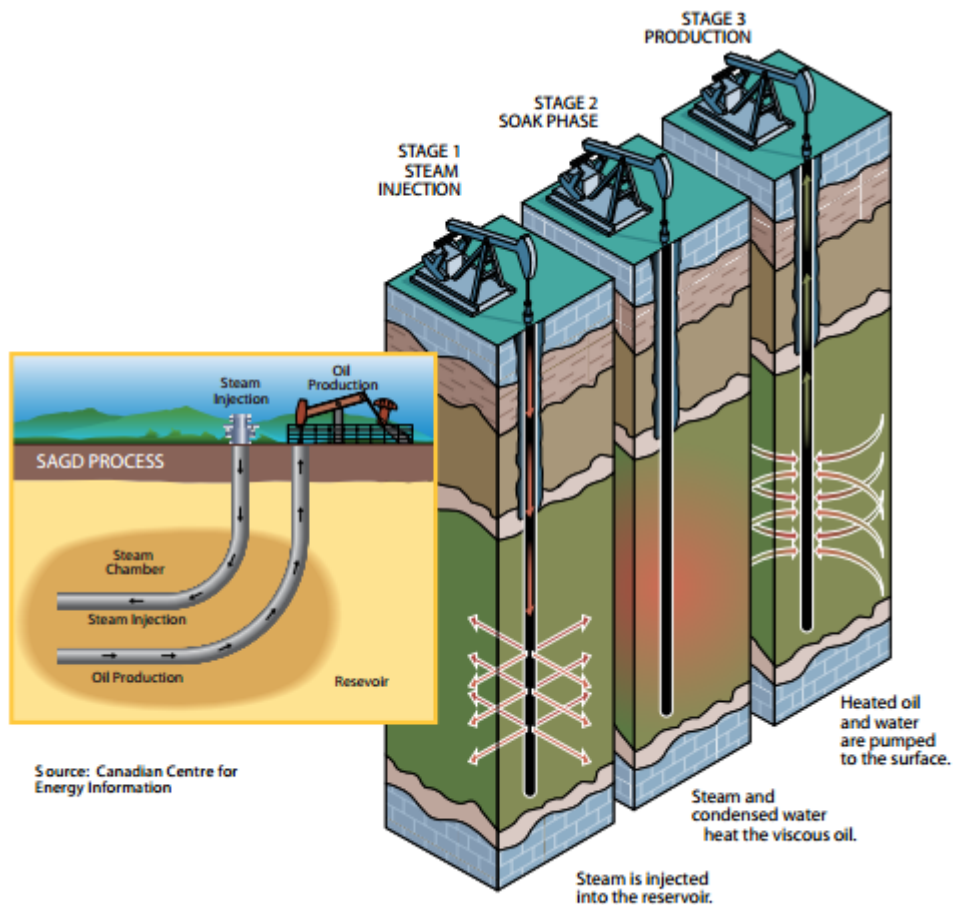


Figure 2.1-2 Steam-assisted gravity drainage (SAGD) technique used in oil sands industry in deep deposits (Modified from Government of Alberta, Canada, 2009).

The recovered bitumen requires additional upgrading through the use of temperature, pressure and catalysts. By adding hydrogen or removing carbon the bigger molecules are cracked to smaller ones creating hydrocarbon molecules similar to conventional crude oil.

The oil sands deposits are comprised of quartzose sand, and finer grained lithology. The sand grains are covered by a thin (10 nm) film of water surrounded by bitumen film (Zhu, 2013). It was Albian Boreal Sea which gave birth to Albian Sands about 100 million years

ago resulting in spread of the sand over a large area (Hein et al. 2001). It is believed that oil originated somewhere else and later flowed into the deposits (Jeeravipolvarn, 2010).

2.2 Basic properties of Tailings and Bitumen Extraction Process

Athabasca deposit is the largest of the three mentioned deposits and the thin overburden (less than 75m), mainly composed of muskeg and glacial till, makes this deposits suitable for surface mining (EUB, 2004; ERCB 2011). Fort McMurray formation (Athabasca) is a mixture of bitumen (12% in average of total mass), water (3-6%) and silts and clays minerals (84-86%) (Chalaturnyk et al. 2002). The clay minerals are mainly composed of kaolinite and illite and small amounts of smectite, vermiculite, chlorite, and mixed layer clay mineral, as summarized in Kaminsky (2008); Kotlyar et al. 1984; Ignasiak et al. 1985. One may thus expect oil sands tailings to have low Cation Exchange Capacity (CEC) and low surface area; however, this is not the case and these tailings often illustrate poor settling behavior. Researchers found that mixed layer clay minerals (kaolinite-smectite and illite-smectite) in oil sands with < 50% swelling characteristics, are the main reason for this discrepancy (Bayliss and Levinson, 1976; Ignasiak et al. 1983; Dusseault et al. 1989; Smith and Ng, 1993). It is not yet clear whether the swelling characteristic are due to smectite layers or surface charge distribution alteration of kaoline and illite particles (Nadeau et al., 1984).

As of today the four major companies (Syncrude, Suncor, Shell and Canadian Natural Resources) in Fort McMurray, Canada use the Clark Hot Water Extraction (CHWE) process to separate bitumen from oil sands. In this process a combination of steam, hot water and sodium hydroxide (NaOH) is used for the extraction process (Clark and

Pasternack, 1932). In case of Athabasca tar sand, where bitumen exists between the voids of water-wet sand structure, the Hot Water Process is the most successful technique for bitumen extraction process (Chalaturnyk et al. 2002). Fine clay particles exist either in the water film layer around the sand particles or as discontinuous thin beddings.

Figure 2.2-1 illustrates the hot water process utilized to extract bitumen from oil sands. First step after crushing the ore, called conditioning, is where the sodium hydroxide is added to aid in bitumen liberation from sand particles at 80-85⁰C. Sodium hydroxide facilitates changes in surface chemistry that induce repulsion of bitumen from the solids. The material is then transported to the separation vessels where steam is pumped and bitumen flotation takes place. Flotation is promoted by the air trapped in oil sands while the coarse fraction settles to the bottom of the primary separation cone. In order to recover the bitumen from the unfloated part, the central part of the slurry is then transferred to the scavenging cell, where additional air is injected. The fine solids are then removed from the froth through additional process. After additional recovery (in tailings recovery unit) of bitumen from the separation units the underflow is then combined with the coarse from the separation vessel and sent to tailings pond. Depending on the grade, fine content and origin of the oil sands the recovery could be anywhere between 88% to 95% (BGC Engineering Inc. 2010).

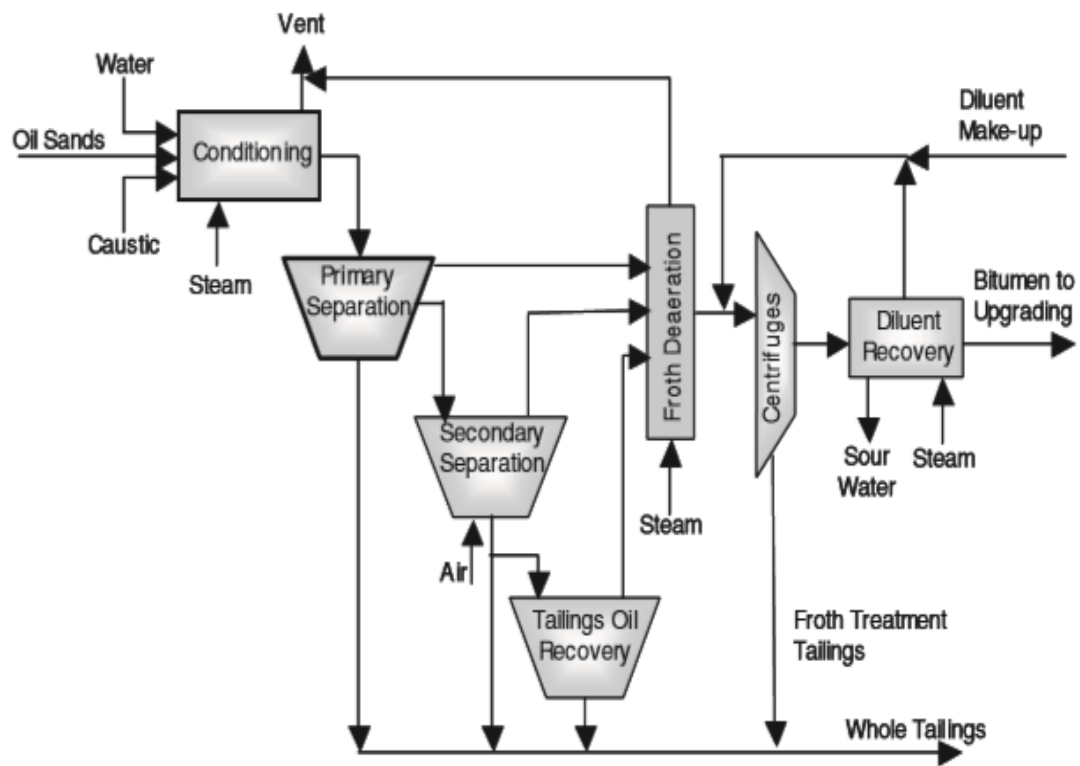


Figure 2.2-1 Schematic of HWP bitumen extraction (Chalaturnyk et al. 2002).

2.2.1 Mature Fine Tailings

Current HWE processes require large volumes of water (9m³ of water for 1m³ of bitumen) and produce high water content tailings with very poor consolidation properties (partially due to their low hydraulic conductivity). In conventional deposition, upon deposition of tailings into ponds, the coarser portion (sand) drops out forming a beach while the finer fraction along with residual bitumen will flow into the pond at a solid content of around 8%. With settling taking place over time, a clear water zone will be formed at the top of the tailings, this water is then pumped back to the extraction plant.

Although initially the settling rate is high (no significant stress transfer between the particles), after reaching a solid content of around 15-20%, the settling rate decreases

significantly. This is mainly due to the presence of bitumen and clay particles (Scott et al. 1985). Settling to 20% solid content happens rather quickly after which consolidation comes into play but happens very slowly bringing the solid content up to around 30%. In this stage the slurry is called Mature Fine Tailings (or MFT). The low rate of consolidation is attributed to both the low hydraulic conductivity of MFT, and the development of preconsolidation pressure due to thixotropy, which has been shown to reduce effective stress in long-term studies of MFT consolidation (Scott et al. 2013). Aside from the small pore-sizes of the MFT due to high degree of dispersion, residual bitumen content is believed to be a contributing factor to the low hydraulic conductivity (Scott et al. 1985 and Jeeravipoolvarn, 2005).

2.3 Challenges Associated with Oil Sands Tailings

Addition of caustic soda during the extraction process promotes dispersion and higher bitumen extraction by inducing negative surface charges. This process also slows down the sedimentation and consolidation potential of tailings clays thus producing large volumes of un-reclaimable fluid fine tailings.

In addition to handling of large volumes of fluid tailings, water management is also an issue since there is no allowance for effluent discharge to the environment. Reclaim water has to return to the plant for additional oil extraction, but quality of the reclaimed water will affect the extraction efficiency. For instance, ion accumulation in the recycle water will make extraction less efficient and raises the need for additional fresh water from lakes or water streams

Technologies used to accelerate dewatering of fluid fine tailings rely on a combination of physical and/or chemical processes. Chemical processes mainly rely on overcoming or reducing the steric and electrostatic forces between the particles. Different mechanisms can help in the destabilization: For instance, coagulants can help neutralize repulsive charges helping floc formation, or they can bind to a surface and produce opposite charges which aids in attracting other particles (Watson et al. 2011).

Previous attempts have been made to induce flocculation by adding inorganic coagulants (gypsum, lime) to increase the dewaterability potential of MFT. However, due to salt accumulation in reclaim water and the consequent harm to the extraction process, they are now typically replaced with high molecular weight flocculant (Demoz and Mikula, 2012).

2.3.1 Tailings Regulation

Directive 074 is an Alberta provincial regulation introduced previously in 2009 with the aim to reduce fluid tailings volume and to create trafficable surface such that tailings impoundment could be reclaimed within a few years upon deposition. A trafficable surface would require a minimum undrained shear strength, S_u , of 10kPa and the ERCB (Energy Resources Conservation Board of Alberta) requires the tailings to attain an undrained shear strength of 5kPa within a year and 10kPa after 5 years upon deposition. Tailings strength is directly measured in tailings deposits.

In March 2015, the Government of Alberta released Tailings Management Framework for Mineable Athabasca Oil Sands (TMF), and repealed Directive 074. During this time new requirements were developed. This policy provided guidelines to the Alberta Energy

Regulator (AER) on regulating fluid tailings volumes, and the reduction of risks associated with the buildup of fine tailings on the landscape. Minimizing tailings accumulation, through proper management of fluid tailings right from the start of the project was the main objective of TMF. All fluid tailings should be reclaimed within 10 years of the end of the mine life.

Recently, in July 2016, Directive 085: Fluid Tailings Management for Oil Sands Mining Projects was released. In this new government policy, new application and performance reporting requirements were introduced, where management plans were set as part of the phased approach to implement the TMF. While Directive 074 used a single requirement - shear strength of MFT- for tailings reduction performance, the TMF and Directive 085, use the overall volume of tailings to track tailings volume reduction (<https://www.aer.ca/about-aer/spotlight-on/alberta-tailings-managment-framework>).

As a result of this new regulation, operators have started investigating different technologies for dewatering these fluid tailings at large scales (Beier et al. 2013) some of which are explained in the next section:

2.3.2 Tailings Dewatering

Different technologies are available for dewatering oil sands tailings:

a) Filtered Tailings

Filtration of the whole tailings can be done through pressure or vacuum forces. However, the use of vacuum filtration for oil sands industry has been unsuccessful. This is due to the faster settling rates of coarser particles compared to the fines and formation of a layer with a low hydraulic conductivity on top of the porous filter cake and consequent

deterioration of the whole filtration process. However, coagulation and filtration have shown to be more efficient by forming a more permeable cake.

b) Centrifuge Tailings

In this technique, dredged tailings from the tailings pond are fed into a centrifuge upon mixing with gypsum and polymer. Under a force much larger than the force of gravity, the fluid (mainly consisting of water, bitumen and fines) is separated from the material leading to tailings streams with solid content as high as 60% (Devenny, 2010). Degree of densification can be controlled by the rotating speed and angle of centrifuge (Read, 2014). The centrifuged water is then pumped back to tailings pond.

One of the main advantages of centrifugation is the instantaneous water release and a cake of clay material which is strong enough for reclamation. Recently, following several years of research consisting of field pilot and commercial demonstration at Syncrude and Shell, ability of centrifuge technology to produce clay strong enough for reclamation purpose has been proved. Syncrude's centrifuge plant with 18 centrifuges, total cost of \$1.9 billion, was commissioned in 2015 (Read, 2014).

c) In-line flocculation

In this technique the fines are separated from water by adding chemical additives and subsequent deposition on sloped beds. Polymer is added to dredged MFT collected from tailings pond and right before re-deposition into cells. After flocculation tailings will be either deposited in subsequent thin layers which mainly rely on settlement, evaporation and

seepage for additional dewatering or they will be deposited in very thick lifts (>10m) which promotes further dewatering through self-weight consolidation (Beier et al. 2013).

d) Electrical

One of the emerging technologies in tailings dewatering is the electrical treatment process. In this technique dewatering is done through the application of an AC or DC current where negatively charged particles (clay) are directed to the positive electrode causing rapid dewaterability. However, many issues such as high energy costs, unfamiliarity with the technique and problems associated with anodes corrosion in commercial scale have led to difficulties in implementing this technique.

2.3.3 Flocculation

Flocculation is a process through which fine particles are binded up together to make larger particles (flocs). This process can be divided into three stages: destabilization, floc formation and floc degradation (Hogg, 2000).

Destabilization occurs by suppression of interparticle repulsion forces and compression of the double layer. This allows the particles to come closer to the point where attractive forces become dominant. Further floc growth is promoted in the second stage through particle-particle interaction. Although mixing will help the particle-particle collision, excessive shearing will break the previously formed flocs. Therefore, the optimum mixing time for maximum dewatering should first be investigated.

Ultra-high molecular weight flocculants act as a binding agent which spans the gap between particles. It has been shown by Hogg (1999) that the adsorption rate of flocculant

to particles is high thus it is essential to ensure uniform distribution of the polymer. High molecular weight flocculant can absorb on to multiple particles at once along their length or end points. Flocculant charge will also help in stretching the polymer and creating extra space for more particles to adhere. The rate at which flocculation takes place is very important in determining the rheological behaviour of the material. For instance, in multilayer casting of fresh concrete a high rate of flocculation will prevent the mixing of the two layers creating a weak interface.

Flocculation of MFT is conducted in the following steps: first, the polymer is blended with the MFT. Then, alignment of particles take place to help form flocs after which excessive care should be taken to avoid floc breakage by controlling the shear rates. It can be observed that these two steps have conflicting requirement. On one hand high shear rates are required to achieve a better blending and capture all the fines, on the other hand, the flocs will break under excessive shearing. A schematic of the flocculation process is illustrated below (Figure 2.3-1).

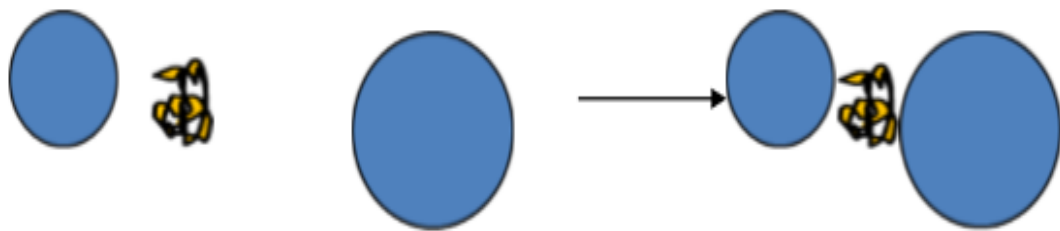


Figure 2.3-1 Schematic of flocculation process.

2.3.4 Characteristics of Flocculated MFT

Characteristics of Flocculated MFT can be evaluated based on both dewaterability potential and yield stress (rheology). The first term is linked to flocculation efficiency and the second to flow and beaching behaviour.

Dewaterability is defined as the net water release considering both water used in flocculant solution and water in initial MFT (Watson et al. 2012):

$$\text{Net Water Release} = \frac{W_R - W_A}{W_0} \times 100 \quad 2.3-1$$

Where,

W_0 is the initial water in MFT

W_A is the water added to floc solution

W_R is the water released.

Water removed from the tailings is commonly measured after 24 hours upon mixing (Najafi et al. 2014; Demoz and Mikula, 2012). For the material to be considered as well flocculated the NWR should be positive.

2.3.5 Sub-aerial Deposition and Dewaterability

After flocculation, tailings are deposited in multiple sloped cells (1-5%) to assist in the dewatering process through settlement, evaporation and seepage. These cells are separated by perimeter dykes with several spigots lined on them. Deposition points are either placed on all sides or on the header berms for a better coverage. Operational and topography parameters also control material spreadability in the cells. The other important factor is the pour quality itself. The more fluid (low viscosity) the material the further distance they are

going to reach, therefore a horizontal surface will be expected after filling the cells. On the other hand, the more viscous material tend to stack up near the discharge point where the final geometry is mainly dependent on the yield stress and flow rate. A combination of both processes will help maximizing footprint utilization and minimizing construction work related to perimeter dykes.

Different kinds of flow can be observed during deposition: stacking, sheet flow, laminar and turbulent. Charlebois 2012, for instance, used visual observations to characterize the flows. In stacking flows a rising stack or cone of material is observed where the horizontal momentum are small. Laminar flows occur when flows have relatively low velocity or when well flocculated material form stable flows. On the other hand, turbulent flows happen when low viscosity material is produced or high flow rates are used for deposition.

2.4 Role of Rheology in Tailings Management

Behaviour of oil sand tailings is characterized by the existence of a yield stress, which is the stress that must be exceeded before the fluid can flow. Mizani et al. (2013a) has shown that for gold tailings, the yield stress that best characterizes when the tailings stop flowing, can be very different from the yield stress that characterizes when the tailing start flowing. This distinction is even more important in polymer amended fine tailings, since breakage or reformation of flocs during flow could also affect the “stopping” yield stress.

As the material flows down gradient, shear rates decrease due to energy losses; causing shear stresses to fall below the yield stress and eventually bring the flow to a sudden stop.

The following paragraphs will explain the role of rheology for studying the microstructural changes of fine material under shearing and resting conditions.

2.4.1 Effects of Micro-structure on Rheological Behaviour

Rheology is very common in chemical and food science in which the mechanical behaviour of fluids and plastic bodies are studied under external stresses. Considering that the main components of the mechanical strength of soils are processes at the particle-particle or particle to liquid scales rheological methods may be used to relate mechanical behaviour to microstructure.

Structure of material is oriented in a state, which is a function of its minimum energy. When an external force is applied the system will resist deformation by showing a high resistance either in the shape of viscosity or yield stress. As the applied force increases, depending on the microstructure, material will either align in the direction of flow, or deform, or the aggregates decompose to the initial state (Chhabra and Richardson, 2008). These changes in the microstructure result in the material's flow. However, at very high stress levels the microstructure will reach an equilibrium state and the material will exhibit a constant viscosity. Figure 2.4-1, illustrates the various structures at rest and under shear.

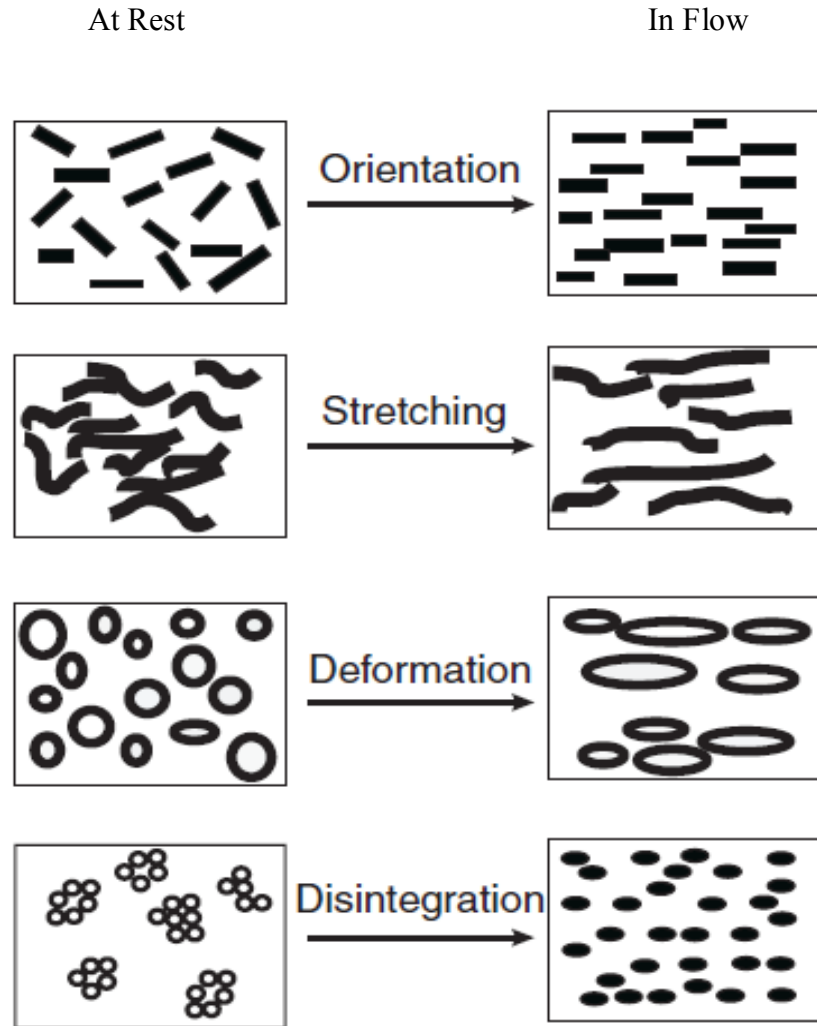


Figure 2.4-1 Various structures at rest and in flow (Modified from Chhabra and Richardson, 2008).

Each of these structures can pose different rheological behaviour. For instance, kaolin, which consists of plate like particles, can form aggregates in the form of edge-face or face-face type (depending on surface charges). While behaving as a yielding material in the edge-face form, in its face-face configuration it shows a much lower viscosity and hardly any yield stress.

2.4.1.1 Particle Association

According to Van Olphen (1963) particle association in suspension may be described as follows:

- I. Dispersed-with no face to face association of particles
- II. Aggregated- in a face-to-face (FF) association of several particles
- III. Flocculated-in an edge-to-edge(EE) or edge-to-face (EF) association of aggregates
- IV. Deflocculated- where there is no association between aggregates.

Aggregation of clay particle is dependent on the pH values (Jasmund and Lagaly, 1993). Structures formed by the edge to edge and edge to face association of clay particles may collapse under applied stress, but generally higher structural stabilities are expected in case of thicker and larger face to face associations (Rosenqvist, 1959 and 1962). However, depending on chemical composition and structure they may exhibit different mechanical behaviour (Figure 2.4-2).

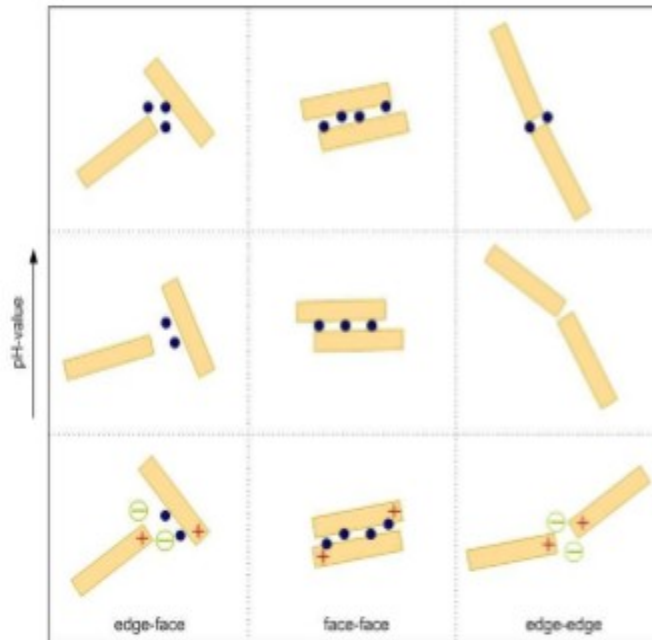


Figure 2.4-2 Dependency of clay particle aggregation on the pH-value (Jasmund and Lagaly, 1993).

2.4.1.2 Deformation

According to Kézdi, (1974) and Mitchell and Soga, (2005) strains consist of elastic and plastic parts; thus, soil can be defined as visco-elastic material. In soil mechanics, at low stress levels the strain increases linearly with stress, (elastic range); however, beyond a certain stress level soil reaches a plastic state, and strain increases continuously (DAS, 2008). In other words, plastic strains develop only when the stress state satisfies some failure criterion. Referring to this definition, the yield point is the transition point where the state of soil changes from elastic to plastic (viscous). In solid mechanics, the small strain shear modulus G is defined as:

$$G = \tau_c / \gamma_c \tag{2.4-1}$$

Where,

τ_c is shear stress

γ_c is shear strain.

In case of linear elastic material there exists a linear relationship between stresses and strain. However, real material's behaviour do not show a perfect linear behaviour and viscoelastic material models such as Kelvin-Voigt and the Maxwell model are more frequently used to describe the behaviour of plastics, polymers or, soil. Maxwell model uses a combination of dashpots and springs assembled in a row and is mainly used for modelling viscoelastic fluids. Kelvin Voigt model is mainly used for viscoelastic solids where combination of dashpot and springs are set up in parallel (Kézdi, 1974; Mezger, 2006; Markgraf, 2006). Soil stiffness in the linear elastic zone may be used to evaluate soil response under dynamic loadings also used as an indirect means to study the structure of the soil (Garciano et al. 2001).

2.4.1.3 Amplitude sweep test

Amplitude tests are conducted at a constant frequency while varying the shear stress or the shear strain. This type of tests are useful in case of high viscosity material such as soils and for obtaining information on the structural changes especially in the elastic part (in the linear viscoelastic zone) where the storage and loss modulus run parallel (Guerrier et al. 2015). A schematic illustration of the above test is shown in Figure 2.4-3.

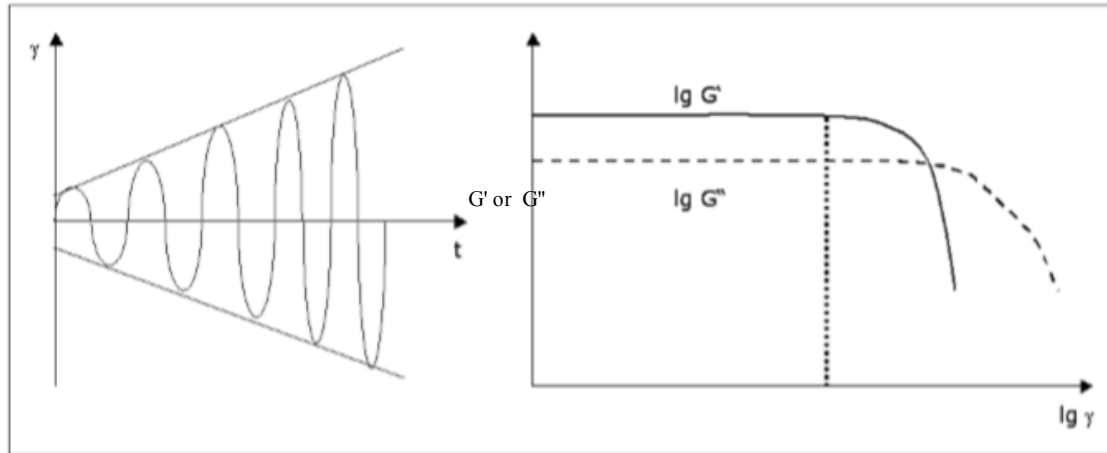


Figure 2.4-3 Amplitude sweep test at a constant frequency and variable deformation. G' is the storage modulus (elastic behaviour) and G'' is the loss modulus (viscous behaviour) (Markgraf 2006).

Jardine (1992) and Jardine et al. (2004), defined four zones to characterize deformation (or stiffness degradation):

Zone 1: true elastic region

Zone 2: nonlinear elastic region

Zone 3: pre-yield plastic region

Zone 4: full plastic region

The four zones are observed in the amplitude sweep tests (oscillatory conditions), where a transgression from elastic to plastic (viscous) state is evident (Markgraf, 2006).

According to this definition, above a certain stress level the soil deforms irreversibly, exhibiting plasticity. This behaviour is not limited to soils, non-Newtonian fluids may also exhibit elasticity in certain conditions: where they exhibit reversible deformation under

small strain. On the other hand, the fluid will start flowing if larger strains are applied or strains are applied for longer durations of time.

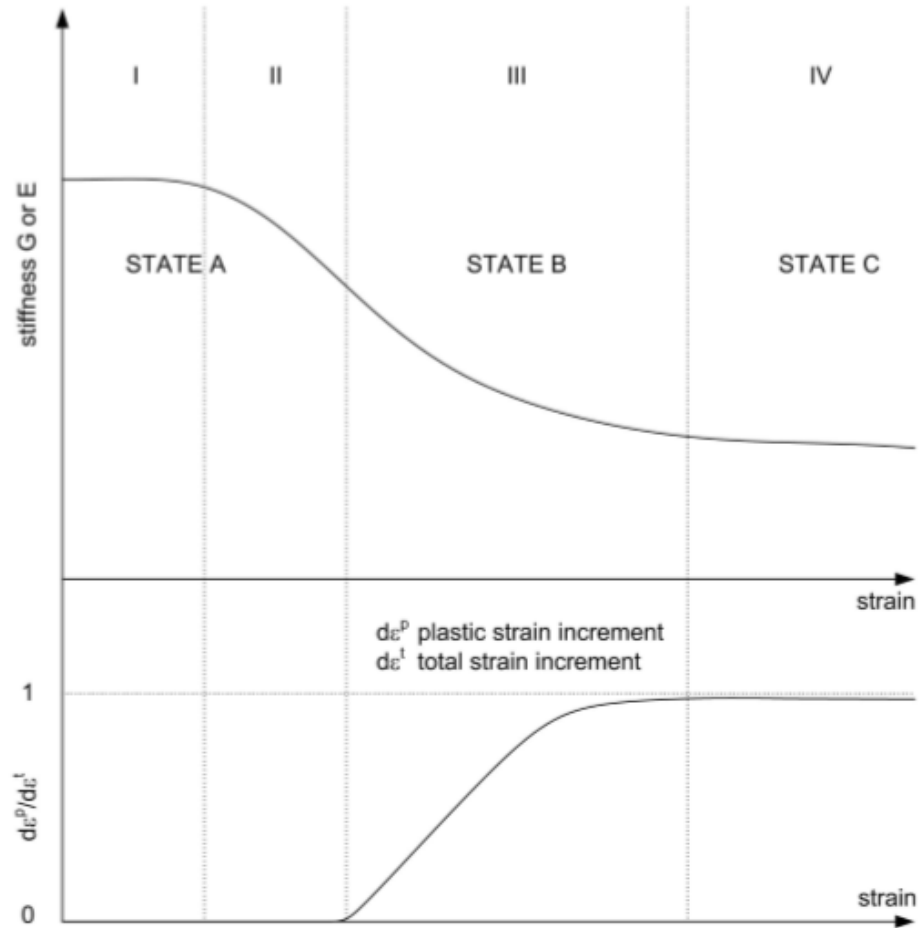


Figure 2.4-4 Four zones of deformation as defined by Jardine, (1992): Zone A, plastic strain ($d\epsilon^P$) is 0, zone B the region of true and non-linear elasticity, zone C or the full plastic region where $d\epsilon^P$ equals total strain ($d\epsilon^T$).

2.4.2 Fabric of Clay Material under Shear

When a clayey soil is sheared, depending on the grain size (coarse or fine), different behaviour could be observed. In finer material, shearing will not disrupt the continuity of

the structure and microstructure will reform instantly upon shearing. But in coarser material (i.e kaolinite) a local disruption will form along the shear zone.

Osipov et al. (1984), using SEM (scanning electron microscopy), showed only minor displacements occurring under static shearing for clayey soil. While deformations were elastic in the first stage of shearing, (particles going back to their initial state upon load removal), they can change to visco-plastic deformation if loading continues. In this stage rebuilding of the structure can also take place. Thus decrease in the strength of the material can be explained by both destruction and shear zone development, where the bondings become weaker between particles.

In oil sands tailings, which are mainly composed of kaolinite, a local disruption will occur during shearing causing porosity to increase. Formation of shear plane and structural rebuilding reduces the strength of the material. Given sufficient time after shearing (upon load removal) the structure will reform to its initial state where the soil strength starts to increase (Jeeravipoolvarn, 2005).

Different types of macroscopic behaviour could be observed when the material is exposed to shear. These include: shear thinning, thixotropic, yield stress and viscoelasticity (Mewis and Spaul, 1976; Russel et al. 1989; Coussot and Ancy ,1999).

In case of an ideal yield stress fluid, stress tends to a finite value at shear rates very close to zero, this would also imply that the stress should be above a critical value for the fluid to start flowing. If viscosity of the fluid decreases as a function of time, when it is subjected to flow, the fluid is said to be thixotropic (Coussot et al. 2002b). This time dependency may be explained by the reversible change of the microstructure when the fluid is sheared (Roussel, 2005). On the other hand, the fluid structure will reform when left at

rest; thus, the behaviour of the material is a function of both aging and destruction of the structure. Given the above discussion, a yielding fluid can be considered as a special case of thixotropic behaviour where the flocculation rate is very slow and the destruction rate is very fast.

Mizani and Simms, (2016a) showed that though tailings exhibit the characteristics of a typical thixotropic material at high shear stresses, at low stresses, their behaviour is dependent on the structure (or degree of jamming as defined by Coussot et al. 2002b; Quemada, 1999; Coussot and Ancy, 1999) of the material. Despite initial resistance to shearing, the material will start to flow gradually if the stress is held for longer time (Mizani and Simms, 2016a). This critical stress which determines the initiation of flow is not only time dependent but is also a function of flow history. Similar behaviour was observed by others on natural bentonite (Coussot et al. 2002a), which showed a time dependent yield stress (thixotropic behavior) in low stress ranges.

2.4.3 Thixotropy

Thixotropy is defined as a reversible and time dependent process which occurs after a material loses structure and liquefies when subject to shear, and rebuilds itself when left at rest or when its under a low shear rates (Mitchell and Soga, 2005). Figure 2.4-5 illustrates the properties of a thixotropic material as defined in Mitchel, (2005). Thixotropic strength ratio is defined as the ratio of the aging strength to remoulded strength (S_A/S_R).

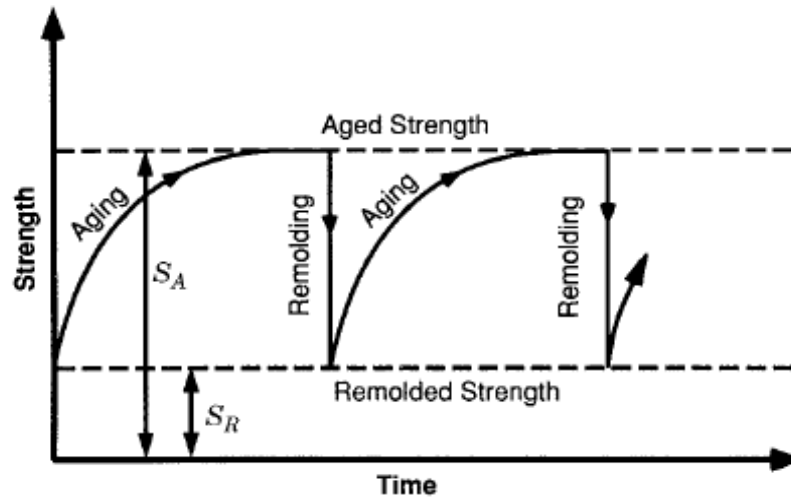


Figure 2.4-5 Thixotropic Material (Modified Mitchell and Soga 2005).

When material is at rest (i.e after remoulding, compaction,...), particles flocculate and water cation structure reorganize to a lower energy state. However due to existence of viscous forces acting on particles and ion movement, both processes would require some time to take place. This explains the time-dependency behaviour of material.

When thixotropic clay are sheared, initially a jump in the pore water pressure takes place. Pore water pressure will gradually go back down after sufficient time. This would imply an increase in effective stress with time and a consequent increase in undrained strength (Mitchell and Soga, 2005).

In terms of clay mineralogy, oil sands fine tailings are generally composed of 80 % kaolinite, 15 % illite, 1.5 % montmorillonite, 1.5 % chlorite, and 2 % mixed-layer clays (FTFC, 1995). Since kaolinite shows no thixotropy and illite shows only moderate regain in strength, oil sands fine tailings in their natural form are not expected to be thixotropic (Skempton and Northey, 1952). However, kaolinite can be made thixotropic by using a dispersing agent to reduce the degree of flocculation present in the natural material

(Mitchell, 1960). Due to the presence of sodium hydroxide (used as a dispersing agent in the bitumen extraction) and organic matter (in the form of residual bitumen), some thixotropic behaviour is expected from the tailings (Miller, 2010).

2.4.3.1 Thixotropy Models

Thixotropy fluids (i.e. clay suspensions, drilling fluid, cement...) have been extensively studied in the literature and several rheological models describing their behavior have been proposed (see e.g. Mewis and Wagner, 2009; Barnes 1997; Roussel, 2006; Coussot 2002 (a, b)).

Coussot et al. (1993), introduced a new model to describe the particulate systems exhibiting yield behaviour. In this model, transition from solid-like to liquid-like behaviour was described by a viscosity bifurcation rather than by a yield stress. The present study follows the development of the model which is described in Roussel et al. (2004), where the components τ and Υ of the viscosity, (i.e. $\mu = \tau / \dot{\gamma}$) depend on the current state of structure, λ , and where λ is considered to be a function of time and shear rate:

$$\mu = \mu_0(1 + \lambda^n) \quad 2.4-2$$

$$\frac{d\lambda}{dt} = \frac{1}{T} - \alpha \dot{\gamma} \lambda \quad 2.4-3$$

Where n , T , μ_0 and α are four material parameters.

This model does not contain an explicit yield stress, and instead, the unyielded region is identified by monitoring the changes in viscosity with respect to time. Under constant stress, viscosity will tend to infinity or to a very low value depending on the value of the

constant stress applied. When stresses are below the critical value viscosity increases in time until flow stops.

Other rheological model, such as that proposed by Hewitt and Balmforth (2013), involves inclusion of implicit yield stress value. This rheological model is adapted from Coussot et al. (2002a, b), where the original model is modified with a maximum value of structure, and the rate of aging is proportional to difference between the current structure value and the maximum value. The modified ageing term is a function of the maximum structure value as follows:

$$\frac{d\lambda}{dt} = \frac{(\lambda_0 - \lambda)}{T} - \alpha \dot{\gamma} \lambda \quad 2.4-4$$

Where λ_0 represents the fully structured state of the fluid and $\lambda < \lambda_0$ represent a material that is destructured to some degree (Hewitt, 2012). Hewitt and Balmforth, (2013) defined viscosity as a function of structure in the following form:

$$\mu = \frac{\mu_0 \lambda_0}{(1 - \lambda)(\lambda_0 - \lambda)} \quad 2.4-5$$

Where μ_0 is a constant reference viscosity.

Further details on these thixotropy models are presented in chapter 4 (section 4.6).

2.4.3.2 Effects of Consolidation on Thixotropic Strength

Thixotropy which is a function of mineralogy, water content, time and shear strain, has been shown to be one of the factors delaying consolidation of oil sands tailings (Banas, 1991). When soils undergo self-weight consolidation bondings are weakened and thixotropic strength between the particles are reduced. However, Banas (1991) has shown

that reduction rate is dependent on the rate and amount of consolidation. Both consolidation and thixotropic behaviour of fine tailings help them gain strength over time, but may have adverse effects on one another.

In summary, for surface deposition of oil sands tailings both aspects of thixotropic behaviour should be considered. Material gain strength when at rest (deposition times in order of days) and deflocculate under flow which happens as they come out of the pipe. This would mean that there exists no specific value for the yield stress but rather it is dependent on the flow history where viscosity could increase due to aging or lead toward a steady state where the flow will continue with a low viscosity (Cousset et al. 2002a).

2.5 Methods to Estimate Beach Slope Employed in Practice

Geoenvironmental and geotechnical (i.e consolidation, shear strength,...) properties of oil sands tailings and in general any type of thickened tailings is strongly influenced by the stack geometry. In previous sections the importance of tailings behaviour (rheological properties) on the final geometry has been discussed. This section reviews a number of methods for beach slope prediction which have previously been proposed and developed.

2.5.1 McPhail Stream Power

McPhail, (1995) model is applicable to laminar open channel flows and is based on a basic assumption where the stream power at any point is directly related to the velocity. In this method the slope of the deposited profile is linked to the energy dissipation of energy as the material flow down the beach. Assuming pressure head is very small, the power stream could be obtained through:

$$P_x = \rho Q g \left(\frac{v_x^2}{2g} \right) \quad 2.5-1$$

Where,

Q is volumetric flow rate,

ρ is density and

v_x is velocity at distance of x.

McPhail (1995) derived an equation based on maximizing entropy equation as follow:

$$P(x) = -\frac{1}{\beta} \ln \left[(1 - \exp^{-\beta P_0}) \frac{x}{L} + \exp^{-\beta P_0} \right] \quad 2.5-2$$

Where P_0 is the stream power at the plunge pool and β is the shape factor for the stream power decay curve and is related to the stream's rheology. For two points sufficiently close to one another, the assumption of constant density and flow rate is valid; therefore, the change in velocity head will be equal to the changes in the stream power. The slope of the profile at any distance x could be obtained by differentiating the above equation:

$$S_B(x) = -\frac{(1 - \exp^{-\mu P_0})}{L \mu \exp^{-\mu P(x)}} \quad 2.5-3$$

Since the elevation difference between these two points is equal to the velocity head difference, then one can assume the slope of the power stream to be parallel to the slope of the beach profile. Thus, tailings elevation at any point along the profile can then be obtained through:

$$y(x) = y(x + \nabla x) + S_B(x) \nabla x \quad 2.5-4$$

These equation require the determination of initial slope which is calculated through:

$$S_0 = \frac{\tau}{\rho g R_H} \quad 2.5-5$$

Where the shear stress is calculated using the Herschel and Bulkley (H&B) model and the rheological parameters measured in the laboratory. During the calibration process the fluid parameters are adjusted such that the shear stress calculated from the H&B model (sustainable shear stress) and that obtained using the flow velocity and channel geometry

$$\tau = f \frac{\rho V^2}{2} \text{ are within reasonable agreement.}$$

Charlebois, (2012) has previously employed this model on Suncor oil sands tailings; where the in-line mixing technique is used for flocculation. However, no spillbox was used in this operation and tailings fell out of the pipe with a horizontal momentum and some vertical momentum, due to gravity, causing a depression in the bed material. This contact will reduce the velocity of the particles and dissipates the initial energy of the tailings in the pipe.

In this study a model was developed to describe the relation between rheology and energy for the overland flow of flocculated tailings, where energy of the system was described by the kinetic energy alone. All measurements were taken within 2m of the discharge pool to make sure that the flow is stable and representative of the maximum unit volume kinetic energy ($E_k = \frac{\rho v^2}{2}$) of the material.

This model showed that at lower energy levels, laminar flow was initially dominant (at lower yield stresses), but eventually became turbulent as the energy level increased. Transition from laminar to turbulence flow was shown to be around 0.96m/s. Generally, at high yield stresses the flow forms a stack (above 200 Pa). It was also shown that in stacking

flows, yield stress fluid stoppage is dominant, causing a large areal extent of the tailings as oppose to channel flows. In channel flows, on the other hand, overbanking and narrow corridors along the beach were formed and sometimes even erosion in cases of turbulent flow.

2.5.2 Fitton Method

Fitton, (2007) developed three methods for estimating the equilibrium slope of tailings deposits: simple empirical, a priori and semi-empirical. The first method is based on flow rate and slurry concentration, which can be used as a fast and easy way to make reasonable slope prediction without any specific testing:

$$i = \frac{26.6C_w^2}{\sqrt{Q}} \quad 2.5-6$$

Where,

Q is flow rate from each spigot (l/s)

C_w is slurry concentration (w/w).

The Prior method, which integrates both non-Newtonian open channel flow and sediment transport, is based on minimum transport velocity of tailings which depends on the segregation nature of the tailings:

a) For segregating slurry

$$V_c = 3.8C_v^{1/4} \left(\frac{d}{4R_H} \right)^{1/6} \left(\frac{8gR_H(\rho_s - \rho_L)}{\rho_l} \right)^{1/2} \quad 2.5-7$$

Where,

C_v is the solids concentration by volume fraction,

d is median particle diameter,

R_H is the hydraulic radius of the naturally forming channel

With the densities referring to solid particle density and density of the carrier fluid respectively

b) For non-segregating slurry

$$V_C = 0.145 \ln \left(\frac{\rho V R_H}{\mu_{BP}} \right) \quad 2.5-8$$

Where μ_{BP} is Bingham viscosity.

This method is based on an initial guess for flow depth, using which the hydraulic radius is calculated R_H (the ratio of A/P). Then the average velocity (equal to Q/A) is calculated and compared with V_C . This process is repeated until the values obtained from V and V_c are equal.

The slope for a uniform flow in the channel could then be obtained through:

$$S_0 = fV^2 / (8gR_H) \quad 2.5-9$$

Friction factor f can be calculated through:

$$\frac{1}{\sqrt{f}} = -2 \log \left[\frac{k_s}{14.8R_H} + \frac{2.51}{\text{Re} \sqrt{f}} \right] \quad 2.5-10$$

and $K_s = 2D_{90}$ and Re is Herschel-Bulkley Reynolds number

Fitton and Mcphail method are only applicable to channelized flow, usually occurring after sometime in deposition and are probably not applicable to early evolution of the stack (Simms et al. 2011). The later method is based on finding the point at which sedimentation and erosion are in equilibrium and using a certain geometry for the flow. Also this

techniques is very sensitive to yield stress, thus accurate determination of rheological properties that are pertinent to field are necessary.

2.5.3 Lubrication Theory

Lubrication theory (LT), a simplified form of the momentum and continuity equations, has previously been used (Simms, 2007; Henriquez and Simms, 2009; and Mizani et al. 2010) to model the steady state and transient flow of yield stress fluid. The steady state profile of a Bingham fluid on a flat surface and inclined surface can be determined through:

$$\tau_y(x - x_0) = \frac{\rho g}{2}(h^2 - h_0^2) \quad 2.5-11$$

Where,

ρ is the density,

τ_y is the yield stress

h is the height of the free surface and is measured perpendicular to x

$$h' - h_0' + \ln(1 - h') = x' - x_0' \quad 2.5-12$$

where:

a is the angle of inclined surface

$$h = h' \left(\frac{\tau_y}{\rho g \sin a} \right) \quad 2.5-13$$

and

$$x = x' \cot \theta \left(\frac{\tau_y}{\rho g \sin a} \right) \quad 2.5-14$$

Also, Mizani et al. (2013a) applied the Lubrication Theory to multilayer depositions and found that while first few layers can be well predicted, the geometry start to exhibit a

convex profile as the number of layers deposited increase. By contrast, LT predicts an increasing linear slope as the number of layers increases.

2.6 Atmospheric Fines Drying (AFD) - Pilot scale Deposition of In-line Thickened Tailings

Atmospheric fines drying (AFD) technology is a version of in-line flocculation coupled with deposition in lifts implemented at Shell MRM (Muskeg River Mine). MFT (slurry at 35.5%) is harvested from a barge located at an existing tailings pond, transported via pipelines to AFD cells, with in-line mixing and discharge in to the bed. Flocculant (a high molecular weight anionic polymer) is injected at a distance before the end of the pipe (Figure 2.6-1). Additional conditioning of the material will then take place via submerged pipe outlet within the spill box. The deposited material then dewateres through a combination of mechanisms (immediate water release upon floc formation, settling and consolidation, drainage through the foundation, evaporation; and freeze-thaw for near surface of deposits over winter) where solids content and strength increases over time.

As mentioned previously, regardless of the deposition scheme, one key operational term that must be designed for optimization of surface deposition of oil sands tailings is lift thickness and the time to place the subsequent layer. In order to investigate the performance of both schemes, a pilot scale testing was conducted at Shell Muskeg River Mines where tailings were deposited in a single deep stack and another in Thin (~0.5m) and Thick (~1m) lifts. In Multilayer thick lift cell, a 1-2m lift were aimed for each deposition whereas, in Multilayer thin lift 0.5m lifts were deposited to get a total thickness of 4m. The total

thickness of tailings deposited in the deep stack was around 5m where tailings were deposited in one shot and over 11 hours.

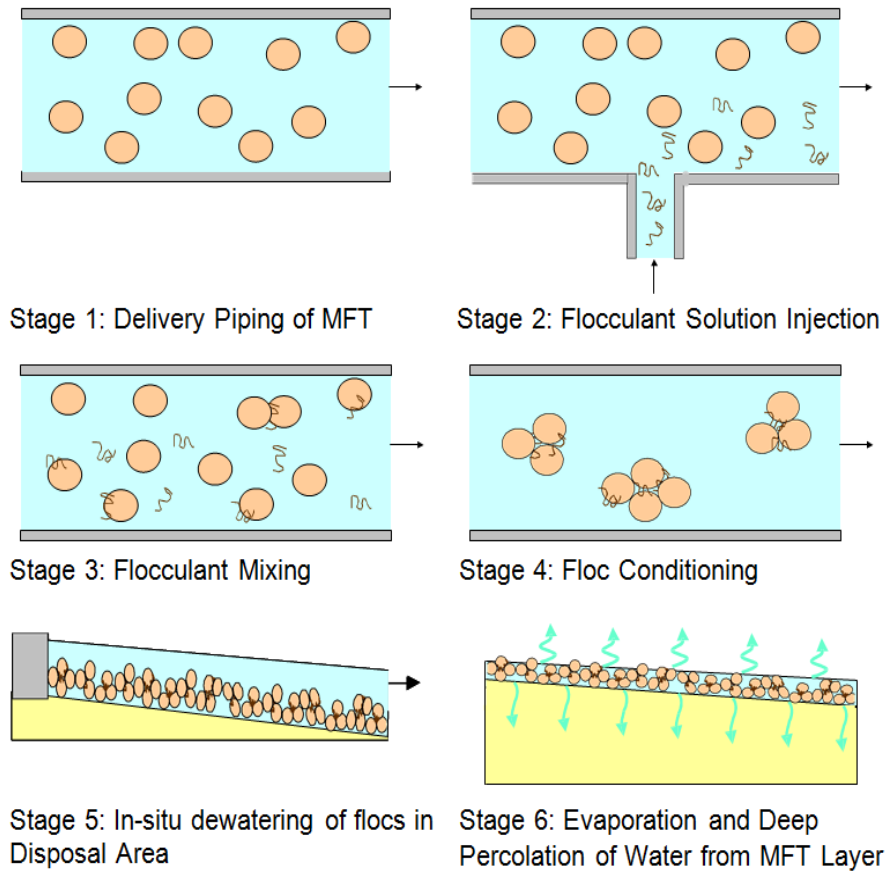


Figure 2.6-1 Generalized AFD Process (Modified from Barr Engineering report, 2012)

Schematic of deposition schemes in each cell are illustrated in Figure 2.6-2.

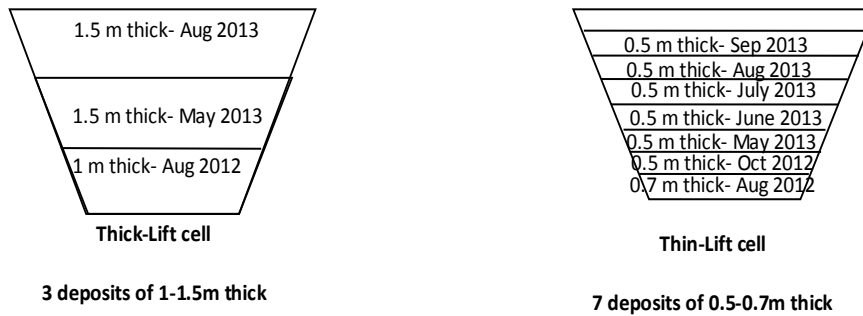


Figure 2.6-2 Schematics of deposition scheme for 2012-2013 depositions.

Two sets of pipeline are extended to all test cells with one conveying raw MFT and the other bringing the flocculant solution. Both MFT and flocculant are injected into one single pipe of 8 inch where a rapid mixing of polymer in a 17 feet pipeline is accomplished prior to pipe outlet (flocculation process). Flocculated material fell into spill boxes where the piping day lighted for additional conditioning and to decrease momentum before overflowing into the cells. All spill boxes were made out of LOS (Lean Oil Sands) and covered an area of 25m². The side berms constructed for the spill boxes were 2m high. The piping configuration and spill box used in all test cells is illustrated in Figure 2.6-3.

"On spec" material were identified as having a yield stress greater than 150 Pa and filtration constant greater than 1, as specified by Shell. This criteria was based on the finding from 2010 and 2011 field trials at Shell MRM, where the material which met the "on-spec" requirement had high initial water release potential and shear strength gain. A solid content of 35% was targeted for the raw MFT feed to each cell; however, some lifts had slightly lower solid concentration. Note that the higher flocculent dose was used in the

2012 compared to 2013. In 2012 operations, tailings were flocculated at 700– 950 g/tonne, which fluctuated as a function of field condition and pour quality.



Figure 2.6-3 Spill box and discharge piping configuration in Test Cell.

2.6.1 Velocity Measurements in Test Cells

Surface velocity measurements were also conducted during the August 2013 deposition in both thin and thick Multi lift cells. Although the velocity varies throughout the depth, but at the time of measurements no device with this capability was available. Velocities were measured using a polyethylene disk which was placed in the spillbox. The time was

tracked using a chronometer while the tracer passed between different measuring posts.

Some of the velocity measurements are illustrated in Figure 2.6-4 and Figure 2.6-5.

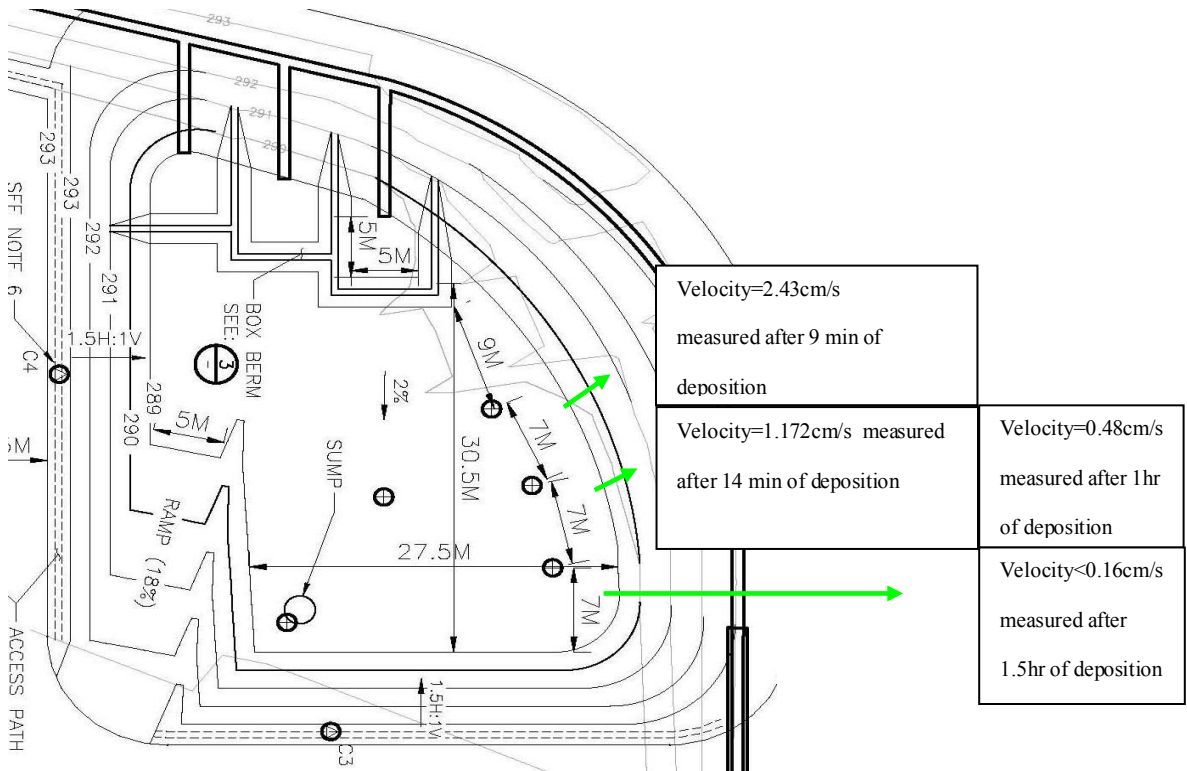


Figure 2.6-4 Velocity measurement during the 6th layer deposition in Multi-lift cell Thin.

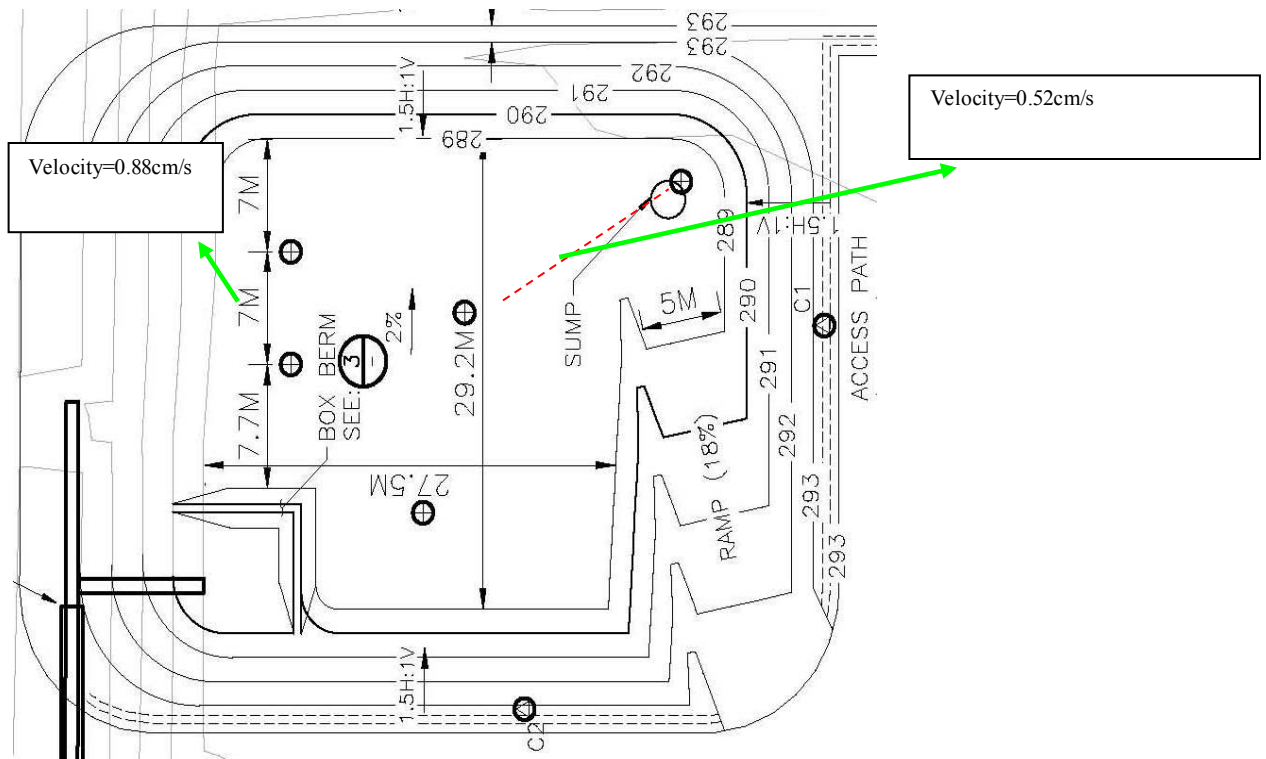


Figure 2.6-5 Velocity measurement during the 3rd layer deposition in Multi-lift cell Thick.

2.6.2 Rheological Characterization of Deposited Material

To investigate the impact of pour quality on flow behaviour and footprint optimization yield stress and filtration constants were measured during each lift at various times. All yield stress measurements were made on site after 30 minutes upon sample collection and decanting the release water. Yield stress values were measured using a HAAKE RotoVisco (RV1) rheometer through the stress growth technique at a shear rate of 0.1 s^{-1} . This shear rate was chosen as recommended by Shell. Slumps test were also conducted on all of these samples.

Sampling was conducted during each lift deposition where the material were collected at regular intervals from the spill box. Some yield stress measurements were also conducted

on samples collected at mid cell and downstream during deposition. Figure 2.6-6 illustrates how each sample was collected.

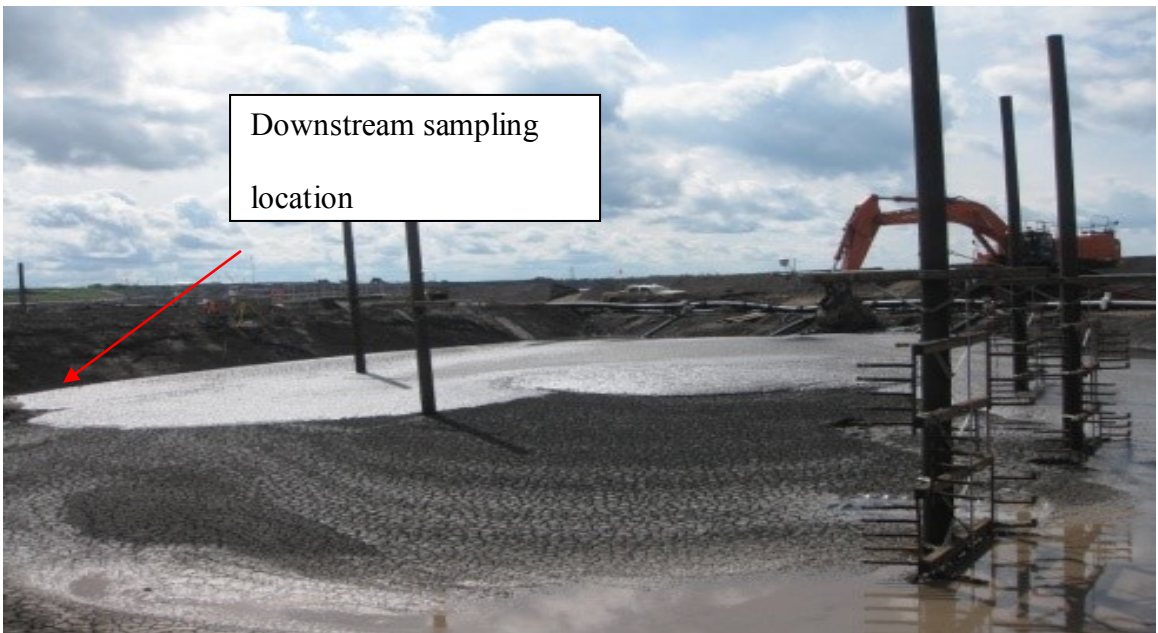


Figure 2.6-6 Collection of sample from upstream and downstream during deposition

Yield stress and slump heights measured during deposition events that Carleton crew were present are summarized in Table 2.6-1.

Table 2.6-1 Yield stress and slump heights as measured in on site laboratory

	Slump (cm)			Yield Stress (Pa)			Floc Dose (g/ton)	
	Mean	Median	Mean	Mean	Median	Range	Mean	Range
Thin Multi-Lift 1	5.3	5.3	[3.3, 6.9]	384.5	385.6	[266.0, 500.7]	835.6	[775, 863]
Thin Multi-Lift 2	5.9	6.0	[4.7, 6.9]	414.1	392.2	[266.2, 584.6]	899.5	[855, 940]
Thin Multi-Lift 4	4.2	4.1	[3.4, 6.2]	118.7	92.4	[82.3, 275.1]	895.6	[860, 935]
Thin Multi-Lift 5	4.3	4.2	[2.9, 7.9]	163.6	133.4	[48.6, 528.1]	1025	[1010, 1046]
Thin Multi-Lift 6	3.1	2.85	[2.4, 4.2]	75.5	68.15	[53.6, 126.1]	762.8	[705, 815]
Thick Multi-Lift 1	6.0	6.1	[5.6, 6.5]	339.5	316.1	[276.7, 469.9]	799	[781, 827]
Thick Multi-Lift 2	5.3	5.2	[4.0, 6.7]	221.8	223.3	[75.1, 376.4]	799	[779, 818]
Thick Multi-Lift 3	2.9	3.1	[1.9, 3.3]	76.5	77.2	[57.4, 93.4]	755.5	[713, 783]
Deep Stack	5.7	6.0	[4.4, 7.2]	392.4	401.0	[237.3, 512.5]	864.1	[809, 886]

2.6.3 Slopes of Deposits

In order to investigate the effects of rheological properties (yield stress and viscosity) on the beaching behaviour of tailings the slope and runout of deposit after each lift was recorded. Figure 2.6-7 and Figure 2.6-8 illustrates the deposition height, slope and runout after each lift in 2 sections as of Sep 2013.

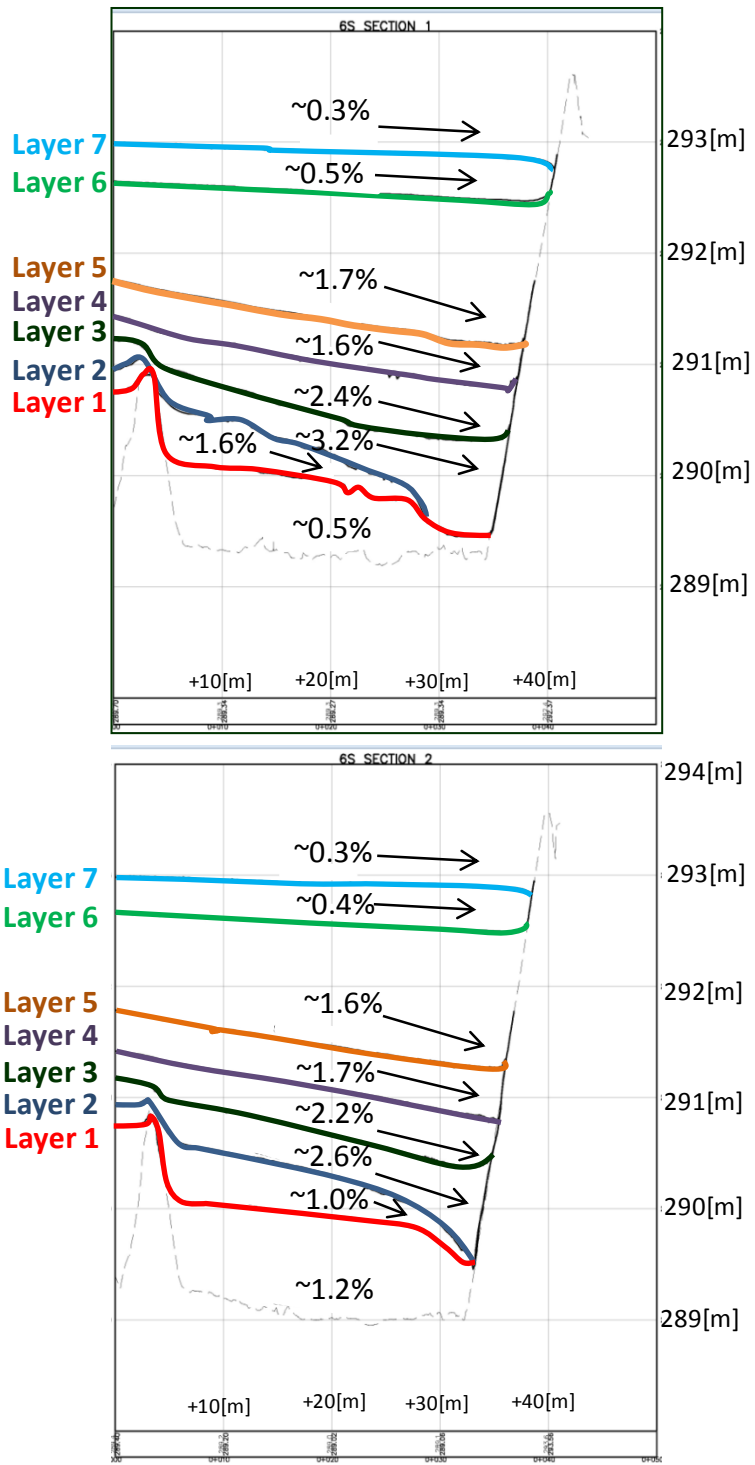


Figure 2.6-7 Thin Multilift cell profile after deposition of 7 layers in September 2013

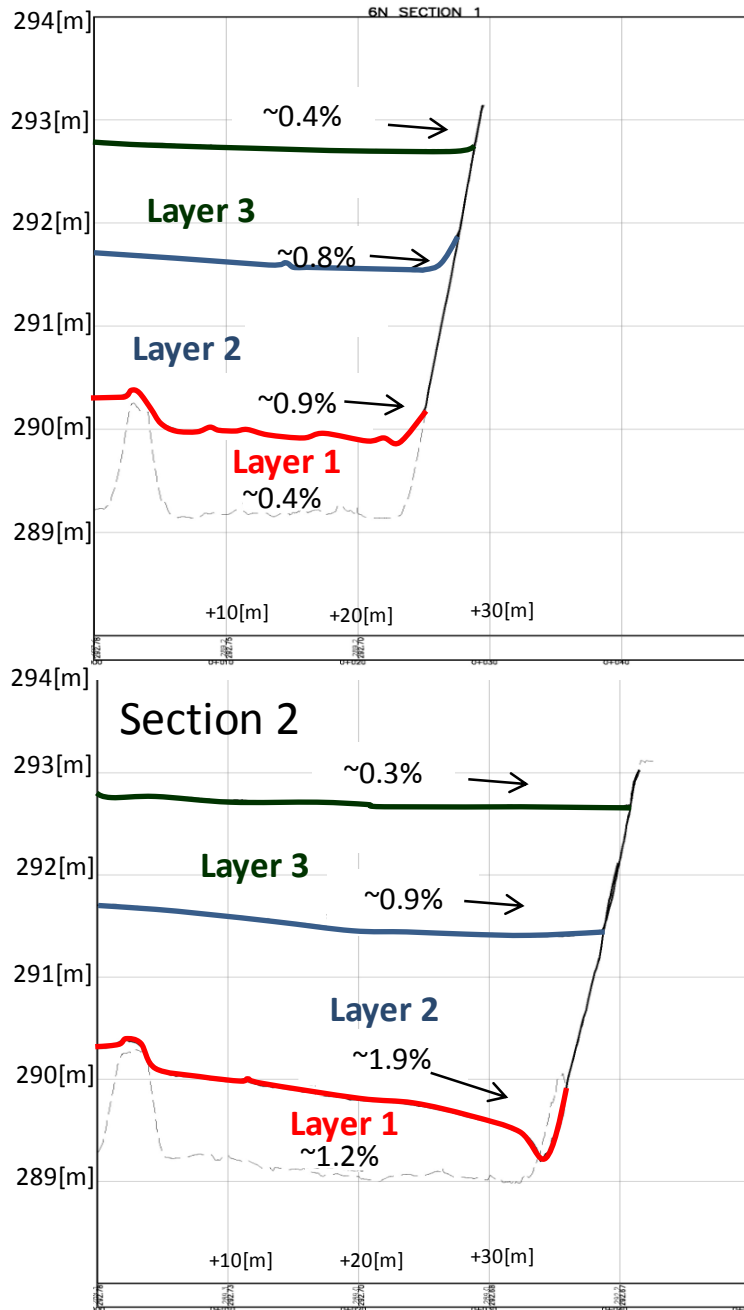


Figure 2.6-8 Thick Multilift cell profile after deposition of 3 layers in September 2013.

It is worth noting that the material deposited in 2013 campaign were mainly off spec having a yield stress <150Pa.

2.6.4 Slopes of Deposits at Field Scale

Figure 2.6-9 illustrates the tailings profile deposited at Shell Atmospheric Drying cell during the fall 2010 program. Total volume of tailings deposited in this cell was 7953 m³ with an average slope of 2.1%. Although rheological data was not available for this particular cell, 83.3% of tailings deposited during this year had an average yield stress 186 Pa and remaining had an average value of 459 Pa, according to Shell 2011 report (Dunmola, 2011). The predictions used Equation. 2.5-12, fixing the volume of tailings but using two different values of yield stress, 100 Pa which is the value represented by the flume tests (chapter 7), and 240 Pa, which is representative of the yield stress for the stress growth tests (chapter 4). While the higher yield stress value best predicts the maximum height of the tailings at the deposition point, the lower yield stress value better predicts the maximum run-out (Mizani et al. 2013b).

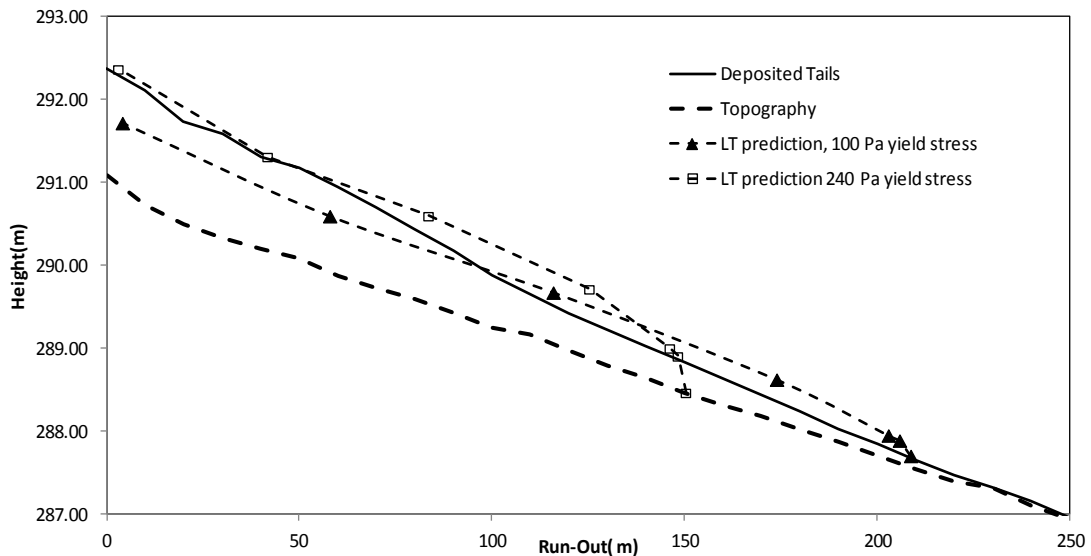


Figure 2.6-9 Tailings profile measured at Shell Atmospheric Fine Drying (AFD) operation at cell 4 during 2010 campaign.

Figure 2.6-10 illustrates the transient profile of the 6th layer in the Multilift cell along with the yield stress measurement over a course of 7 days.

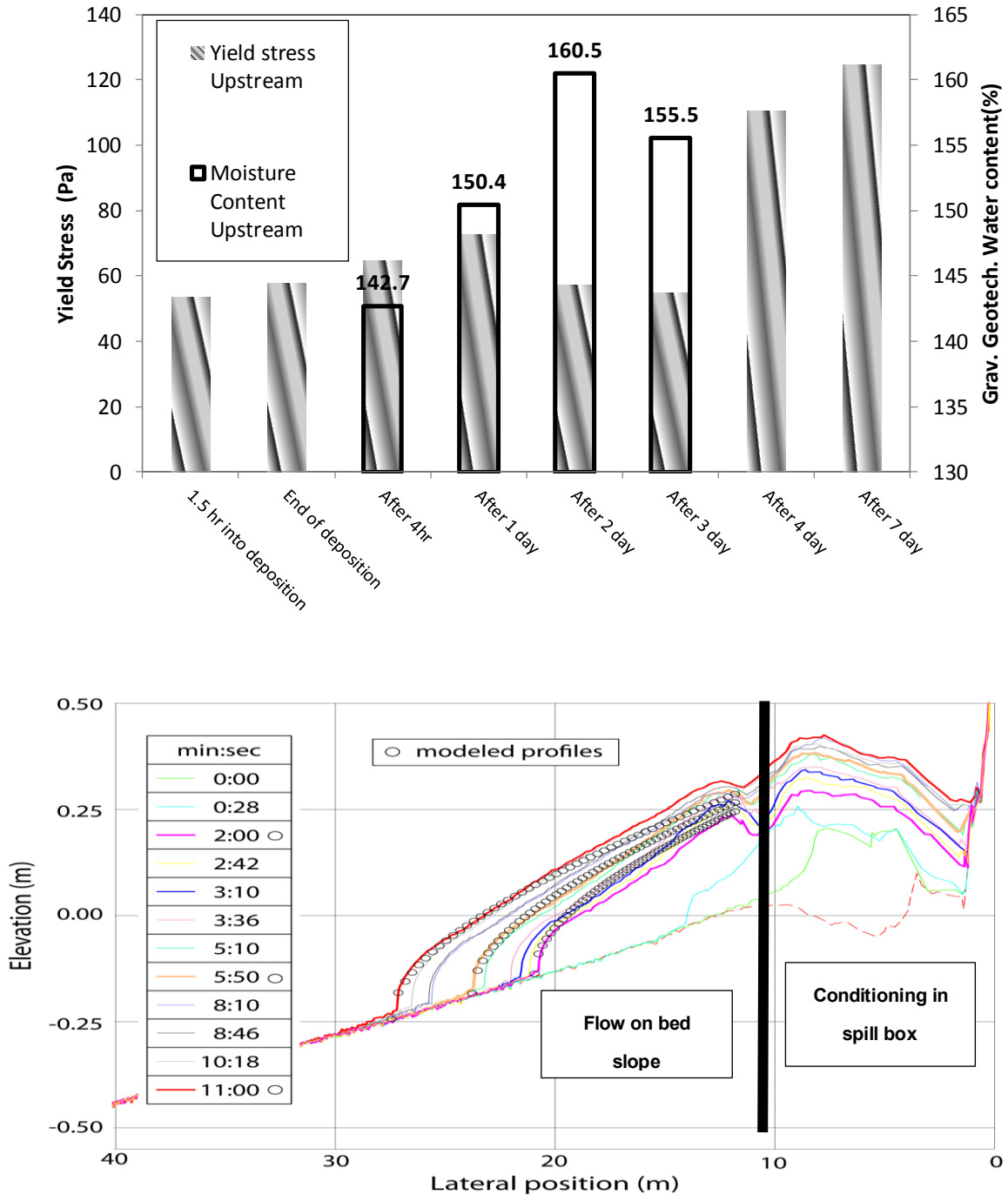


Figure 2.6-10 Yield stress measurement and dynamic scanning of Thin Multi Lift (Layer 6) from Barr Engineering.

The literature review explained in this chapter will be used in next chapters to investigate the influence of stress history (ageing and shearing) on rheology and in particular yield stress. Thus, in chapter 4 various methods of yield stress measurements on laboratory prepared samples will be examined. The later chapter aims to find the more appropriate technique for measuring the yield stress from surface deposition prospective.

2.7 Numerical Modelling of Non-Newtonian Fluids

Flows of tailings down the beach are initially dominated by inertia effects; however, as the material moves down the beach it slows down and viscous flow comes into play. Numerical simulation of dam break flows of various materials (where materials collapse under their own weight), has long being the research topic of many researchers since 1892 (Minussi and Maciel, 2012). Although initially materials experience high levels of stress, as the viscous regime becomes dominate the flow also becomes steady. The main issue in free surface flows is to find the wave front position. For material posing yield stress behavior, the front wave is comprised of two parts: lower sheared part and upper part or plug flow which moves with the same speed as the lower part. In the upper zone the fluid is subjected to smaller stresses allowing it to restructure with time. This results in higher flow resistance as a result of increase in viscosity (Chanson et al. 2006). Fluids posing a yield stress will eventually come to a stop when the gravitational forces become less than yield stress on slopes or when there is a balance between pressure cross flow and viscosity forces on flat surface (Ancy and Cochard, 2009).

There are different techniques to tackle complex problems such as flow behaviour of Non-Newtonian fluids: Finite Element, Finite Volume and SPH (Smoothed Particle Hydrodynamics).

2.7.1 Finite Volume

The finite volume method (FVM) has been used by several researches for flow behaviour of Non-Newtonian fluids (Spelay, 2007; Keslerova and Kozal, 2010). One of the main advantages of this technique over the others is the conservation of mass and momentum. In the finite volume method the domain is first divided into small volumes (meshing), where the conservation principles are applied and the partial differential equations are integrated over time and space. FVM can be applied in two modes: centre node based FVM and vertex based FVM. In the first version each element makes up a control volume, where the equations are integrated over each control cell. Values obtained for each variable are then stored in the central node. In the second version, control volumes are built around cell corners (Stenmark, 2013).

2.7.2 Finite Element

In this technique the domain is first divided in smaller elements and the equations are solved in each element. This method has also being used by several researches (Dean et al. 2007; Glowinski and Wachs, 2011). Naef et al. (2006) used the finite element method to simulate the laminar debris flow using the depth average shallow water equations.

2.7.3 Smoothed Particle Hydrodynamics

Smoothed Particle Hydrodynamics (SPH) is a mesh free Lagrangian based method where calculations are performed at the particles centered locations (Mcdougall, 2006). In this method the fluid is replaced by a set of particles. SPH has been previously applied to dam break problems and landslides of various rheology. Babaoglu, (2014) modelled the flow behaviour of high density tailings, using an SPH approach, where single layer flume test were successfully modelled using a bi-viscosity model (Babaoglu and Simms, 2013).

While the Lagrangian nature of SPH provides some advantages over the Eulerian based methods such as concentration of computational efforts in areas of fluid presence and elimination of complications of tracking the free surface, this approach has some limitations. For instance, boundary conditions are often challenging to implement in this method and particles penetration into boundaries should also be prevented. Also, the interpolation techniques used in this method may result in large gaps between particles and thus affect the accuracy of the results. Moreover, the computation times are longer compared to other mesh based methods with computational costs increasing with the number of particles.

Two frame of references can be used for solving the equations of motions:

- i) Eulerian frame of reference: which tracks the element from a fixed point in space similar to a person standing on the shore and witnessing the flow of a river.
- ii) Lagrangian frame of reference: where the reference moves with the fluid or particle i.e. a person standing on a boat. For the same number of grid points the Lagrangian frame can

give more accurate results; however, distortion of the mesh can lead to some numerical problems.

The use of Lagrangian reference is relatively simple: the cell remains identified with the same fluid element at all times, where the dynamic response of each element may be computed based on the body and surface forces. In this case the grid moves with computed velocities. In an Eulerian reference form, on the other hand, the grid is fixed and the identity of the fluid element is not maintained (Hirt and Nichols, 1981) and the fluid element are moved to the next position after the velocities are calculated. Averaging processes may be required when fluids of different properties find themselves in a single cell. This process results in smearing of the free surfaces. Therefore, it is of great importance to implement a treatment that avoids the averaging process on surfaces of discontinuity.

In this work simulations were carried out using an available commercial computational fluid dynamics (CFD) software ANSYS CFX.

2.7.4 Governing Equation

The equations solved for the numerical simulation of tailings down the beach are the conservation equation:

$$\frac{\partial \rho}{\partial t} + \nabla \cdot (\rho U) = 0 \quad 2.7-1$$

and momentum equations:

$$\frac{\partial(\rho U)}{\partial t} + \nabla \cdot \rho U \otimes U = -\nabla \cdot \tau + \rho g \quad 2.7-2$$

Where,

ρ is density, U is velocity vector and τ is stress tensor

$$\tau = \begin{Bmatrix} \sigma_x & \tau_{xy} & \tau_{xz} \\ \tau_{yx} & \sigma_y & \tau_{yz} \\ \tau_{zx} & \tau_{zy} & \sigma_z \end{Bmatrix}$$

σ representing normal and τ shear stress.

For an incompressible fluid the equations can be simplified to:

$$\nabla \cdot (U) = 0 \quad 2.7-3$$

$$\rho \left(\frac{\partial U}{\partial t} + \nabla \cdot U \otimes U \right) = -\nabla \cdot \tau + \rho g \quad 2.7-4$$

Rewriting Equation 2.7-3 and 2.7-4 gives the following mass and momentum equations:

$$\frac{\partial u_x}{\partial x} + \frac{\partial u_y}{\partial y} + \frac{\partial u_z}{\partial z} = 0 \quad 2.7-5$$

$$\rho \left(\frac{\partial u_x}{\partial t} + \frac{\partial(u_x^2)}{\partial x} + \frac{\partial(u_x u_y)}{\partial y} + \frac{\partial(u_x u_z)}{\partial z} \right) = - \left(\frac{\partial \sigma_x}{\partial x} + \frac{\partial \tau_{yx}}{\partial y} + \frac{\partial \tau_{zx}}{\partial z} \right) + \rho g_x \quad 2.7-6$$

$$\rho \left(\frac{\partial u_y}{\partial t} + \frac{\partial(u_y u_x)}{\partial y} + \frac{\partial(u_y^2)}{\partial x} + \frac{\partial(u_y u_z)}{\partial z} \right) = - \left(\frac{\partial \tau_{xy}}{\partial y} + \frac{\partial \sigma_y}{\partial x} + \frac{\partial \tau_{zy}}{\partial z} \right) + \rho g_y \quad 2.7-7$$

$$\rho \left(\frac{\partial u_z}{\partial t} + \frac{\partial(u_z u_x)}{\partial y} + \frac{\partial(u_z u_y)}{\partial z} + \frac{\partial(u_z^2)}{\partial x} \right) = - \left(\frac{\partial \tau_{xz}}{\partial y} + \frac{\partial \tau_{yz}}{\partial z} + \frac{\partial \sigma_z}{\partial x} \right) + \rho g_z \quad 2.7-8$$

Some modifications should be applied to viscosity term in the above equations, in order for them to represent a non-Newtonian problem. The modifications and advection transient scheme used in this study are thoroughly described in Chapter 7.

3 Chapter: Materials and Methods

Characterization tests were performed on raw MFT and process water received in 1m³ totes/drums. These tests were conducted with the purpose of establishing a baseline characteristic of the tailings and to ascertain consistency among samples received over the course of two years. Due to settlement of tailings during transportation supernatant water was collected at the top of the drums/totes. Drums/totes were remixed using a drum mixer (Model No DLM150VGD, Mixer Direct) at an average speed of 120 rpm for 24 hr alternating every 2hr between forward and backward mode to bring them back to their initial solid content. Tailings were then transported into 20 gallon buckets.

3.1 Mature Fine Tailings

MFT used in this study were obtained from Shell Canada's Muskeg River Mine (MRM). MFT were delivered to Carleton at 35.5% solid content. Tailings were remixed with the bleed water released during the transportation in barrels to bring them to their initial

condition. The geotechnical properties and particle size distribution (PSD) of the tailings are shown in Table 3.1-1 and Figure 3.1-1, respectively.

Table 3.1-1 Geotechnical properties of raw MFT

Property	Value	ASTM	Jeeravipoolvarn et al. 2014
Specific gravity	2.20	ASTM D854	2.45-2.48
D ₁₀ , D ₅₀ , D ₆₀ (microns)	0.8, 6.4, 11.1	ASTM D422 – 63	
Cu (D ₆₀ /D ₁₀)	14.1		
Liquid limit (%)	62.4	ASTM D4318 – 10	52.1-58.3
Plastic limit (%)	26.7	ASTM D4318 – 10	26.9-28.2
Hydraulic conductivity (cm/s) at e=4	4.3×10 ⁻⁶	ASTM D5084 – 10	
Fines content (<44µm, %)	78.7		

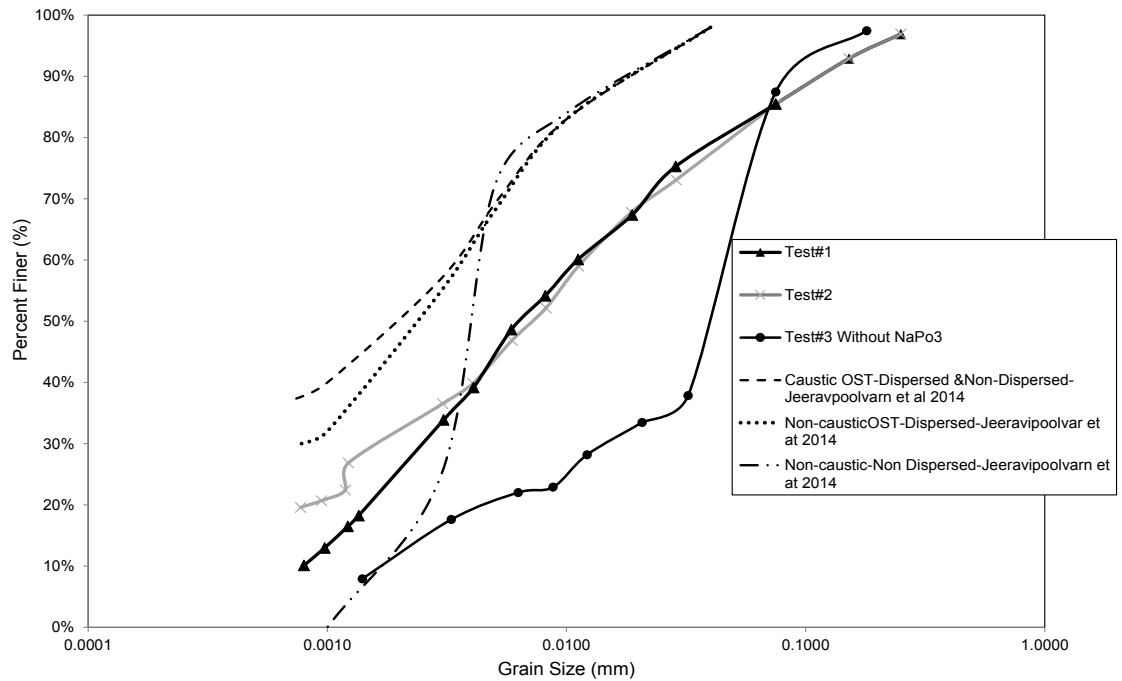


Figure 3.1-1 Particle size distributions of raw MFT from hydrometer and sieve analyses with and without using 4% sodium hexa-metaphosphate (NaPO₃)

Also presented in Figure 3.1-1 are the PSDs from caustic and non-caustic fine tailings from Suncor Energy. Inc. As expected, no difference was seen between the dispersed and non-dispersed hydrometer test since the caustic extraction process fully disperses the fines (Jeeravipoolvarn et al. 2014). On the other hand, for the non-caustic fine tailings, the test where no dispersant agent was used had less fine material. No significant change was observed for particles coarser than 4µm.

3.2 Property Test

Initially tailings properties such as solid concentration (C_s), moisture content, GWC, bitumen content and void ratio were measured in the laboratory:

3.2.1 Solids Content (C_s)

In the oil sands industry, solids concentration (C_s) is defined as the ratio of the mass of solids (including bitumen and other minerals) to total mass. To measure solid concentration, samples were dried in an oven for a period of 24 hours and at 105°C, the percentage solid was then calculated through:

$$C_s = \frac{M_s}{M_T} \quad 3.2-1$$

Where,

C_s = Solids Content (%);

M_s = Mass of solids;

M_T = Total mass.

3.2.2 Water Content

The amount of water in a given sample may be expressed either in reference to the total mass of the material (3.2-1), or the mass of solids. In this case it is referred to as gravimetric water content, (GWC), as shown in equation 3.2-3:

$$C_w = \frac{M_w}{M_T} \times 100 \quad 3.2-2$$

$$w = \frac{M_w}{M_s} \times 100 \quad 3.2-3$$

3.2.3 Bitumen Content

The bitumen content of oil sands tailings are often determined through the Dean Stark Analysis (Bulmer and Starr, 1979). In this technique a solvent (toluene), is used to extract water and bitumen from the solids in a sample.

3.2.4 Shrinkage Limit

Shrinkage limit is the water content between the solid and the semisolid states. The solid state is reached when the soil sample reaches a minimum volume, meaning that further drying will not cause a decrease in volume of soil mass.

The shrinkage limit, using the Wax Method, was determined to be around 14% for flocculated MFT dosed at 850g/tonne.

3.2.5 Void Ratio

In soil mechanics, void ratio is defined as the ratio of the volume of voids to the volume of soil particles, computed using Equation 3.2-4. While all voids are filled with water in a saturated soil, in case of an unsaturated soil, the voids are partially filled with air.

$$e = \frac{V_v}{V_s} \quad 3.2-4$$

Where,

V_v = Volume of void space (air and water),

V_s = Volume of solids.

3.3 Water Chemistry

The chemical nature of the extraction processes and process water as well as water chemistry of oil sands ore, are the factors that affect the pore water chemistry (Miller, 2010). For instance, an increase in the level of sodium ions in the pore water will increase the dispersion of clay particles (Mitchell and Soga, 2005). On the other hand, Tang et al. (1997) found that adding gypsum to MFT produces stronger clay structure; mainly due to replacement of Na^+ ions by Ca^{2+} , reducing the double layer thickness, leaving clay particles in a less dispersed state.

Water chemistry plays an important role in rheology (flow behavior) and post deposition behaviour of tailings such as consolidation and desiccation. Not just limited to post deposition behavior, water chemistry also plays a crucial role in the flocculation process (Omotoso and Melanson, 2014). For example, Sworska et al. 2000, showed that the

presence of divalent cations (such as Mg^{2+} and Ca^{2+}) can significantly effect the flocculation behavior of fine tailings.

Samples of process water received over a course of two years (2013 and 2014) from Shell Muskeg River were placed into sample bottles and sent to an external laboratory for analysis of major cations and anions concentrations, conductivity, pH, Total solids and alkalinity.

3.3.1 Results

Two samples of reclaimed water (pond water) as received from Shell Muskeg River Mine over a period of two years were sent to Exova lab for analysis of major cations, anions, conductivity and other parameters as indicated in Table 3.3-1.

Table 3.3-1 Water chemistry of pond water

Analyte	Units	Current study		Author	
		Reclaim water 2013	Reclaim water 2014	Innocent-Bernard, 2013	Jeeravipoolvarn, 2005
Alkalinity as $CaCO_3$	mg/L	388	367	762-820	
Cl	mg/L	135	118	311-463	87-100
Conductivity	$\mu S/cm$	1660	1510	2400-3070	1181-2363
F	mg/L	4.18	3.72		5-12
pH		8.62	7.84	8.23-8.5	8.3
SO_4	mg/L	180	162	8-80	3-8
TDS	mg/L	1080	920	1560-2000	
Total Suspended Solids	mg/L	42	12	10-775	
Ca	mg/L	14	24	5-7	5.7-6

Fe	mg/L	0.5	0.05	12.5-33.5	
K	mg/L	21	20	12-18	7.5-7.9
Mg	mg/L	11	12	6-9	4-4.3
Mn	mg/L	<0.01	<0.01		
Na	mg/L	339	298	514-689	254-260
Ferric Iron	mg/L	<0.5	<0.5		
Ferrous Iron	mg/L	<0.5	<0.5		

Generally, the 2013 sample showed a higher ionic concentration with the exception of Ca^{2+} . The higher values of dissolved solids obtained for the 2013 samples correspond to higher values of soluble salts including major cations such as sodium (Na^+), magnesium (Mg^{2+}) and major anions like sulphate (SO_4^{2-}), and chloride (Cl^-). Moreover, higher electrical conductivity values were obtained for the same said samples. Electrical conductivity, which is a measure of ions ability to conduct electrical currents, match the TDS values.

The greater values obtained for total suspended solids for the 2013 samples, is an indication of higher values of fines in suspension.

3.4 X-Ray Fluorescence (XRF) Analysis.

This test is commonly used for analysis of major and trace elements of rocks, minerals, and other geological matters. XRF is a non-destructive and relatively cheap method, but can only be used for analysis of larger fractions.

The analysis is based on the fundamental principles of atoms and radiation interaction. The material is first excited with radiation (high energy, short wavelength) and becomes

ionized. If the energy of radiation is high enough, the inner electrons will be dislodged and the outer electron will replace the missing inner electron. As a result of this displacement, energy will be released where the emitted radiation is of lower energy than the primary incident x-ray. This is called fluorescent radiation and is used to detect the abundance of the elements present in mineral matters (Barth and Wirth (n.d.)).

Four Samples were sent to actlabs for analysis.

3.4.1 Results

Elemental compositions of tailings received over a period of two years (2013 and 2014) are presented in Table 3.4-1.

Table 3.4-1: Elemental composition of raw MFT.

Analyte	Unit	Detection	Analysis	#1 MFT	#2 MFT	#3 MFT	#4 MFT
Symbol	Symbol	Limit	Method	2013a	2013b	2014a	2014b
Al₂O₃	%	0.01	FUS-XRF	20.05	20.08	20.88	21.13
CaO	%	0.01	FUS-XRF	0.35	0.37	0.44	0.44
Cr₂O₃	%	0.01	FUS-XRF	0.01	0.01	0.01	0.01
Co₃O₄	%	0.005	FUS-XRF	< 0.005	< 0.005	< 0.005	< 0.005
CuO	%	0.005	FUS-XRF	< 0.005	< 0.005	< 0.005	< 0.005
Fe₂O₃(T)	%	0.01	FUS-XRF	3.5	3.5	4.72	4.76
K₂O	%	0.01	FUS-XRF	2.27	2.29	2.21	2.26
LOI	%		FUS-XRF	3.14	3.08	3.33	3.31
MgO	%	0.01	FUS-XRF	0.86	0.84	0.8	0.82
MnO	%	0.001	FUS-XRF	0.059	0.058	0.079	0.078
Na₂O	%	0.01	FUS-XRF	0.26	0.26	0.23	0.23
NiO	%	0.003	FUS-XRF	0.003	0.005	0.006	0.01
P₂O₅	%	0.01	FUS-XRF	0.12	0.12	0.15	0.15
SiO₂	%	0.01	FUS-XRF	68.64	68.74	66.17	65.96
TiO₂	%	0.01	FUS-XRF	1	1.01	1.05	1.06
V₂O₅	%	0.003	FUS-XRF	0.028	0.028	0.032	0.035
Total	%	0.01	FUS-XRF	100.3	100.4	100.1	100.3

Results obtained for four different samples were more or less consistence with silicon (Si) acting as the main contributor to the element composition followed by aluminium (Al) and Iron (Fe).

3.5 Mineralogical Composition. X-Ray Diffraction Analysis.

The principle behind this test is similar to XRF in a sense that it's based on the diffraction pattern formed from the constructive interference of scattered waves. The radiation source would become scattered and the beam splits into various paths, depending on the density of electrons (higher density closer to atoms) different diffraction patterns will be formed. Upon constructive interference of two or more beams diffraction takes place and the diffraction can be mathematically calculated when the path difference equals the integral number of wavelength (Λ). For most solid matters (95% can be described by crystalline (Scintag, 1999) atoms are arranged in regular patterns (parallel planes) and thus the path difference can be calculated as follow (Bragg's law) :

$$2d \sin \theta = n\Lambda \quad 3.5-1$$

Where d is the spacing between the two planes and θ is the angle between the incident beam and the plane of atoms as illustrated in Figure 3.5-1:

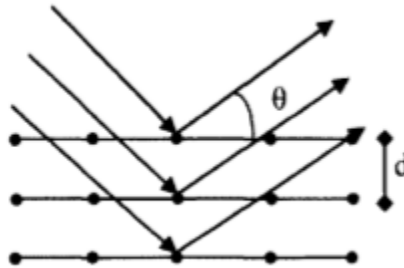


Figure 3.5-1 Schematic representation of Bragg's law.

From the above equation it can be seen that diffraction occurs only if the interplanar distance is in the order magnitude of the diffracted beam. Also, from the angle of diffraction the distance and placement of atoms may be determined. The diffraction pattern along with the d -spacing (basal spacing) is then compared with standard XRD patterns (available from

International Centre for Diffraction Data), from which the unknown crystalline will be identified.

Due to the polycrystalline nature of most samples, the angle between the X-ray and sample should be changed to excite the different planes and to identifying the different crystals. As a result of this variation, several peaks will be recorded (peak overlap) since the constructive interference will now occur for the different plane angles characterized by the angle of incidence for crystalline solids (Kaminsky, 2008).

This issue can be resolved using the Rietveld method (Rietveld, 1969), which separates the overlapping peaks. This method employs a non-linear least squares algorithm to model the XRD pattern until the experimental and measured patterns fit (Kaminsky, 2008). Usually, and to improve the quality of refinement, either a known quantity of well-ordered material is added to the mixture, or geometric functions are used to model the different phases (Langford and Louer, 1996).

3.5.1 Results

Four samples (two from 2013 shipment and two from 2014 shipment) were submitted for quantitative X-ray diffraction analysis including clay speciation. A portion of each sample was pulverized, mixed with 10 wt % corundum and loaded into a standard holder. Corundum was used as an internal standard, to determine the X-ray amorphous content of the samples. For the clay speciation analysis, a portion of each sample was dispersed in distilled water and clay minerals in the < 2 μm size fraction separated by gravity settling of particles in suspension. Oriented slides of the < 2 μm size fraction were prepared by placing a portion of the suspension onto a glass slide. In order to identify expandable clay

minerals, the oriented slides were analyzed air-dry, after saturation with ethylene glycol and after heating for one hour at 375⁰ C.

The X-ray diffraction analysis was performed on a Panalytical X'Pert Pro diffractometer equipped with Cu X-ray source and an X'Celerator detector and operating at the following settings:

40 kV and 40 mA;

range 5 - 70 deg 2 θ for random specimens and 4 – 35 deg 2 θ for oriented specimens;

step size 0.017 deg 2 θ ;

time per step 50.165 sec;

fixed divergence slit, angle 0.5⁰ or 0.25⁰;

sample rotation 1 rev/sec.

The quantities of the crystalline mineral phases were determined using Rietveld method. As previously mentioned, the Rietveld method is based on the calculation of the full diffraction pattern from crystal structure information. The semi-quantitative amounts of clay minerals in the < 2 μ m size fraction were determined based on calculation of basal-peak areas.

The minerals identified in the bulk samples are quartz, kaolinite, muscovite/illite, rutile and pyrite. K feldspar and halite may be present in trace amounts. The samples also contain X-ray amorphous material. Diffraction patterns are shown in Appendix I, figures A-1 to A-4.

The clay minerals identified in the < 2 μ m size fraction are kaolinite and illite. The clay speciation procedure showed that in all samples illite contains about 10 % smectite component. The presence of smectite component is indicated by illite peak at 9.9 Å that is

asymmetric in the low-angle direction, becomes sharper after saturation with ethylene glycol and increases in intensity after heating. The quantitative amounts of minerals in bulk samples are in Table 3.5-1 and the semi-quantitative amounts of clay minerals in the < 2 μm size fraction are in Table 3.5-2. Diffraction patterns of < 2 micron fraction are presented in Appendix II.

Table 3.5-1 Mineral amount in bulk samples (wt%)

Sample ID	MFT 2013a	MFT 2013b	MFT 2014a	MFT 2014b
Quartz	30.7	29.9	26.7	26.2
Kaolinite	29.1	28	28.3	26.6
Muscovite	19	19	15	11.8
Rutile	0.5	0.5	0.3	0.3
Pyrite	n.d.	n.d.	0.4	0.3
Amorphous	20.7	22.6	29.3	34.8

Note: n.d. = not detected; muscovite includes illite; amorphous refers to X-ray amorphous material

Table 3.5-2 Clay minerals identified in the <2 μm size fraction and their semi-quantitative amounts

Sample ID	MFT 2013a	MFT 2013b	MFT 2014a	MFT 2014b
Kaolinite	70	68	72	72
illite	30	32	28	28

The samples investigated by Omotoso et al. (2002) (on Athabasca oil sands tailings in Fort McMurray), also showed that illite and kaolinite (and some minor quantities of chlorite) comprised the clay fraction of mature fine tailings. However, they found that illite and kaolinite are not the contributor to high surface area, and that interstratification of very

fine illite and kaolinite with smectite were the key contributor to the high surface area of the oil sands tailings.

3.6 Methylene Blue Index Tests

This test is commonly used for quantifying the clay content and activity of clay. Methylene blue is a cationic dye with strong affinity to exposed surfaces (internal and external) of clays which can be used to describe the cation exchange capacity (CEC) of clays. Other have used this test as a mean to measure the surface area of clay (Kaminsky, 2014). The Methylene Blue cation displaces Na^+ , Ca^{2+} , K^+ , and Mg^{2+} cations on the surfaces of clay. Further details on this test can be found in Kaminsky, (2008) and Boxill, (2011).

3.6.1 Method

The methylene blue index test has been modified from the ASTM standard by Amar Sethi at MRRT labs (Sethi, 1995) to be used in the oil sands industry. Some key differences from ASTM standard are: the use of 0.006N MB solution instead of 0.01N, use of sodium hydroxide instead of distilled water for the dispersion phase and use of a different filter paper type.

For these tests the sample was first fully dispersed through stirring, boiling sonication and with the aid of sodium bicarbonate. The sample is said to be thoroughly dispersed when no lumps or floating pieces are visible. The sample is then acidified and titrated with methylene blue in 0.5-1 mL increments. The test is said to be complete when a sample containing methylene blue leaves a blue halo on Whatman filter paper. The methylene blue

index (MBI) is calculated using the total volume of the methylene blue added during the last process and expressed in meq/100g. The percentage clay is then calculated using the following empirical relationship derived between the MBI and the % clay mineral as measured by Sethi for oil sands tailings (Yong and Sethi, 1983):

$$\%clay = \frac{MBI \frac{meq}{100g} + 0.04}{0.14} \quad 3.6-1$$

The MBI test is not only useful for predicting the surface area and CEC of clays, but can also be used to calculate the amount of bounded water and cation sites available for chemical reaction (Kaminsky, 2014). Others have obtained correlations between the MBI values and flocculation dosage and/or yield stress (Revington, 2014; Omotoso and Melanson, 2014; Diep et al. 2014).

3.6.2 Results

Table 3.6-1 shows results from the MBI analysis and calculated clay percentages using Equation 3.6-1. Clay fraction calculated from the MBI test generally lie above the values obtained from hydrometer test (Figure 3.1-1). This could mean that the hydrometer was not able to disperse clay particles present in the silt size portion. Also presented in this table are the MBI and clay content of raw MFT from other studies. Kaminsky, (2008) also reported a MBI of 9 meq/100g on the 0.2-2 micron fraction of tailings. Tailings used in this study exhibited a lower activity in comparison.

Table 3.6-1 MBI Data

Sample#	Current study		Author			
	MBI(meq/100 g)	Calculated percent clay(%)	Innocent-Bernard, 2013		Miller, 2010	
			MBI(meq/100g)	percent clay(%)	MBI(mL0.006N/100g)	percent clay(%)
1	3.96	28.57	4.57	33	1183	51
2	3.96	28.57	5.2	37.7	1122	48
3	4.41	31.79				
4	4.11	29.64				

3.7 Dean Stark Analysis

This test is commonly used in the oil sands industry to quantitatively determine the bitumen, solids, and water content of oil sands tailings, using a solvent and toluene (Bulmer and Starr, 1979). For this test the sample is first placed in a thimble of a modified soxhlet extractor and bitumen and water are separated from the solid by passing toluene vapour over the given sample. Solids which have passed through the thimble will be centrifuged/filtered. Extraction is said to be complete once dripping toluene from the thimble is clear and colorless and all the water is collected in the water trap (Barber, 2004).

3.7.1 Results

Results obtained from Agat laboratory are presented in Table 3.7-1. A small portion of the sample was lost during this process, which was probably due to the fine material sticking to the coarse material of the thimble, and not the thimble filter. On average sample from the 2013 shipment had a lower oil percentage (1%).

Table 3.7-1 Dean Stark Data

Sample code	Sample Wet wt(g)	Oil wt(g)	% Oil	Water wt (g)	% water	Mineral Dry wt (g)	% Mineral	% Cumm
Raw MFT 2013(A)	298.36	6.46	2.165	191.01	64.02	100.85	33.801	99.986
Raw MFT 2014(A)	314.02	10.95	3.487	198.83	63.318	104.16	33.17	99.975
Raw MFT 2013(B)	308.78	7.59	2.458	197.61	63.997	103.14	33.402	99.857
Raw MFT 2014(B)	309.32	10.8	3.492	195.13	63.084	102.39	33.102	99.678

3.8 Polymer solution

In this study an anionic polyacrylamide (PAM) macropolymer commercial flocculants, A3338, was used as the flocculant for fast dewatering of MFT samples. A3338 is a branched polymer, with an average molecular weight of 18×10^6 g/mol, supplied by SNF. Figure 3.8-1 illustrates the structure of the anionic PAM.

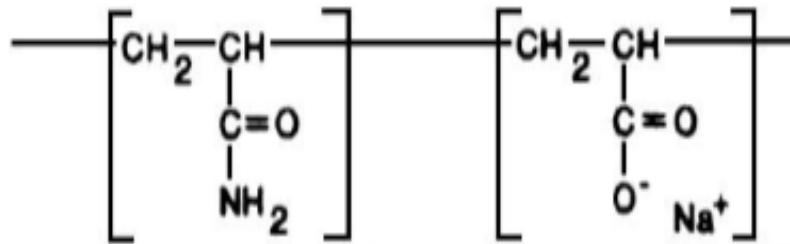


Figure 3.8-1 Structure of anionic PAM (<http://www.snfcanada.com/product-literature.php>)

Solutions of 0.4% (w/w) were prepared by adding 4 grams of polymer to 996 g of reclaimed water. Reclaimed water was also received from the Muskeg River Mines. Flow curve of the flocculant prepared at concentration of 0.4% (w/w) is presented in Figure 3.8-2. According to Figure 3.8-2, the flocculant solution classifies as Pseudo-plastic or shear-thinning fluid in which viscosity decreases with increase of shear rate and the flow curve becomes linear only when the shear rates reach high values. The material showed a yield stress (τ_y) of 0.1 Pa, consistency index (K) of 1.79 Pa.sⁿ and power index of 0.38 when fitted with the Herschel-Bulkley model ($\tau = \tau_y + KY^n$) (Mizani et al. 2013b).

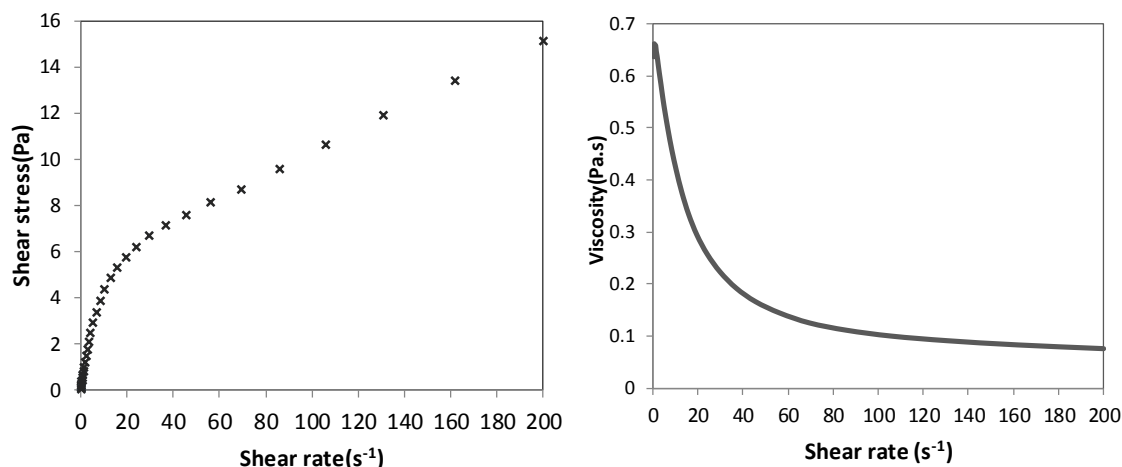


Figure 3.8-2 Flow curve for A3338 polymer prepared at concentration of 0.4% w/w (left), viscosity profile with shear rate (right).

3.9 Procedure for Preparation of Flocculated MFT

First a four blade impeller with radius of 8.5 cm was immersed in 1,800g of MFT (Figure 3.9-2). Mixing was then initiated at a fixed speed of 250 rpm. The flocculant solution is then added but mainly directed near the impeller during mixing. After adding the 0.4% flocculant solution mixing was continued for another 10 seconds. Rheology tests on the flocculated MFT were conducted 30 minutes following mixing. Delays in yield stress measurement is a common practice in thixotropy material, as manual preparation of samples does not ensure the same initial state (Mahaut et al. 2008). Such long resting time will minimize initial irreproducibility on the structure.

The mixing speed was initially adjusted and optimized, by trial and error, to produce material with consistent rheology with those obtained during pilot scale testing at Shell's AFD trials. For this purpose, MFT and floc solution were mixed at different speeds (200-300rpm). The flocculated product was then tested for yield stress at a constant shear rate

of $0.1(\text{s}^{-1})$. The following figure (Figure 3.9-1) illustrates the yield stress values of the mixture measured after 30 min and upon decanting the bleed water at various mixing rates. It can be observed from this figure that mixing speeds above 250rpm resulted in over shearing of the material; whereas, the use of lower speeds were indicative of insufficient mixing. The increase in yield stress is possibly due to ongoing polymer mixing and strength gain of the material during the test.

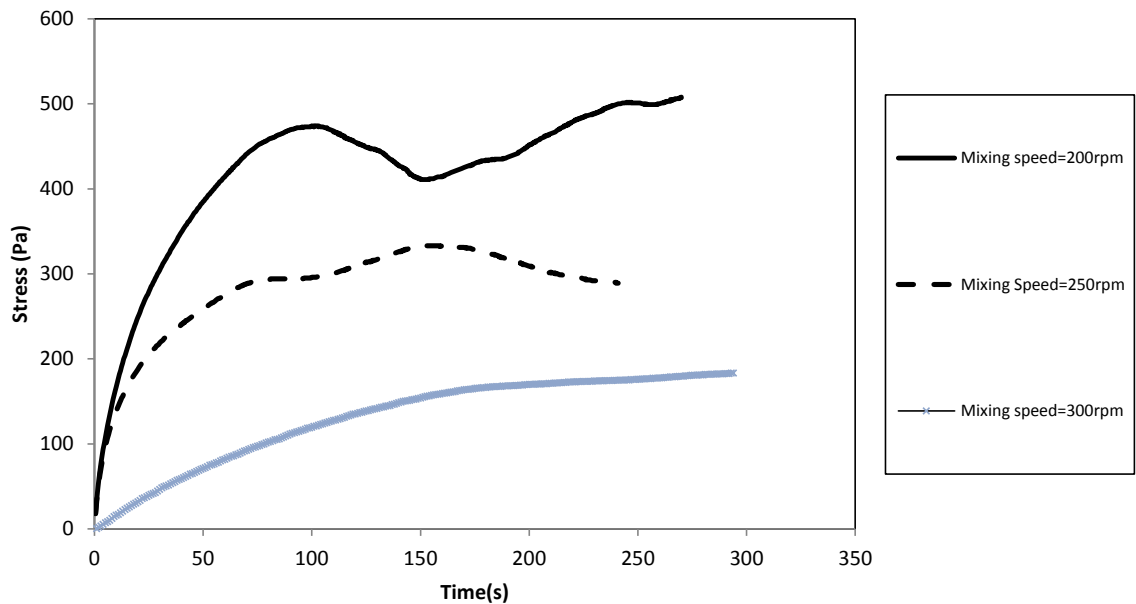


Figure 3.9-1 Effects of mixing speed on yield stress values of flocculant MFT at 850g/tonne.

The delay was also used in testing protocols on field samples obtained from Shell's AFD trials. Due to sensitivity of flocculated MFT to time and shearing, any new measurement (i.e permeability and rheological characteristics) were conducted on a new sample following the procedure explained above.

Mixing of MFT and flocculant were conducted using different dosages and mixing times. In this study polymer dosages of 650, 725, 850, 1,000, 1,200 and 1,500 g/tonne were examined, while mixing time was varied between 5 to 20 seconds. After repeating this test for various flocculant dosages, it was visually observed that mixing times above 10 seconds resulted in collapse of the floc structure causing irreversible floc breakage possibly due to high shearing (Figure 3.9-3). Therefore, 10s was deemed as the optimum mixing time using this setup.



Figure 3.9-2 Mixing of flocculant with MFT.

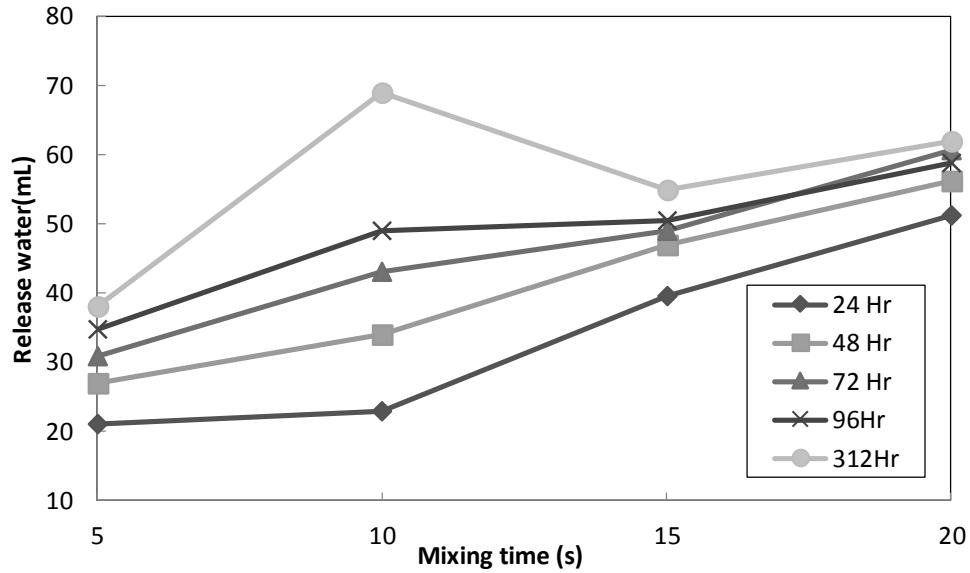


Figure 3.9-3 Effect of mixing time at 250rpm on rate of water release for tailings prepared at 725g/tonne.

Figure 3.9-4 shows a comparison between the yield stress measured in field during the pilot scale test and the ones measured in the laboratory. Both measurements were conducted using the stress growth method with a shear rate of 0.1 s^{-1} . In this operation the flocculant solution was mixed with the MFT in 17 ft pipes before deposition into cells (as explained in chapter 2). Tailings were deposited at a flow rate of around $900 \text{ m}^3/\text{hr}$ while the flocculant dose fluctuated between 770 and 950 g/tonne. Samples were collected at regular times and as close as possible to the deposition point. As it is shown in Figure 3.9-4, the yield stresses obtained in the field overlaps well with the yield stresses obtained in the laboratory with the same polymer dosage; hence the mixing time and intensity used to prepare the flocculated MFT in the laboratory was representative of field mixing conditions.

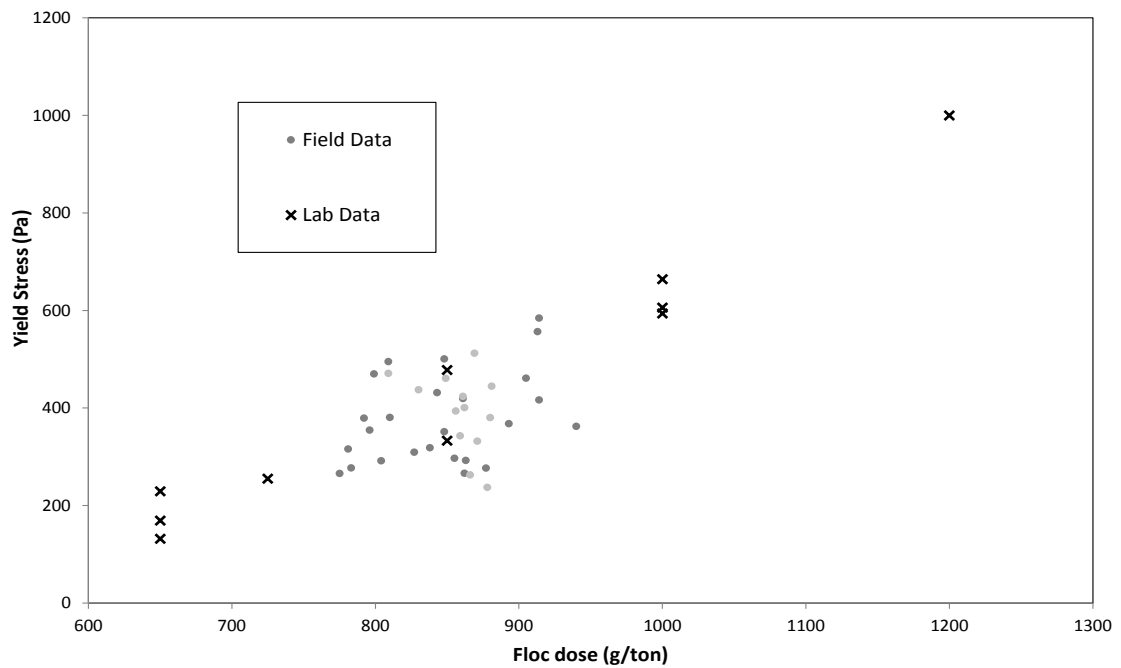


Figure 3.9-4 Comparison between yield stress values measured in laboratory and deposition in Muskeg River Mines tailings site during Aug-Oct 2012.

The performance of flocculation processes are usually evaluated using settling rate, supernatant turbidity or sediment compressibility (Hogg, 2000). In this study release water and total solids of supernatant was measured as an indication of settling rate and supernatant turbidity. For this purpose, the flocculated MFT were poured in 50mL, 500 mL, 2L graduated cylinders to a height of 0.01, 0.3 and 0.5m and covered to prevent evaporation (Figure 3.9-5). Although water release determinations of field samples are typically conducted within a day or two, in this study measurement of released water was performed over a longer time (i.e., 14 days) to investigate the dewaterability potential due to consolidation as well. Total solid concentration measurement of released water was

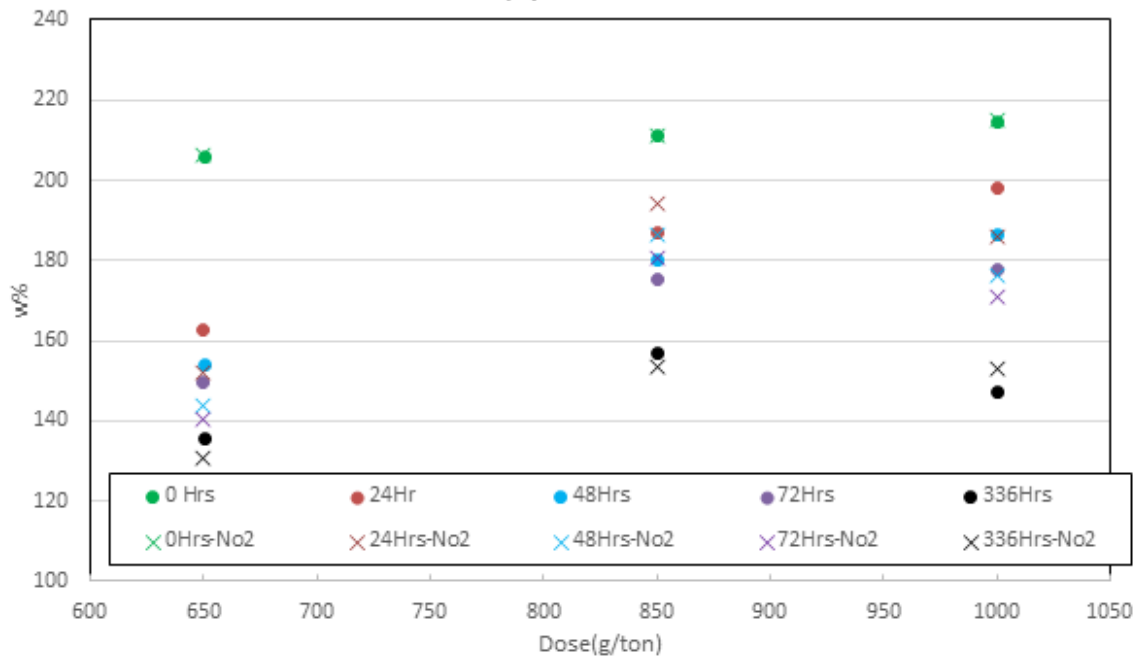
performed on day 6 to evaluate the supernatant turbidity (Figure 3.9-7). Solid concentration was measured by oven drying of 15 mL of released water collected from the 30cm columns.

The effects of flocculant dosages were investigated by measuring the release water from tailings prepared at different dosages. Figure 3.9-6 illustrates the water content as a function of flocculant dosages at different times. With addition of floc dosage more water was introduced into tailings thus giving the flocculated MFT a higher initial water content. The dosage of 650 g/tonne had the highest water release. One possible explanation for this observation is formation of stiffer floc structure at higher floc dose and hence reduction in consolidation at this very low stress (5 kPa). Jin et al. (2004) found that in wastewater sludge the dewaterability potential will be reduced by formation of bigger flocs and high viscosity of the material. It is also believed that high flocculant dosage increases the amount of free floc, consequently increases the negative charges.

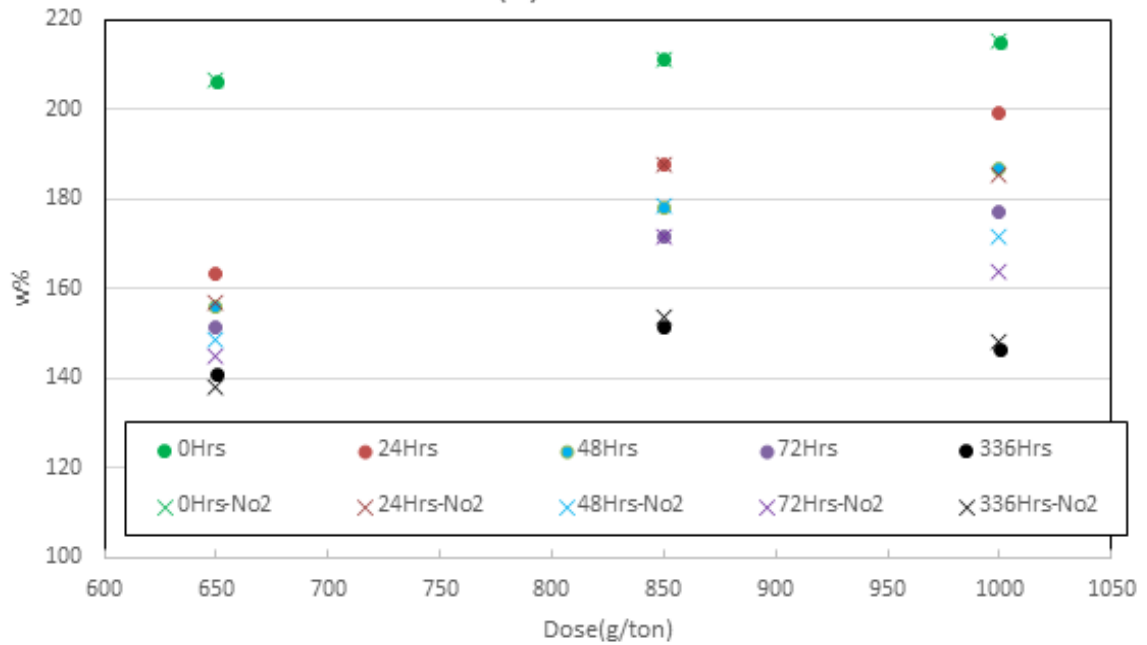


Figure 3.9-5 Settling column setup.

(a) 50cm column



(b) 30cm column



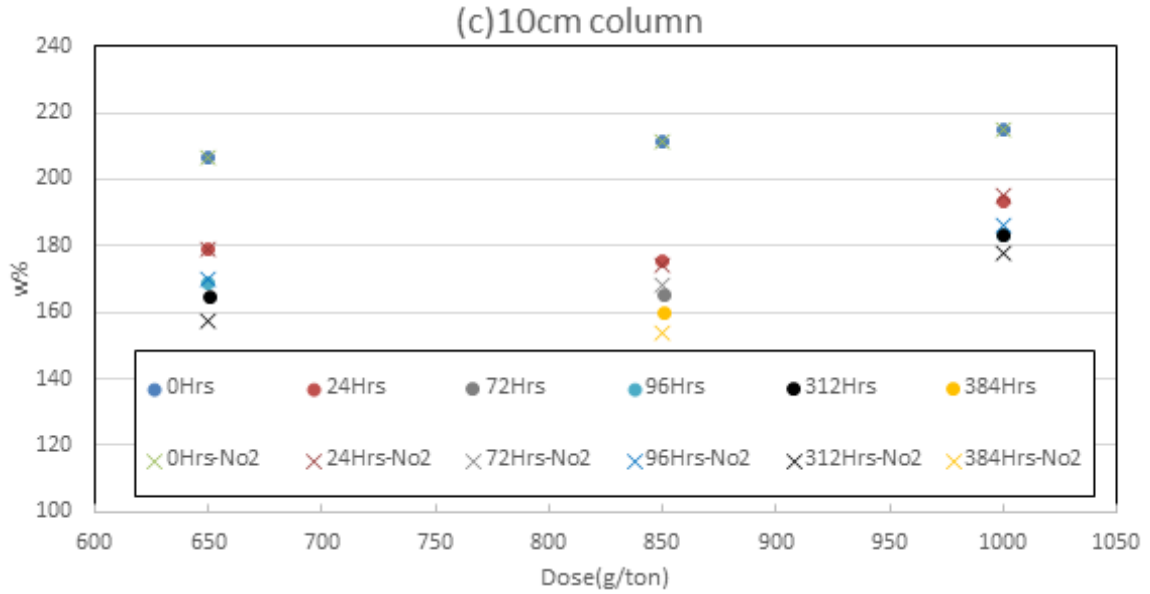


Figure 3.9-6 Water content as a function of flocculant dosage and time for column height of (a)50 and (b)30 cm and (c)10cm respectively.

Figure 3.9-7 shows the total solid concentration in the released water which is representative of turbidity of the water and is usually used to evaluate flocculation performance. As shown in Figure 3.9-7, clearest water was obtained at the flocculant dosage of 1,000 g/tonne. Observation of high turbidity water can be explained by either inadequate flocculant dosage to provide particle neutralization for all the dispersed particles or improper mixing to break the formed flocs. Hence, it may be interpreted that at flocculant dosages of less than 1000 g/tonne, the amount of flocculant was not enough to neutralize all the particle charges.

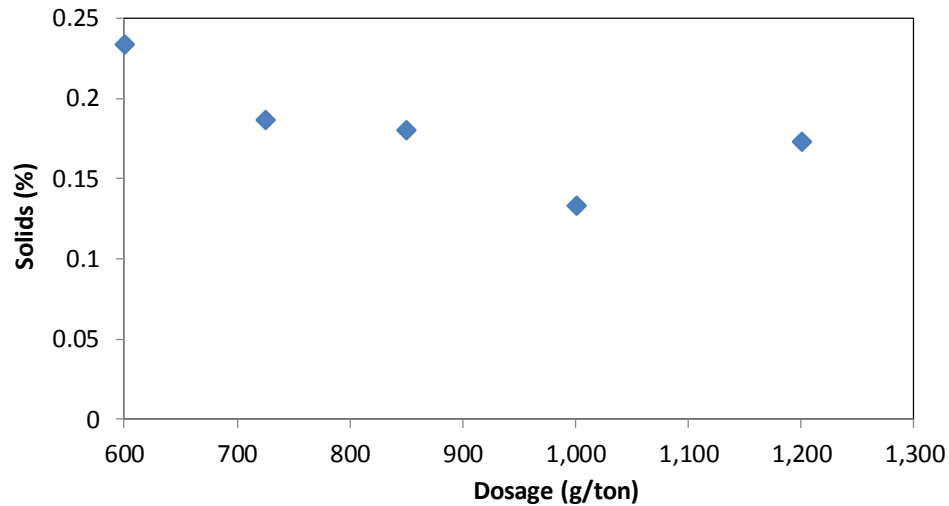


Figure 3.9-7 Total solid concentrations in released water as a function of flocculant dosage.

Bitumen extraction and forth treatment is highly affected by the process water chemistry (Allen, 2008). Bitumen recovery is optimized at alkaline pH (increases activity of surfactant and negative charges on clay and sand surface) and is negatively correlated with calcium and magnesium concentration (Cuddy et al. 2000). The effectiveness of bitumen extraction can also be improved by controlling the hardness concentration. In addition, clay content or suspended solids should be kept within 0.5%-2% limit such that the reclaimed water can be recycled back to the extraction process (Allen, 2008).

3.10 Soil Water Characteristic Curve (SWCC)

Since water can only flow through the water part of the soil, the amount of water in the soil is a key factor in finding the permeability function. This could be done through integration of the soil water characteristic curve or SWCC. Soil desiccation and seepage is a function of hydraulic conductivity and it is therefore important to find the relation between soil suction and water content.

In this study the water retention curves were determined through the use of Fredlund device and a costume setup at lower suction values and WP4-T Potentiometer, measuring total suction, at higher suction values.

Flocculated and raw samples of MFT were placed in sample rings (Figure 3.10-1). Weight, height and shrinkage of the sample were recorded after reaching equilibrium and before each pressure increment. Higher suction values (above 800Pa), obtained through thin surface drying, only the water content was recorded. The SWCC for raw and flocculated MFT dosed at 850g/tonne and 650g/tonne are illustrated in Figure 3.10-2, showing the equilibrium water content at a set suction value and upon removing diffused air.



Figure 3.10-1 Flocculated MFT before transferring sample to total suction machine.

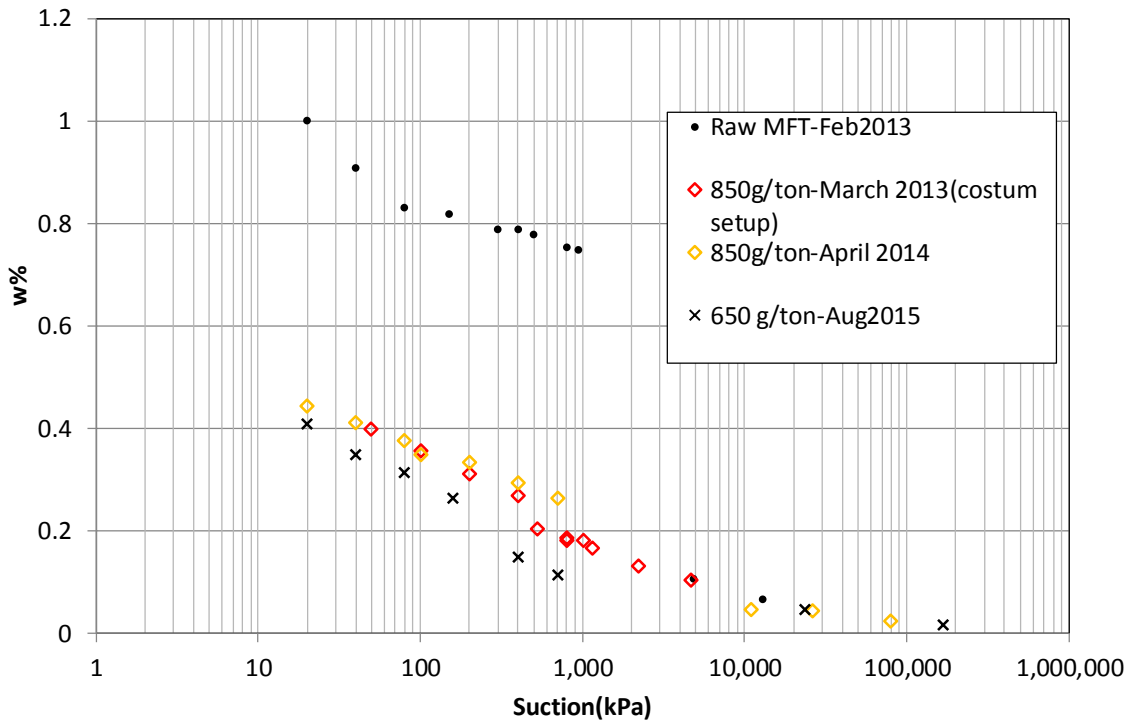


Figure 3.10-2 SWCC for Flocculated and raw MFT.

Due to formation of larger flocs, as a result of flocculation process, the moisture content of the flocculated samples were much lower, at the same suction value.

4 Chapter: Rheological Properties

This chapter investigates the rheological properties of polymer amended MFT. The impact of various process variables such as flocculant dosage, shear history and flow rates will also be presented. Due to the shear sensitivity of flocculated MFT, rheological tests were conducted on bench scale produced samples and not on samples produced during field operations. Results from stress growth tests on freshly prepared samples were compared to data from Shell's on-site laboratory used to monitor quality of the AFD material in the field to ascertain that the mixing time and intensity used to prepare the flocculated MFT in the laboratory was representative of field mixing conditions (3.9).

Rheology of tailings were characterized using slump tests and an Anton Paar Physica MCR301 model rheometer while samples were prepared at different dosage (650-1500g/tonne). Rheology is the study of flow behaviour and deformation of plastic and fluid bodies under externaly applied loads. While relationships such as Hooke's law of elasticity, Newton's law for viscosity, are well known in this field, some material illustrate a behaviour in between and are often difficult to describe them using a single model.

Although this science is more popular in chemical industry, this study aims to show that rheometry techniques may be used to explain the mechanical behaviour of these tailings.

4.1 Slump Test

Slump test has become very popular among engineers for determination of undrained yield stress of thickened tailings, mainly because of its simplicity. In this test, an open ended cylinder is filled with material and lifted from a flat surface, where the material will then flow outward due to gravity. The drop height is then correlated with the yield strength (τ_y), once the slurry is in equilibrium and stops flowing. Figure 4.1-1 illustrates the geometry of slurry after slump test.

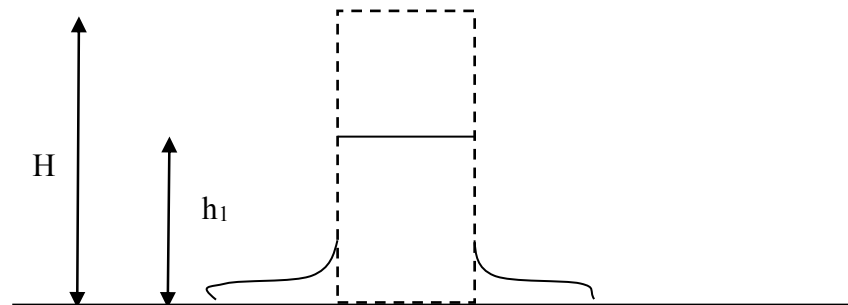


Figure 4.1-1 Graphical illustration of slump test.

4.1.1 Experimental Procedure

Before the test, tailings were mixed with polymer solution and kept in the bucket for 30 minutes, after which the bleed water was drained out. An open ended cylinder was placed on a smooth flat plate and was filled with sample and then lifted in one continuous motion.

The cylinder had an inner diameter of 5.25cm and height of 10.5cm. Care was taken to avoid any lateral movement by lifting up the cylinder with two hands, change in height between the cylinder and deformed material was then measured. The midpoint of the slumped material was taken as the representative height due to the uneven top surface. Also, the diameter of the outward flow was recorded. Several slump tests were done using different floc dosage. All the tests were performed at room temperature (22-24⁰).

4.1.2 Analysis

In the model developed by Pashias et al. (1996), the maximum shear stress is assumed to be half the hydrostatic pressure; therefore, the stress increases linearly with depth from zero at the top to its maximum value at the bottom. When the stress falls below the yield stress the height would stop decreasing. Assuming the geometry of the material above the yield surface remains cylindrical and sinks as the material beneath it flows, the dimensionless slump can then be related to yield stress by the following equation:

$$S' = 1 - 2\tau'_y [1 - \ln(2\tau'_y)] \quad 4.1-1$$

Where,

$$S' = (H - h_1) / H$$

The dimensionless yield stress can then be obtained through:

$$\tau'_y = \frac{1}{2} - \frac{1}{2} \sqrt{s'} \quad 4.1-2$$

The yield stress is then calculated by multiplying the above value by unit weight and height of the cylinder.

$$\tau'_y = \frac{\tau_y}{\rho g H}$$

4.1-3

Other assumptions used in this derivation are:

- i) Flat surface between the yielded and unyielded surface remains horizontal,
 - ii) No friction exists between the material and the walls of the cylinder
- and
- iii) Relation between pressure and stress distribution is that for an elastic solid.

4.1.3 Results

Figure 4.1-2 shows the plots of dimensionless slump height (s') with polymer dosage.

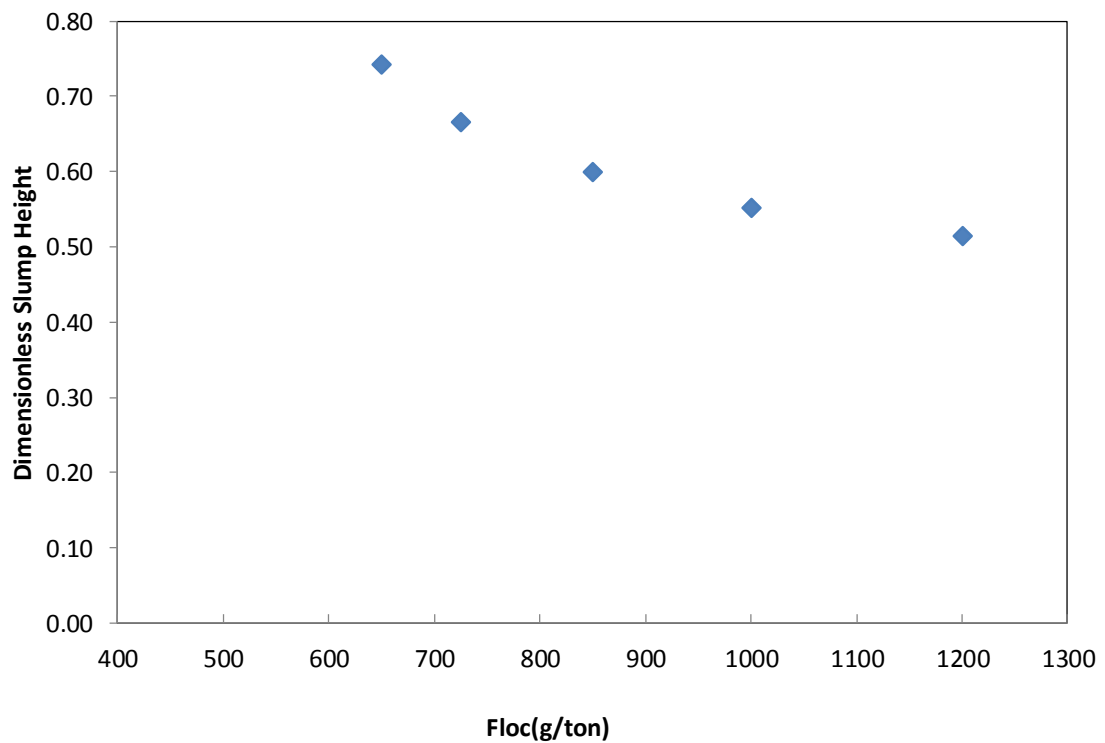


Figure 4.1-2 Dimensionless slump height versus polymer dose in g/tonne after 30minutes upon mixing.

The yield stress is then obtained by multiplying the dimensionless yield stress by $\rho g H$.

Figure 4.1-3 presents the values of yield stress at each polymer dose using Equation 4.1-3.

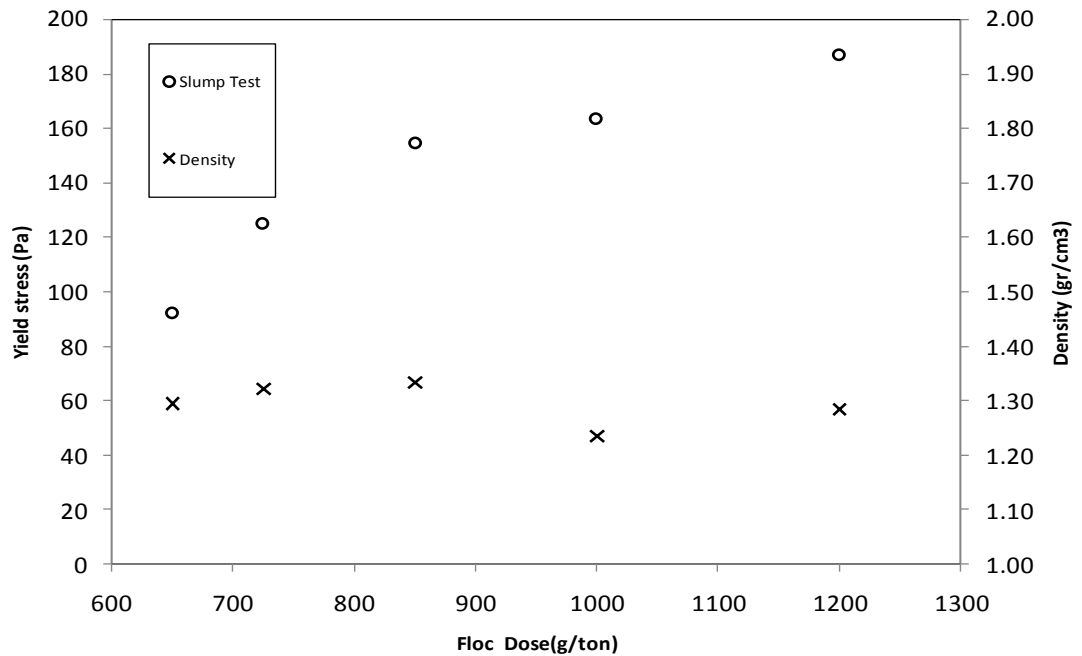


Figure 4.1-3 Yield stress and density values versus polymer dose in g/tonne after 30minutes upon mixing.

4.2 Rheology and Test Procedure on Laboratory-Prepared Polymer-Amended MFT

An Anton Paar Physica MCR301 model rheometer with a vane fixture was used to characterize the rheology of the tailings. The vane has become very common among geotechnical engineers for measuring the shear strength of very soft soils which are too soft for triaxial testing. The current rheometer used has an air bearing fixture together with a synchronous motor to virtually eliminate system compliance problems. Magnets mounted on the rotor disc produce a constant magnetic field, providing delay-free coupling of the

fixture to the rotor. For these sets of tests, tailings were loaded into the CC27 cup provided for the vane geometry. The vane has a diameter of 22mm and a depth of 40mm. Rheology tests on the flocculated MFT were conducted 30 minutes following mixing. The cup is then placed into a depression in the rheometer base (See Figure 4.2-1). The vane fixture was then lowered by the rheometer into the centre of the sample, submerging the fixture beneath the sample surface.



Figure 4.2-1 An Anton Paar Physica Rheometer.

Measurements were initiated no later than 1 minute after the submersion of the vane fixture. During the measurement of each flow curve the shear rate will be that commanded and the shear stress will be the average torque measured over the measuring point duration multiplied by the CSS (controlled shear stress) factor for that particular tool. For a shear

rate sweep the measuring point duration for each measurement is as follows: when commanding a specific speed or rate there is a required time to reach steady state. The time required to reach steady state is approximately the measuring duration for that particular shear rate. The software ignores the first 30% of the measuring time due to adjusting the set speed/shear rate. The last 70% of the data is recorded, and the final 50% is averaged for the measuring point. It is assumed that an equilibrium has been reached in the last 50% of the measuring time. If the measuring time is changed (lowered or raised), this may affect the results. If the measuring duration is lowered too much, the average may incorporate the start up behavior and thus the discrepancies.

Rheometry techniques performed included measurements of dynamic oscillation and determination of flow curves (where shear rate increases in steps after obtaining equilibrium shear stress at each step), stress growth (where material is sheared at a constant shear rate), stress relaxation, and controlled stress.

4.2.1 Wall Slip

While the use of vane geometry over other conventional geometries has proven to be advantageous from many aspects such as minimization of the errors associated with the intrusion of the vane and allowing the material to yield within itself; the errors related to wall slip are also eliminated (Dzuy and Boger 1983).

When measuring the yield stress and viscoelastic properties of thickened materials a phenomenon called slip can occur. That is, near the yield point due to the movement of the materials particles away from the walls of the measuring container a water rich layer will form. As a result, causing lubricating effects which will then make flow easier.

Moreover, wall slip could be further increased as a result of gravitational forces.(Saak et al. 1999). The influence of slip becomes more dominant with an increase in the solids concentration; therefore, the likelihood of slip increases when measuring the rheological properties of tailings. Also slip is more pronounced when using lower ranges of strain.

The effects of slip could be eliminated if vane geometry is used. That is because shearing takes place along the area circumscribed by the vane. In the study conducted by Saak et al. (1999) the results from the stress growth experiments showed that the results obtained from the vane was more consistent to the expected behavior (Figure 4.2-3). However, the results from the concentric cylinder showed evidence of wall slip. That was at several points a decrease in the stress was observed due to the formation of slip layer.

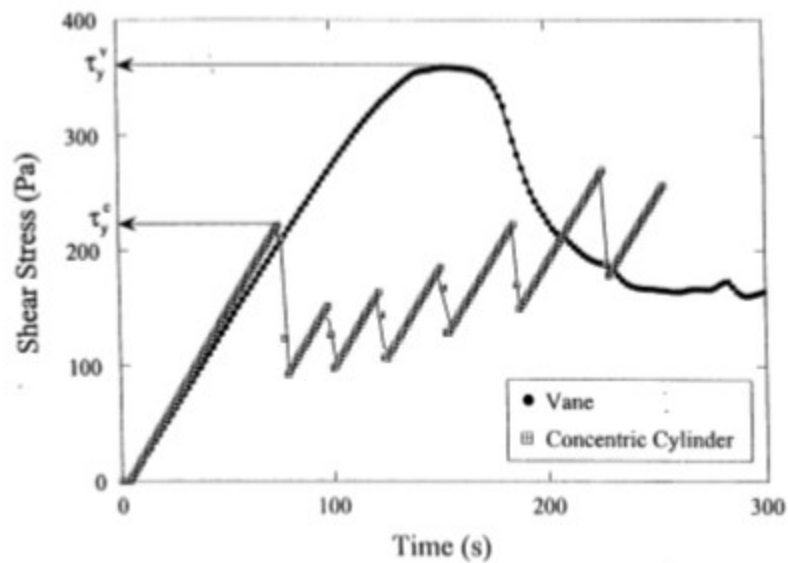


Figure 4.2-2 Stress growth test on type I Portland cement and deionized water at water to cement ratios of 0.30.

4.2.2 Flow Curve

Flow curves for raw and a few selected dosage of flocculated MFT are presented in Figure 4.2-3. Unlike typical flow curves for an ideal Bingham yield stress, these show an initial spike in shear stresses at the start of the test. Although testing on raw MFT was conducted at various measuring point durations, no substantial change in the behaviour was seen (Figure 4.2-4). Both ascending and descending curves are illustrated in this plot, which shows a hysteresis loop that becomes more apparent as the floc dosage increases. Shearing of the flocs would explain the decreasing shear stress with increasing shear rate observed in the 725 g/tonne sample. This is also in line with the fact that the breakdown rate is larger than the built-up rate. It is important to note that, despite shearing, these samples retain a substantial yield stress (about 100– 150 Pa) on the descending loop.

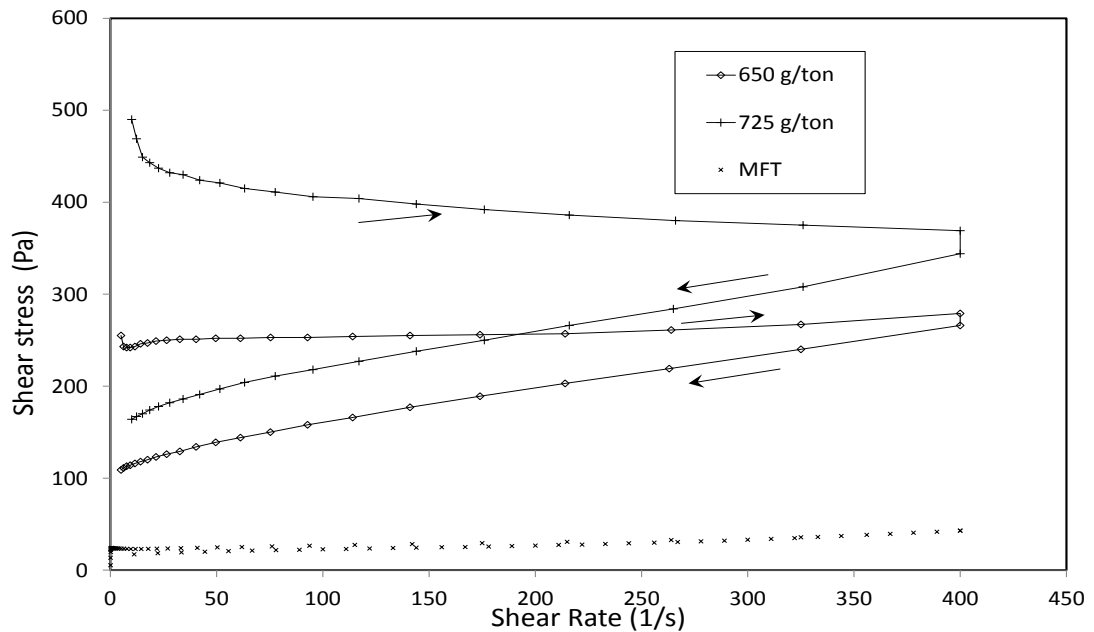


Figure 4.2-3 Flow curves on raw and flocculated MFT.

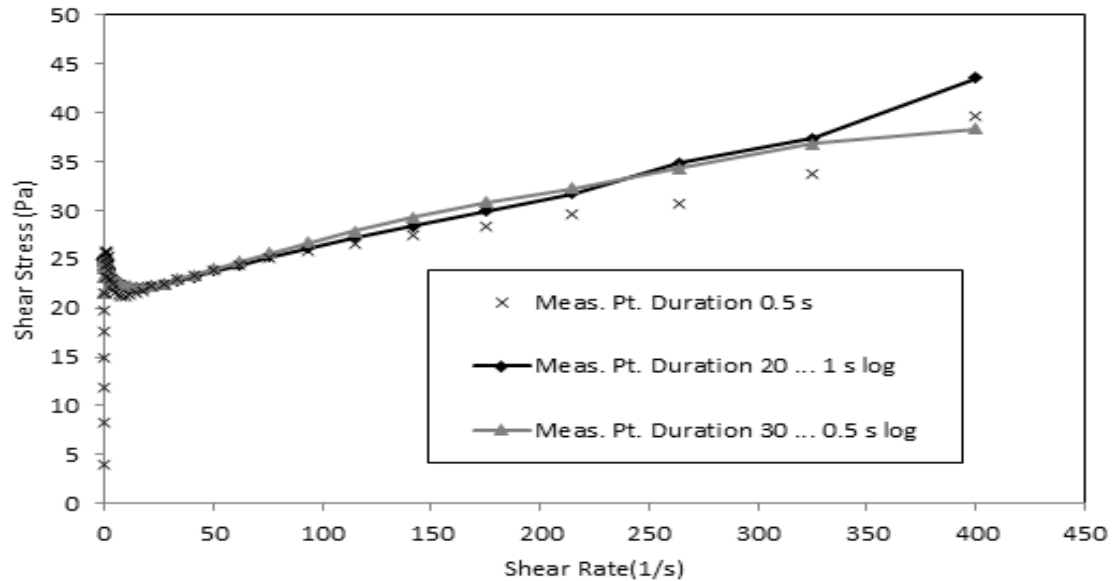


Figure 4.2-4 Flow curves on raw MFT at various measuring point duration.

4.2.3 Stress Relaxation

Yield stress fluids will show a finite non-zero value when shear rate tends to zero. This characteristic was used to determine the yield stress through the stress relaxation technique. In this test, after loading the sample into the cylinder, the vane was rotated at a chosen speed and the evolution of the torque was measured as a function of time. When an equilibrium condition was reached the vane was brought to a sudden stop and the shear stress remaining on the rotating device in the relaxed condition was taken as the yield stress. In order to ascertain the results, the test was repeated at different shear rates, sequentially testing the same sample in the rheometer.

Figure 4.2-5 shows results for flocculated MFT at a dosage of 850 g/tonne. It is clear that a residual stress remains on the vane after all shearing modes. This means that the material would still show a yield stress (although small) after considerable shearing. However, the residual stress decreased with an increase in the shear rate, indicating the

effects of excessive shearing on floc breakage (Mizani and Simms, 2014b). An average yield stress of 17 Pa was found. However, this level of shearing would not likely occur in the field.

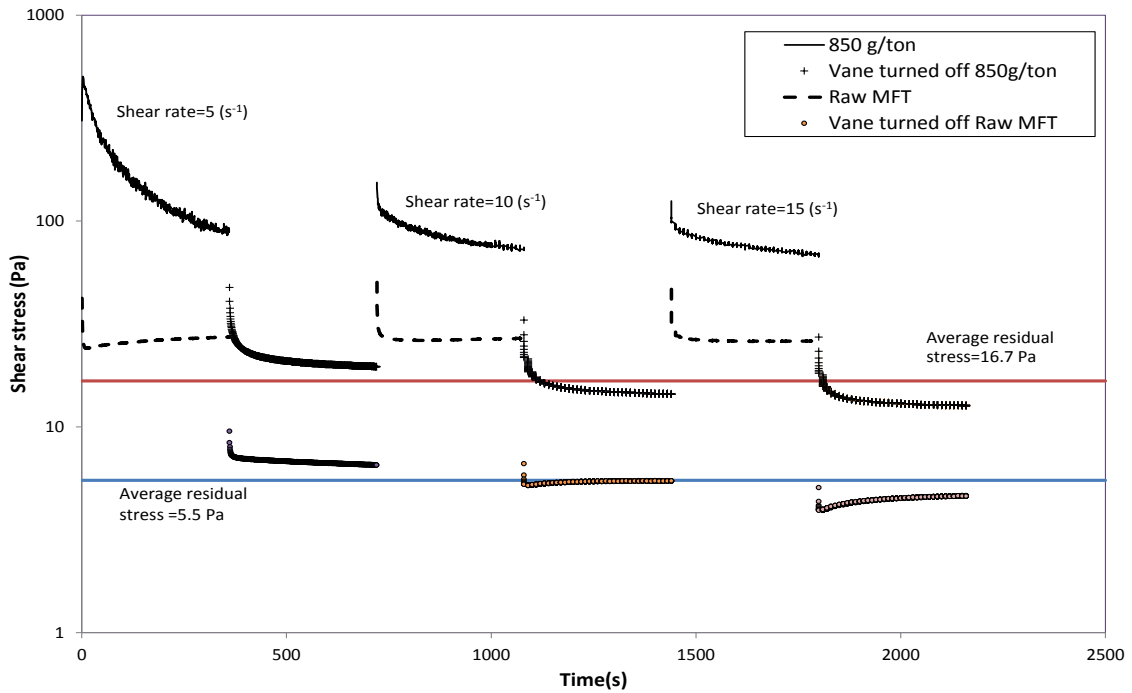


Figure 4.2-5 Stress relaxation test on raw and flocculated MFT at 850 g/tonne dose.

4.2.4 Stress Growth

These tests were performed on individual samples prepared at 850g/tonne. The peak in the torque-time curve is related to the yield stress of the material and the maximum stress in the stress-time profile is determined as the yield stress. The stress was calculated from the measured torque through:

$$T_m = \frac{\pi D_v^3}{2} \left(\frac{H}{D_v} + \frac{1}{3} \right) \tau_y$$

4.2-1

Where,

T_m is the measured torque,

D_v is the diameter of the vane,

H is length of the vane and

τ_y is the shear stress.

Figure 4.2-6 illustrates the yield stress as a function of applied rotational speed, while Figure 4.2-7 illustrates the stress-strain plots for the same tests.

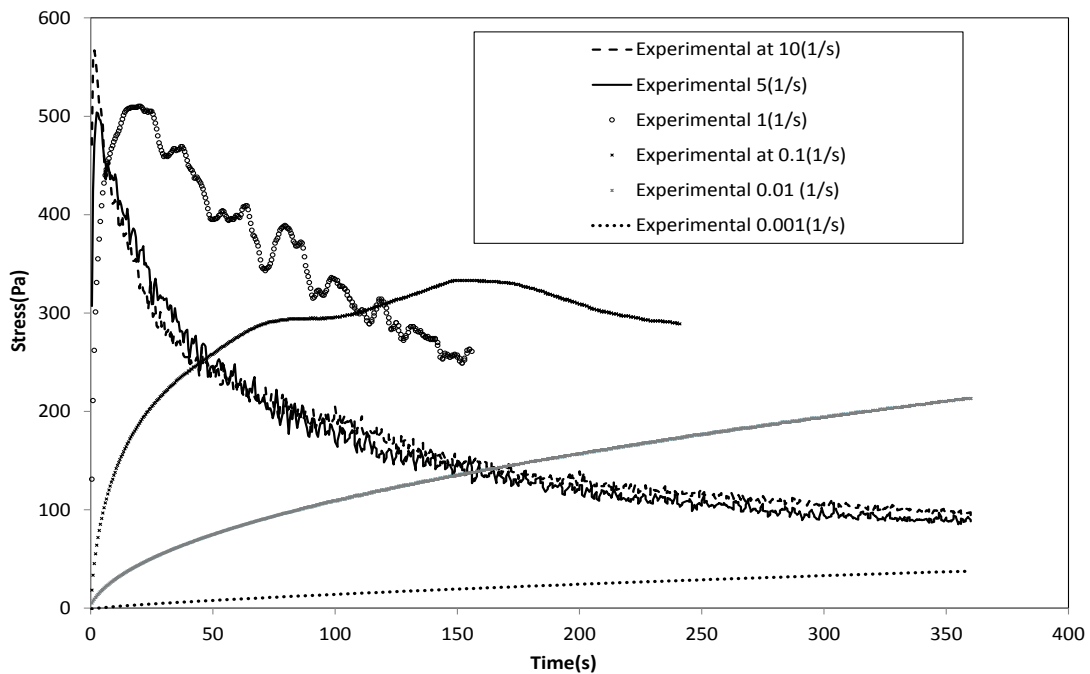


Figure 4.2-6 Stress growth test on flocculated MFT at 850 g/tonne dose at various rotational speed.

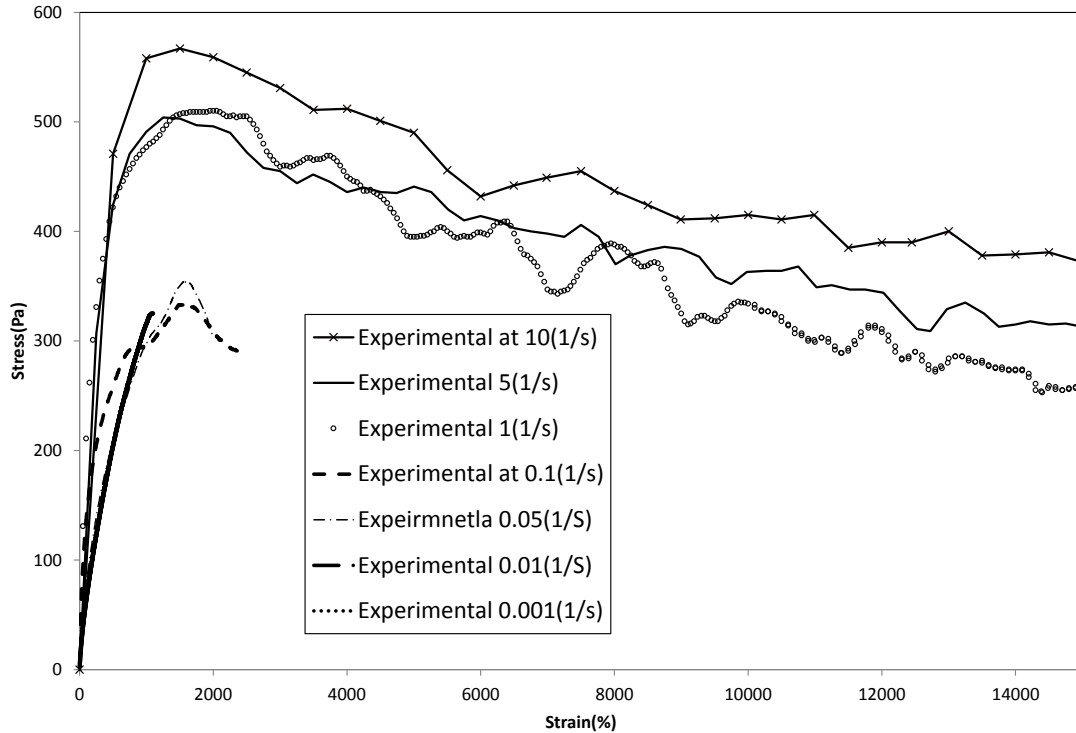


Figure 4.2-7 Strain-stress plots of MFT dosed at 850 g/tonne for various rotational speeds.

The results from the Table 4.2-1 show that there is a region (between 0.01 and 0.1 s^{-1}) where the maximum stress measured is independent of rotational speed. It can be observed from Figure 4.2-7 that the maximum stress increases with an increase in the rotational speed. A possible explanation for this behaviour is that, at higher shear rates, the network bonds are rapidly pulled apart not giving the suspension sufficient time for the elastic response. On the hand, at lower shear rates, more time is required for material to reach their peak stress since the material will have a chance to recover during the longer shearing times. That is, the rate at which the bonds are reformed is higher than the rate at which they are broken. Moreover, it seems that below the shear rate of 0.1 (s^{-1}) a maximum stress could not be observed within the timeframe of the test.

Table 4.2-1 Maximum stress versus rotational speed at 850gr/tonne

Shear rate (s ⁻¹)	0.001	0.01	0.05	0.1	1	5	10
Maximum stress (Pa)	Not Observed	326	350	333	510	504	567

4.2.5 Controlled Stress Rheometry

While material exhibit a low shear viscosity (steady state) when subjected to stresses slightly higher than the yield stress, stresses tend towards a finite non zero value when shear rates tend to zero (Coussot et al. 2002b); In other words, viscosity will jump to infinity when the yield stress is reached from above and eventually behaves like a solid (Figure 4.2-8).

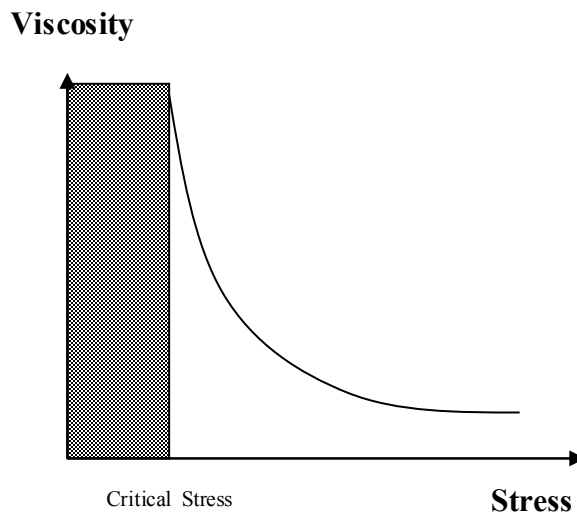


Figure 4.2-8 Variation of viscosity with stress (Coussot et al. 2002b).

Microstructure is mainly responsible for the yielding behaviour of tailings and when the material becomes subjected to flow the microstructure gets destroyed. This can be confirmed by a decrease in viscosity over time. On the other hand, the microstructure rebuilds itself when it's left at rest. This could also mean that the yield stress would increase over time (this will be later discussed in section 4.6). It is therefore not surprising to say that yield stress is not an intrinsic property and it is dependent on the shear history of the material.

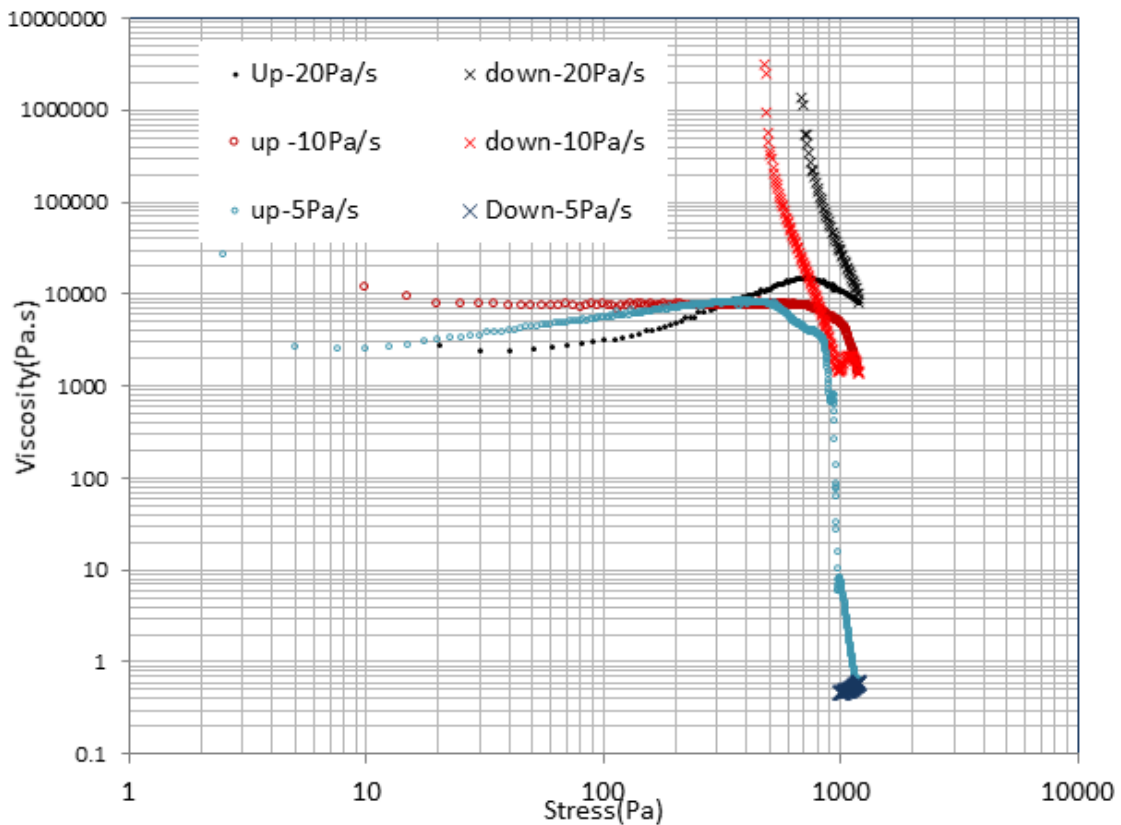


Figure 4.2-9 Variation of viscosity with time under various shear stress rates.

Figure 4.2-9 illustrates the changes in viscosity under various loading rates. Though for all shearing rates a decrease in viscosity values were observed (stress ramping up), viscosity changes were more evident (sharp drop) at the lowest shearing rate (5Pa/s). This figure also shows the different behaviour the said sample shows when stress is ramping up and down. In all cases the yield stress is smaller in the descending branch, which could be explained by destruction under high shear stresses.

The following figure illustrates the bifurcation in viscosity when the sample is subjected to various levels of stress. Under a certain stress level, the viscosity will increase ultimately leading to a flow stoppage. On the contrary, when stress exceeds a certain level, viscosity falls rapidly leading to a steady state flow. It is worth mentioning that this critical value is dependent on flow history and resting time.

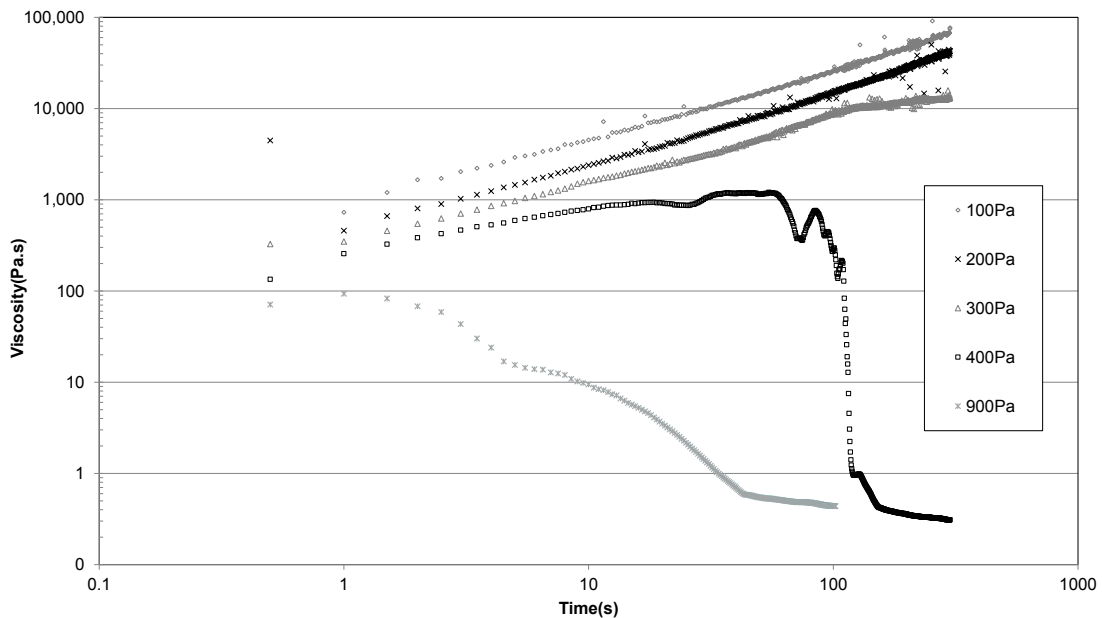


Figure 4.2-10 Variation of viscosity with time under various shear stress levels.

As pointed out earlier shear history plays a significant role on the behaviour of the microstructure in particular the arresting behavior. Therefore, in this section we will try to simulate the shear history of the material as they flow down the beach to monitor the arresting behaviour of the material.

As shown by McPhail (1995), material experiences the highest level of shearing close to deposition point, the imposed stresses will gradually decrease as the material flows down the beach. In order to simulate the field shear stress history of the material, controlled stress tests were conducted on samples dosed at 850g/tonne. High stress levels were initially applied to the sample but gradually decreased in steps until the material stopped flowing. Figure 4.2-11 to Figure 4.2-12, illustrate the variation in viscosity over time under constant decreasing stresses. All of these tests were conducted on MFT samples dosed at 850 g/tonne, where the stress was decreased from 800 Pa to 5 Pa in only 45 seconds (Figure 4.2-11) and from 250 Pa to 30 Pa in nearly 50 minutes (Figure 4.2-12).

Duration of shearing was varied to investigate the effects of time on the yielding behaviour. Each stress level was held for five seconds in the first test and 10 minutes in the second test. Due to overflowing of tailings from the rheometer at high stress levels, the 50-minute test (pertaining to data in Figure 4.2-12) was started at lower stress levels. A dramatic increase in viscosity was observed when stress reached a level of 50 Pa in all cases. Therefore, the duration of shearing did not have a significant effect on the arresting behaviour.

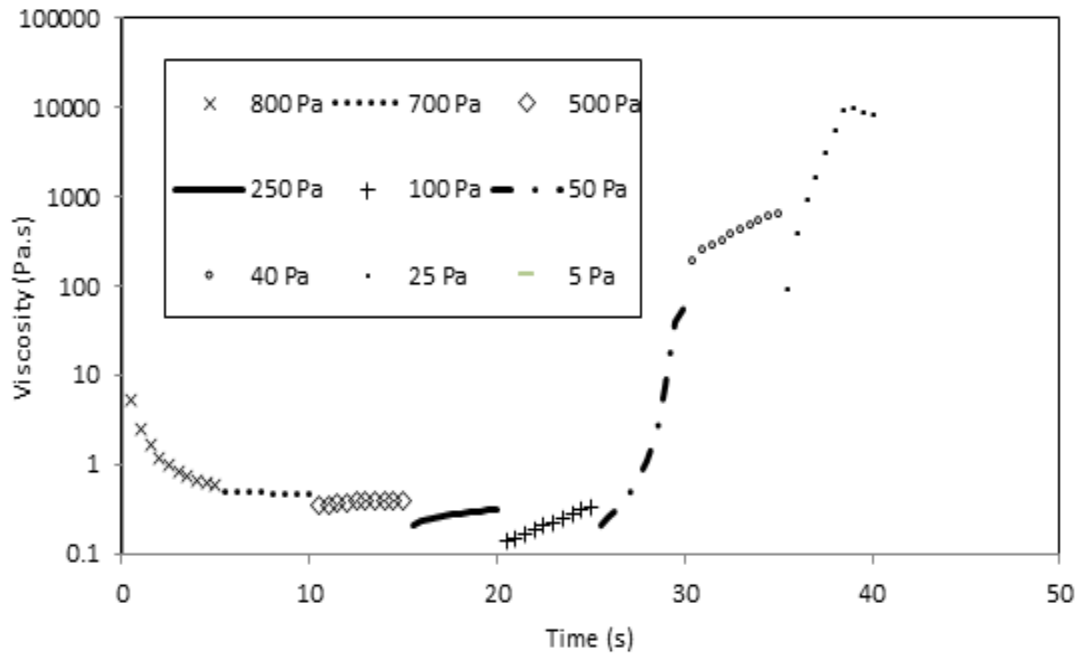


Figure 4.2-11 Viscosity variation over 45s for a sample prepared at 850 g/tonne. Stress was decreased in steps from 800 Pa to 5 Pa.

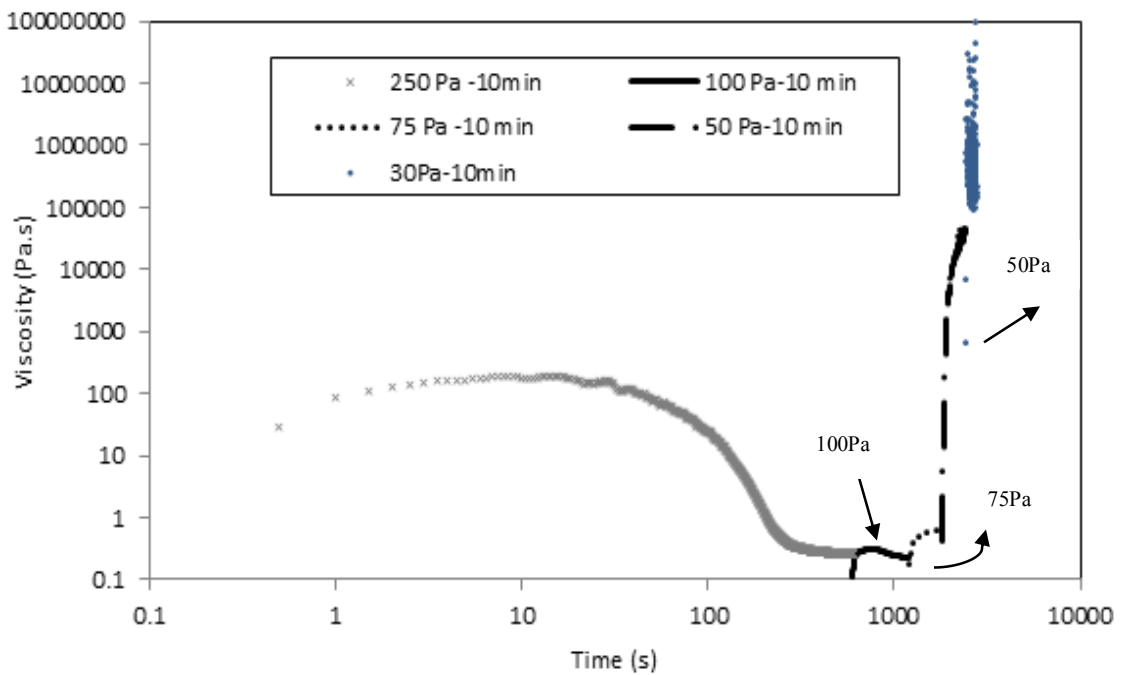


Figure 4.2-12 Viscosity variation over 50min for a sample prepared at 850 g/tonne. Stress was decreased in steps from 250 Pa to 5 Pa.

From these tests it can be concluded that the arresting yield stress is much smaller than starting yield stress, mainly because the structure gets destroyed under shear.

4.3 Theoretical Background on Rheometry

In case of a Newtonian fluids, used to describe viscous material, all the input energy to the system will be vanished due to deformation of the material. On the contrary, for perfectly elastic solid, often described by Hooke's law, the input energy will be recovered and deformation restored upon load removal.

4.3.1 Oscillatory shear

As pointed out in chapter 2, it is often hard to classify material based on a single model where the fluid or solid show a combination of both elasticity and viscosity known as “viscoelasticity”. In this case additional terms may be defined to quantify the elasticity loss under oscillatory conditions: a complex dynamic modulus G^* , a storage modulus G' (dynamic rigidity) and an imaginary loss modulus G'' (Markgraf, 2006).

4.3.2 Oscillatory Tests for Determination of Elastic Response Zone

While constant stress and stress relaxation tests are more appropriate for measuring the material response over longer time, dynamic testing are more accurate for measurements over shorter times.

Oscillatory tests are conducted by applying a sinusoidal strain ($\gamma = \gamma_0 \cos(\omega t)$) and recording the output stress, where γ is shear strain and ω is frequency in Hz. In the case of a Hookean elastic solid, stress is linearly related to strain, $\tau = G\gamma$, where τ is shear stress and

G is shear modulus. However, for a Newtonian fluid, stress is proportional to the rate of shear ($\dot{\gamma}$). Thus, it has a phase difference of $(\pi/2)$ with the applied strain as follows (Chhabra and Richardson, 2008):

$$\dot{\gamma} = \gamma_0 \omega \sin(\omega t) \Rightarrow \tau = \mu \gamma_0 \omega \cos(\omega t + \frac{\pi}{2}) \quad 4.3-1$$

When a viscoelastic material undergoes a sinusoidal stress, at steady state, a sinusoidal strain at the same frequency is obtained within a few cycles, but lags a phase angle δ . The stress and strain functions are illustrated in Figure 4.3-1 and can be formulated as (Macosko, 1994):

$$\gamma = \gamma_0 \cos(\omega t) \quad 4.3-2$$

$$\tau = \tau_0 \cos(\omega t + \delta) \quad 4.3-3$$

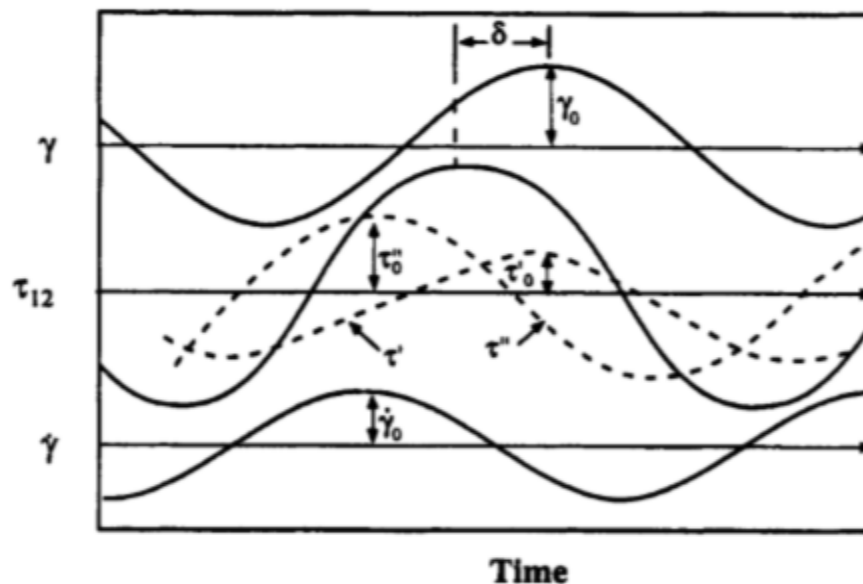


Figure 4.3-1 Sinusoidal applied strain and corresponding sinusoidal stress response (Macosko, 1994).

Decomposing stress into two component, one in phase with strain and one out of phase (90°):

$$\tau^* = \tau_0' \cos(\omega t) + i \tau_0'' \sin(\omega t) \quad 4.3-4$$

One can thus find that:

$$\tan \delta = \tau_0'' / \tau_0' \quad 4.3-5$$

$$|\tau^*| = \tau_0 = \sqrt{(\tau_0')^2 + (\tau_0'')^2} \quad 4.3-6$$

$$\tau_0' = \tau_0 \cos \delta \quad 4.3-7$$

$$\tau_0'' = \tau_0 \sin \delta \quad 4.3-8$$

Using the complex form of stress function two different moduli can be defined:

$$G' = \tau_0' / \gamma \quad 4.3-9$$

and

$$G'' = \tau_0'' / \gamma \quad 4.3-10$$

Using Euler relation for complex numbers, stress and strain functions may be expressed as:

$$\gamma = \gamma_0^* e^{i\omega t} \quad \& \quad \tau = \tau_0^* e^{i\omega t} \quad 4.3-11$$

And the complex moduli:

$$G^* = \tau_0^* / \gamma_0^* \quad 4.3-12$$

G' is called the *elastic modulus*, and represents the amount of energy stored in a cycle of deformation; the *loss modulus*, G'' , measures the energy dissipation in each cycle (Gandhi and Salovey, 1988).

The complex shear modulus (G^*) can also be expressed as (Figure 4.3-2):

$$G^* = G' + iG''$$

4.3-13

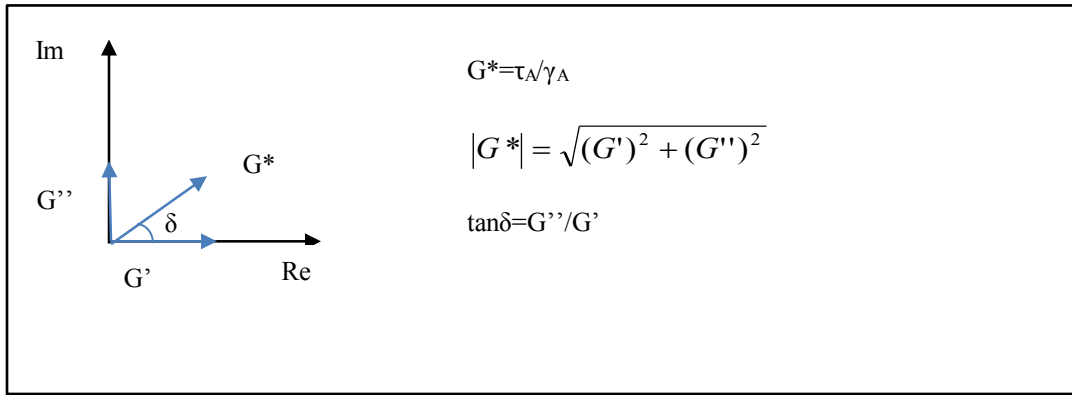


Figure 4.3-2 Schematic illustration of complex shear modulus (Markgraf, 2006).

4.4 Mathematical Model for Viscoelastic Response

4.4.1 Maxwell's Model

One of the simple mechanical models used to describe the mechanical behavior of viscoelastic material is the Maxwell model. The “Maxwell” model is represented by a Hookean spring and a Newtonian dashpot connected in series (Figure 4.4-1). Assuming τ_s and τ_d as γ_s and γ_d are respectively stress and strain of spring and dashpot we have (Chhabra and Richardson, 2008):

$$\tau = \tau_s = \tau_d \tag{4.4-1}$$

$$\gamma = \gamma_s + \gamma_d \tag{4.4-2}$$

$$\dot{\gamma} = \dot{\gamma}_s + \dot{\gamma}_d = \frac{\dot{\tau}}{G} + \frac{\tau}{\mu} \tag{4.4-3}$$

Where,

G is the shear modulus

μ is viscosity of the damper.

Defining θ as the ratio of viscosity to shear modulus (μ/G) the following relationship between stress and strain may be obtained:

$$G\dot{\gamma} = \dot{\tau} + \frac{\tau}{\theta} \quad 4.4-4$$



Figure 4.4-1 Maxwell Model.

Under a constant strain value of γ_0 one may seek the following stress-time relationship:

$$\tau(t) = \tau_0 e^{(-t/\theta)} \quad 4.4-5$$

Since, initially, only the spring deforms, the relaxation modulus can then be obtained through (Chhabra and Richardson, 2008):

$$G(t) = \frac{\tau(t)}{\gamma_0} = \frac{\tau_0}{\gamma_0} e^{(-t/\theta)} \quad 4.4-6$$

In case of a dynamic response Equation 4.4-4 can be written as:

$$G(i\omega)\gamma_0^* e^{(i\omega t)} = \tau_0^* e^{(i\omega t)} \left(i\omega + \frac{1}{\theta} \right) \quad 4.4-7$$

Complex moduli G^* is then:

$$G^* = \frac{Gw^2\theta^2}{1+w^2\theta^2} + i \frac{Gw\theta}{1+w^2\theta^2} \quad 4.4-8$$

The complex shear modulus is composed of two parts: real part (G' : storage modulus) and imaginary part (G'' : loss modulus).

4.4.2 Kelvin-Voigt model

While the Maxwell model is mostly used for material illustrating fluid like responses, the Voigt model is prominently solid-like. In this model the spring and dashpot are arranged in a parallel mode as shown in Figure 4.4-2:

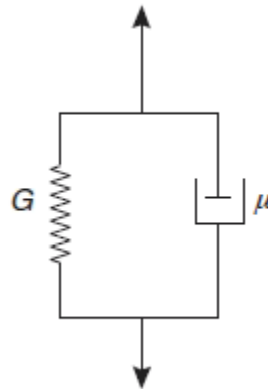


Figure 4.4-2 Kelvin-Voigt model (Chhabra and Richardson, 2008).

For this model (parallel arrangement), the strain is equal while the stress in the system is obtained by adding stress in both components:

$$\tau = G\gamma + \mu\dot{\gamma} \quad 4.4-9$$

Complex shear modulus can then be obtained (Kramer, 1996):

$$G^* = G + i\omega\mu \quad 4.4-10$$

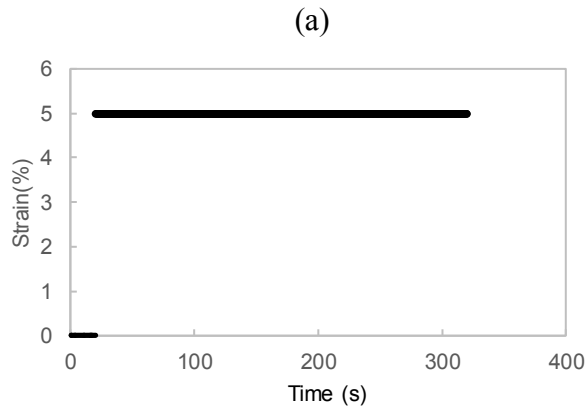
A simple experiment was conducted in order to investigate the behavior of flocculated MFT dosed at 850g/tonne. For this purpose a small strain (5%) was applied for a certain duration of time. Figure 4.4-3 shows an instantaneous response upon application of strain, meaning that initially only the spring deforms; however, over time, a decay in stress values were observed. At this point stress was transferred to dashpot and dissipated. This is a typical behavior for the case of a Maxwell fluid.

Stress decay over time may be obtained using the following equation:

$$\tau(t) = \tau_0 e^{(-t/\theta)} \quad 4.4-11$$

then:

$$G(t) = Ge^{(-t/\theta)} \quad 4.4-12$$



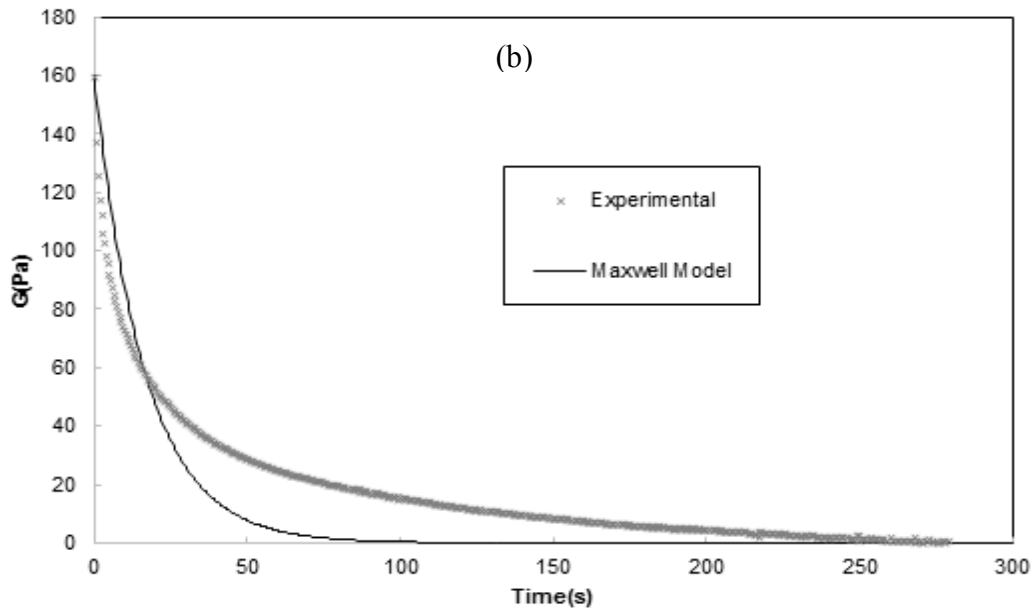


Figure 4.4-3 Stress response (b) to a step input of 5% strain (a).

4.4.3 Amplitude Sweep test

In case of high viscosity material such as soils, amplitude sweep tests are generally recommended to investigate the role of the structure and water content on the viscoelastic behavior (Markgraf et al. 2006).

The limit of linear viscoelastic behaviour of tailings can be determined through the single frequency sweep test. In this test the maximum strain at each cycle will increase while a constant frequency for the oscillations is maintained (2.4.1.3). Figure 4.4-4 illustrates the results of this test conducted on MFT samples dosed at 850 g/tonne. Two sets of tests were conducted at the three different frequencies, 10 Hz , 5Hz and 1.60Hz. Figure 4.4-4 shows how G' and G'' change with maximum stress applied during a cycle. Below about 50 Pa, G' and G'' do not appreciably change, and G' is much larger than G'' . These data imply that, below 50 Pa, the structure of the material is not disturbed by the

oscillations of the vane, and the behaviour of the material is largely elastic. Beyond that point, structure degrades, and eventually, beyond 300-500 Pa (depending on frequency), G' drops below G'' , and the material is dominated by viscous behaviour.

Results from this test can be compared to a stress growth test on the same material (Figure 4.4-5). One can see an elastic region to about 50 Pa, while the material completely yields at around 330 Pa (Mizani et al. 2014b).

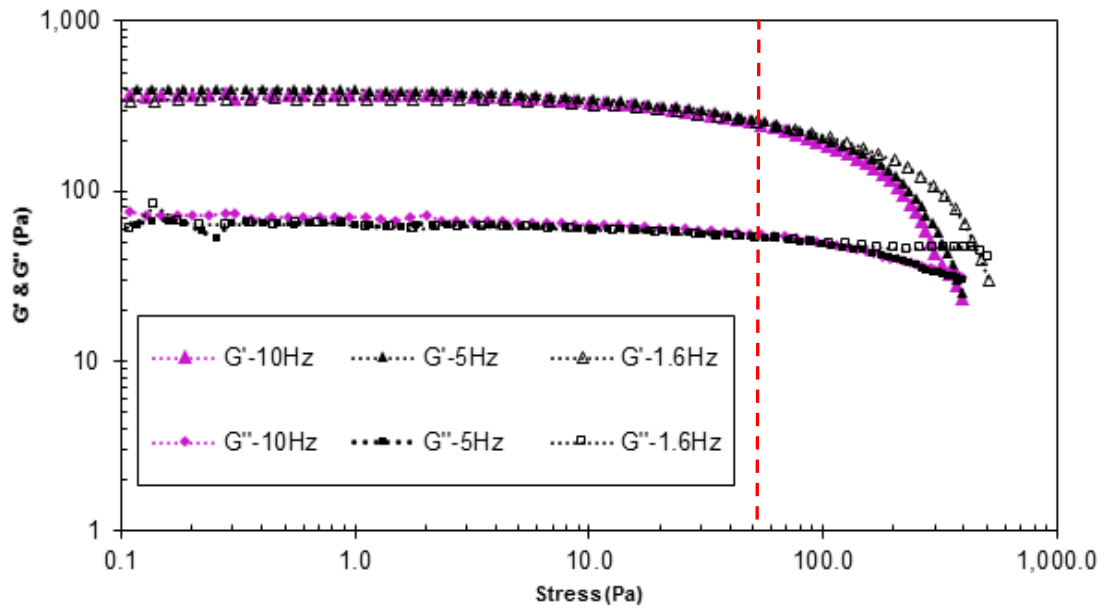


Figure 4.4-4 Response to strain sweeps showing the linear viscoelastic region at three different frequency.

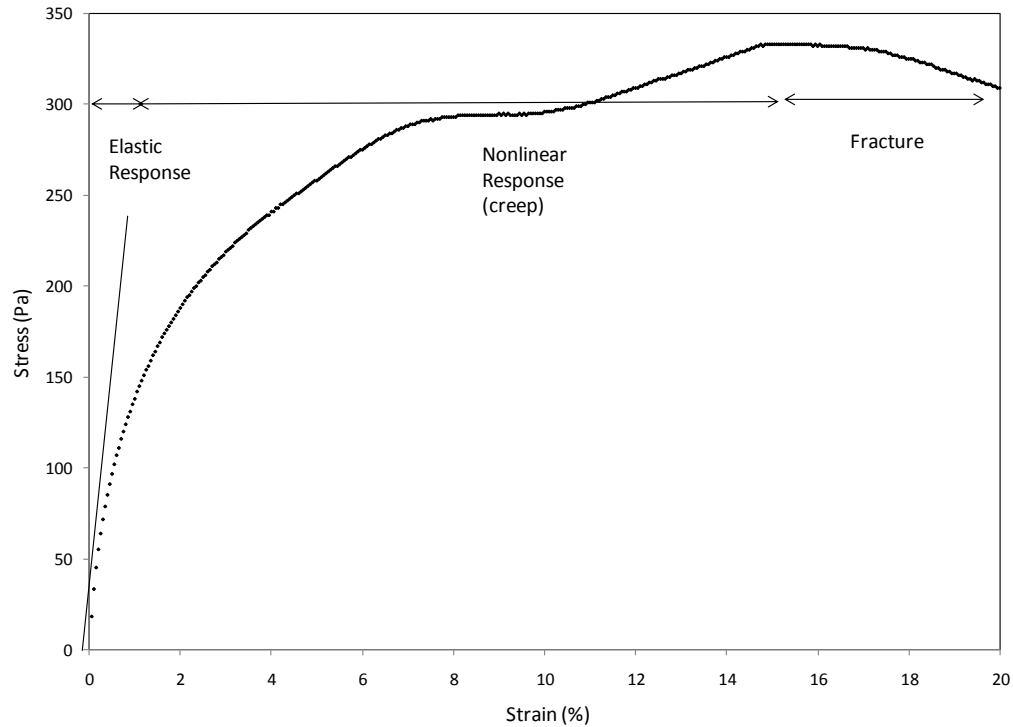


Figure 4.4-5 Stress versus strain plots for material prepared at 850 g/tonne under constant shear rate of 0.1 s^{-1} .

Effects of frequency- The timescale of the oscillatory testing (frequency) was changed from 1.6 to 10Hz to evaluate its effects on elastic response of the material. Figure 4.4-4 illustrate that at smaller stress values the G' response are very similar and discrepancies starts to occur once the creep region is approached. This shows that the elastic response of the flocculated MFT is independent of timescale; thus, the elastic limit yield stress is not dependent on timescale of the testing.

The limit of linear viscoelastic behaviour of raw MFT at solid concentration of 40% were also determined through the single frequency sweep test as illustrated in Figure 4.4-6.

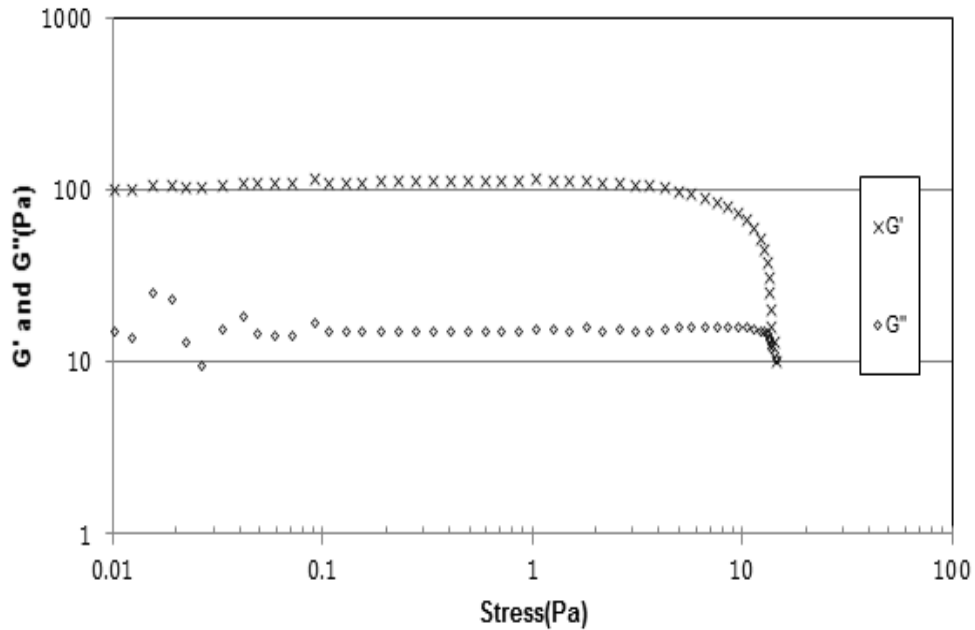


Figure 4.4-6 Response to strain sweeps showing the linear viscoelastic region at 10 rad/s for raw MFT.

Comparing the values of the two modulus and LVE range for raw and flocculated MFT it can be seen that the granular structure of flocculated MFT provides a higher rigidity to the structure thus a higher resistance to an external force. In the case of raw MFT, however, due to its lower stiffness, the viscous state is reached at smaller deformations.

4.5 Thixotropic Behaviour of Flocculated MFT

Thixotropy is a rheological process through which viscosity decreases over time when the material is exposed to shear. Conversely, the structure rebuilds when it is left at rest (Mewis, 1979). In geotechnical engineering, matters involving clay-water suspensions, thixotropy effect is responsible for softening upon remoulding and strength gain at constant water content and porosity over time (Mitchell, 1960). Seed and Chan, (1957) have shown that sensitivity and thixotropic hardening are closely related. In addition, Khaldoun et al.

(2009), showed that thixotropy behavior of muds and clay is the main reason for sudden and long runouts of mudslides and avalanche behavior of quick clays.

Thixotropy is a function of many factors such as water content, clay mineralogy, time and strain (Banas, 1991). While water content plays a significant role in thixotropy gain (the higher the water content the more pronounced the thixotropic effects), time is the key player in the strength gain compared to the former mentioned factor. As a result, if the deposition of a given layer at field scale takes long enough, the shape of the layer would be influenced by the gain in yield stress due to dewatering of the tailings and aging. In order to investigate the effects of aging on the yield stress, a set of tests were conducted at various resting times and at various solid concentrations. Recovery of the sample under simultaneous effects of shearing and aging will be presented in the next section.

Changes in the strength gain of flocculated MFT over time (thixotropic effects), were quantified using the stress growth tests on samples ranging in solid content and age. The peak shear strengths were then determined to investigate the increase in yield stress over time. Amended MFT were placed in containers 10cm in height after preparation and were tested at different times. Due to initial water release and self-weight consolidation over the extended time of the experiment, difficulty in maintaining a constant water content throughout the test was inevitable. Thus, interpolation techniques were used to correct for these effects as per Banas, 1991 and Jeeravipoolvarn 2005. Ten (10) cm was chosen as it is the minimum height required for samples in the rheometer; this would minimize the role of self-weight consolidation (Figure 4.5-1).

In Figure 4.5-3 Figure 4.5-4, shear strength and thixotropic ratio of flocculated MFT dosed at 850g/tonne, at two different solid content of 32.65% and 43.31% (void ratio 4.54

and 2.87 respectively) are illustrated. As the water content decreased over time so did the changes in maximum stress. The measured solid content at various times are also shown in Figure 4.5-2. Figure 4.5-5 illustrates the thixotropic gain in strength due to aging alone at a solid content of 43.3.6% and 39.4% using the following interpolation techniques:

First the difference in solid concentration at each time is calculated (using the two curves in Figure 4.5-2 (I-II)). For thixotropic strength at higher solid concentration (43.3%) the difference between the solid concentration at each time and the solid concentration of interest is calculated (I- 43.3%). The correction value is then calculated by multiplying the ratio of these two values (I-43.3%)/(I-II) by the difference in strength at each point (III-IV). Finally the interpolated strength at each time is calculated by subtracting the correction value from the strength at time of interest (III).

For the lower solid concentration the same procedure was followed, but this time the solid concentration of interest 39.4% subtracted by II, was used to calculate the correction value: (39.4%-II)/(I-II). The interpolated strength at each time was calculated by adding the correction value to the strength at time of interest (IV).



Figure 4.5-1 Samples prepared for thixotropy testing

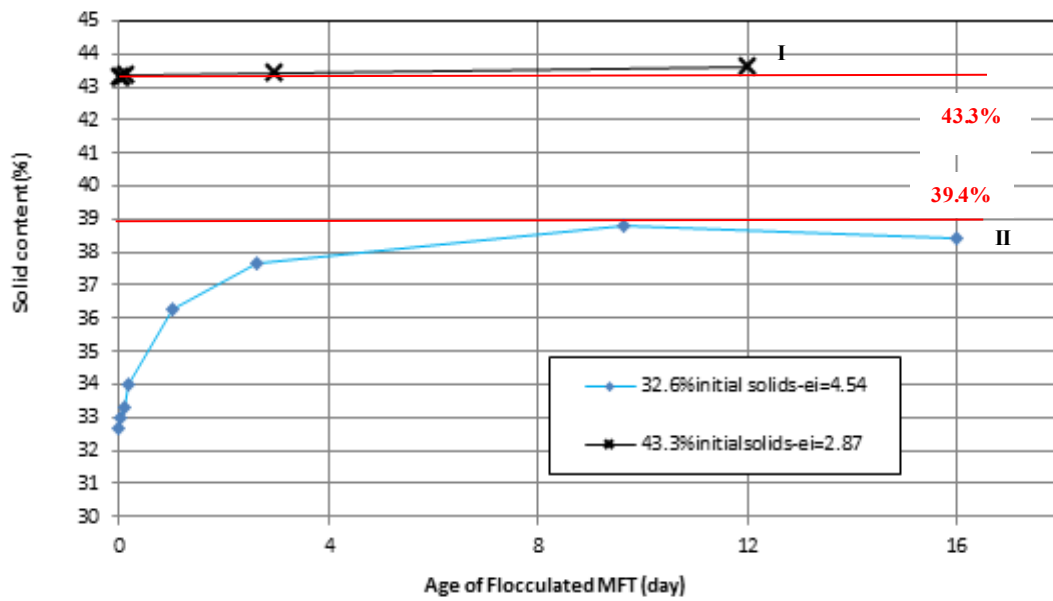


Figure 4.5-2 Solid content measurement of flocculated MFT for three different samples at various times.

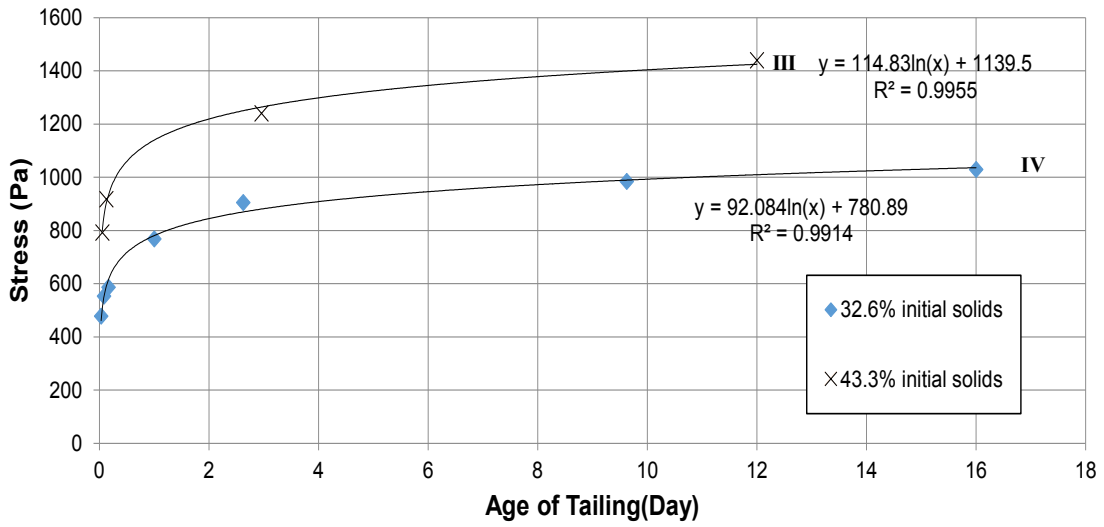


Figure 4.5-3 Strength measurement for flocculated MFT dosed at 850g/tonne for different solid contents over time.

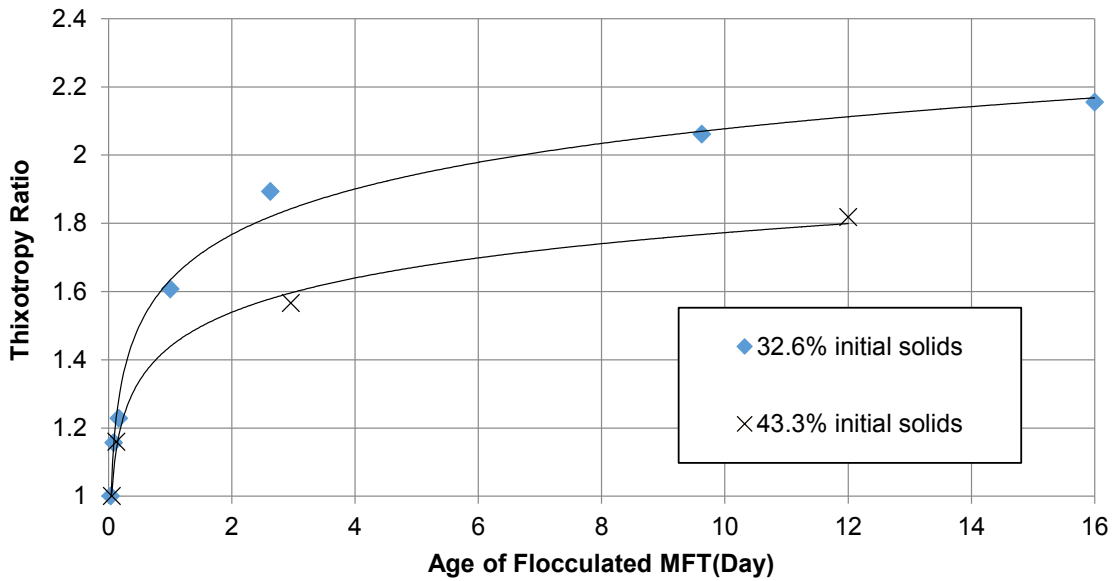


Figure 4.5-4 Thixotropic ratio for flocculated MFT dosed at 850g/tonne for different solid contents over time.

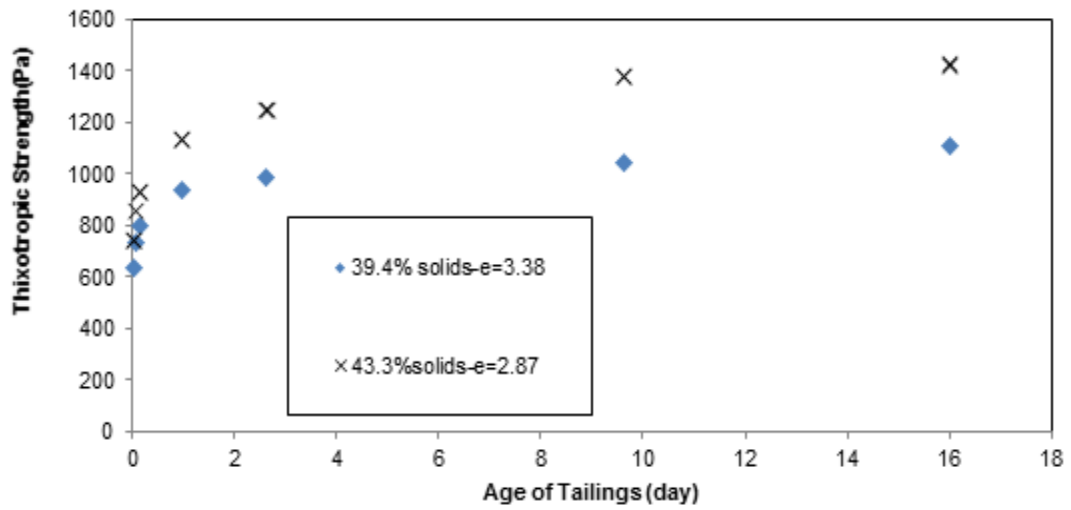


Figure 4.5-5 Interpolated thixotropic strength at 39.4% and 43.3% solid content using the procedure in Miller, 2004.

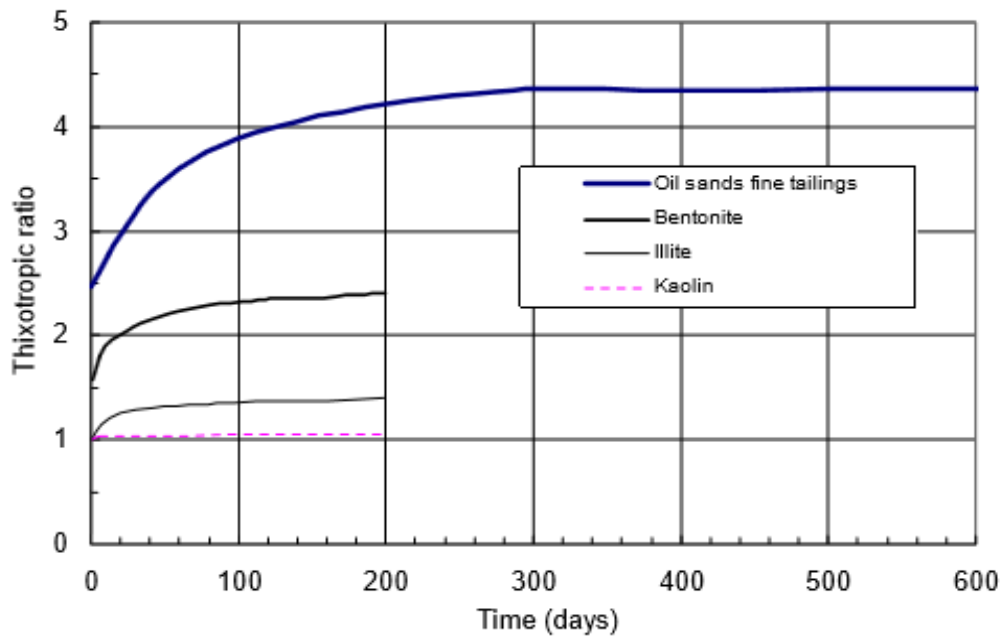


Figure 4.5-6 Thixotropic ratio in different clay type and raw MFT (Jeeravipoolvarn, 2005).

While raw MFT has been previously shown (Jeeravipoolvarn, 2005 and Banas, 1991) to be highly thixotropic (Figure 4.5-6), flocculated MFT in this study showed thixotropic behaviour much closer to clayey systems (illite and bentonite) both illustrating relatively small thixotropic effects compared to unflocculated MFT.

The discrepancy observed in different clayey systems (fine and coarse particles) could be attributed to the different shearing mechanism. Shearing in clay systems having finer particles, such as bentonite, causes volumetric deformations and no significant disruption in material structure, whereas, in coarser clayey material (kaolinite), both volumetric deformation and structural disruption along the shearing plane takes place.

The evolution of storage modulus with solid content over time is presented in details in chapter 5.

4.5.1 Effects of Aging and Shearing on Tailings Structure

Although the material can rebuilt itself when left at rest, shearing will result in restructuration of the material. One method previously used by Watson et al. (2011) to evaluate floc breakage and reformation is the three-interval thixotropy test. After finding the linear viscoelastic (LVE) region through single frequency sweep test, the baseline rheology is determined by applying an oscillating stress (below the LVE range). This is to ensure that the material is undergoing elastic deformation only, during shearing. The material is then sheared at a constant stress for a certain amount of time, after which an oscillating stress (the same as in the first step) is applied on the material. Recovery of the sample over time is then determined as the ratio of storage modulus from the end of the

third interval to the storage modulus at the end of the first interval. Figure 4.5-7 shows a schematic of this test.

In order to investigate the effects of shearing on the percentage recovery of flocculated MFT at 850 g/tonne, the three stage thixotropy test was used where an oscillatory stress of 10 Pa was applied on freshly prepared samples for five minutes in the first and third stages. A high stress level (500Pa) was then applied for different time intervals (90 s and 300 s), after approximately 1 hour upon mixing, to see the effects of shearing time on sample recovery. Figure 4.5-8 illustrates recovery of the MFT sample dosed at 850 g/tonne, along with a plot of G' before and after applying a high stress level.

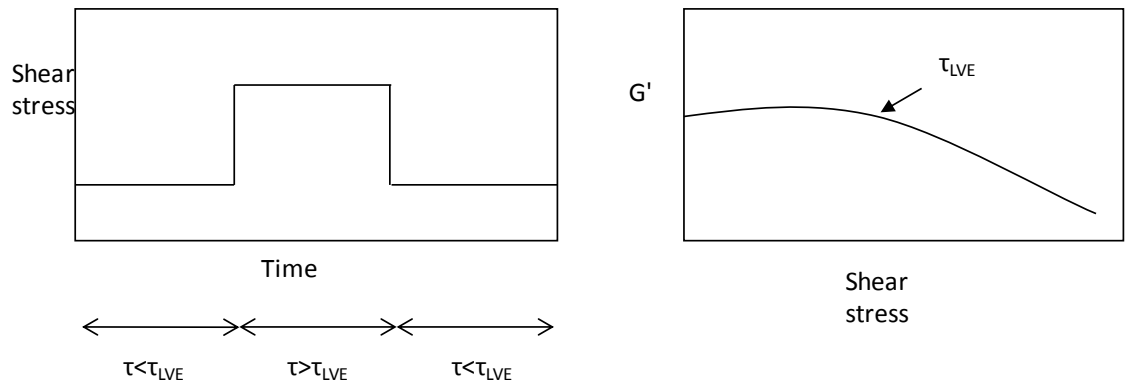


Figure 4.5-7 Three-interval thixotropy scheme.

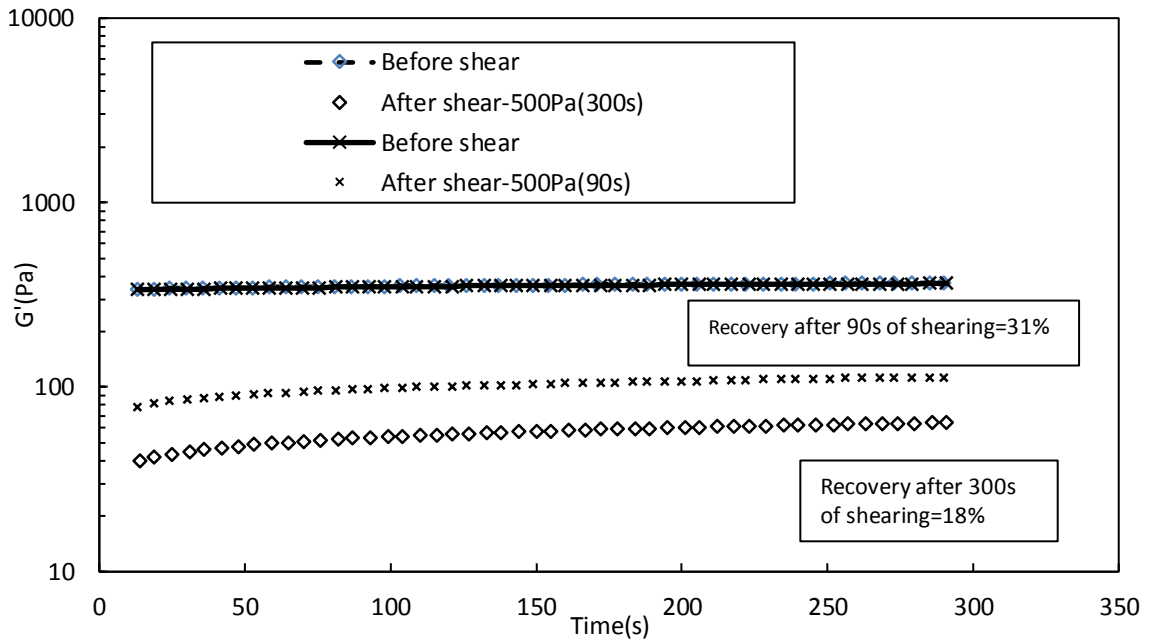


Figure 4.5-8 Postshear recovery for samples prepared at 850 g/tonne after applying a shear stress of 500 Pa for different times (90s and 300s).

Although in all cases, partial reformation of floc was observed with time, a longer shearing time at the same stress level resulted in a lower recovery rate. Figure 4.5-8 also illustrates that the thixotropic process (aggregates requiring some time to reform), can overcome the adverse effect of shearing (floc breakage) dependent on loading conditions.

The scenario above is probably extreme when applied to the field, as no time is given for recovery of rheology due to aging. Therefore, percentage recovery of samples was also measured under shear loading similar to that experienced during deposition (see Section 4.2.5). After applying an oscillating shear stress of 10 Pa, the MFT material dosed at 850 g/tonne was sheared at 500 Pa for 10 seconds. The stress was then gradually decreased in steps (250 Pa, 100 Pa, 50 Pa, and 20 Pa), and each stress level was applied for only 10 seconds, giving a total time spent in stage 2 of 50 seconds.

The test was then repeated on a newly prepared sample, but this time, all stress levels were held for one minute (Figure 4.5-9). A higher recovery rate was recorded in the latter case, which could be attributed to the longer time spent at low stress levels, despite the longer time at higher shear levels, thus giving the material more time to recover from the damage experienced. From these results it could be concluded that the material recovers structure even as it flows (at low shear levels).

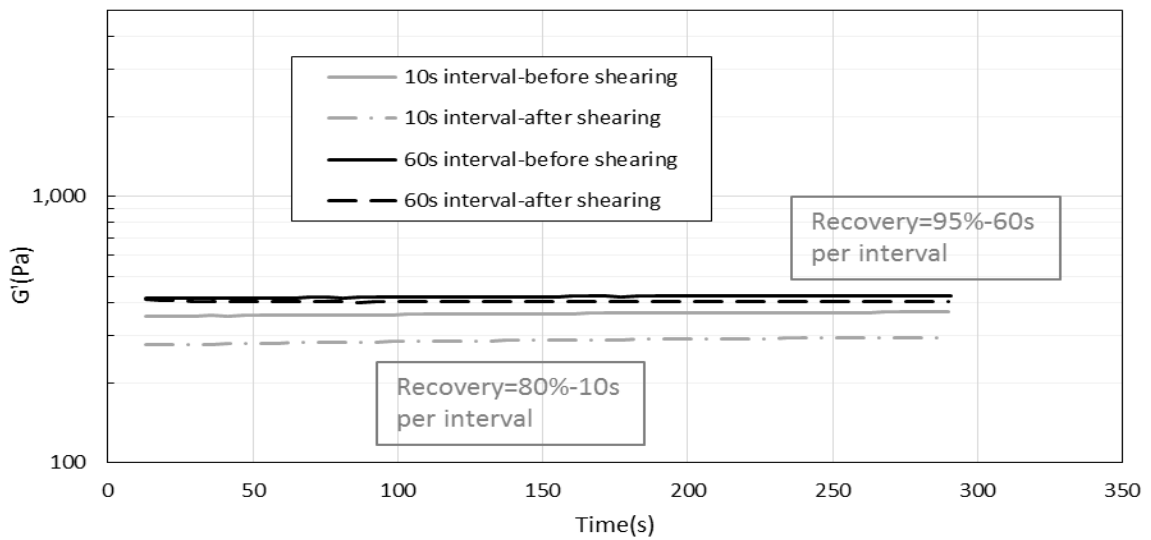


Figure 4.5-9 Post shear recovery for samples prepared at 850 g/tonne under constant decreasing shear stresses.

In the next section (4.6), the structure of material will be quantified using some mathematical models under various loading conditions (constant shear stress and shear rate).

4.6 Comparison of Thixotropic Models to Rheological Data

From the previous sections it can be seen that tailings showed a complex behavior, under shear, and thus cannot be explained by a simple yield stress model (i.e Bingham, Herschel Bulkley,...). Looking at the values from stress growth and constant decreasing stress it can be seen that a much larger stress is required for flow initiation, the critical stress itself, dependent on how long the fluid was left to age. On the other hand, flow ceases at a much smaller stress level. Constant stress tests also showed that while structure break down under high stress levels are rapid, structural rebuilding takes place at a much slower rate. All this gives rise to the idea that the behavior of flocculated MFT is stress dependent. In this section, applicability of a few thixotropic model to the rheological data obtained under various loading conditions, is studied. While in the first model no explicit value for yield stress is used, and variations in viscosity are used to detect this critical value under different shear histories, in the second model a yield stress value is included in the model. Finally modifications were applied to the model to include dewatering behaviour.

4.6.1 Coussot Thixotropy Model

Coussot et al. (1993), introduced a new model to describe the particulate systems which are usually considered to exhibit yield behaviour. In this model, transition from solid-like to liquid-like behaviour is described by a viscosity bifurcation rather than by a yield stress. The present study follows the development of the model which is described in Roussel et al. (2004), where the components τ and Υ of the viscosity, (i.e. $\mu = \tau / \dot{\gamma}$) depend on the current state of structure, λ , and where λ is considered to be a function of time and shear rate:

$$\mu = \mu_0(1 + \lambda^n) \quad 4.6-1$$

$$\frac{d\lambda}{dt} = \frac{1}{T} - \alpha \dot{\gamma} \lambda \quad 4.6-2$$

where n , T , μ_0 and α are four material parameters. For this model to represent a fluid with yield behaviour, n has to be greater than or equal to one. This condition ensures that τ does not tend to zero when the shear rate approaches zero.

As implied above, unlike other yield stress models, the Coussot model does not contain an explicit yield stress, and so this property does not have to be determined. Instead, the unyielded region is identified by monitoring the changes in viscosity with respect to time. Under constant stress, viscosity will tend to infinity or to a very low value depending on the value of the constant stress applied. When stresses are below the critical value viscosity increases in time until flow stops.

Steady state is said to be reached when the structure λ does not change with time, i.e., $d\lambda/dt=0$, this occurs at a critical shear rate, denoted $\dot{\gamma}_c$. Therefore, the stress decreases when $\dot{\gamma} < \dot{\gamma}_c$ and increases otherwise. This critical shear rate can be calculated by identifying the point at which:

$$\frac{d\tau}{d\dot{\gamma}} = 0 \quad 4.6-3$$

from which it follows that

$$\dot{\gamma}_c = \frac{k}{\alpha T} \quad 4.6-4$$

Where,

$$k=(n-1)^{1/n}.$$

For shear rates below the critical shear rate, flows are unstable, where the material will either fracture or show shear localization resulting in non-homogeneous flows. This critical shear rate corresponds to a critical shear stress, τ_{cc} . This critical stress may be defined as:

$$\tau_{cc} = \mu_0 \left(\frac{n}{n-1} \right) \dot{\gamma}_c \quad 4.6-5$$

Which is the stress at which viscosity decreases and reaches a steady state value of μ_0 when exceeded. On the other hand, for a stresses below this critical value, viscosity increases until the flow comes to a halt. It should be noted, that the critical stress is identified as a time-dependent yield stress (Coussot et al. 2002b). Thus, it is better to scale the shear stress and shear rate by their critical values respectively:

$$\psi = \frac{\tau}{\tau_{cc}} \quad \text{and} \quad \Gamma = \frac{\dot{\gamma}}{\dot{\gamma}_c} \quad 4.6-6$$

Figure 4.6-1 illustrates the variation in dimensionless viscosity versus dimensionless time when material is under constant stresses. It can be observed that this model can perfectly capture the bifurcation in viscosity when stress approach the critical value τ_{cc} , reaching very high values (apparent stoppage) for $\tau < \tau_{cc}$ and tending toward a low value when $\tau > \tau_{cc}$. Defining a dimensionless stress (ψ) as the ratio of the applied stress to the critical stress and a dimensionless shear rate, from the above equations it is found that:

$$\psi = \frac{n-1}{n} (1 + \lambda^n) \Gamma \quad 4.6-7$$

$$\frac{d\lambda}{dt^*} = 1 - k\Gamma\lambda \quad 4.6-8$$

where t^* is the dimensionless time ($t^*=t/T$).

In cases where the material is subjected to a constant stress (Ψ_0), at which stress is maintained at its initial value and structure at its initial state λ_0 , Equation 4.6-8 can be expressed in the form:

$$\frac{d\lambda}{dt^*} = 1 - \frac{nk\psi_0}{n-1} \frac{\lambda}{1+\lambda^n} \quad 4.6-9$$

Note that α was eliminated through the introduction of Γ and has effectively been replaced by $\dot{\gamma}_c$; thus, only the parameters n and λ_0 need to be estimated. For the model to represent a yielded stress material, n has to be equal or greater than 1; therefore, a value of 2 was chosen for n , and λ_0 , representing the initial state of the structure, is chosen to be 1.

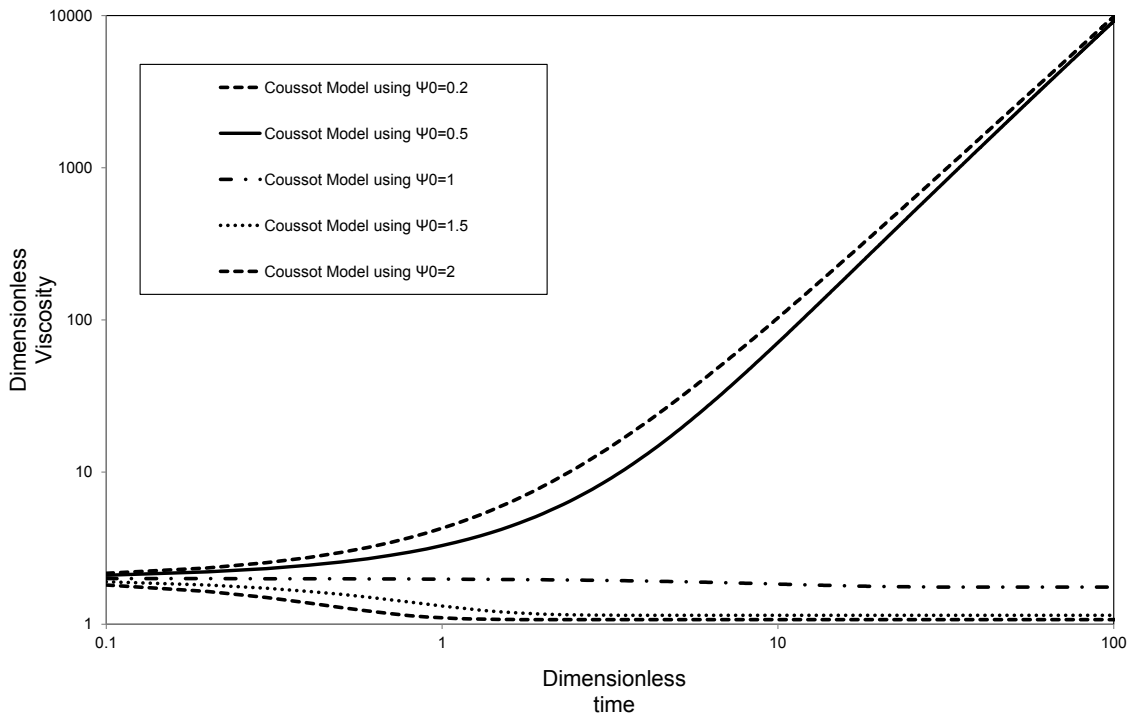


Figure 4.6-1 Dimensionless viscosity versus dimensionless time for various dimensionless stresses (using $n=2, \alpha=1$ and $\lambda_0=1$).

4.6.1.1 Experimental Data

In this section a comparison is made between the model prediction and experimental data. Data presented in section 4.2.5 are replotted in Figure 4.6-2, but this time showing the changes in viscosity and shear rate against time for various stress levels, from 100 Pa to 900 Pa. Real quantities of viscosity and time are illustrated in this figure since measured values from experimental data are presented. While Figure 4.6-2a shows the changes in viscosity, Figure 4.6-2b is presenting flow behaviour under various stress levels. One important observation from this figure is that for stresses below the critical shear stress, viscosity increases over time tending to an infinite value; whereas, for stresses above that value, viscosity shows a continuous decrease with time. On the other hand, the critical stress value is dependent on the initial states of the material which will be incorporated into Coussot model through λ_0 . Thus, at various initial states the material may show different behaviour under the same stress level.

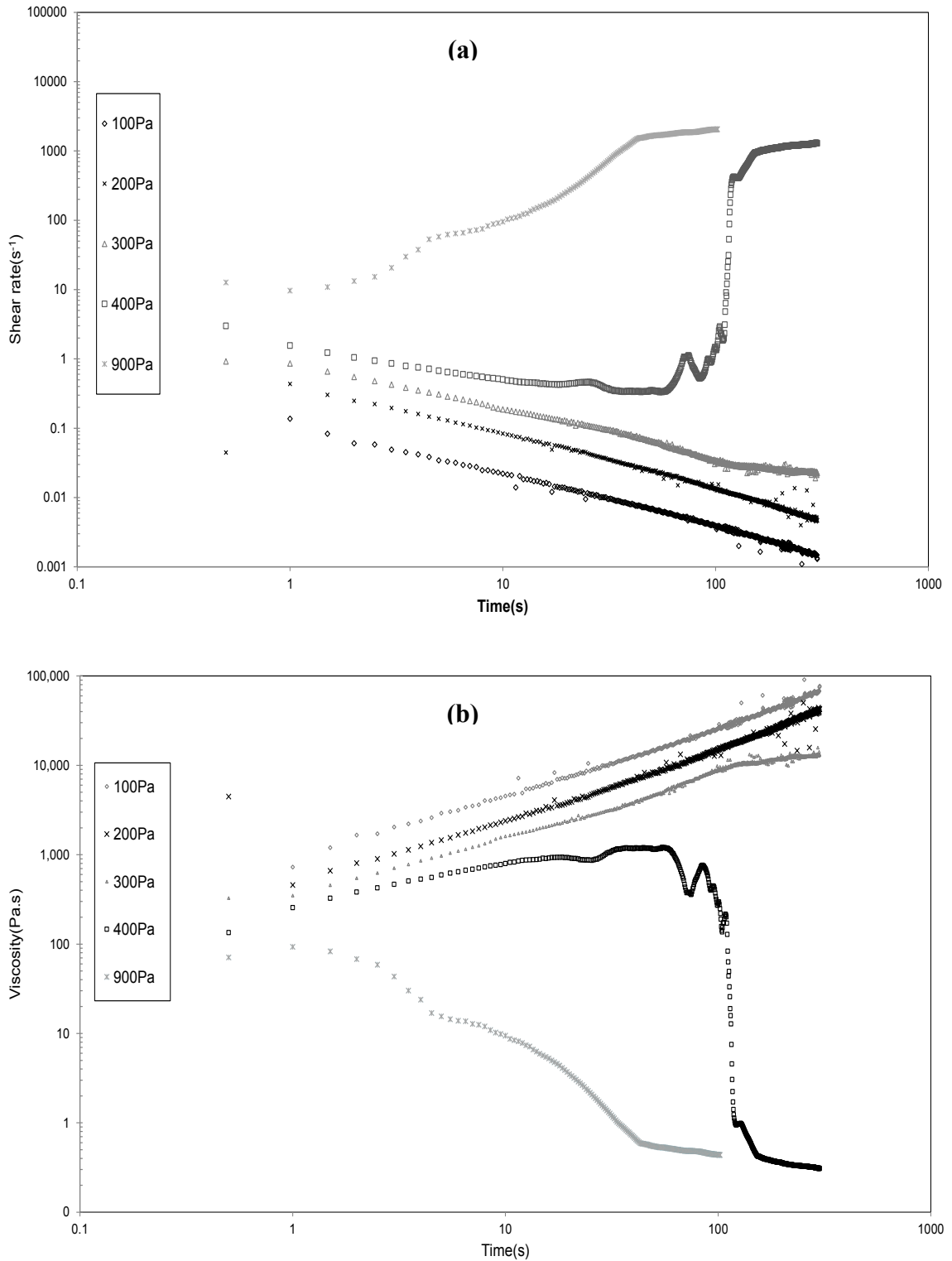


Figure 4.6-2 Viscosity (a) and shear rate (b) versus time for flocculated MFT dosed at 850g/tonne exposed to different levels of stress over a period of 120 seconds.

It is noted that the bentonite suspensions used by Coussot et al. (2002b) showed the same behavior to the above tailings. That is, for that material, flow either stopped or led to an avalanche effect when different levels of stress were applied. The following figure presents fits of a thixotropy model to controlled stress experiments conducted on bentonite suspensions.

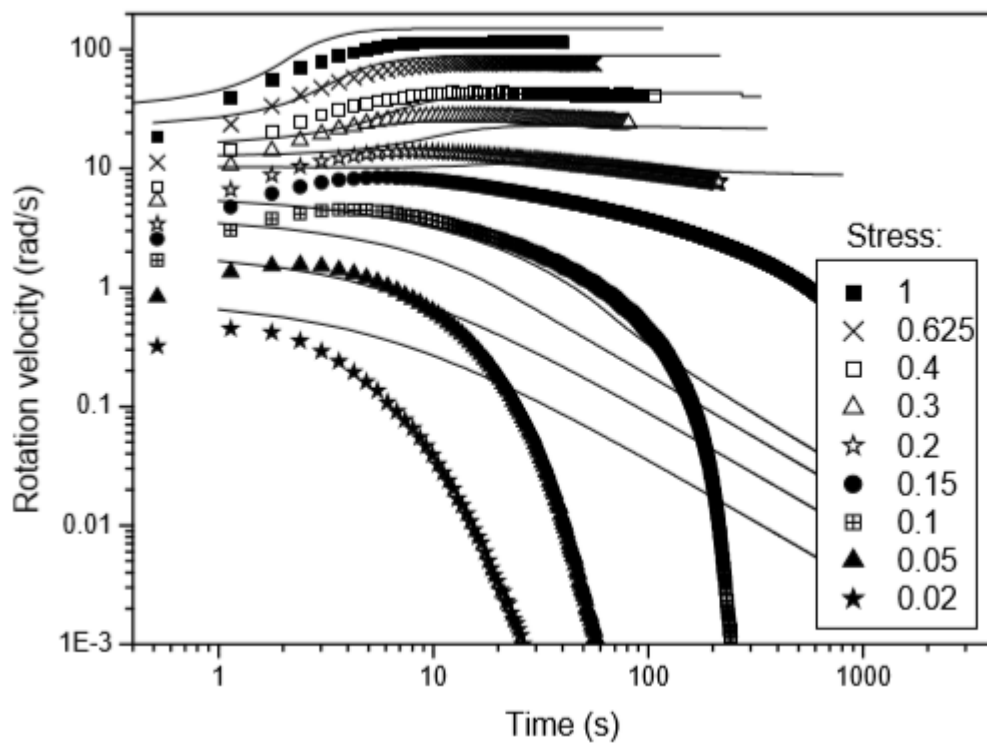


Figure 4.6-3 Predictions of Coussot thixotropy model (continuous lines) and measured experimental data (symbols) at different imposed (dimensionless) stresses (Roussel et al. 2004).

As pointed out earlier n must be larger than or equal to unity to simulate yield behaviour. By trial and error, it was found that the values $n=1.075$ ($k=0.09$) and $\lambda_0=80$ best represent the experimental data. For these values, a numerical analysis was conducted for different stress levels– for Ψ_0 from 0.2 to 4– to investigate the critical condition. The change in λ at each time step was calculated from 4.6-9:

$$\Delta\lambda = \left(1 - nk\psi_0 \frac{\lambda}{(1 + \lambda^n)(n-1)}\right)\Delta t \quad 4.6-10$$

The new values for λ were then calculated by applying the changes in λ to the previous value. In Figure 4.6-4, Coussot model curves are shown along with the experimental data, for various stress levels Ψ_0 and for $T=0.01$ and $\mu_0=1$.

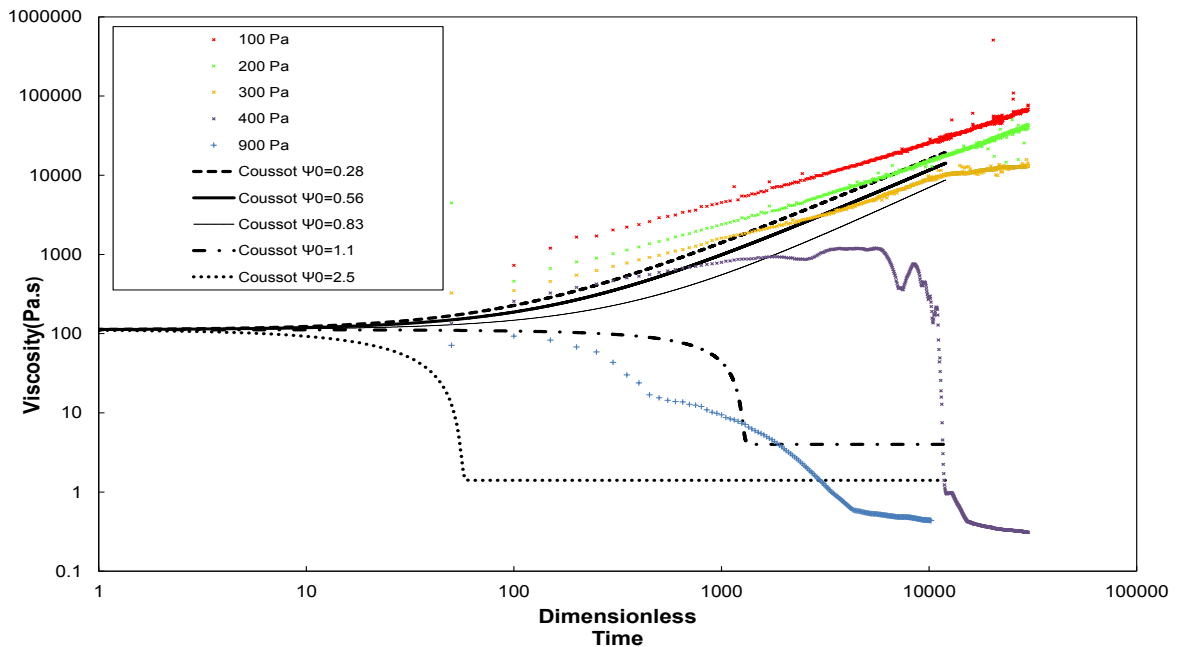


Figure 4.6-4 Viscosity versus dimensionless time as predicted by the Coussot model and as measured by the rheometer, for $T=0.01$ and $\mu_0=1$.

Figure 4.6-4 shows that the Coussot model generally captures the bifurcation in viscosity, where it drops discontinuously from infinity to a low value when stresses reach the critical value ($\Psi_0=1$). This is also evident in Figure 4.6-1.

4.6.1.2 Comparison with Controlled Shear Rate Data

Next the applicability of Coussot model under constant shear rates will be investigated. In this case a constant shear rate (Γ_0) is imposed on the fluid, starting at an initial state of λ_0 , structure evolution of the material at any time can then be obtained by integrating Equation 4.6-8:

$$\lambda = \frac{1}{k\Gamma_0} + \left(\lambda_0 - \frac{1}{k\Gamma_0}\right) \exp(-k\Gamma_0 t) \quad 4.6-11$$

Figure 4.6-5 illustrates plots of viscosity versus dimensionless time, obtained at shear rates of 0.001, 0.01, 0.1, 1, 5, and 10 s^{-1} , after 30 minute upon mixing and after removing release water. In this figure the same colour has been used for the experimental data (dots) and prediction curves from Coussot model, at each shear rate. Liddell and Boger, (1996) referred to these as ‘stress growth curves’. The predictions of the Coussot model, for the six experimental shear rates, are also presented on this graph using a value of $n=1.075$, $\alpha=0.36$ and $\mu_0=1Pa.s$ for the various terms in the model.

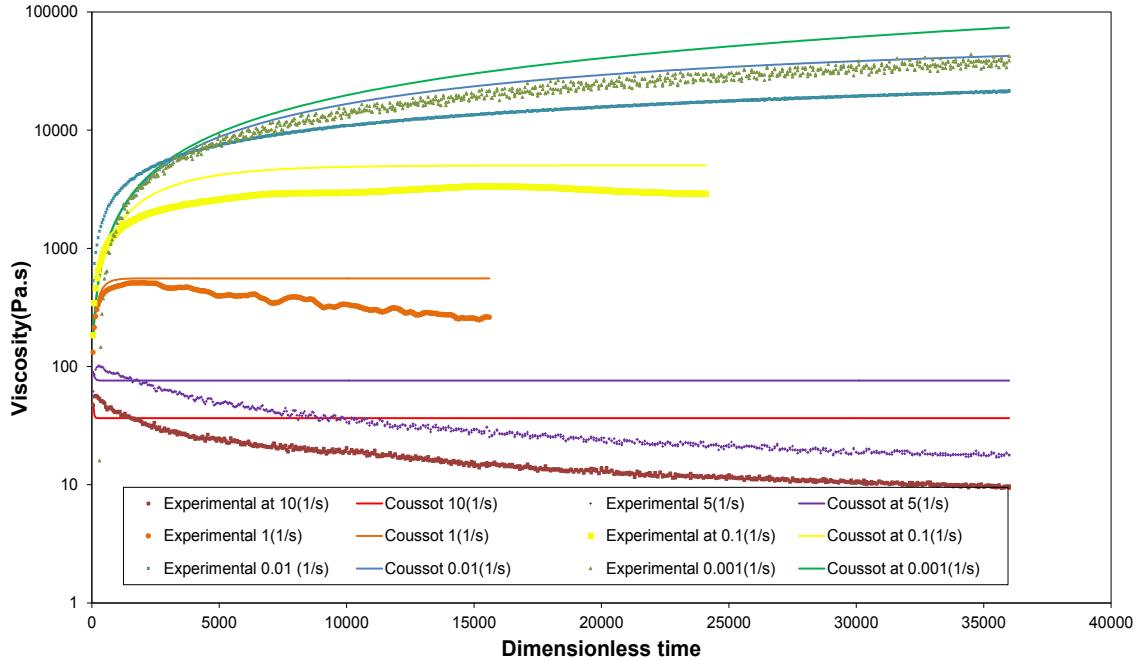


Figure 4.6-5 Measured and predicted values of the viscosity at five shear rates, using Eq. 4.6-11 for $n=1.075$, $\alpha=0.36$ and $\mu_0=1\text{Pa.s}$.

The figure demonstrates that the Coussot model can predict behaviour qualitatively but not quantitatively, especially at high shear rates. This discrepancy could be attributed to the yielding criterion, which is not explicit in the model. Moreover, this model does not account for the hysteresis behavior of the tailings.

4.6.2 Hewitt Thixotropy Model

One of the drawback of the Coussot model is the absence of the yield term in a sense that an infinite-viscosity material will remain solid even at high stress levels. Thus in this section the applicability of another model developed by Hewitt and Balmforth, (2013) will be examined which involves inclusion of implicit yield stress value.

The rheological model used here is adapted from Coussot et al. (2002a and b), where the original model is modified with a maximum value of structure, and the rate of aging is proportional to difference between the current structure value and the maximum value. The modified ageing term is a function of the maximum structure value as follows:

$$\frac{d\lambda}{dt} = \frac{(\lambda_{\max} - \lambda)}{T} - \alpha \dot{\gamma} \lambda \quad 4.6-12$$

Limiting the λ_{\max} to unity representing the fully structures state , $\lambda < 1$ would then represent a material that is destructured to some degree (Hewitt 2012) and defining viscosity as a function of structure in the following form:

$$\mu = \frac{\mu_0}{(1 - \lambda)(1 - \beta\lambda)} \quad 4.6-13$$

Where μ_0 is a constant reference viscosity (Hewitt 2012) and β is a constant. Equation 4.6-12 can then be written as:

$$\frac{d\lambda}{dt} = \frac{(1 - \lambda)}{T} \left(1 - \frac{T\alpha\lambda\tau(1 - \beta\lambda)}{\mu_0} \right) \quad 4.6-14$$

Figure 4.6-6 illustrates the evolution of structural changes over time and with stress.

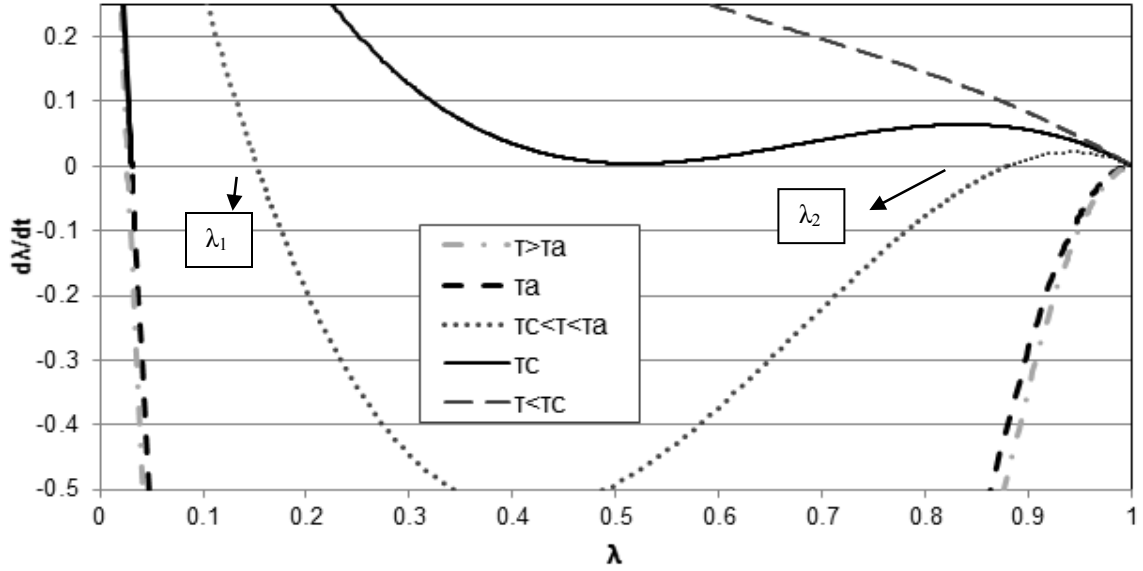


Figure 4.6-6 Variation of λ with time and under various stress level ($\beta=0.97$ and $\alpha T/\mu=0.077$).

Below the critical stress ($\tau_{cH}=4\beta\mu_0/\alpha T$) the structural changes remain positive (although decreasing over time) and eventually reach the maximum structure. This would mean that below this critical stress level the structure will not degrade and viscosity will increase over time. However, as the stress level is increased ($\tau > \tau_{aH}=\mu_0/(\alpha T(1-\beta))$) structural changes will be negative and thus viscosity will decrease irrespective of the value for λ . $d\lambda/dt$ will now become zero at two different points:

$$\lambda_{1,2} = \frac{1}{2\beta} \left[1 \pm \left(1 - \frac{4\beta\mu_0}{\alpha T \tau} \right)^{1/2} \right] \quad 4.6-15$$

For stress level in between τ_{aH} and τ_{cH} the behavior of the material is dependent on the shear history of the material (Hewitt, 2012). That is if the material initially has a structure very close to λ_{max} then the shear rate will remain zero up to the point where stress exceeds

τ_{aH} . After this point the structure will decrease and evolve towards λ_1 . If the stress is then lowered (ramp down) the structure will only evolve to $\lambda=1$ when it becomes less than τ_{cH} . At this point shear rate will go back down to zero. The advantage of this thixotropy model over the conventional models (i.e Bingham, H&B,...) is that the it takes into account the shear history of the material and the hysteresis can be controlled through the β term.

In the next section the applicability of the said model to amended oil sands tailings will be investigated.

4.6.2.1 Fitting model to experimental data

The following graph presents the prediction of the proposed thixotropy model to the actual experimental data under different levels of stress (100Pa-900Pa). For these predictions the $T=10$, $\alpha=0.01275$ and $\mu_0=1.5$ and $\beta=0.97$ were used.

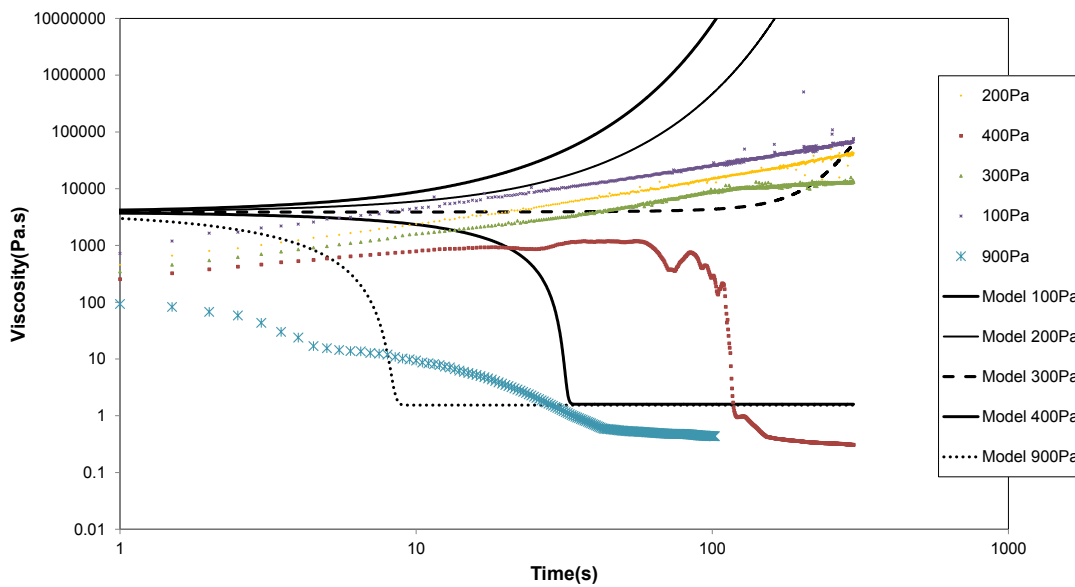


Figure 4.6-7 Creep tests modeled using thixotropy model ($\mu_0 = 1.5$ Pa.s, $T = 10$, $\alpha=0.01275$).

In Figure 4.6-8 we apply the thixotropy model to the stress growth data presented in Figure 4.2-6. A good fit can be obtained to the data for most of the shear rate values with the exception of the lowest shear rate (0.001 s^{-1}), using the same parameters used to model the creep data. For the mentioned case, an order of magnitude difference could be seen between the experimental and modelled values for the peak stress.

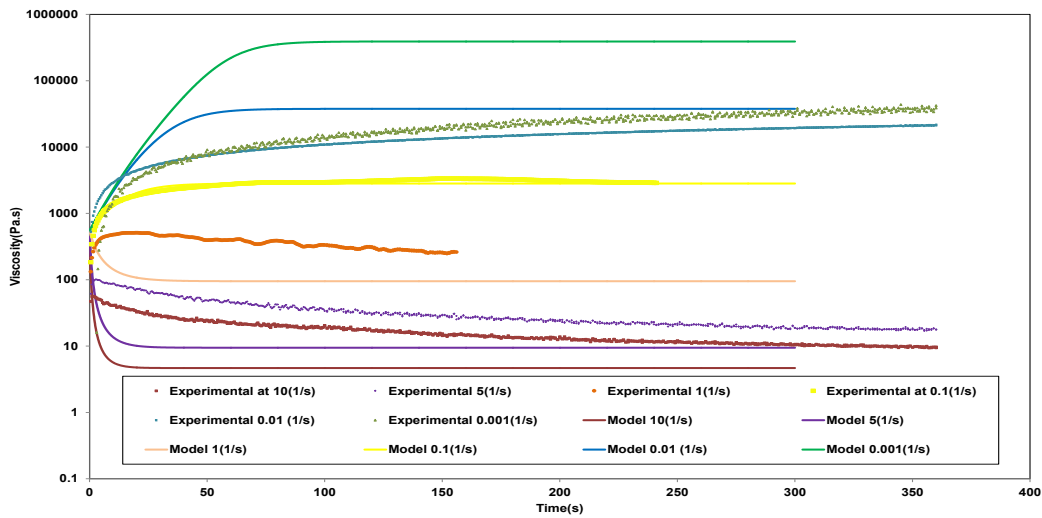


Figure 4.6-8 Stress growth test under various shear rate and as predicted by the proposed thixotropy Model.

4.6.3 Modified Hewitt Thixotropy Model

The Coussot model and Hewitt model were originally developed for bentonite suspensions; however, the behavior of flocculated MFT was observed to be different in that the “ageing “ is at least partially driven by dewatering over longer times. The increase in solid concentration would mean that the material will exhibit higher viscosity (Figure 4.5-2 and Figure 4.5-4) thus a higher value for the structure term. In other words, “ageing” in the case of the flocculated MFT is due to dewatering, as well as true thixotropic

processes that occur at constant density (Figure 4.5-5). This led us to empirically modify the ageing term in Equation 4.6-12 to generate an ageing behavior that includes gravity driven settling over time:

$$\frac{d\lambda}{dt} = \frac{(\lambda_{\max} - \lambda)\chi}{T} - \alpha \gamma \lambda \quad 4.6-16$$

Where χ is a function of time. This change in the ageing term causes the rate of structure buildup to be faster at low values of structure, thereby reflecting the effect of density changes due to dewatering.

λ_1 and λ_2 can be written as :

$$\lambda_{1,2} = \frac{1}{2\beta} \left[1 \pm \left(1 - \frac{4\beta\mu_0\chi}{\alpha T\tau} \right)^{1/2} \right] \quad 4.6-17$$

And τ_{aH} and τ_{cH} are formulated as:

$$\tau_{low} = \frac{4\beta\chi}{\Gamma} \quad 4.6-18$$

$$\tau_{high} = \frac{\chi}{\Gamma(1-\beta)} \quad 4.6-19$$

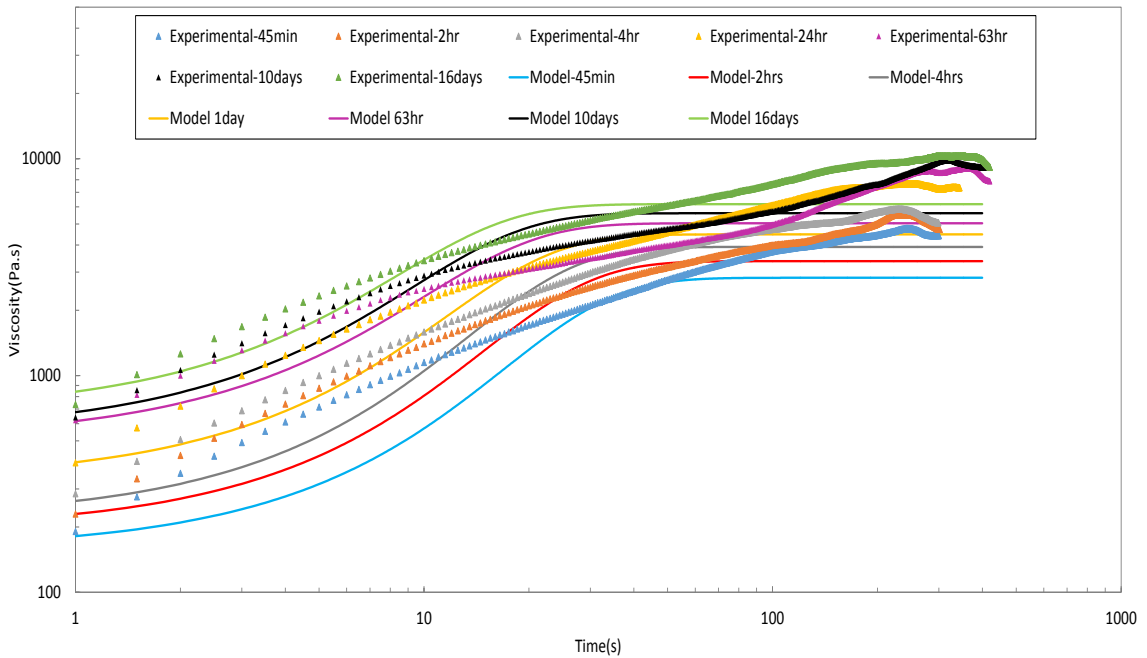


Figure 4.6-9 Viscosity variation for flocculated MFT at 850 g/tonne dose for different times of rest.

Figure 4.6-9 shows the data for samples tested at constant shear rate of $0.1(\text{s}^{-1})$ for different resting time along with prediction using the modified version of Hewitt model. The sensitivity of viscosity values to the resting time (under same shear rate values) is due to the building/aging of the structure.

4.6.4 Discussion on the Proposed Thixotropy Models

To explain the results, two viscosity models were empirically fit to the rheological data. Both are variants on the model developed by Coussot et al. (2002a). Though both the original Coussot model and the modified model are not perfect, they seem to reasonably explain the ageing and shearing processes in the tailings.

In the first model, transition from solid-like to liquid-like behavior is described by viscosity bifurcation rather than by a yield stress. In the second model the ageing term was modified to be dependent on the structure value in relation to some maximum structure value. This modification in ageing term causes the rate of structure buildup to be faster at low values of structure and to decrease as the structure term increases, thereby reflecting the effect of dewatering. Moreover in this model and through the introduction of β term, the degree of hysteresis between a material initially fully structured and a material fully destructured may be controlled: the size of the hysteresis loop will increase as β increases ($\beta \rightarrow 1$), where τ_{high} tends toward ∞ but τ_{low} remains finite. The system will illustrate no hysteresis if the value of β is set to 0.5 and would then represent the rheology of Bingham fluid.

As with earlier models, yield stress behaviour emergent from this model in the form of rapid increase in viscosity. In Hewitt's model, there are two critical stresses, τ_{low} and τ_{high} . For a full structured material, the structure will not decrease below applied stresses of τ_{high} , whereas for a fully destructured material, the viscosity will only increase once the shear stress is below τ_{low} and therefore manifest yield stress behavior. For intermediate values of initial structure, the stress at which yield is manifested depends on the shear history. This is the main difference between the two models and it is thus believed that the rheological properties of tailing upon pumping may be better represented by the second model as it accounts for the shear history of the material.

As part of the scope of Carleton's collaborative research and development program with COSIA and NSERC on optimizing post-deposition amended oil sands tailings was to

work on a variety of tailing types. A summary of rheological testing on tailings as received from Shells centrifuge cake trials at the Muskeg River Mine is presented in Appendix C.

5 Chapter: Microstructure and Rheological changes over time

5.1 Introduction

Fabric (as defined by Mitchell and Soga, 2005) refers to arrangement of particle and pore space whereas structure refers to the effects of fabric and interparticle forces. While soils are made of a wide range of particles, most fabric effects are associated with clays or clay size particles (Mitchell and Soga, 2005). The structural and geometric configuration of soils below the threshold of visibility is defined as the microstructure. Microstructural studies will help understand the higher structural level, interaction, and material behavior under various stress state conditions (Romero and Simms, 2008). Moreover, these studies are helpful in relating microstructure to macroscopic behavior, for instance, the difference in permeability of a soil compacted wet of optimum or dry of optimum (at the same porosity) may be explained with the changes in arrangement of clay particles (Lambe, 1958).

To date, there exists various microstructure techniques such as scanning electron microscopy (SEM), mercury intrusion porosimetry (MIP), micro computed tomography, optical microscope, and laser scanning microscope (Kochmanova and Tanaka, 2010;

Delage 2010; Romero and Simms, 2008; Mitchell and Soga 2005; and Nielson, 2004). SEM has been previously used successfully in various field application such as: quantitative and qualitative measurements of compacted clay (Monroy et al. 2010) and dewatering potential of flocculated tailings (Zbik et al. 2008). Others have used this technique to study the macroscopic behaviour changes of various materials such as oil sands tailings, glacial till, compacted silt and cement backfills (Yilmaz et al. 2011; Delage, 2010; Delage et al. 2006; Jeeravipoolvarn, 2005; Simms and Yanful, (2005 and 2004); Griffith and Joshi, 1989). In this study Scanning Electron Microscopy (SEM) was used to investigate the fabric changes of polymer amended MFT over time and under shear.

5.2 Scanning electron microscopy (SEM)

In SEM technique a beam of electrons is aimed at a sample (under vacuum conditions), using an electron gun. Secondary electrons are generated as a result of this interaction. Reflected electron are then detected by Backscattered Electron detectors (BSE) and gaseous secondary electron detectors (GSED), from which an image is generated. Although vacuum condition provide an effective condition for the electron beam, but may have unfavorable impact on the quality of the image. SEM is commonly conducted on dehydrated sample and using a conductive coating (to minimize electron scattering), which means that there is a high chance of sample disturbance when the sample is wet or at a high void ratio (Mitchel and Soga, 2005). For instance, in expansive clays, vacuum conditions may cause changes in the microfabric of the material and remain undetected.

Recent developments in electron microscopy have allowed the study of soils fabric under controlled environmental conditions where no conductive coating is required. This

technique, known as environmental scanning electron microscopy (ESEM), makes it possible to study wet samples in their original state (Romero and Simms, 2008); however, resolution would be sacrificed in this case. A schematic cross section of the equipment is shown in Figure 5.2-1.

In order to correlated macroscopic (elastic response) of flocculated MFT with the microstructural arrangement; structural changes of flocculated MFT during testing should be prevented. Therefore, the cold stage along with ESEM was used to ensure minimal structural disturbance during the scanning process.

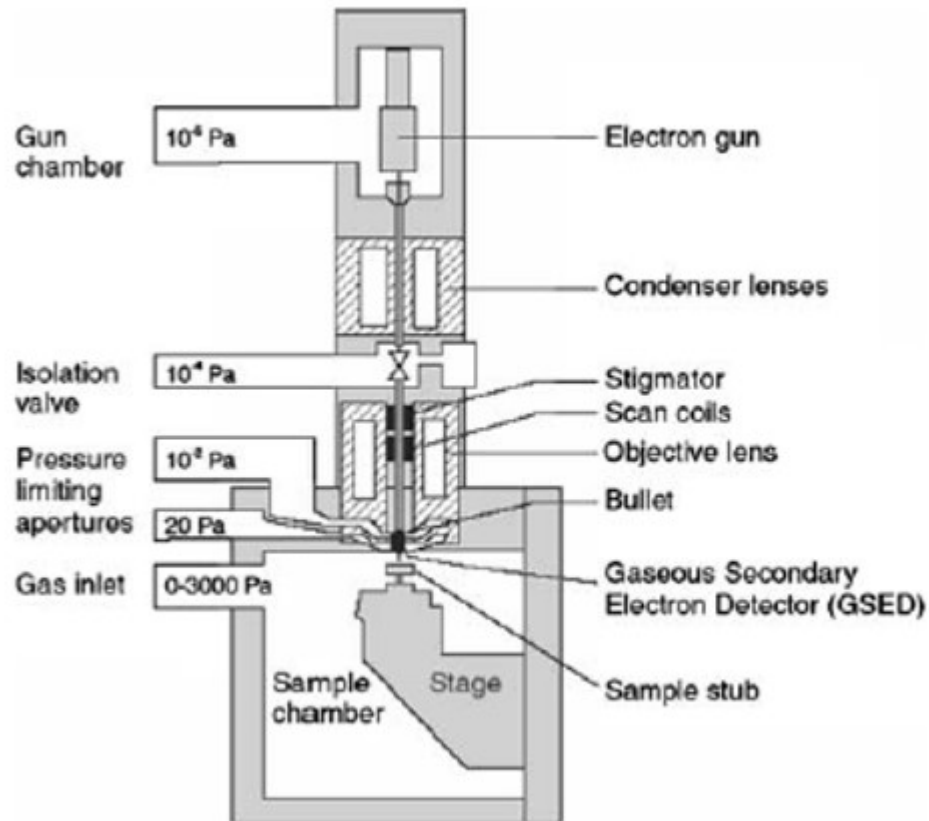


Figure 5.2-1 Schematic of an ESEM (Danilatos, 1993).

5.2.1 Image J analysis

Quantitative measurements of flocculated MFT fabric were conducted using the Image J software through the gray pixel analysis (Ferreira and Rasband, 2012). All micrographs were first optimized for adjusting the threshold between 0 and 255, where zero values correspond to black and 255 represents white. In between gray scale is based on the brightness of a pixel. Before applying the optimization, a bandpass filter was applied on micrographs which help in removing high and low special frequencies (i.e removing blurred image). The particle analyzer was then used to extract the features by defining size range, circularity and choosing to trace particle on by flood filling (Include Holes checkbox). While circularity values of 1 corresponds to a perfect circle, circularity of zero represents infinitely elongated polygon. The software also summarized the particle analysis reporting particle count, total particle area, average particle size and area of the simulated pores. The pore diameters were then calculated based on the area and frequency of the pores in certain bin ranges. The porosity of ESEM micrographs were then calculated based on the classified bins and pore diameters.

5.2.2 Objective of Microstructural Study

As previously mentioned in chapter 4 structural rebuilding can significantly affect material's behavior under shear and strain. Thus a set of microstructural analysis were conducted to correlate the stiffness (elastic modulus) of flocculated MFT with the structural changes over time and under resting conditions. Generally, flocculated fabric are more rigid but are also more unstable compared to deflocculated fabrics (Mitchell and Soga,

2005). A set of ESEM analysis were also conducted on samples, undergoing shearing, to monitor the destruction process in flocculated MFT.

5.2.3 Testing Procedure

The Vega-II XMU VPSEM, Tescan capable of using variable pressure and wet operation was used for SEM imaging in this study. The images were collected at the scanning speed of 148 $\mu\text{s}/\text{pixel}$ and a working distance of 6-10 mm (to minimize the distance the electron beam has to travel). SEM was operated at acceleration voltage of 20 kV using a cold stage to freeze the samples during the observation. The freezing was performed to prevent excessive water withdrawal during the observation under the vacuum condition of the SEM chamber. Samples were collected directly from the bucket from where flocculation took place (after decanting the excess water). A rapid freezing stage of $-40\text{ }^{\circ}\text{C}$ was applied to hydrated samples in the vacuum chamber and the samples were tested at a vacuum of 40Pa.

5.2.4 Microstructural Analysis

Scanning electron microscopy observations were carried out to determine the surface structure of flocculant and morphology and arrangement of flocs in flocculated MFT. Figure 5.2-2 shows the morphology of flocculant solution used in this study. The flocculant used is branch type flocculant with fibrous network morphology (Mizani et al. 2013).

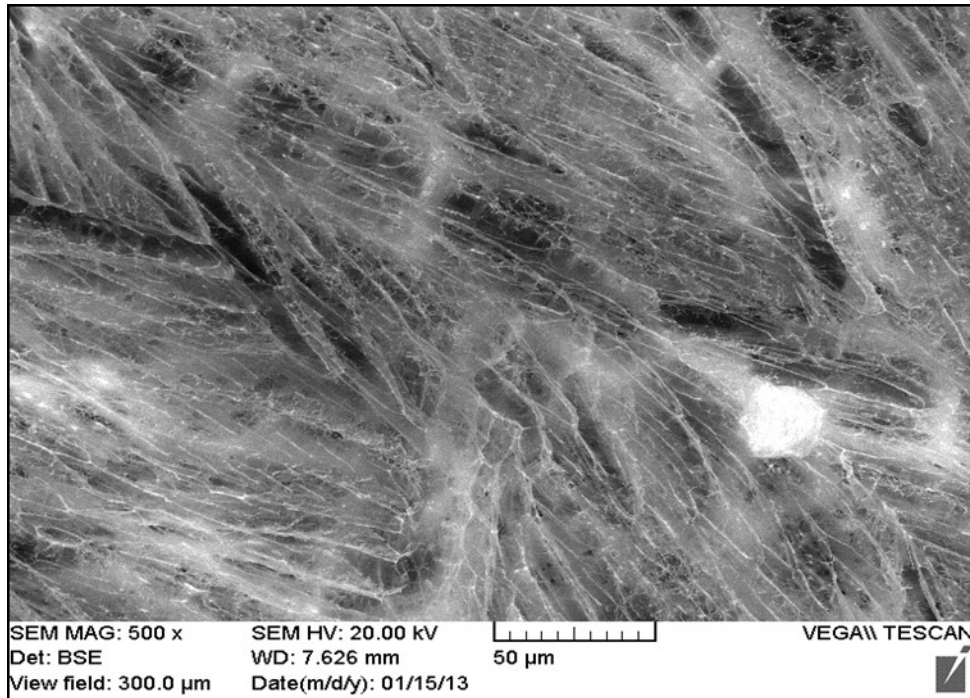


Figure 5.2-2 ESEM micrograph of A3338 polymer used to prepare flocculated MFT (magnification: 500x).

The following figure shows the micrograph of raw MFT at a magnification of 1000. This case is presented first since it shows the base case before mixing with polymer. The figure illustrates a random packing with small void in between particles. Comparing ESEM micrographs of flocculated MFT (Figure 5.2-4 to Figure 5.2-7) with raw MFT (Figure 5.2-3) shows that flocculation process improved aggregation of particles and resulted in the formation of larger voids. The formation of water channels possibly increases the hydraulic conductivity of tailings and improves dewaterability potential. ESEM micrographs of flocculated MFT at 1,200 g/tonne dosage in Figure 5.2-7 showed the presence of free flocculant particles. Figure 5.2-7 also confirms that the presence of free ionic flocculant particles, which increased the amount of negative charges, is possibly one of the reasons for reduction in dewaterability potential at high flocculant dosage.

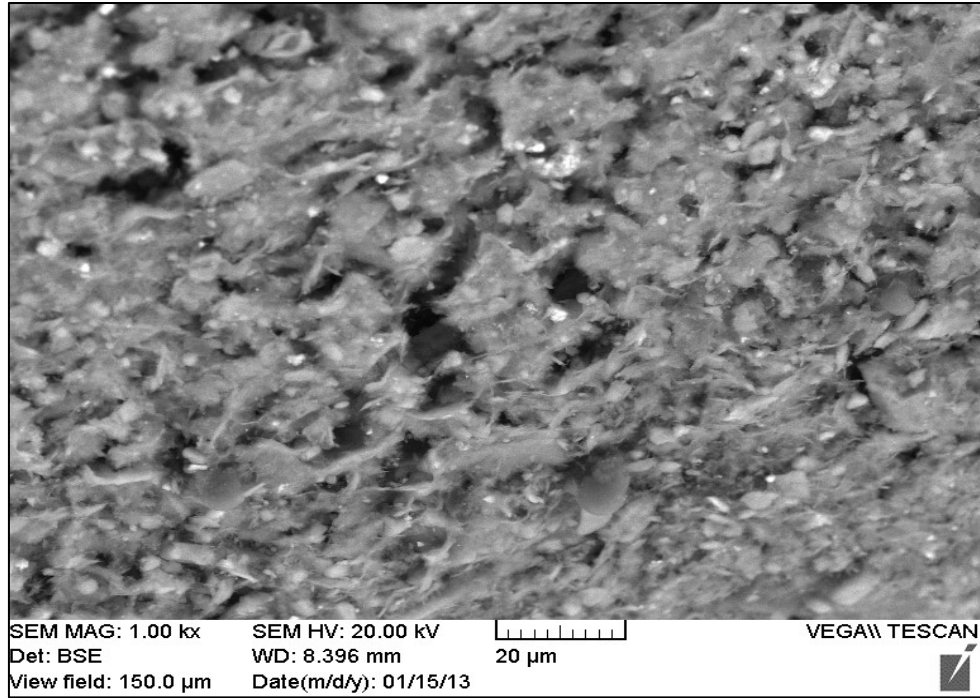


Figure 5.2-3 Backscattered environmental scanning electron of mature fine tailings for a magnification - 1000 x, scale - 20 µm, view field - 150 µm.

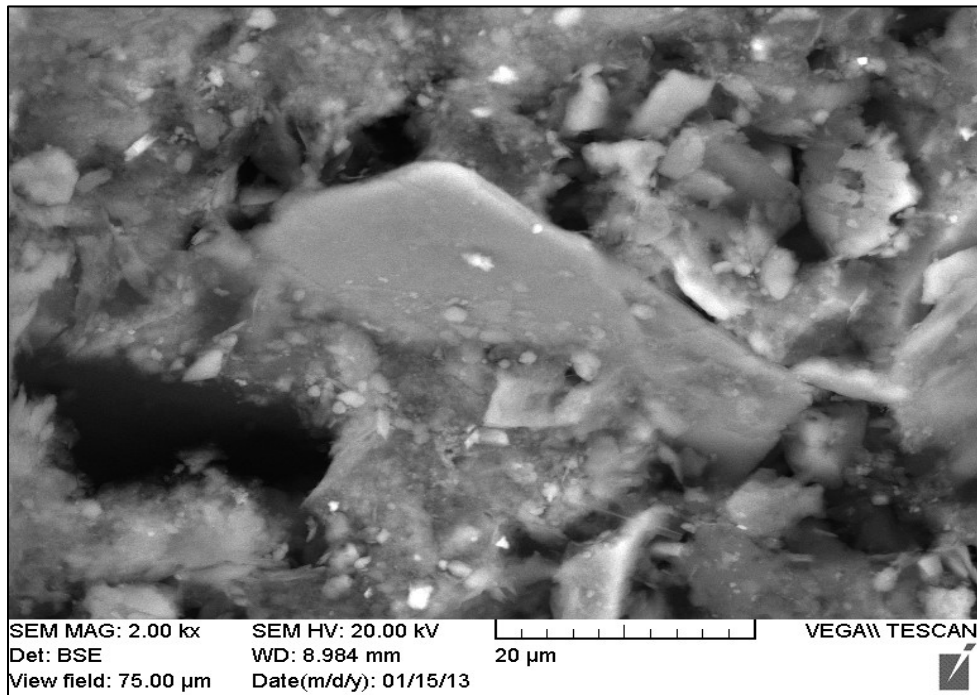


Figure 5.2-4 Backscattered environmental scanning electron of polymer amended MFT at a dose of 650g/tonne for a magnification - 2000 x, scale - 20 µm, view field - 75 µm

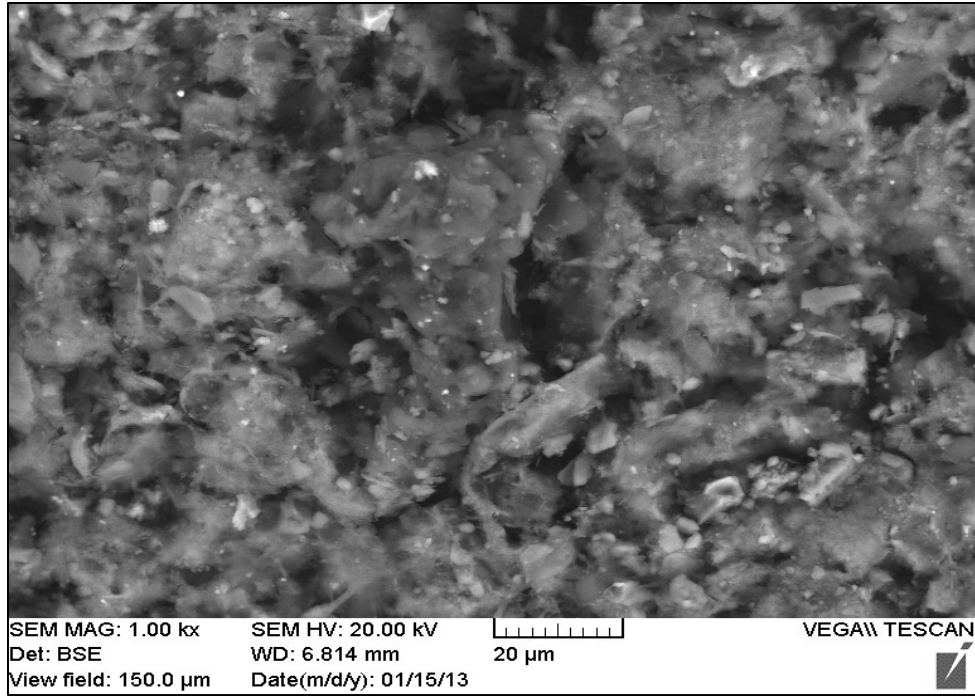


Figure 5.2-5 Backscattered environmental scanning electron of polymer amended MFT at a dose of 725g/tonne for a magnification - 1000 x, scale - 50 µm, view field - 150 µm.

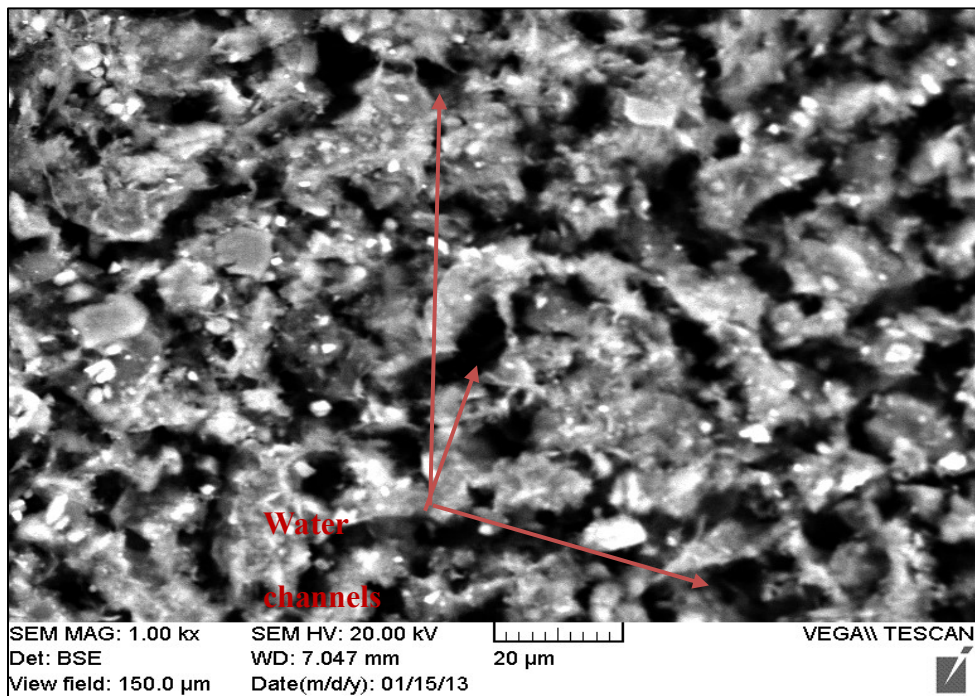


Figure 5.2-6 Backscattered environmental scanning electron of polymer amended MFT at a dose of 1000g/tonne for a magnification - 1000 x, scale - 20 µm, view field - 150 µm.

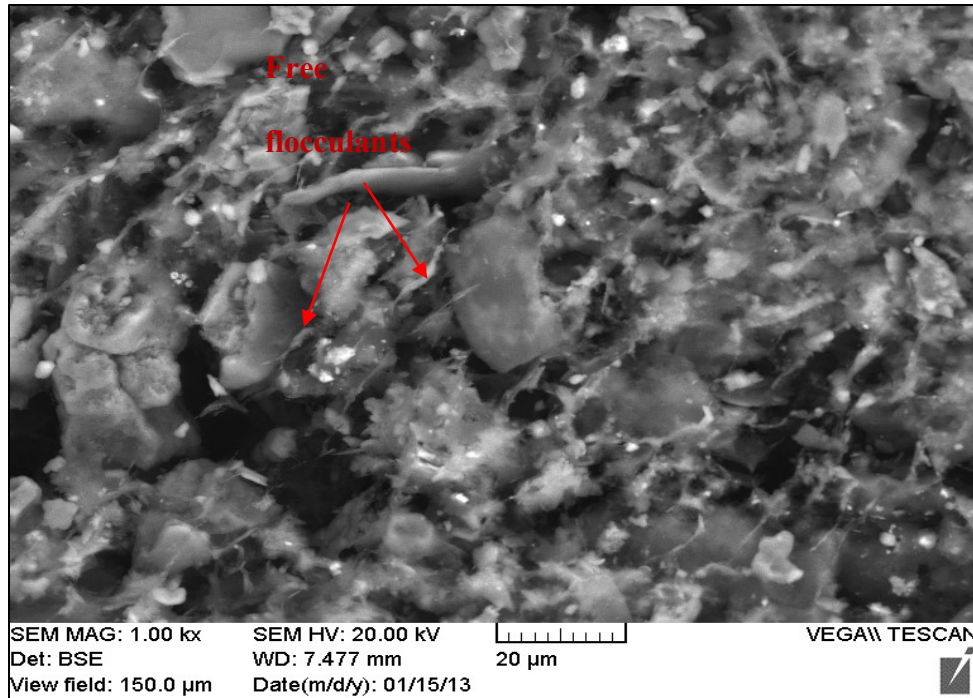


Figure 5.2-7 Backscattered environmental scanning electron of polymer amended MFT at a dose of 1200gr/tonne for a magnification - 1000 x, scale - 20 µm, view field - 150 µm.

By comparing micrographs of various floc dosages and that of MFT (Figure 5.2-3), it could be concluded that small cages formed by fine particles in raw MFT are the main reason for water retention in untreated MFT. Addition of A3338 will assist in bridging fine particles and thus formation of larger pores leading to higher dewatering potential of MFT. However, excessive polymer dosages may result in steric stabilization of the particles (Zhu, 2015) where no additional space is available for polymer adsorption on the surface of the particles.

5.3 Changes in Elastic Modulus at Rest

Figure 5.3-1 illustrate the changes in elastic modulus for various floc dosages and for three individual samples, while Figure 5.3-2 presents a summary of G' measurements over a course of 35days for sample#1 only. All measurements were conducted after decanting the bleed water. The same sample was used for G' measurements conducted on the same day; while testing on the following days were conducted on a different sample but from the same batch. During this time samples were kept in 10cm vials to minimize consolidation effects and ESEM imaging was conducted on samples collected from the top of the vials.

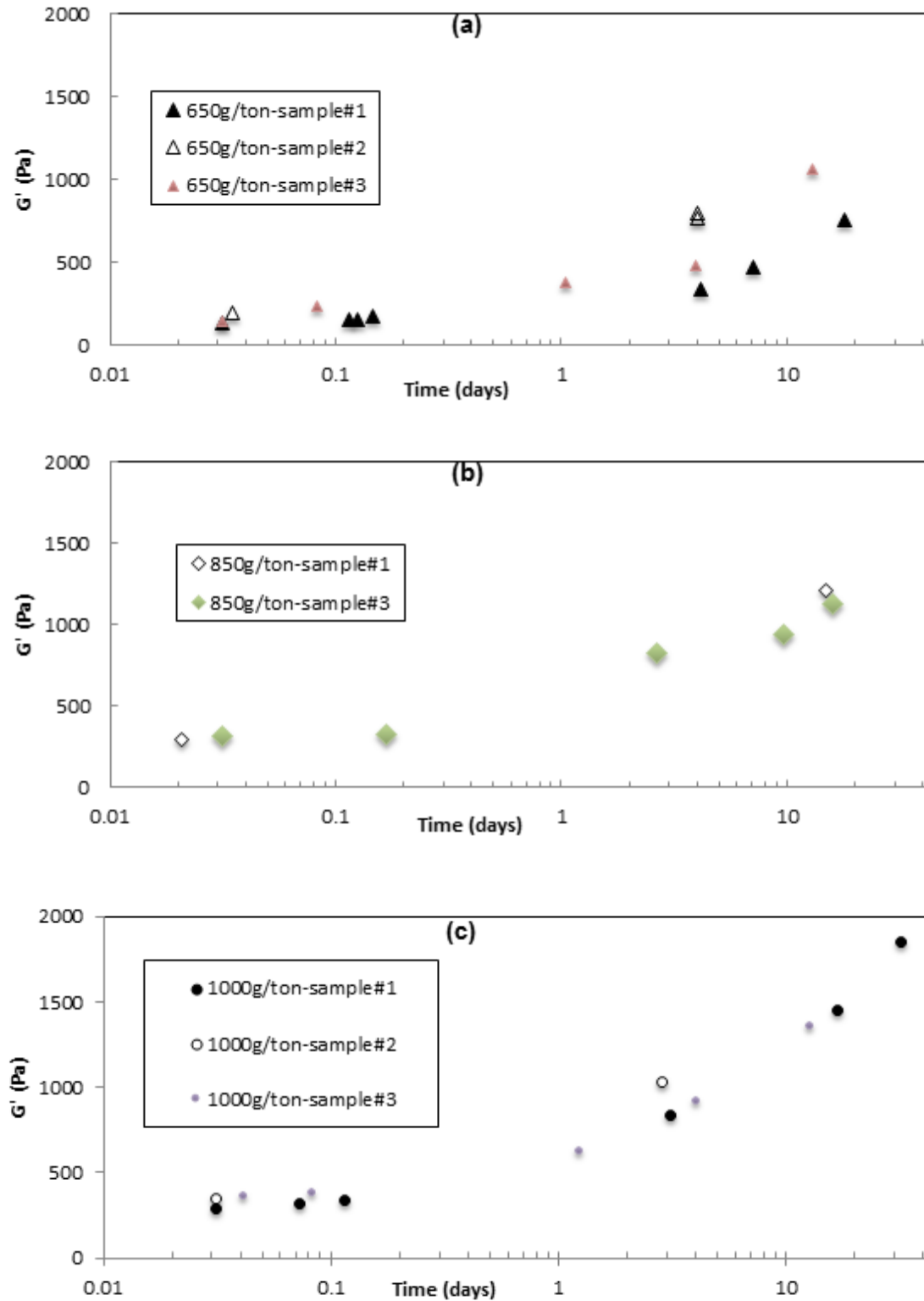


Figure 5.3-1 Elastic modulus values measured over a course of 35 days at (a) 650g/tonne, (b) 850g/tonne and 1000g/tonne and for three individual samples.

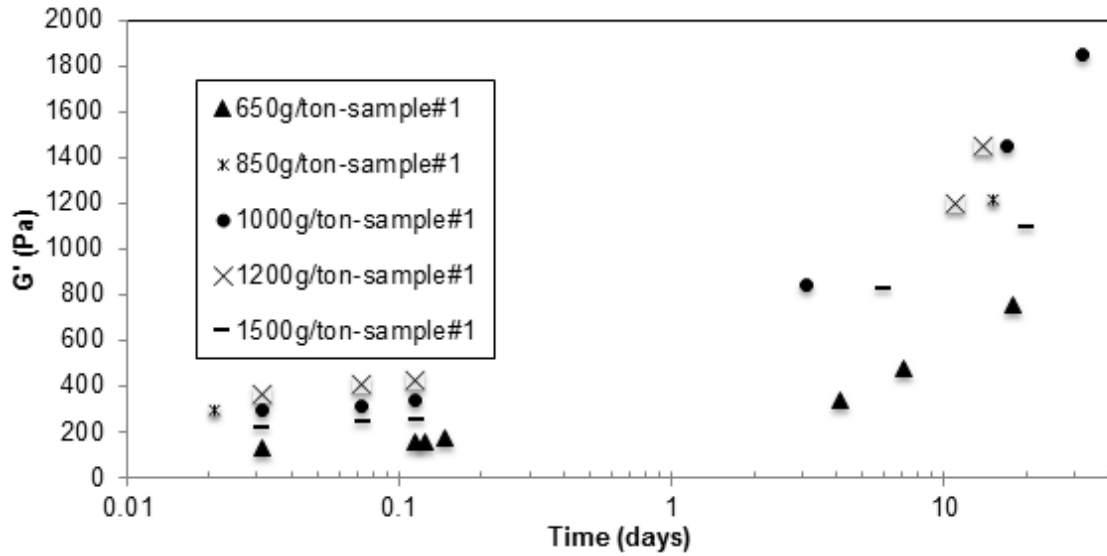


Figure 5.3-2 Elastic modulus values measured over a course of 35days at various floc dosages for sample#1.

In general, the elastic modulus increased with time and dosage; however, it appears that addition of more floc beyond 1200g/ton may have adverse effect on the stiffness.

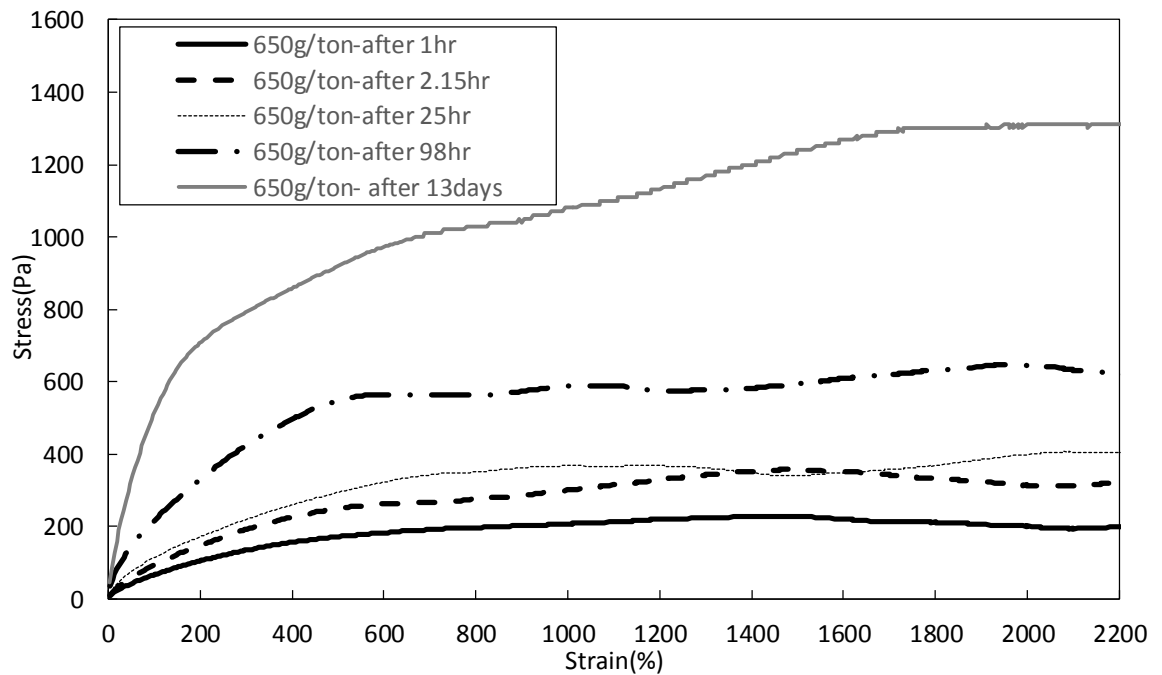


Figure 5.3-3 Yield stress values measured over 13days for polymer dosages of 650g/tonne.

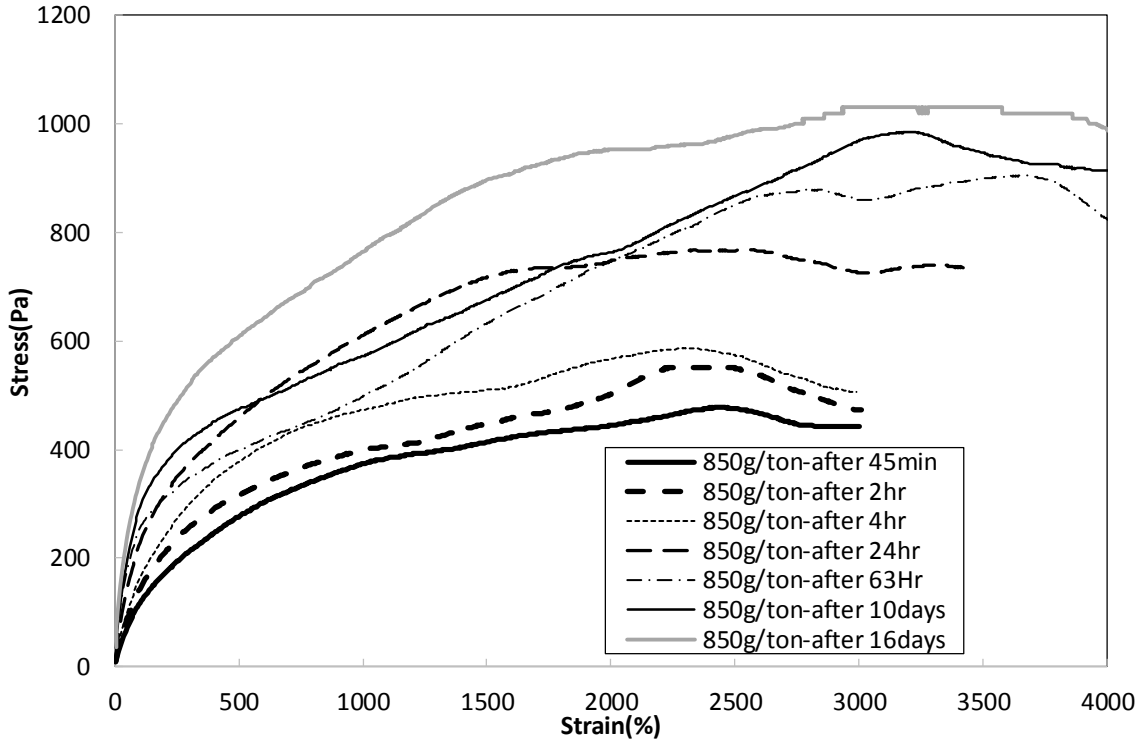


Figure 5.3-4 Yield stress values measured over 16 days for polymer dosages of 850g/tonne.

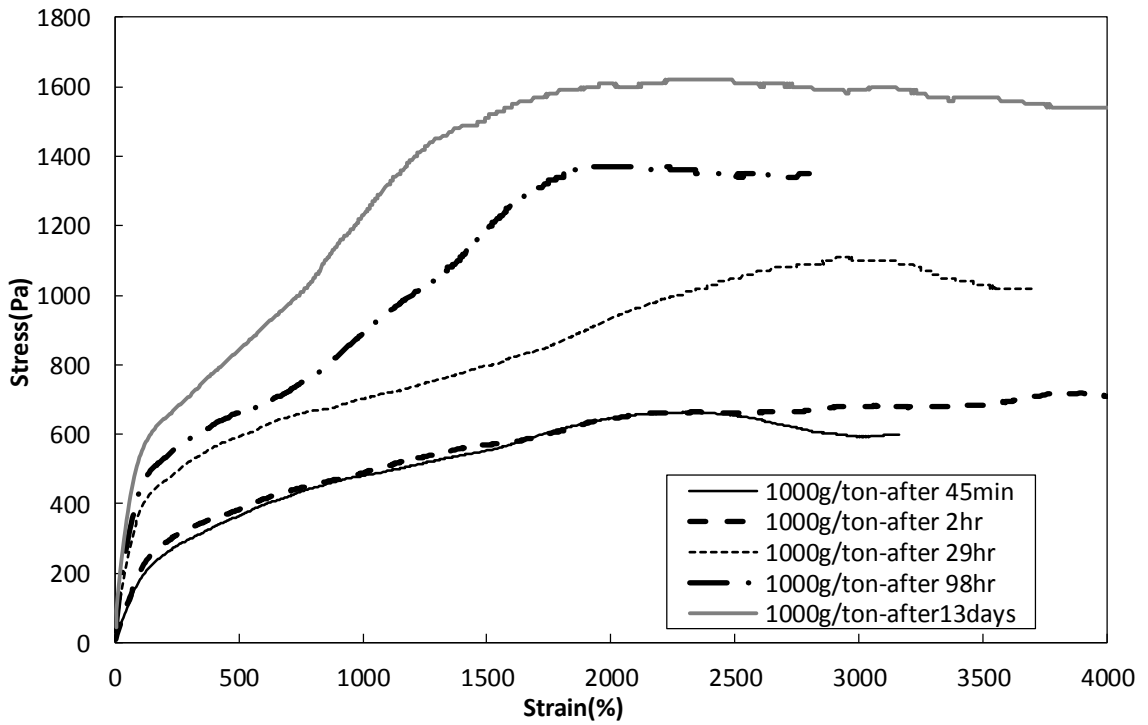


Figure 5.3-5 Yield stress values measured over 13 days for polymer dosages of 1000g/tonne.

The yield stress values, over a course of 14 days, were also measured before the ESEM imaging as illustrated in Figure 5.3-3 to Figure 5.3-5. Figure 5.3-6 presents a summary of yield stress values for sample#3. Although an increase in stiffness was observed in all cases, 650g/tonne dose showed a higher percentage increase in the measured yield stress value.

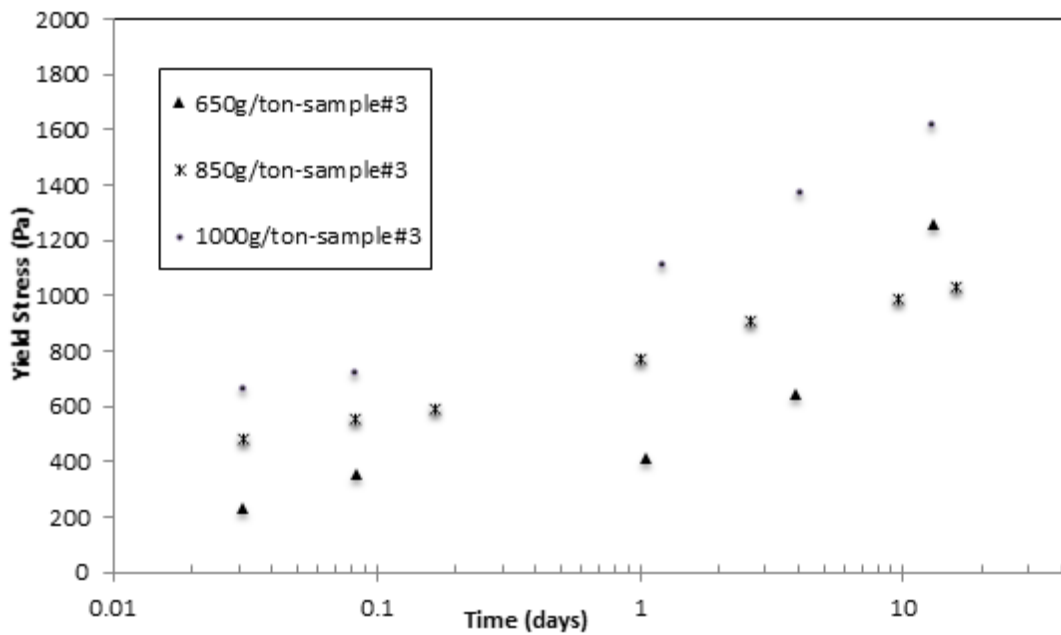


Figure 5.3-6 Yield stress measurement over a course of 16 days at various floc dosages for sample#3.

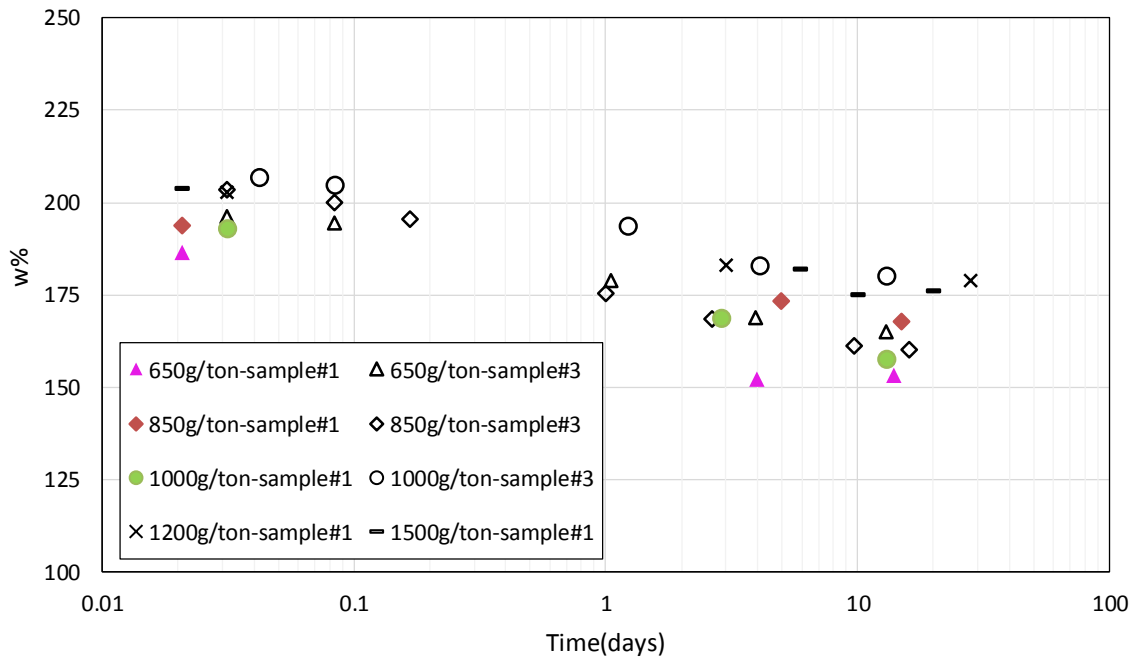


Figure 5.3-7 Moisture content measured for various floc dosages of samples in Figure 5.3-1.

Moisture content measurements of samples were also recorded before the yield stress measurements as presented in Figure 5.3-7. The higher moisture content of the material with higher floc dosage may be explained by formation of larger flocs.

A closer look at the moisture content and thixotropy ratio ($\tau_y/\tau_{y@t=0}$), where τ_y is the peak value obtained from the stress growth technique, illustrates that the highest rate of strength gain took place in the first couple of days after mixing. Moreover, the highest relative thixotropic effects was seen in the 650g/tonne. Ratio of the elastic modulus at each time period is also presented in Figure 5.3-8.

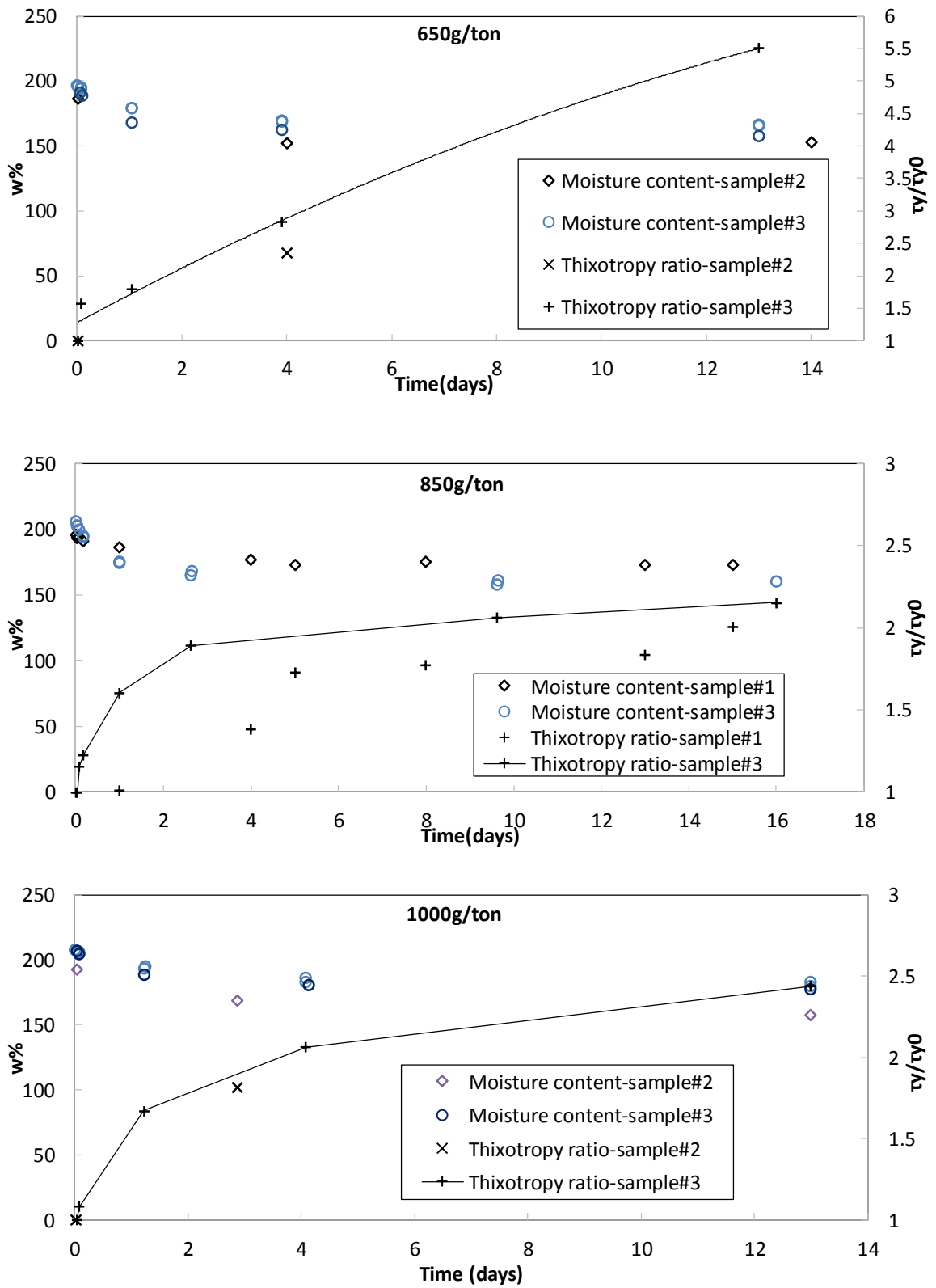


Figure 5.3-8 Moisture content versus thixotropy ratio (τ_y/τ_{y0}) for various floc dosages.

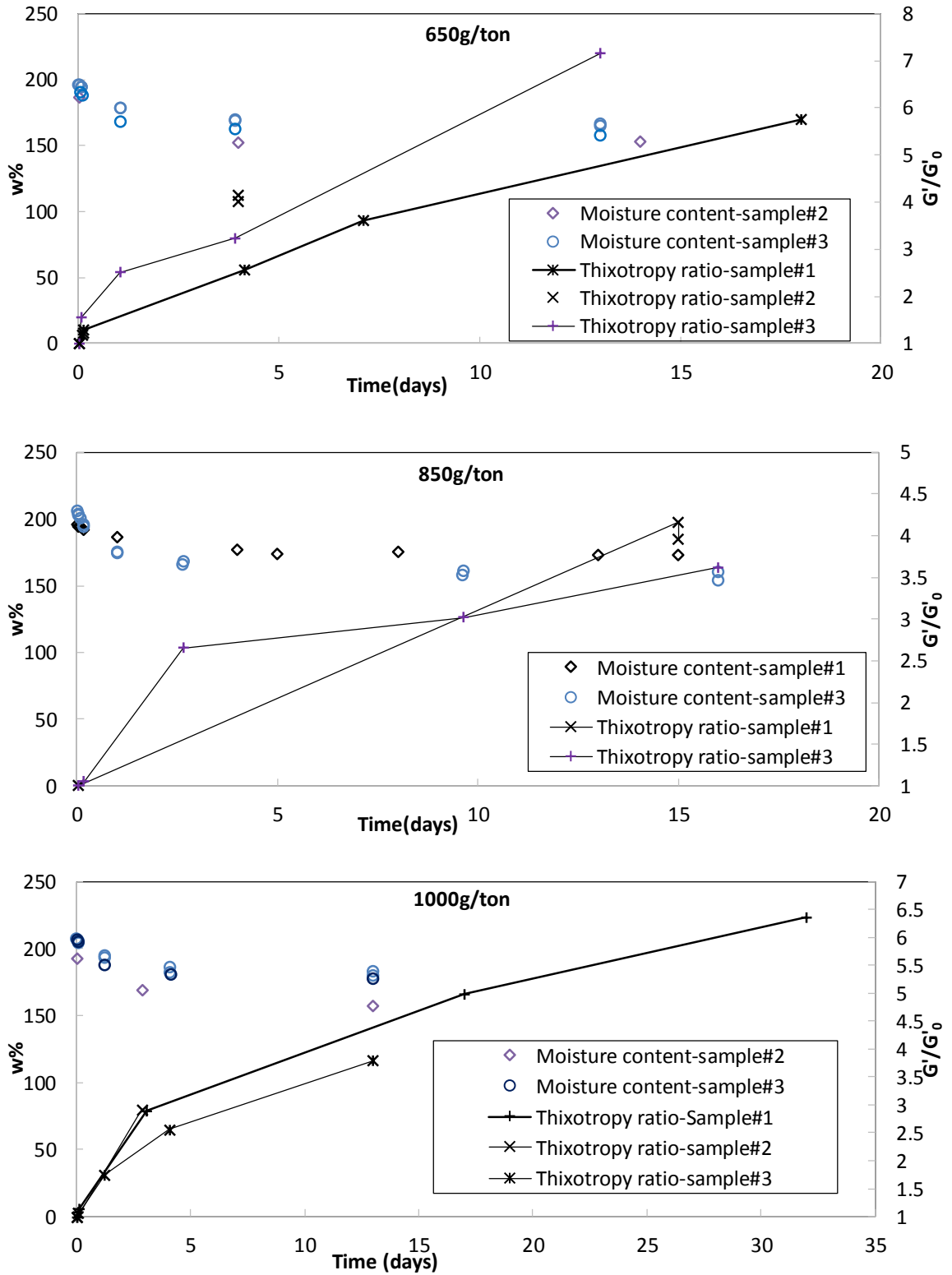


Figure 5.3-9 Moisture content versus (G'/G'_0) for various flocc dosages (subscript “0” denotes initial value).

Figure 5.3-10 and Figure 5.3-11 summarize the data presented in the last two figures for sample#3. While the decrease in void ratio as a result of self-weight consolidation contributes to the increase in strength of flocculated MFT, it can be seen that changes in shear strength continued even after moisture content changes became more or less stable. Also, for all three dosage the changes in elastic modulus were more pronounced compared to changes in peak value from stress growth test. One possible explanation could be that the elastic modulus measurements are made in the elastic region; whereas, yield stress measurement, are made in the nonlinear zone. In the next section an attempt was made to monitor the microstructural changes of various dosage over time.

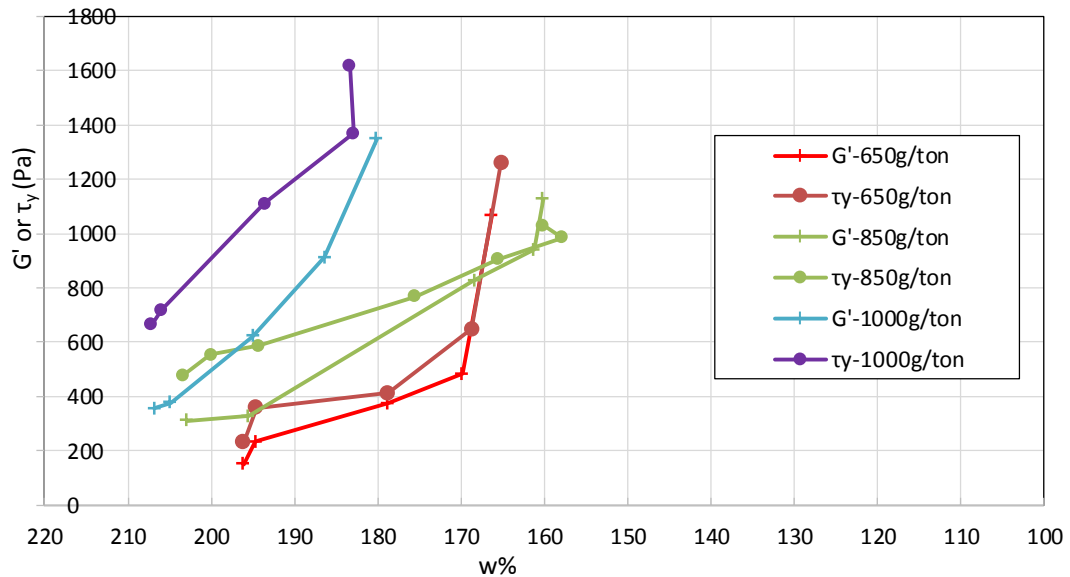


Figure 5.3-10 Moisture content versus G' and/or τ_y for various floc dosages of sample#3.

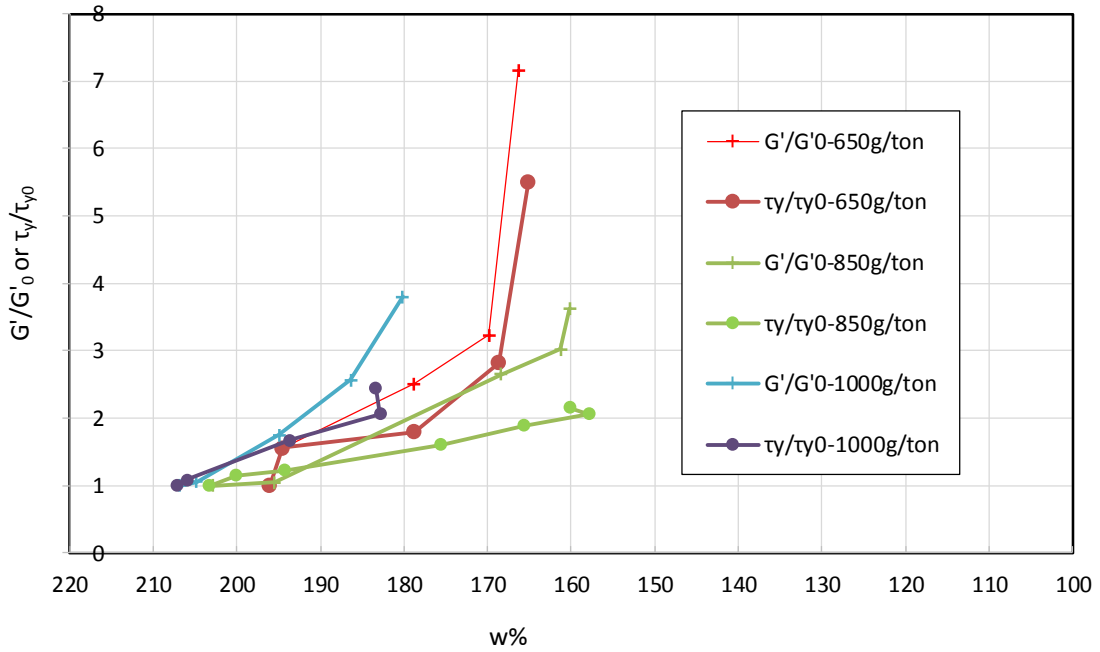


Figure 5.3-11 Moisture content versus (G'/G'_0) and τ_y/τ_{y0} for various floc dosages of sample#3.

5.4 PSD Analysis of ESEM Images from Thixotropic Tests

In this section we tried to observe the microstructure behavior of the amended oil sands tailings with resting time. ESEM images over a course of 2 weeks upon mixing are presented in Figure 5.4-1 to Figure 5.4-4.

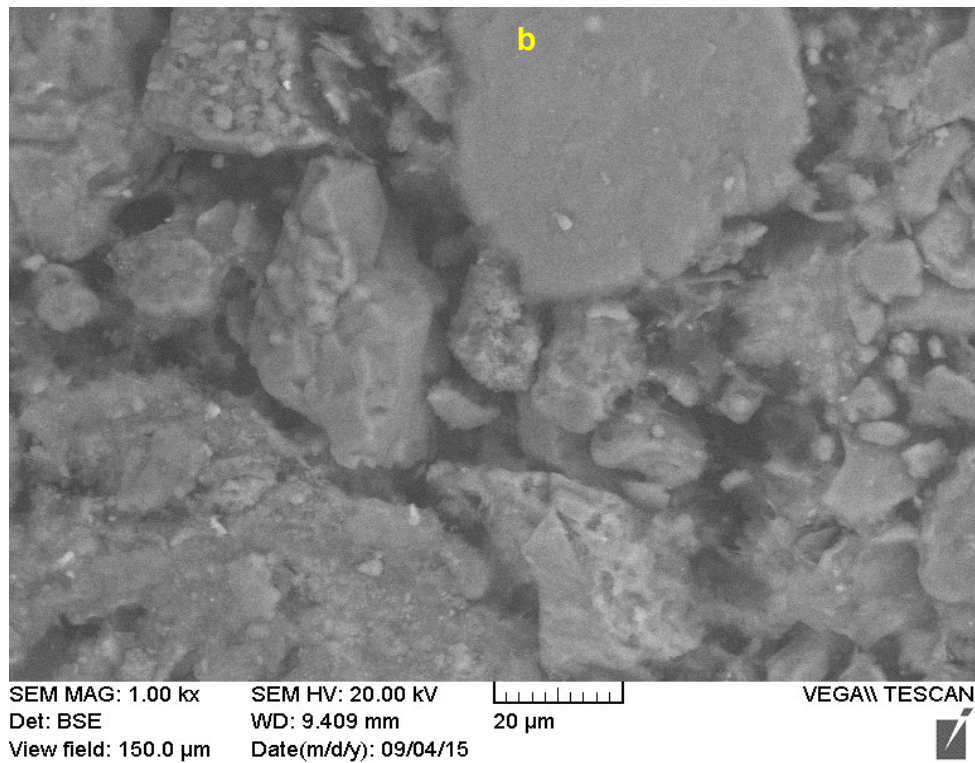
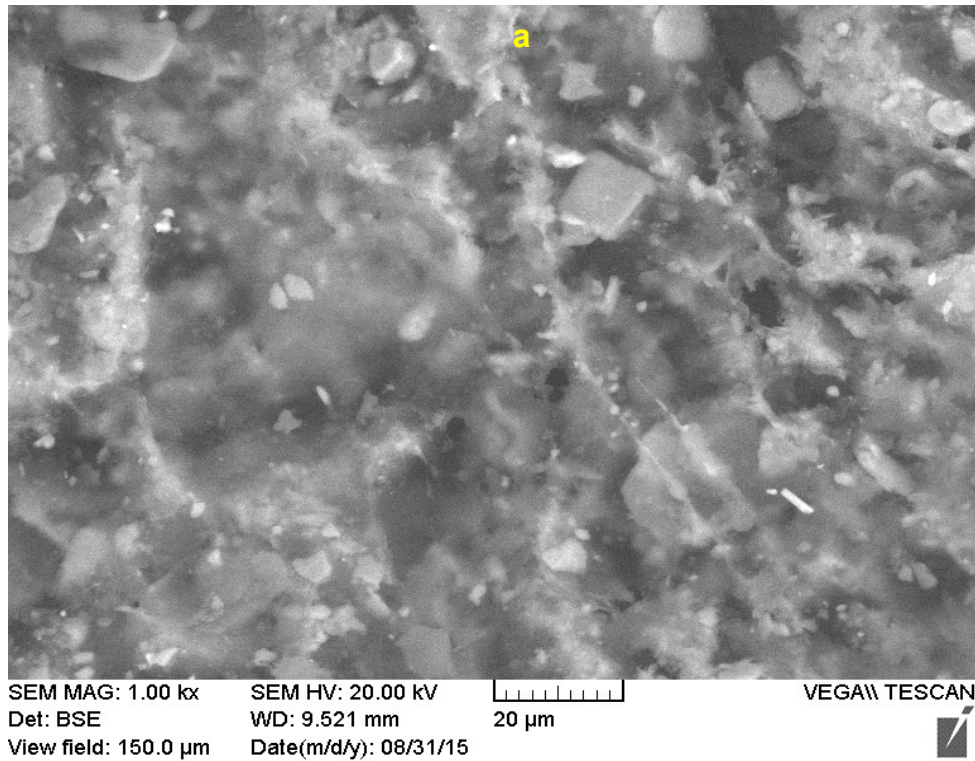
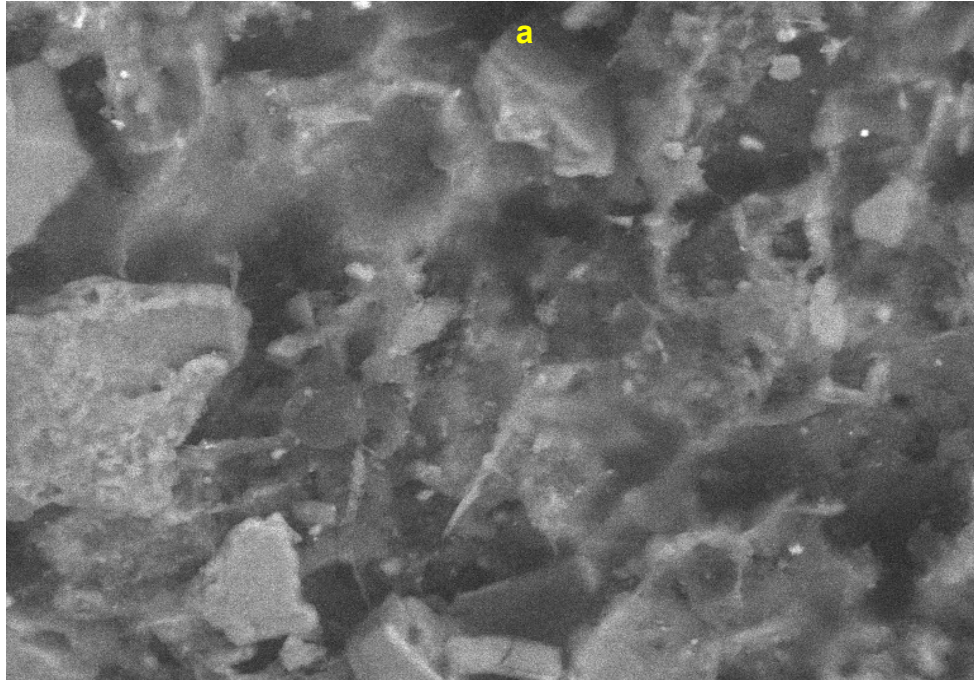
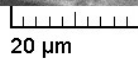


Figure 5.4-1 Scanning electron micrographs of polymer amended oil sands tailings for polymer dose of 650g/tonne a) – two hour after polymer mixing; b)– 96 hours after polymer mixing (sample#1)

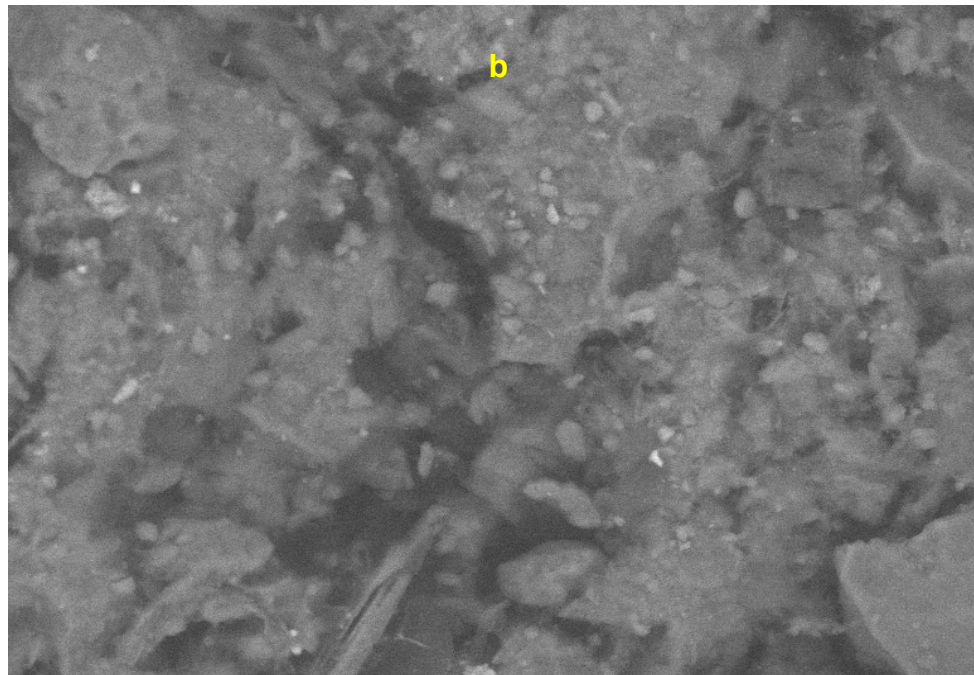


SEM MAG: 1.00 kx
Det: BSE
View field: 150.0 μm

SEM HV: 20.00 kV
WD: 10.25 mm
Date(m/d/y): 04/14/16

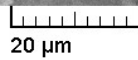


VEGA\\ TESCAN



SEM MAG: 1.00 kx
Det: BSE
View field: 150.0 μm

SEM HV: 20.00 kV
WD: 11.23 mm
Date(m/d/y): 04/18/16



VEGA\\ TESCAN



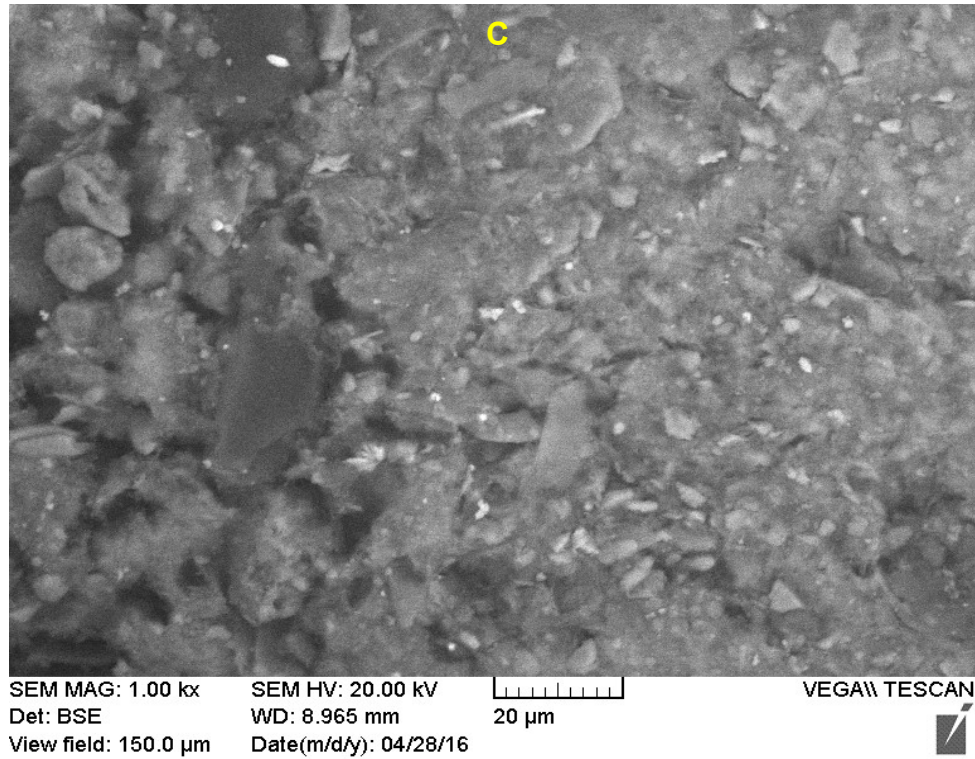


Figure 5.4-2 Scanning electron micrographs of polymer amended oil sands tailings for polymer dose of 650g/tonne a) –four hour after polymer mixing; b)– 96 hours after polymer mixing; c)-14 days after polymer mixing (sample#2)

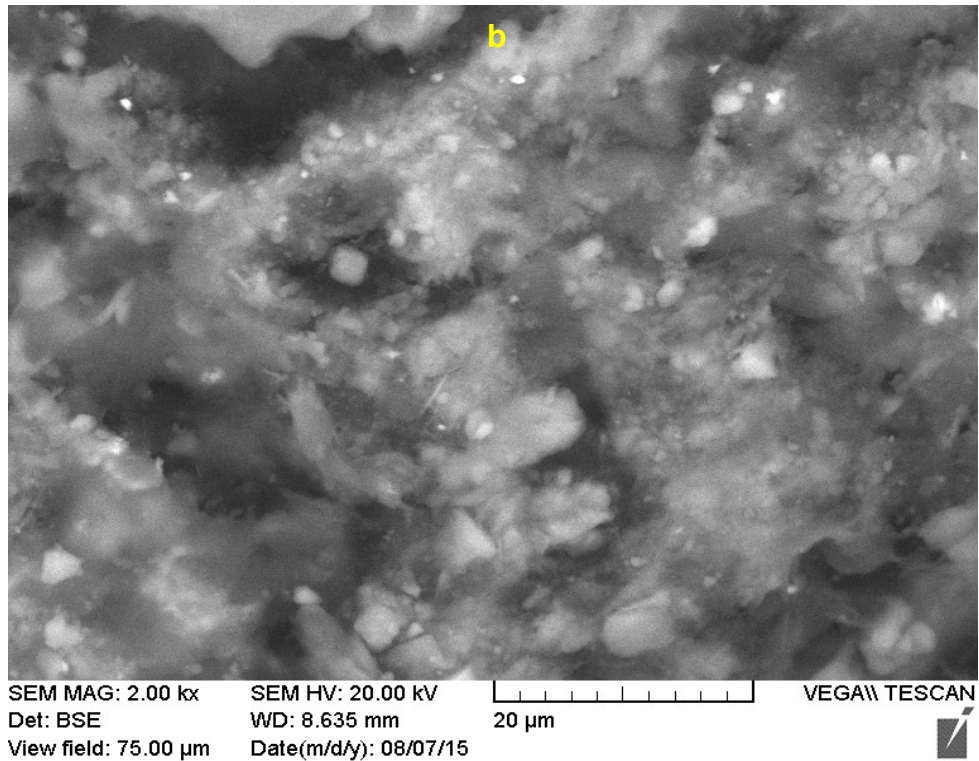
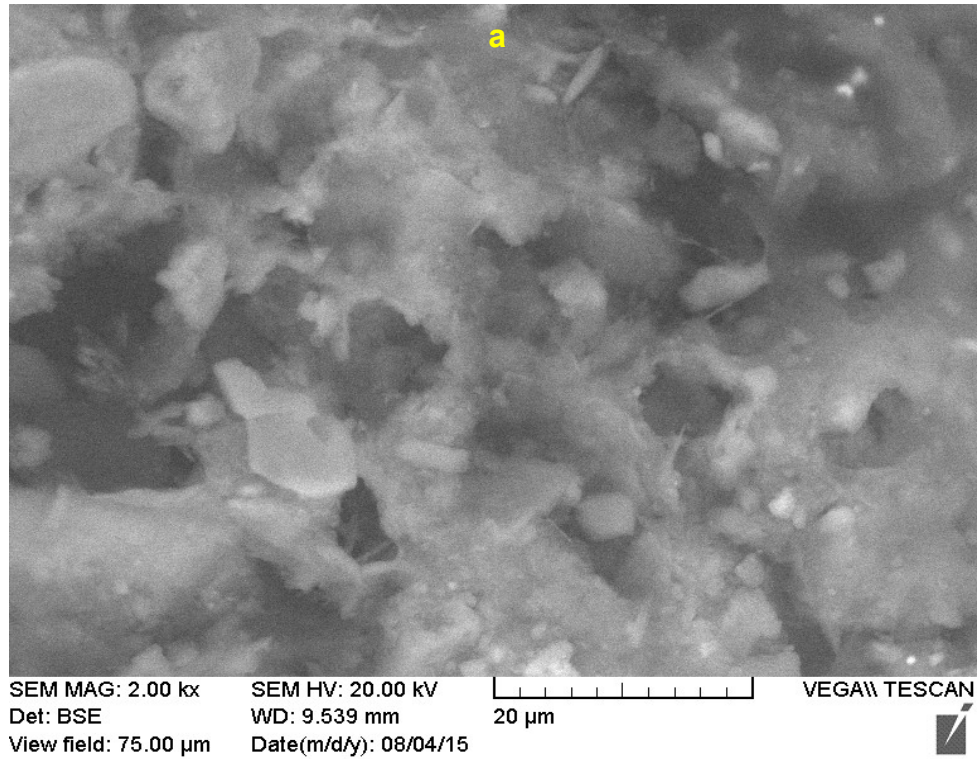
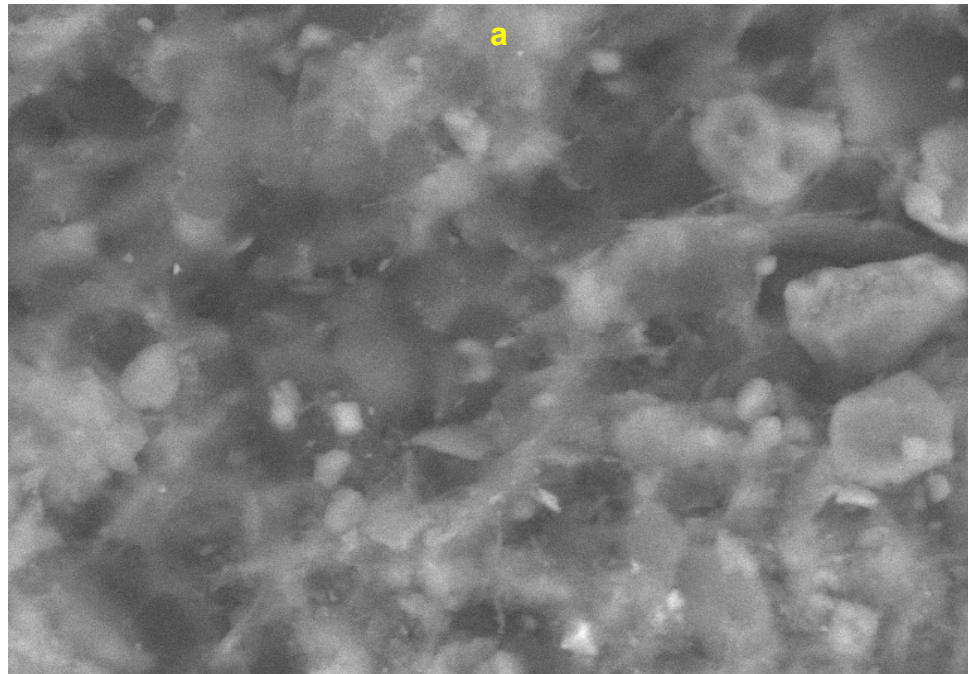
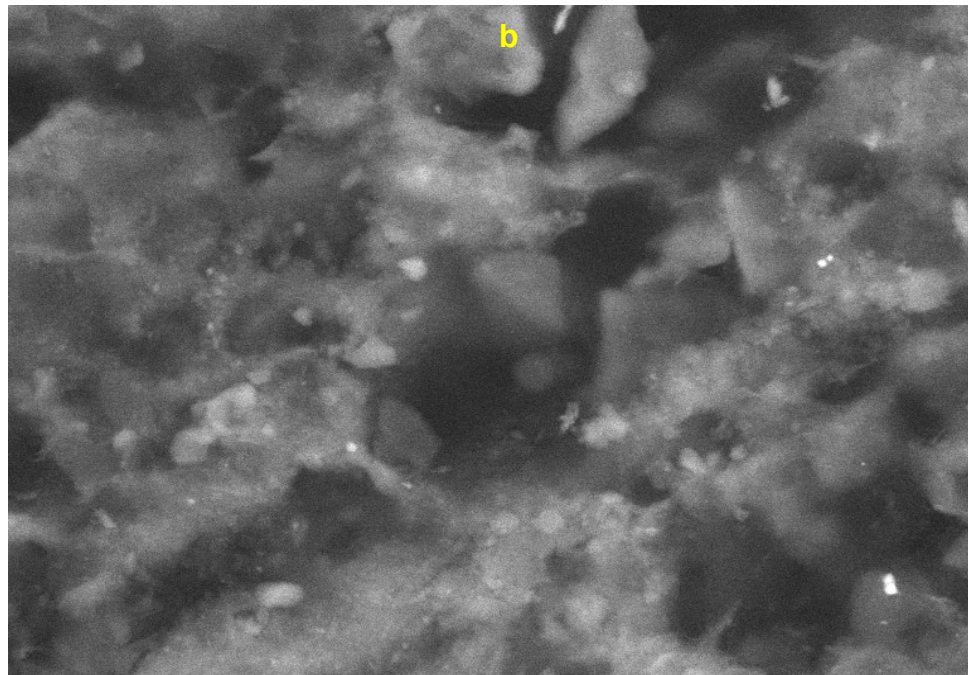


Figure 5.4-3 Scanning electron micrographs of polymer amended oil sands tailings for polymer dose of 1000g/tonne a) – two hour after polymer mixing; b)– 72 hours after polymer mixing (sample#1)



SEM MAG: 2.00 kx SEM HV: 20.00 kV
Det: BSE WD: 9.242 mm
View field: 75.00 μ m Date(m/d/y): 04/14/16



SEM MAG: 2.00 kx SEM HV: 20.00 kV
Det: BSE WD: 9.014 mm
View field: 75.00 μ m Date(m/d/y): 04/18/16

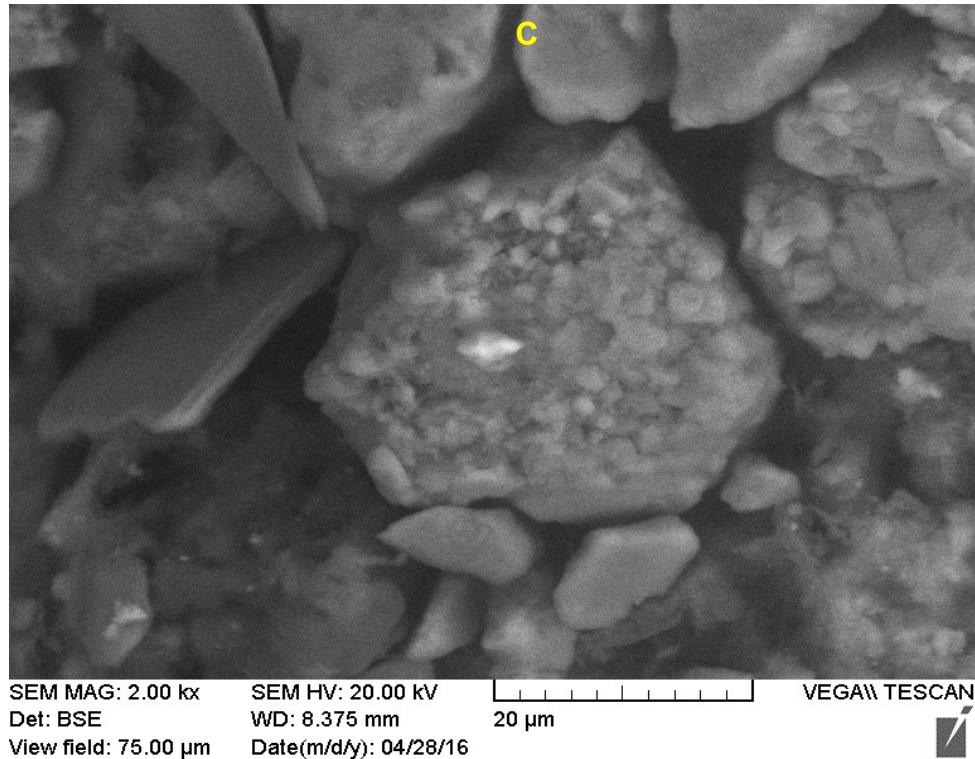


Figure 5.4-4 Scanning electron micrographs of polymer amended oil sands tailings for polymer dose of 1000g/tonne a) – four hour after polymer mixing; b)– 96 hours after polymer mixing; c)– 14 days after polymer mixing((sample#2).

In order to confirm repeatability and reliability of the gray pixel analysis, first, a set of image J analysis were conducted on the same sample and at three different locations. While there exist some variation at the smaller pore sizes, all three analysis lay within reasonable range.

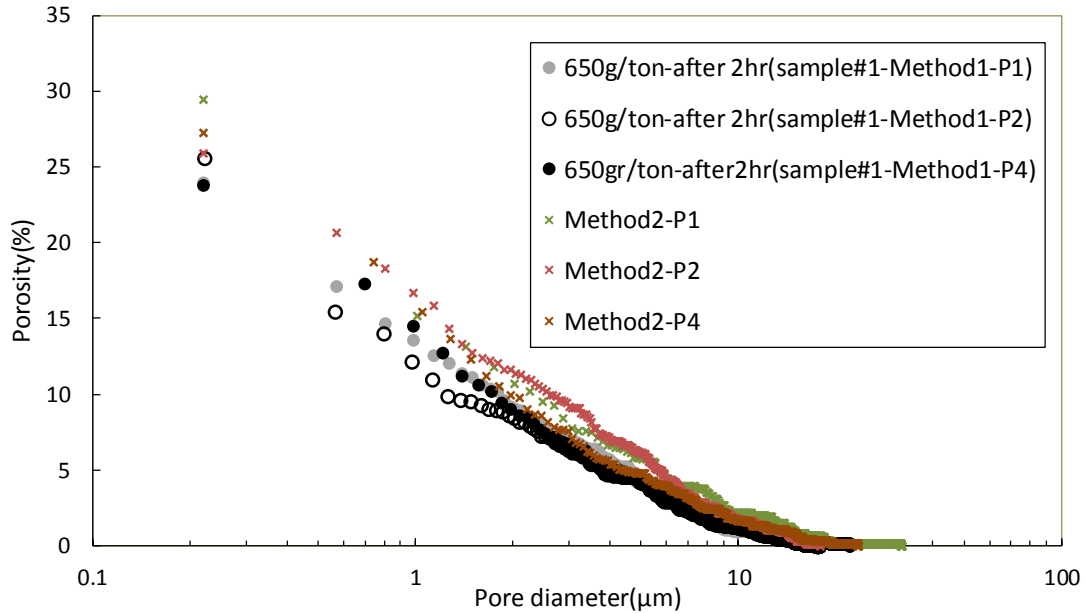


Figure 5.4-5 Gray pixel analysis of polymer amended tailings at 650g/tonne after 2 hours upon polymer mixing at three different locations of P1, P2 and P4.

Figure 5.4-7 and Figure 5.4-9 show gray pixel analysis of polymer amended tailings over a period of 14 days upon flocculation for the ESEM micrographs presented before. The image J analyses was performed with BSE images of 1 kx for 650 g/tonne and 2 kx for 1000g/tonne and view field of 150 μm and 75 μm respectively. Analysis were conducted using the threshold tool where interactively a lower and upper threshold values were set in order to segment the micrographs to distinguish particles and background.

Also illustrated in these figures are another set of image analysis using a segmentation technique developed by the author (explained below) to illustrate the independency of the results to judgement (identified in all figures by “Method 2”).

In order to identify the two phases (pore and particles), it is required to estimate an optimum threshold that converts the image to black and white; i.e., any image pixel below

that threshold is black and if above that threshold, it is white. The following algorithm is proposed:

- 1- For each possible integer threshold value (0 to 255), black and white image (B) is constructed for the original image (P).
- 2- 1-norm distance between P and B is calculated as follows:

$$\|B - P\|_1 = \sum_j |b_j - p_j| \quad 5.4-1$$

Where p_j and b_j are pixels of P and B respectively.

- 3- The first derivative of the 1-norm distance is calculated.
- 4- The optimal threshold is estimated as the one that minimizes the first derivative of the 1-norm distance given in the previous steps.

The algorithm intends to estimate the optimum threshold as the one with the lowest variations in the 1-norm distance compared to its neighboring thresholds (as illustrated in Figure 5.4-6). The output thresholded image was then used for pore size estimations; where the pore diameters were calculated based on the area and frequency of the pores in certain bin ranges.

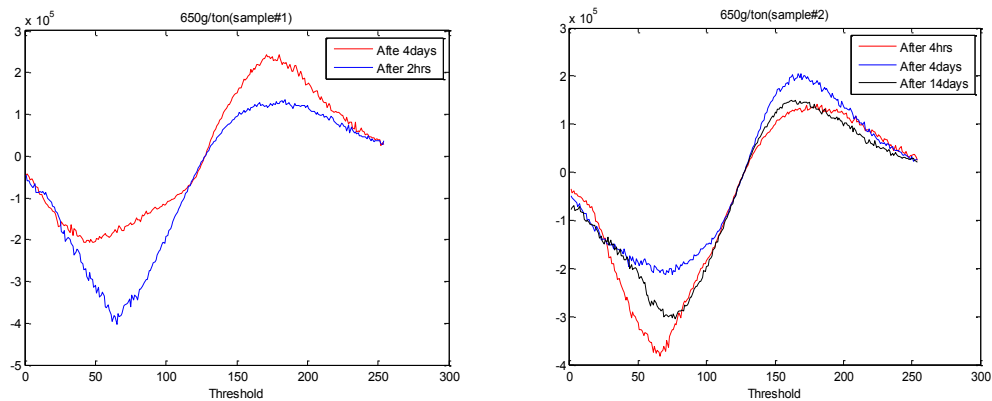


Figure 5.4-6 Optimum threshold for sample#1 and 2 prepared at 650g/tonne over time.

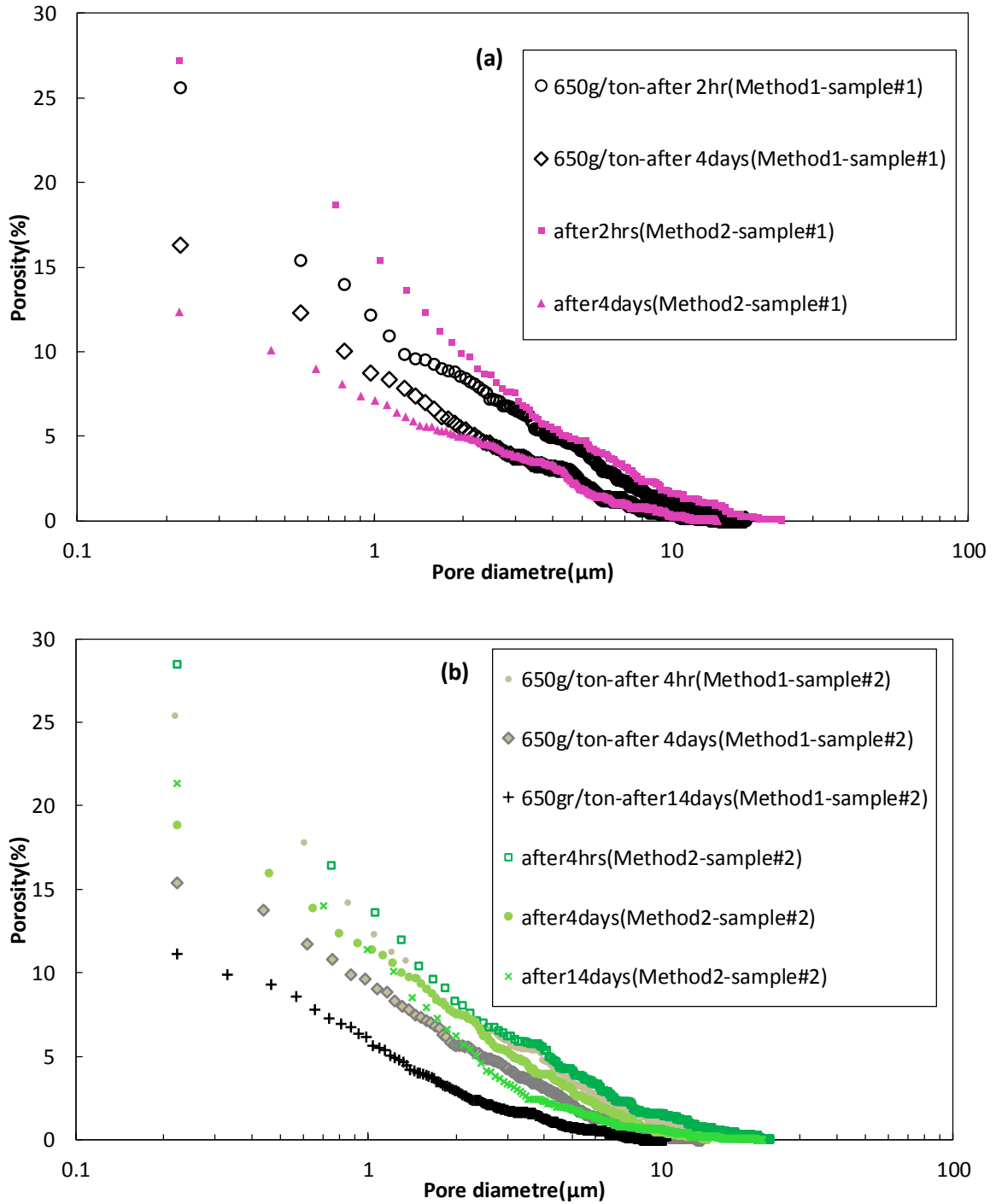


Figure 5.4-7 Gray pixel analysis of polymer amended tailings at 650g/tonne over a period of 14days after polymer mixing for (a) sample#1-Figure 5.4-1 and (b) sample#2-Figure 5.4-2.

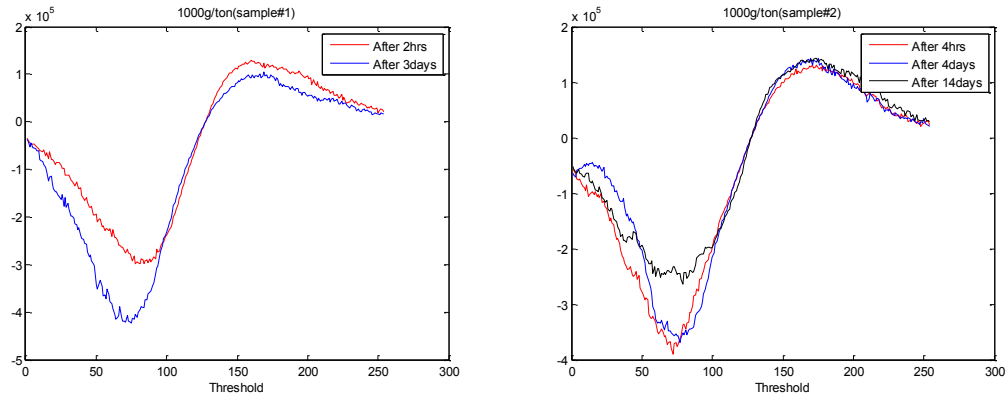
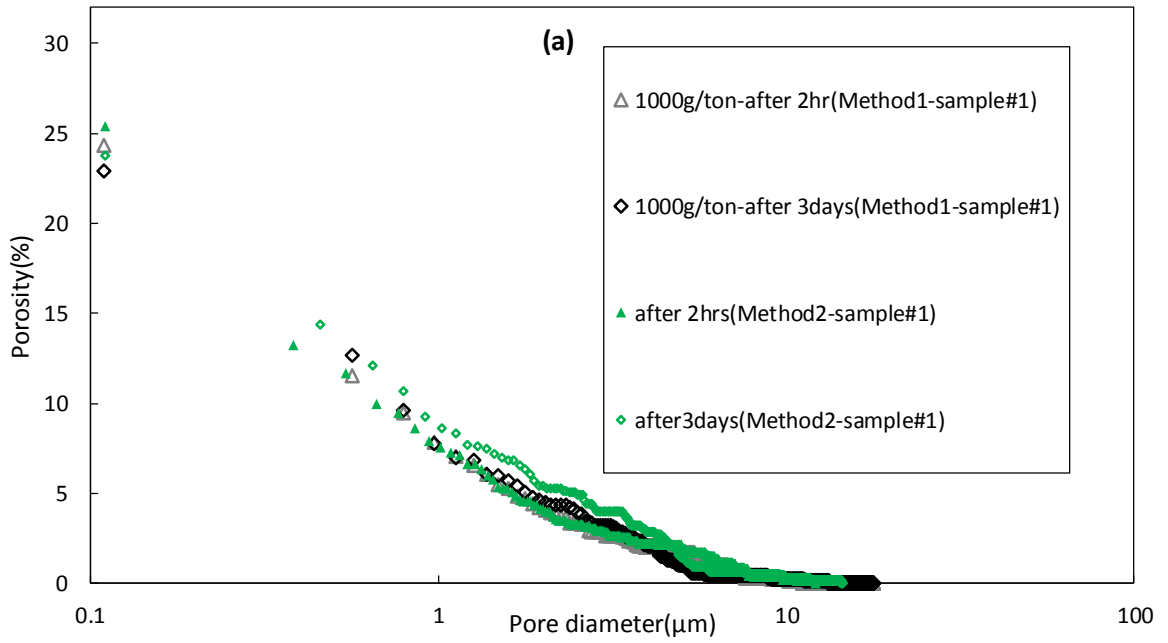


Figure 5.4-8 Optimum threshold for sample#1 and 2 prepared at 1000g/tonne over time.



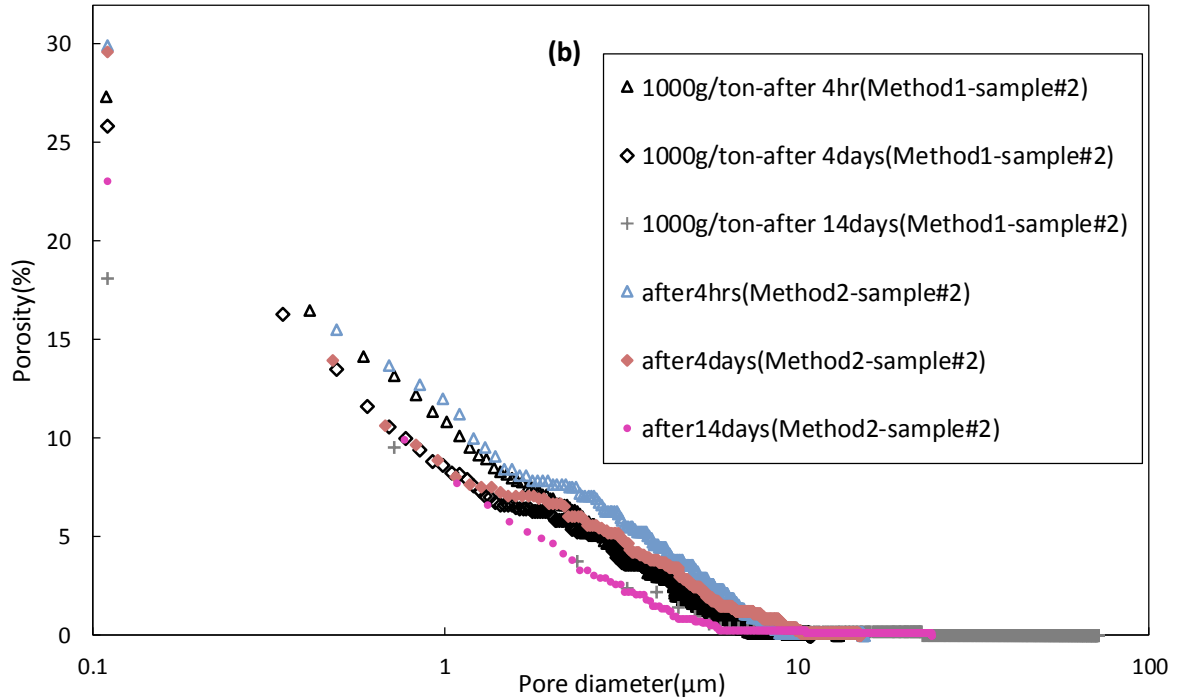


Figure 5.4-9 Gray pixel analysis of polymer amended tailings at 1000g/tonne over a period of 14days after polymer mixing (a) sample#1-Figure 5.4-3 and (b) sample#2-Figure 5.4-4.

The following figure illustrates the effects of thresholding on black and white generated from ESEM image on the sample prepared at 1000g/tonne and rested for 14days (Figure 5.4-4). A number of grayscale values were chosen for segmentation, i.e. 50, 60, 70. It can be seen from figure below that as the threshold values increased an increasing number of pixels were treated as pores (appearance of pores within the regular aggregates). This resulted in increasing amount of apparent porosity. This could be explained by the relatively small contrast during the image acquisition process.

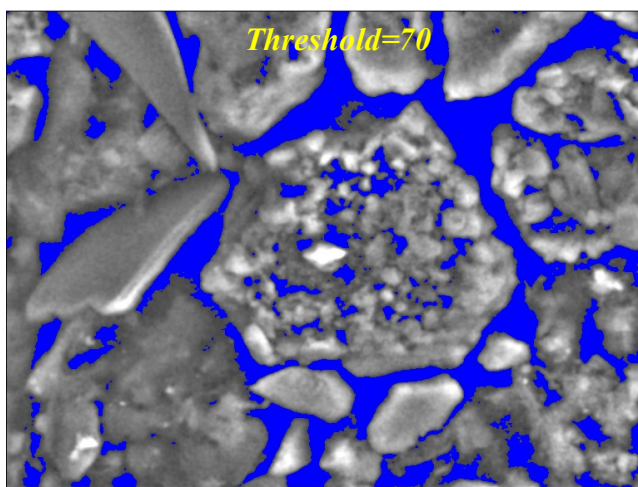
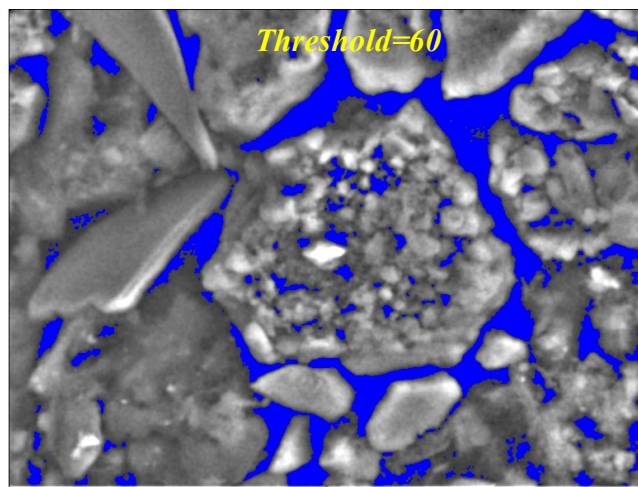
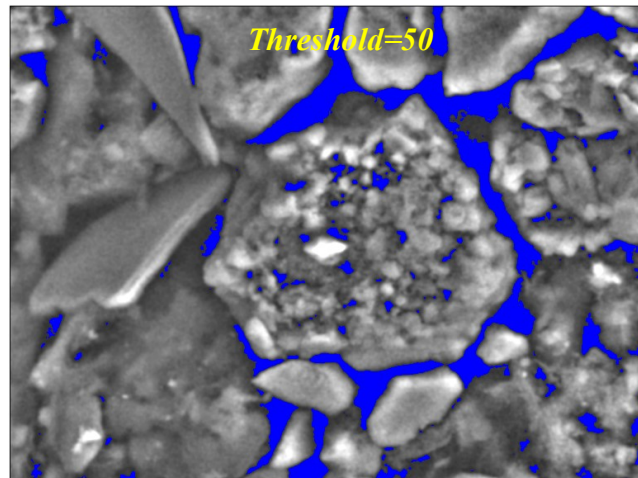


Figure 5.4-10 Scanning electron micrographs of polymer amended oil sands tailings for polymer dose of 1000g/tonne (14 days after polymer mixing (sample#2)) and associated segmented image . Here the dark and light gray represent solids and blue represents pores.

Although fabric changes were observed in both cases, changes were more evident in case of 650g/tonne. In this case, the fabric became more compact and larger aggregates were formed over time. On the other hand, at the higher dosage, changes were less noticeable showing lower changes in the area of void spaces (Figure 5.4-9). This also explains the higher changes in elastic modulus in case of 650g/tonne compare to the other dosages. Over time a lower microporosity was recorded for 650gr/tonne, which explains the more compact structure. This also explains the higher changes in elastic modulus in case of 650g/tonne compare to the other dosages. Bajwa, (2015) also reported lower polymer dosage showing more decrease in microscopy compared to the higher dosages where the microscopy curves shifting towards smaller pores, over a course of 6 days. In this study similar findings were also observed for dewatering potential where the lower polymer doses showed more dewatering potential in comparison to higher doses.

The preceding section is illustrative of the thixotropy hardening phenomenon (common in soft clay) where material stiffens at rest. The increase in stiffness (G' increase) may be explained with formation of larger aggregates (Figure 5.4-1), where the tendency of particle and particle groups towards flocculation will take over time due to the viscous resistance to particle and ion movement. Depending on polymer particle interaction, polymers may also reconfirm on particle surface (Klein, 2014). For instance, Alagha et al. 2013, studying the adsorption of anionic polyacrylamide, showed that the flat conformation of anionic polyacrylamide on kaolinite particle may become extended over time, and thus result in formation of larger flocs (Nasser et al. 2006).

Although the mechanism of adsorption of anionic polymers on negative clay surfaces is not well understood, but it has often been attributed to cation bridging (Farmer 1971; Theng

1979; Aly and Letey 1988). Peng and Di (1994), on the other hand, proved the opposite and explained their results by adsorption of the multivalent cations on anionic polymer, decreasing charge and extensibility of the polymer. Moreover, Aly and Letey, (1988) attributed flocculation of montmorillonite by anionic PAM to osmotic attraction in addition to cation bridging. Irrespective of the phenomenon responsible for the flocculation process of ionic polymer and negative clay particle, it can be concluded that ion concentration considerably change interparticle repulsive forces.

Previous studies on flocculated MFT have shown ion concentration increase at the surface of deposits over time (Rozina et al. 2015). The increase in ionic concentration over time would result in depression of the double layer and thus the repulsive forces, which in return will form stronger and larger aggregates.

Both these phenomenon may be used to explain the increase in yield stress and stiffness (G') of flocculated MFT over time; however, the effects of density variation should not be neglected.

5.4.1 Elastic Modulus versus Yield Stress

It is evident from the last section that all doses undergo structural changes under resting condition which can be represented by elastic modulus. In this section an attempt will be made to correlate the linear response of the material with yield stress.

In this analysis yield stress values, defined by the overshoot in shear stress at constant shear rate of 0.1s^{-1} , at a given resting time were used. Figure 5.4-11 illustrates the relationship between elastic modulus and yield stress values for various polymer dosages.

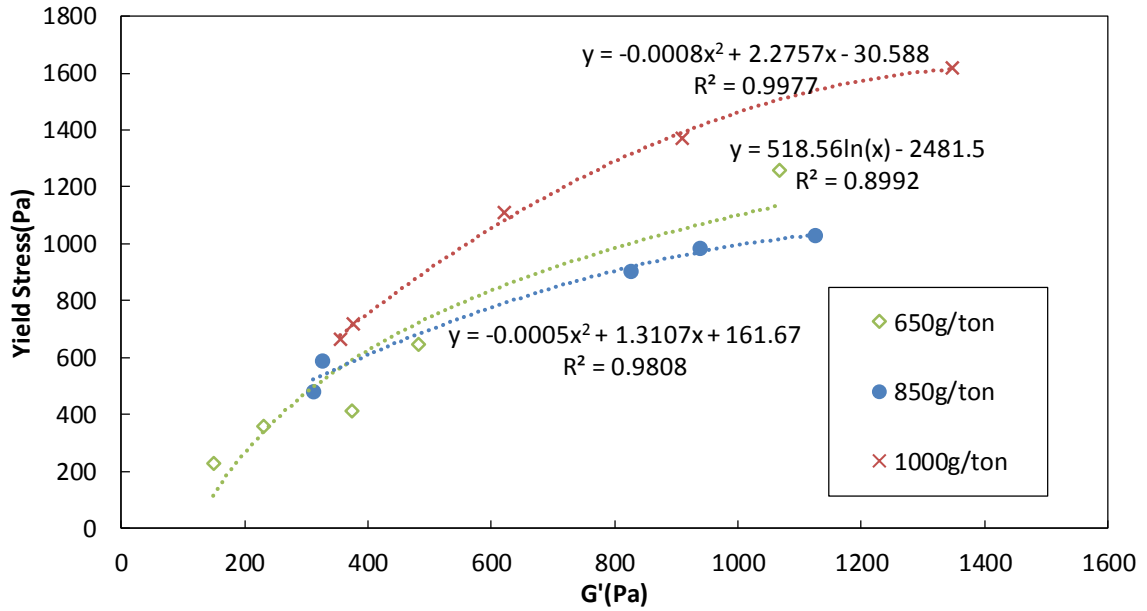


Figure 5.4-11 Yield stress vs elastic modulus for various floc dosage at different resting time as indicated in Figure 5.3-3 to Figure 5.3-5.

Some authors, on the other hand, have correlated the end of the linear elastic deformation (Zhu et al, 2001) with yield stress as some nonlinearity occurs after the linear zone (as shown in Figure 5.4-12). Thus in the next figure the elastic modulus is plotted against the slope of the linear zone as defined by line OB in Figure 5.4-12.

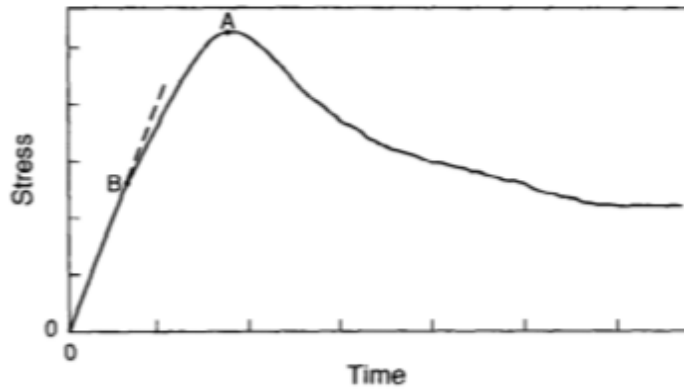


Figure 5.4-12 Typical stress-time response curve for the vane illustrating the slope of linear elastic region (Nguyen et al. 2006).

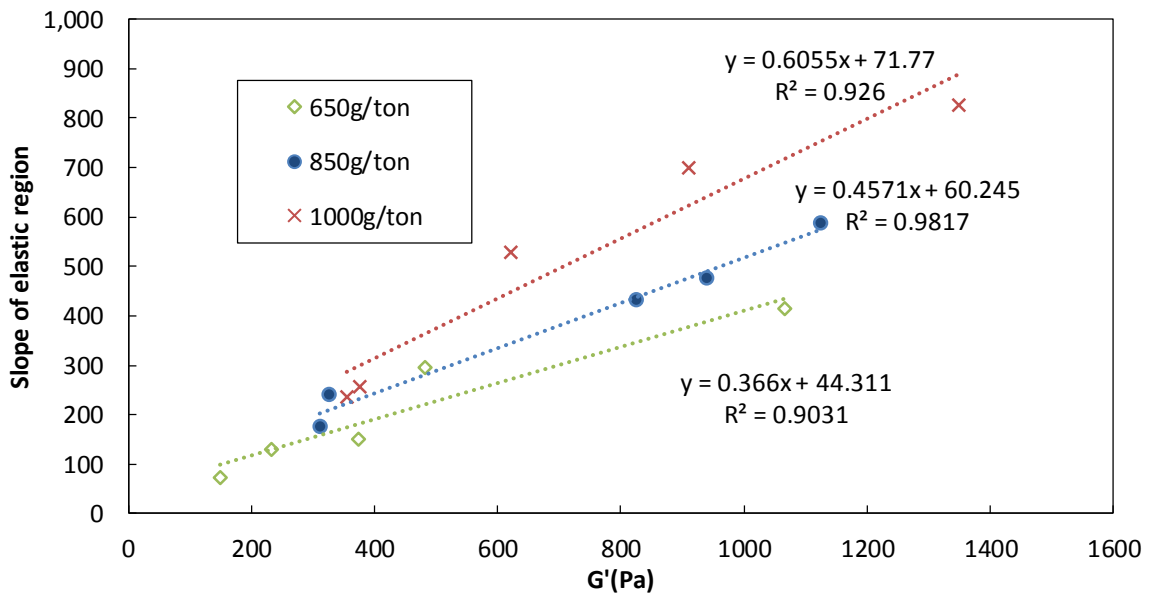


Figure 5.4-13 Yield stress vs slope of linear zone for various floc dosage at different resting time as indicated in Figure 5.3-3 to Figure 5.3-5.

From the latter section it can be seen that the linear properties of the amended oil sands tailings can be used to find nonlinear properties such as yield stress. While some authors have used viscosity measurements (i.e Krieger-Dougherty law) or fine contents/solid concentration to predict yield stress in oil sands tailings (Diep et al. 2014, Omotoso and

Melanson, 2014, Yang, 2009), it can be seen that the elasticity measurement maybe a more reliable technique.

Not just limited to flow behavior, thixotropy affects may also influence geotechnical behavior of MFT. For instance, consolidation of the fine fraction of oil sands tailings is thought to be hindered by thixotropic build up of particle structure. This phenomenon has been shown to slow or even reverse dissipation of pore-water pressures in oil sands mature fine tailings. As a result of higher strength the mixture becomes more resistance to flow (Brenner, 1974), in return, making the settling of particle more difficult (Kaminsky, 2008). Therefore, certain rheometry techniques, as explained here, may be used instead for a more detailed characterization of viscoelastic or viscoplastic behavior.

5.5 Microstructural Analysis Under Shear

Although material will undergo rearrangement and structural build up under resting conditions; shearing (during pumping or deposition), on the other hand, may reversibly break down microstructure, lowering fluids effective viscosity. As mentioned in chapter 2, arrangement of the particles and particle group along with the forces holding them together, define the resistance of a soil towards shearing; thus variation in floc dosage may change the response of flocculated MFT to the same level of shearing.

In order to characterize the thixotropic behaviour of flocculated MFT, their resistance to shear was studied under static conditions. ESEM imaging were performed before and after continuous shear deformation by employing a rotary viscometer. A static shear test was imposed on the tailings using a vane revolving at a constant velocity of 1 rev/min for 4 minutes. For these sets of test a LVDV-E Brookfield viscometer was used where freshly

prepared flocculated MFT at a dose of 850g/tonne was poured into a beaker of 600mL. Although shearing would cause changes to the microstructure it does not occur on the entire sample and it is mainly concentrated near the blades. Thus, sample for the ESEM analysis were mainly taken from where the shear zone had developed.

Figure 5.5-1 illustrates the sample prior to shearing, showing the initial microstructure whereas, the following figure illustrates the microstructure upon static shearing.

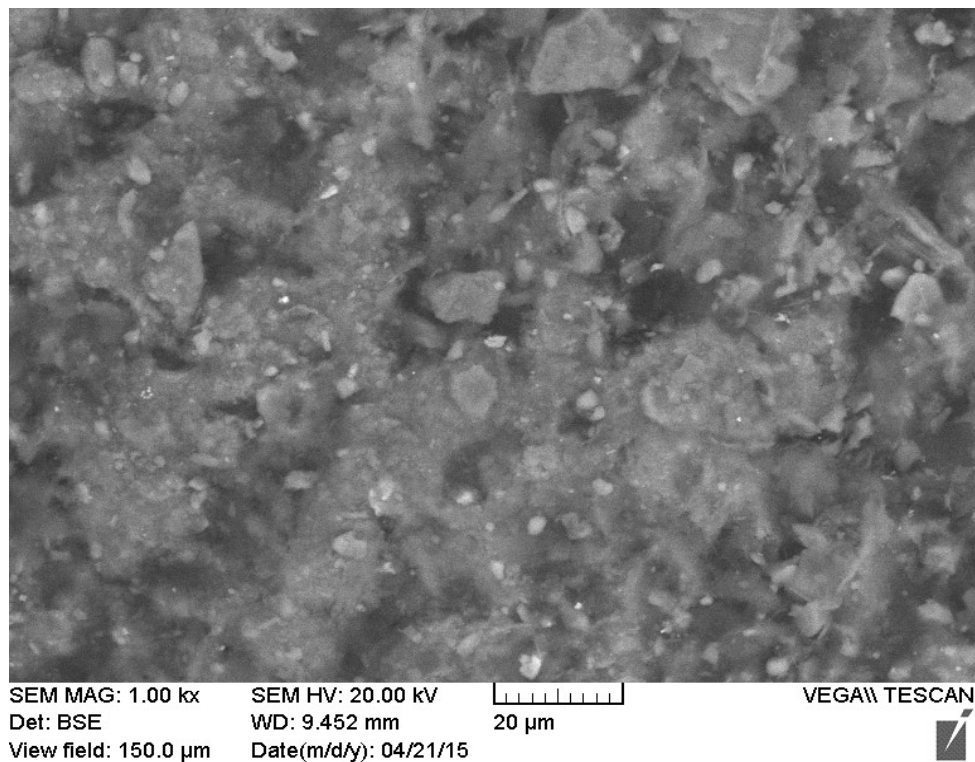


Figure 5.5-1 Backscattered environmental scanning electron of polymer amended MFT at a dose of 850g/tonne for a magnification - 1000 x, scale - 20 μm, view field - 150 μm-before shearing.

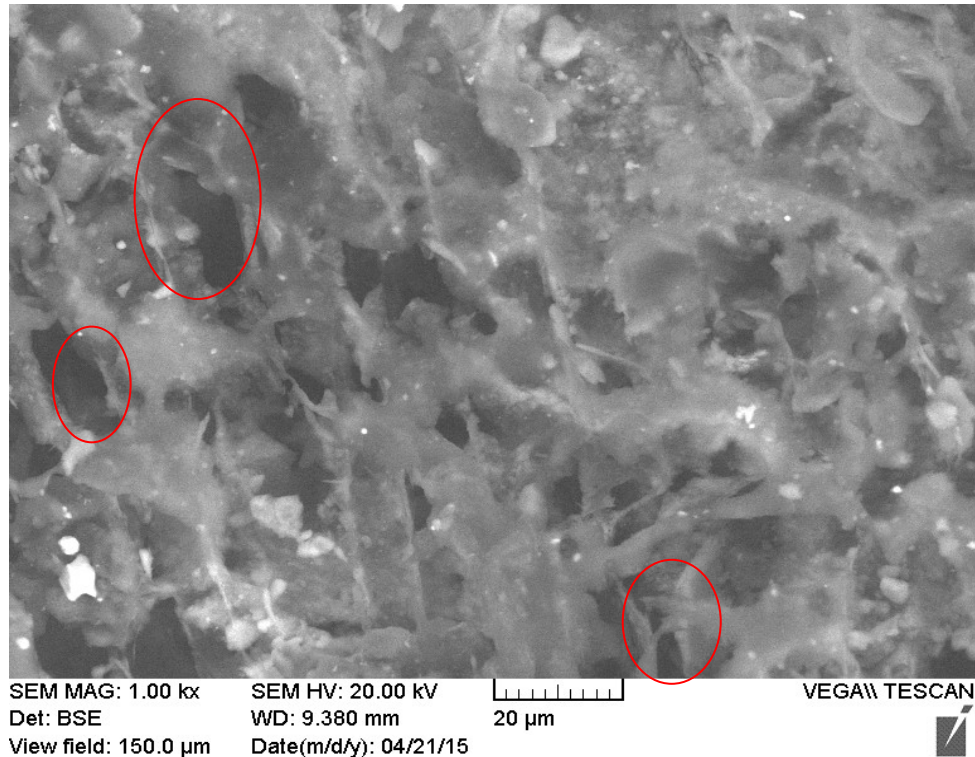


Figure 5.5-2 Backscattered environmental scanning electron of polymer amended MFT at a dose of 850g/tonne for a magnification - 1000 x, scale - 20 μm , view field - 150 μm -after shearing.

Upon application of shear, a high level of orientation was observed in the structure where particle and connectors were stretched in the direction of shear. Also, the appearance of a number of large sized pores elongated in the direction of shear was noticeable right after shearing. Image J analysis show a slight increase in soil porosity in the shear zone.

In this case (low stress levels) not only did the G' decrease, but an increase in G' value was observed once the material was given some time to rest. This shows that the load applied on the sample was not sufficient to break the polymer bonding and even if it did the polymer bridging was rapidly restored. The SEM shows the similarity of the microstructure before and after the cessation of shearing after 50 minutes of resting, where partial tilting of particle in direction of shear was no longer evident and the structure was

rearranged. This may be the reason why the flocculated MFT can restore its elastic properties under lower levels of stress.

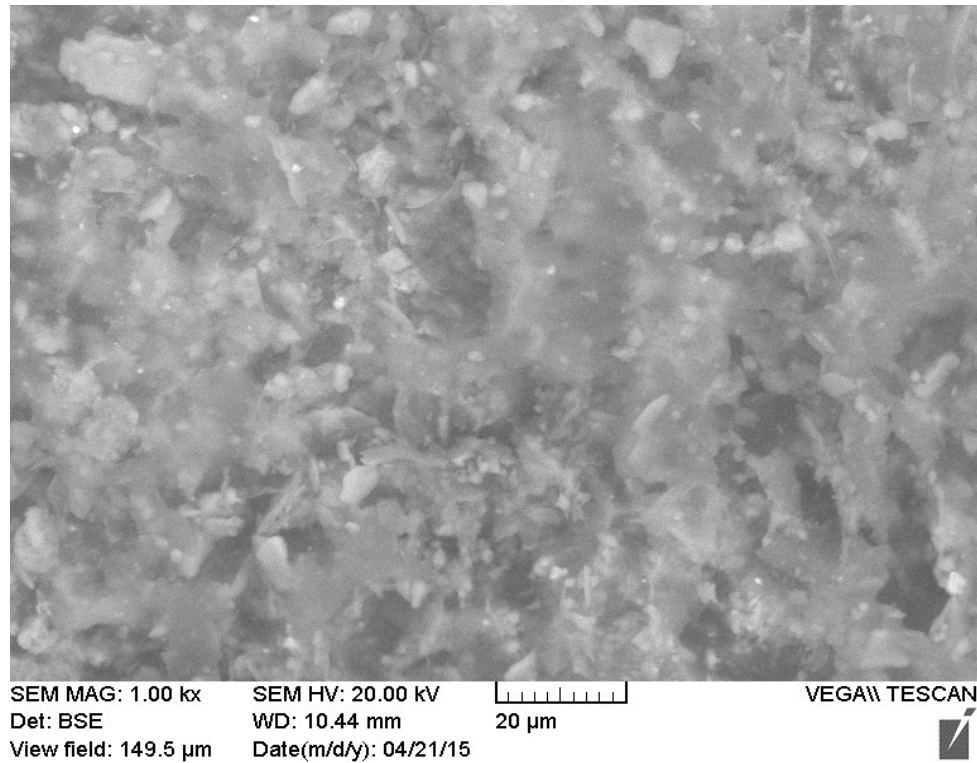


Figure 5.5-3 Backscattered environmental scanning electron of polymer amended MFT at a dose of 850g/tonne for a magnification - 1000 x, scale - 20 μm, view field - 150 μm-after 50 min of resting upon shearing.

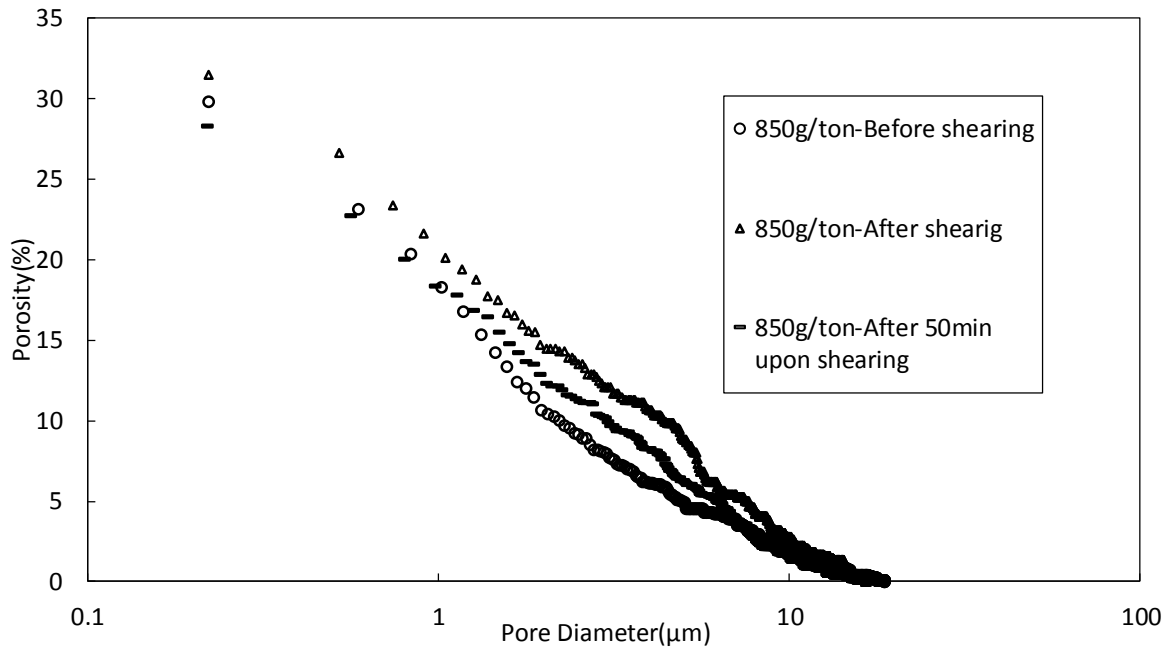


Figure 5.5-4 Gray pixel analysis of polymer amended tailings at 850g/tonne before, after and recovery upon shearing at 1RPM.

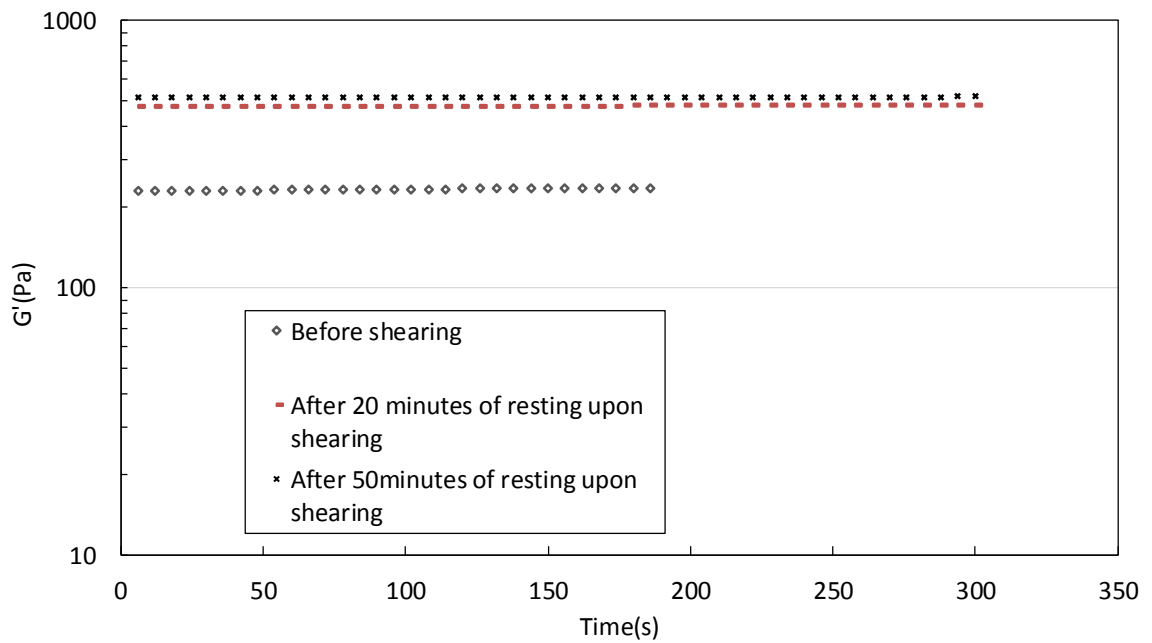


Figure 5.5-5 Elastic modulus values measured at dosage of 850g/tonne before and after shearing.

This behavior may be explained by the formation of granular structure, through the flocculation process of MFT, which provides rigidity to the structure and in return additional resistance to an external force. The material then has a behavior similar to that of an elastic solid. However, when the external force overcomes the intergranular forces, the material behavior changes to viscous state and no longer offers any shear strength (decrease in G').

The next test illustrates the SEM imaging obtained using similar shearing mechanism, but at higher shearing rates (50RPM). In this case a substantial decrease in the storage modulus was observed (Figure 5.5-6). The higher shear resulted in yielding of the flocculated structure where the platy clay particles were aligned in the direction of shearing. Structural disturbance may be the reason for a decrease in strength of the system and consequent decrease in G' values. G' measurements over time and upon cessation of shearing illustrates the reversal process.

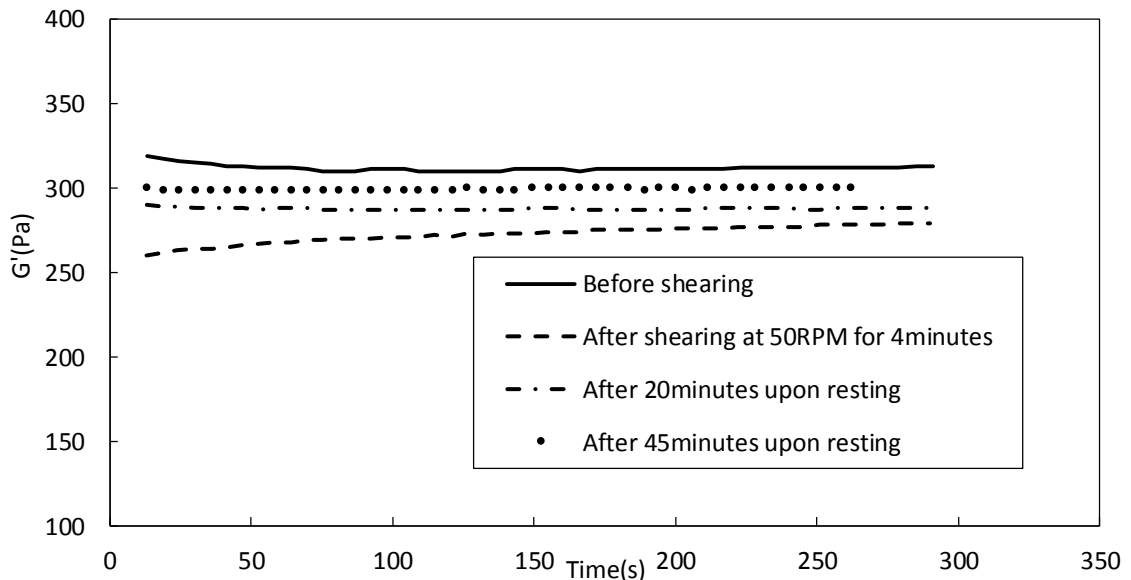
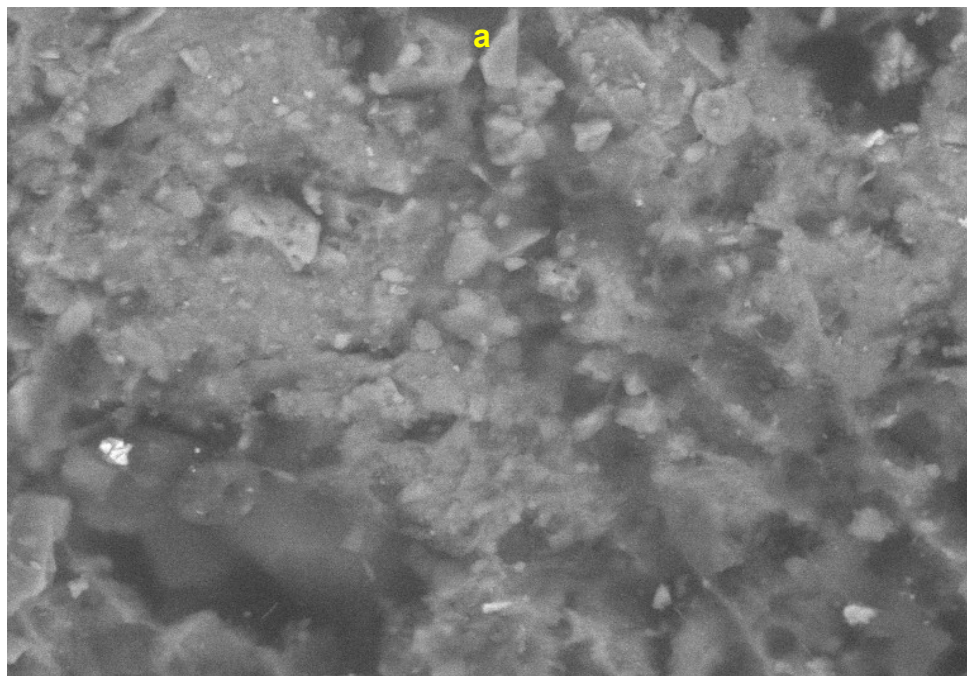
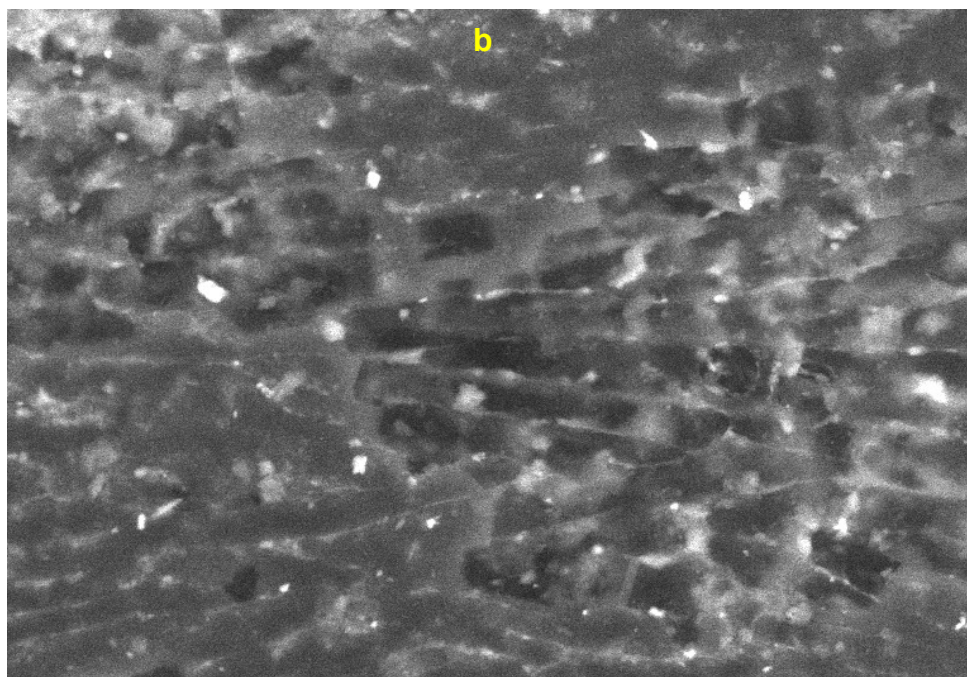


Figure 5.5-6 Elastic modulus values measured at dosage of 850g/tonne before and after (0min, 20min and 45min) shearing at 50RPM for 4 minutes.



SEM MAG: 1.00 kx SEM HV: 20.00 kV
Det: BSE WD: 9.008 mm
View field: 150.0 μ m Date(m/d/y): 09/30/16

VEGA\\ TESCAN



SEM MAG: 1.00 kx SEM HV: 20.00 kV
Det: BSE WD: 10.52 mm
View field: 150.0 μ m Date(m/d/y): 09/24/15

VEGA\\ TESCAN

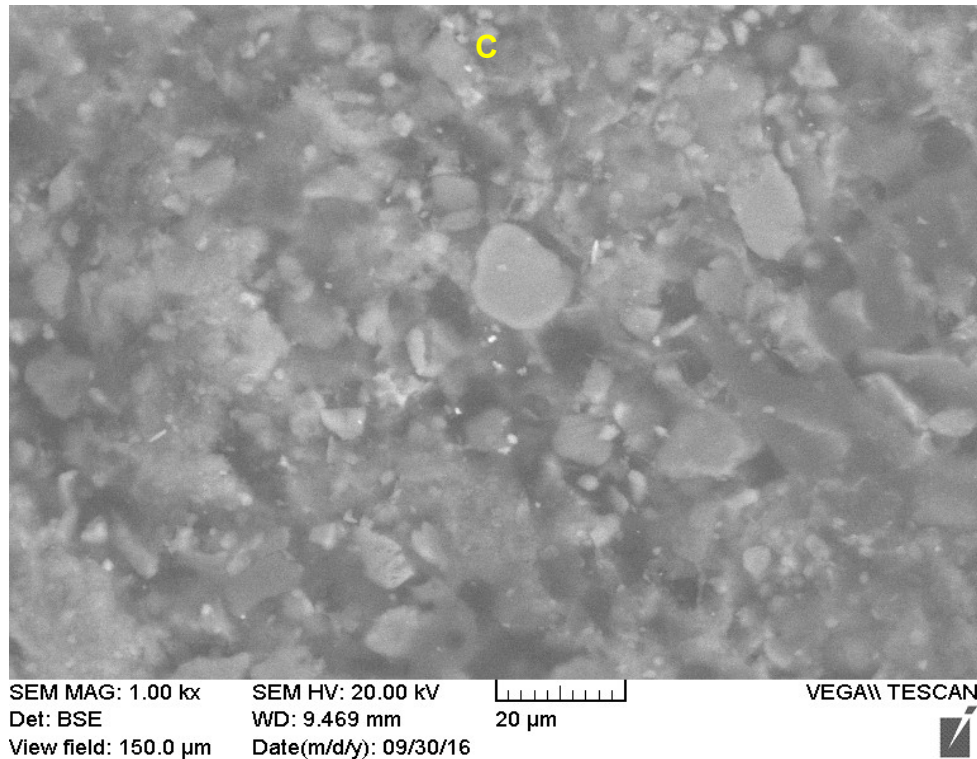


Figure 5.5-7 Backscattered environmental scanning electron of polymer amended MFT at a dose of 850g/tonne for a magnification - 1000 x, scale - 20 μm , view field - 150 μm -(a) before shearing, (b) after shearing at RPM of 50 for 4 minutes and (c) after 45minutes upon shearing at RPM of 50 for 4 minutes.

Figure 5.4-7 presents gray pixel analysis of polymer amended tailings at 850g/tonne before, after shearing and 45 minutes after cessation of shearing for the ESEM micrographs presented before. The imageJ analyses was performed with BSE images of 1 kx for 850 g/tonne view field of 150 μm . Analysis were conducted using both technique: the threshold tool and using the developed algorithm as explained before. Comparing the porosity before and after shearing it can be seen that the applied shear causes the (micro) pore system to collapse. However, Figure 5.5-7 (a) and (c) show similarly of the structure before and after 45minutes upon cessation of shearing where the pores regain their initial size, and microstructure was restored.

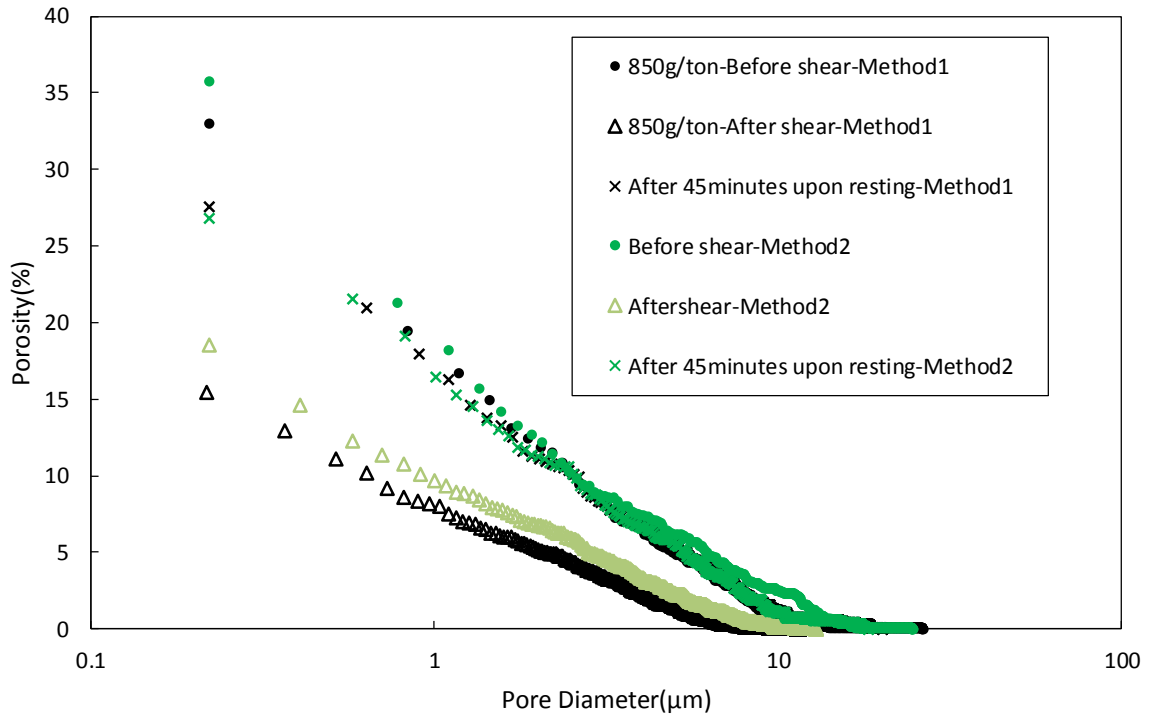


Figure 5.5-8 Gray pixel analysis of polymer amended tailings at 850g/tonne before, after shearing at 50RPM and after 45minutes upon resting.

This behavior is similar to what Markgraf, (2006) found for non-swelling clay materials (i.e kaolinite), having a rigid structure, where large internal friction angle, provides strength to applied external loading. On the other hand, when applied load prevail internal (structural) forces, and the yield stress is exceeded, a sliding shear behaviour that is irreversible may be observed. Markgraf et al. (2006) used the following explanation (Figure 5.5-9) for mechanical behavior of low friction angle soil under oscillatory stress. Similar mechanism may apply to the results presented here.

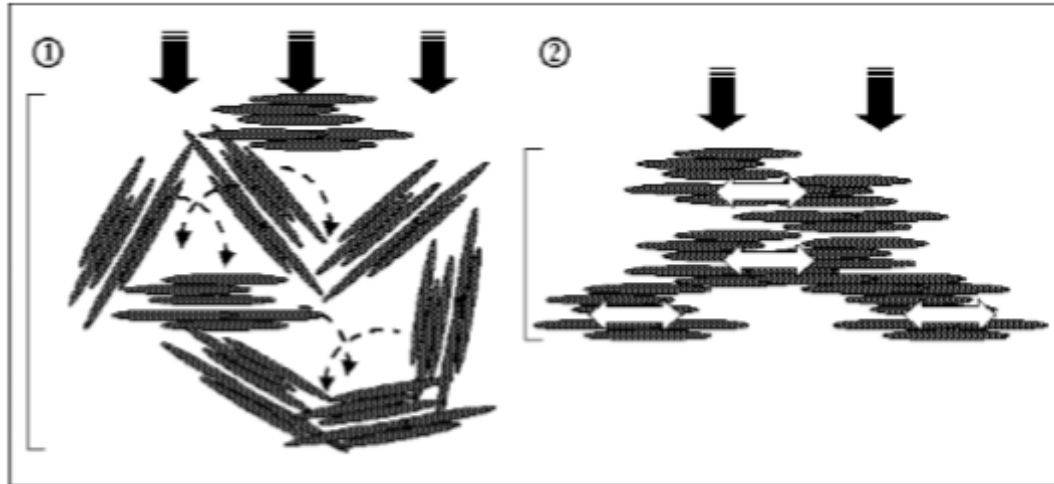


Figure 5.5-9 Mechanical behavior of clay particles under oscillatory stress.

5.6 Mechanical Behavior of Flocculated MFT using Rheology

In case of viscoelastic material like wet soils, there exists a phase shift between strain and stress response. The term $\tan \delta$ is often used to describe the ratio of G'' (viscous modulus) to G' (elastic modulus). Using this term a better description of structural and stiffness degradation may be obtained (Markgraf et al. 2012): At the beginning, G' is higher than G'' and elastic behavior is dominates; At $\tan \delta = 1$ elastic and viscous character become equal. After this stage the structure collapses and soil exhibits irreversible deformation. Thus, as the stress (strain) level increases G' decreases and behavior of flocculated MFT changes to viscous behavior. Referring to Figure 5.6-1, it can be seen that the larger the shaded area, the more elastic/rigid the behavior of the soil becomes.

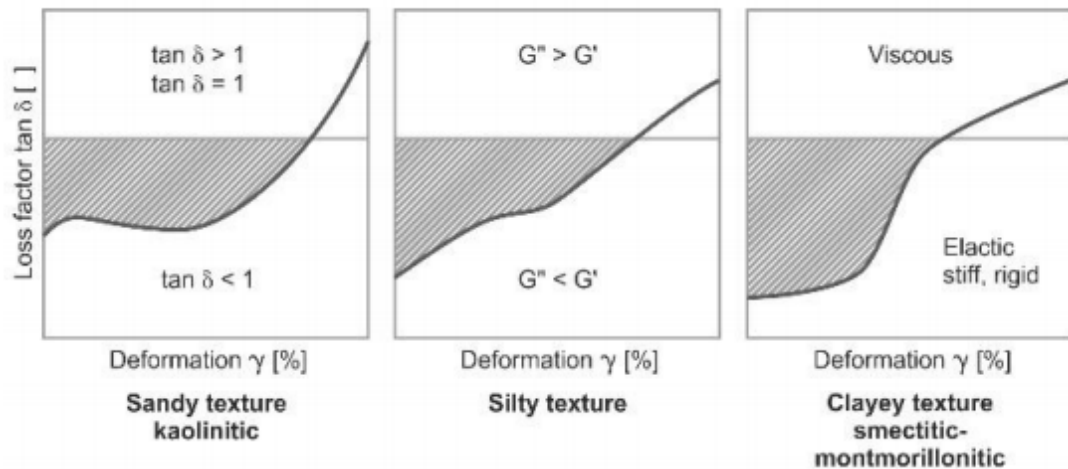


Figure 5.6-1 Phase angle versus strain as a function of soil texture (Markgraf et al. 2012).

The following figure illustrates $\tan\delta$ values versus strain for raw and flocculated MFT. Due to the development of larger aggregates in the course of flocculation process the elastic response was more pronounced as a result of stronger particle-particle interaction. The average values of integral z were 29 and 490 for raw and flocculated MFT respectively at a frequency of 10 rad/s. This change is indicative of a more stable and rigid structure of flocculated structure.

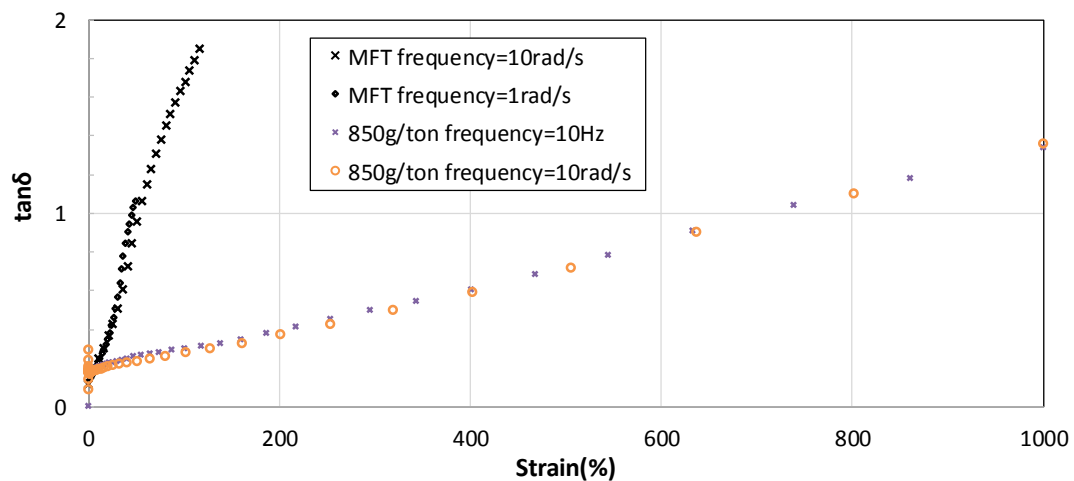


Figure 5.6-2 $\tan\delta$ as a function of strain for raw and flocculated MFT.

6 Chapter: Laboratory Flume Tests

6.1 Objectives of the Flume Tests

Two sets of flume test were carried out (small and large) to investigate the flow behavior of flocculated MFT. The first set were carried at Carleton University in a 2 m flume where already flocculated MFT (as explained in section 3.9) were deposited through a funnel and were designed to study flow behavior of tailings at different dosages. The second sets (conducted at Oil Sands Tailings Research Facility in Devon, Alberta) were designed to investigate the effects of deposits volume and deposition speed on final geometry at a selected dosage. By varying the deposition speed a greater shear can be imposed on the material and the independency of the residual stress to degree of shearing and deposition time can be investigated. Also, the point at which spreading flow changes to channelized flow (a phenomenon commonly observed during field depositions) was investigated by varying deposition parameters (flow rate).

6.2 Small Scale Flume Tests Setup

For simulating the depositional behavior of flocculated tailings under laboratory conditions of various dosages, a flume apparatus with a length of 243 cm, and width of 15.3 cm was used. In order to observe the deposition, the sides were made from clear acrylic. A schematic of the flume apparatus is illustrated in the following figure.

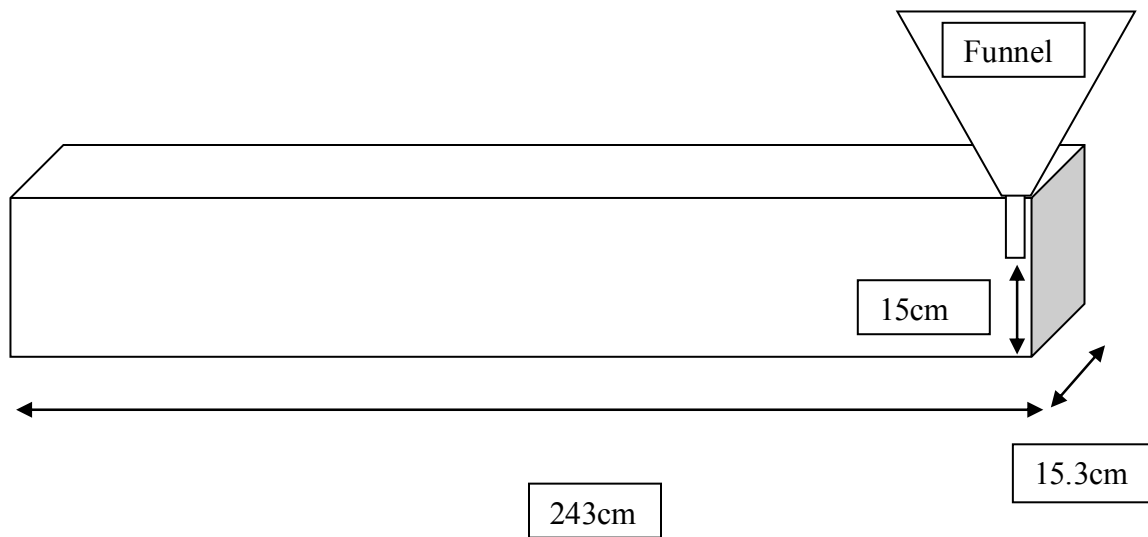


Figure 6.2-1 Dimensions of the flume used (small scale).

6.2.1 Testing Procedure

A set volume of flocculated MFT (5.8kg +/-100gr) were poured at a distance of 15 cm above the flume through a funnel and the length of the flow and the depth were measured at different locations (every 5cm) after the stabilization of flow (Figure 6.2-2). The variability in yield stress was then calculated using lubrication theory for Bingham fluid and using ANSYS CFX. Lubrication theory, a simplified form of the momentum and continuity equations, has previously been used (Simms, 2007; Henriquez and Simms,

2009; Mizani and Simms, 2010) to model the steady state and transient flow of yield stress fluid.



Figure 6.2-2 Flume test.

6.2.2 Test Results

Figure 6.2-3 shows the equilibrium profiles for the tailings deposited at different floc dosage using a funnel. Tailings prepared at the dosage of 650 g/tonne had the longest run-out compared to the other dosages. This indicates that the tailings deposited at higher floc dose gained a steeper slope and shorter run-outs upon deposition. This is also consistent with field observations where higher yield stress materials tend to stack closer to discharge points where little or no material reach downstream of the cells. However, to gain a higher storage capacity, not only a steeper slope is required but also uniform footprint coverage is essential.

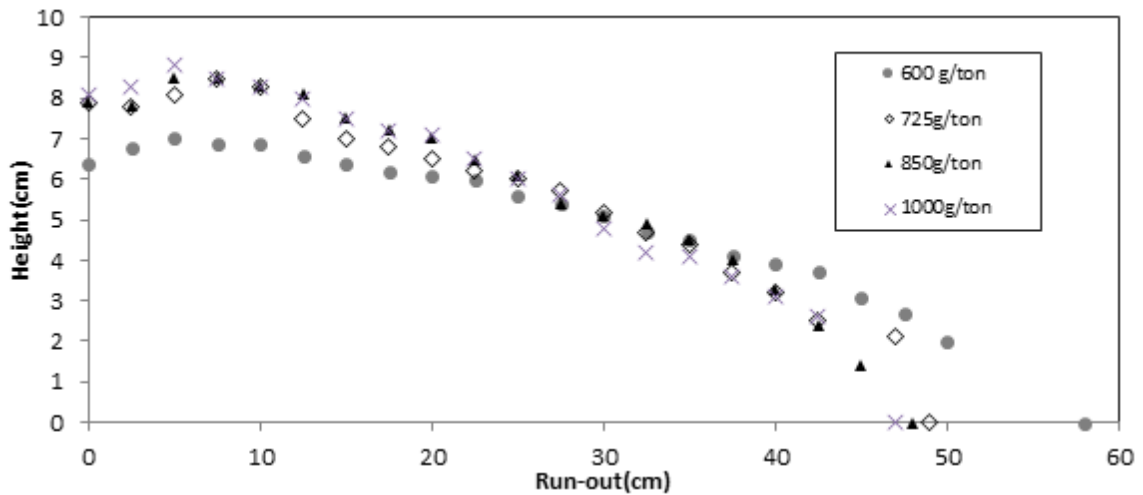


Figure 6.2-3 A single layer flow at various floc dosages.

6.3 Pilot Scale testing at OSTRF

In order to investigate the effects of volume and deposition flow rate on final geometry, flume test at larger scale were conducted at the Oil Sands Research Facility (OSTRF) in Devon. Due to shear sensitivity of flocculated MFT (over shearing at high pumping rate), pumping of already prepared material was not possible. Since dynamic mixers are not capable of handling large inventories of tailings in a timely manner (cubic meters of tailing), the flocculation process was designed to take place before deposition and during pumping and for this purpose static mixers were utilized.

Inline static mixer (or motionless mixers) are second most common tools used (after rotating impellers) for flocculation process (Thakur et al. 2003). Their relatively cheap cost, low power consumption, low maintenance effort makes them a good candidate for use in large scale MFT Flocculation testing. Moreover, owing to the near plug flow behavior, a good mixing can be obtained (Demoz, 2012).

Static mixers used in this study were obtained from Chemineer-Kenics with a 1 inch diameter KMS type. A schematic of the static mixer test is illustrated in Figure 6.3-1. Each static mixer consists of 12 elements where each element splits and recombines the mixture while flow is pushed axially using the progressive cavity pump. A uniform composition and concentration of the material will be obtained when the material is pumped through elements (Demoz, 2012).

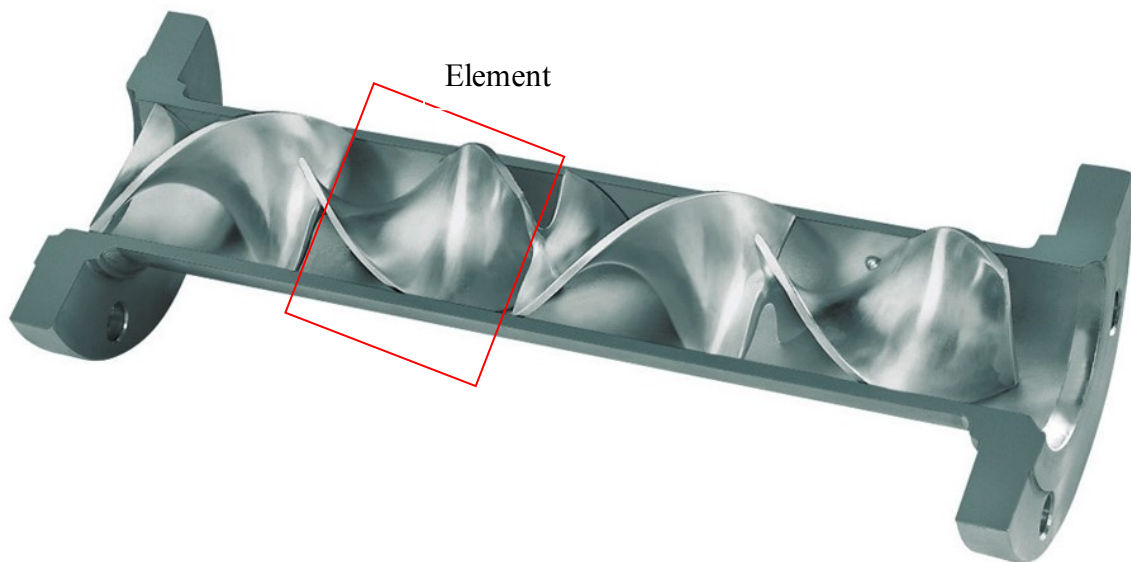


Figure 6.3-1 KMS static mixer.

Although velocity (V) and Reynolds number (Re) are the common terms used for scaling mixing; Demoz (2012), found that mixing energy was a more relevant term for characterization of the flocculation process (dewatering) when static mixers are used. Considering the kinetic energy supplied by the pump provide the mixing energy, the pressure loss over the static mixers can be used for calculating the input energy. For this purpose two pressure gauges were placed before and after the static mixers and pressure loss was monitored throughout deposition to control and maintain a constant mixing energy

for all test. Two Andreas Hauser pressure gauges with 4 to 20 mA analogue outputs were installed where data was acquired using a PC. The energy density of inline static mixer was calculated using the following equation (Demoz 2012):

$$\xi = \Delta P \times \rho^{-1} \quad 6.3-1$$

Where,

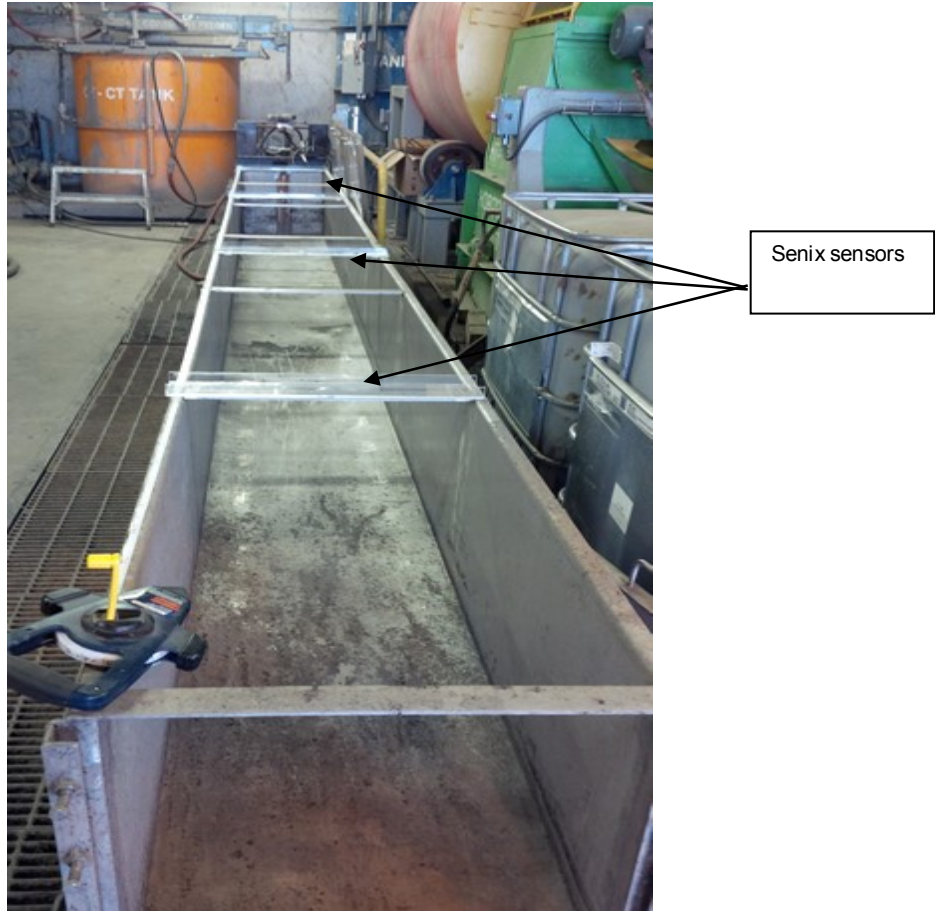
ξ is the energy density,

ΔP is pressure difference in N.m^{-2} and

ρ is density in kg.m^{-3} .

6.3.1 Pilot Scale Flume Tests Setup

The cross-section of the flume used along with its dimension are illustrated in Figure 6.3-2. The flume is 8 meter in length, 66cm in width and 59 cm deep. In order to monitor the variation of deposition height over time (flow behavior during deposition), 5 senix sensors were installed at 1.5m interval, above the flume and along the length of the flume. These sensors were also connected to the data acquisition system after having been calibrated with samples of known heights. A box was also installed at the end of the flume where the drained water was collected and measured at the end of each test.



Pipe Diameter=2.54cm

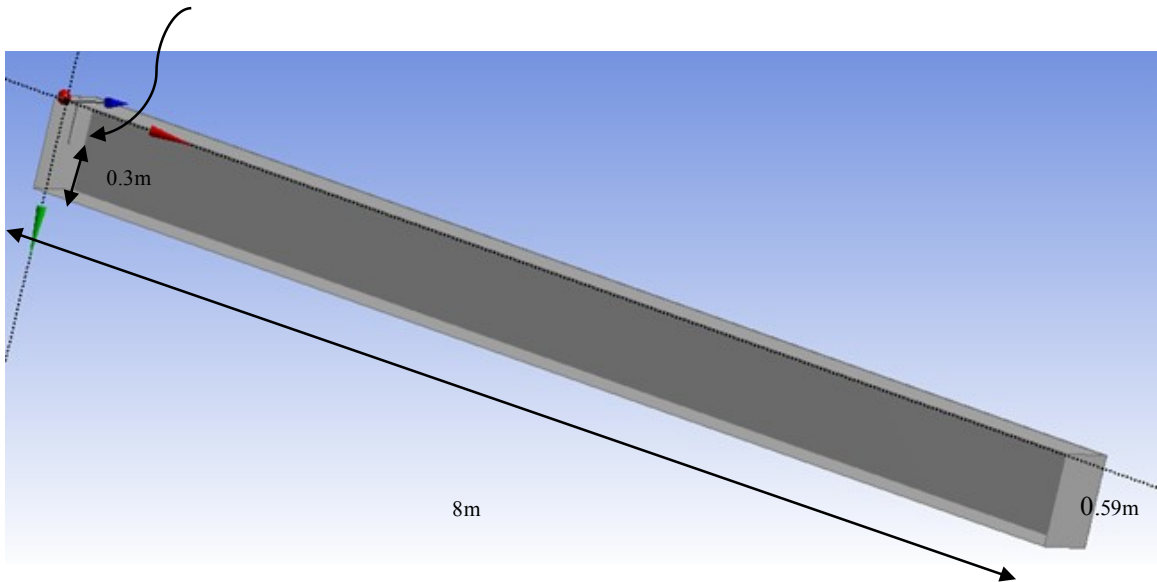


Figure 6.3-2 Flume apparatus used in OSTRF and dimensions

Tailings used in these tests were also obtained from the Muskeg River Mine and were transported to OSTRF facility in several totes. Due to the settlement of tailings during transportation, the content of the totes were initially mixed using a drum mixer for 3hrs. Mixing was then followed by continuous recycling from top to bottom, using a SPX65 high pressure hose pump, at an average speed of 30 rpm for an additional 3 hour alternating every 30 minutes between forward and reverse modes. This was to ensure MFT were thoroughly mixed with the bleed water released during the transportation and to bring them back to their original condition (Figure 6.3-3). Tailings from all three totes were then transferred into a larger tank (CT Tank) of 2.8m³ volume for homogenization (Figure 6.3-4), where tailings were remixed (for additional 24hr) to attain initial solids concentrations of 35.5%. Particle size distribution of tailings are illustrated in Figure 6.3-5. The liquid limit (through fall cone test) and plastic limit were determined to be 51.4% and 30.3% respectively.



Figure 6.3-3 Pump mixing in totes.

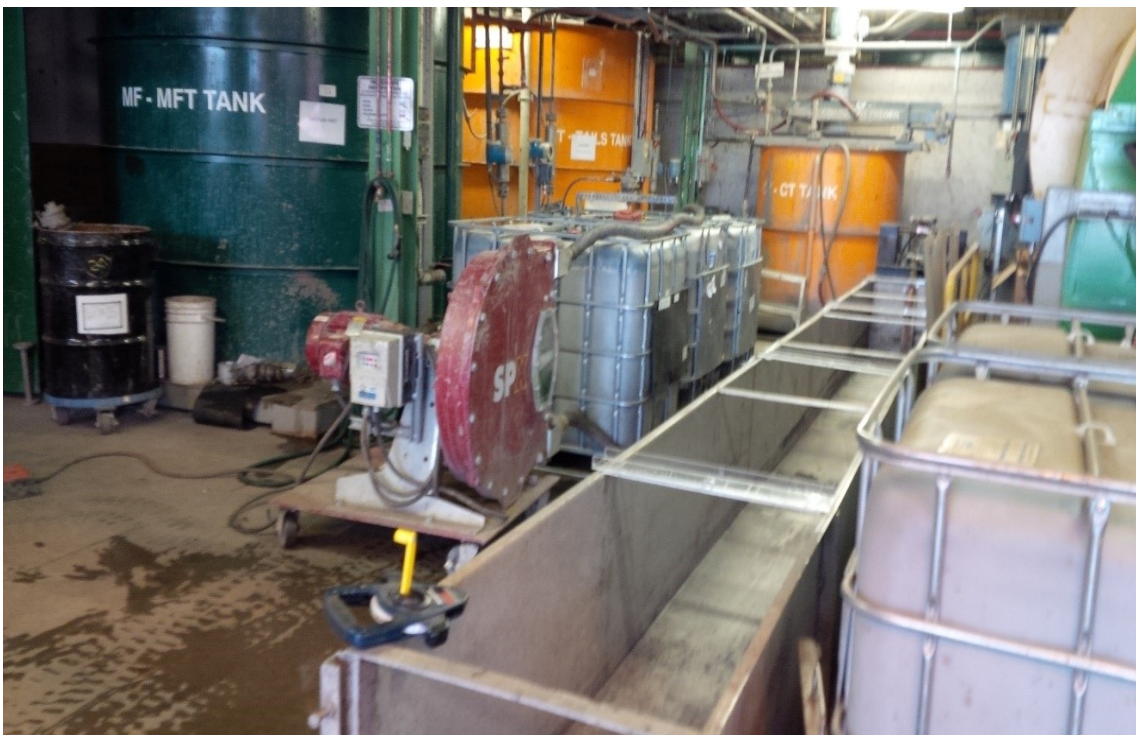


Figure 6.3-4 Tailings transportation into CT tank

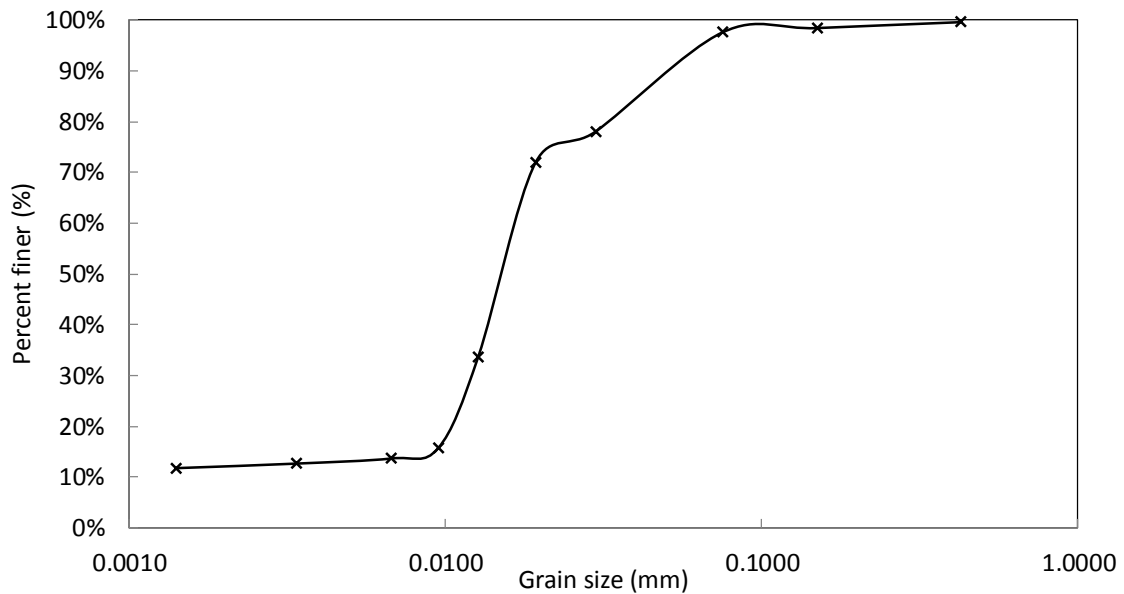


Figure 6.3-5 Particle size distributions of raw MFT used for flume test from hydrometer and sieve analysis.

6.3.2 Experiment Setup

A schematic of the flume test is illustrated in Figure 6.3-6. These test were conducted using a 1 inch diameter pipe, where MFT was fed from the CT tank using a progressive cavitation pump (43 L/min full scale). 0.4% polymer solution was also injected using a flex pro pump model A4, with a smaller capacity of (3 L/min full scale) in the centerline of the pipe just before the static mixers. A branched A3338, anionic polymer supplied by SNF was used for all tests, where flocculant dosage was calculated based on dry mass of polymer.

The deposition speed was controlled (increased/decreased) by changing the number of elements in the static mixers (at higher flow rates less mixing is required) such that mixing energy remains constant for all test. The tailings and floc solution were stirred continuously

(using an impeller installed in the tank) during deposition process, to prevent any settlement.

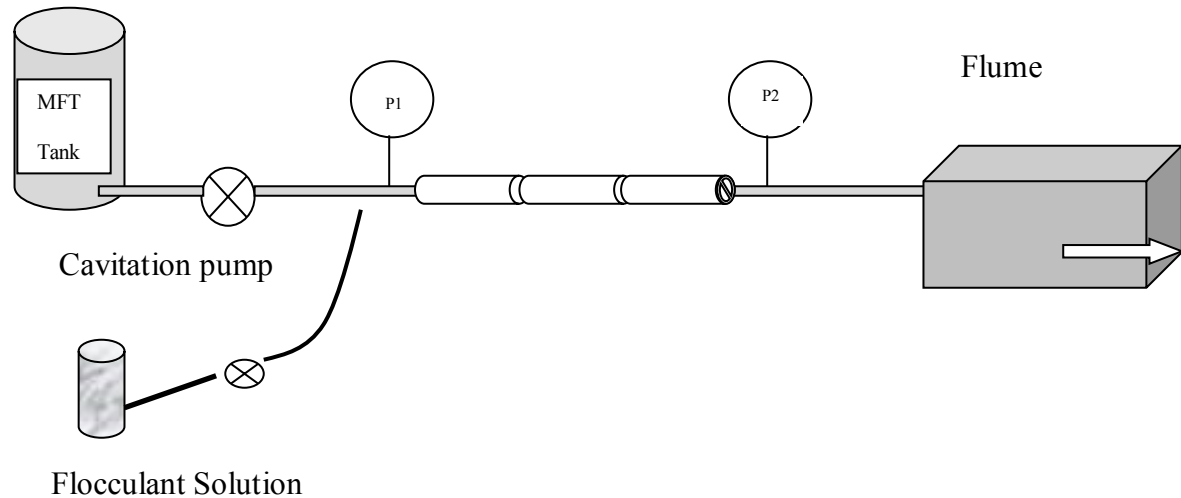


Figure 6.3-6 Illustration of the setup for small pilot scale flume test at OSTRF.

The thickness of the deposits were also recorded by hand at certain intervals. Run-off from the deposit were also collected at the end of the flume. Samples of 500mL volume were taken from the surface, for yield stress measurements using an onsite rheometer at three different locations: deposition point, toe and mid length. Yield stress measurements were conducted for the purpose of understanding the rheological changes during deposition and to monitor structural changes under adverse effects of shearing and aging.

The rheometer used to study the rheology of the material was a Brookfield DV3T model with a vane geometry (V-74& V-75) and with the following dimensions and stress ranges:

Table 6.3-1 Vane Spindle Ranges

Spindle	Vane Length(cm)	Vane Diameter(cm)	Shear stress Range(Pa)
V-74	1.176	0.589	100-1000
V-75	1.61	0.803	40-400

6.3.3 Mixture Quality

The number of mixers was optimized, by trial and error, to produce material with consistent rheology at the deposition point for a given flow rate. For this purpose, MFT and floc solution were mixed at different speeds while changing the number of elements. The flocculated product was then tested for yield stress at a constant shear rate of $0.1(s^{-1})$ using the Brookfield rheometer available onsite. The following figure illustrates the yield stress values of the mixture measured after 30 min and upon decanting the bleed water.

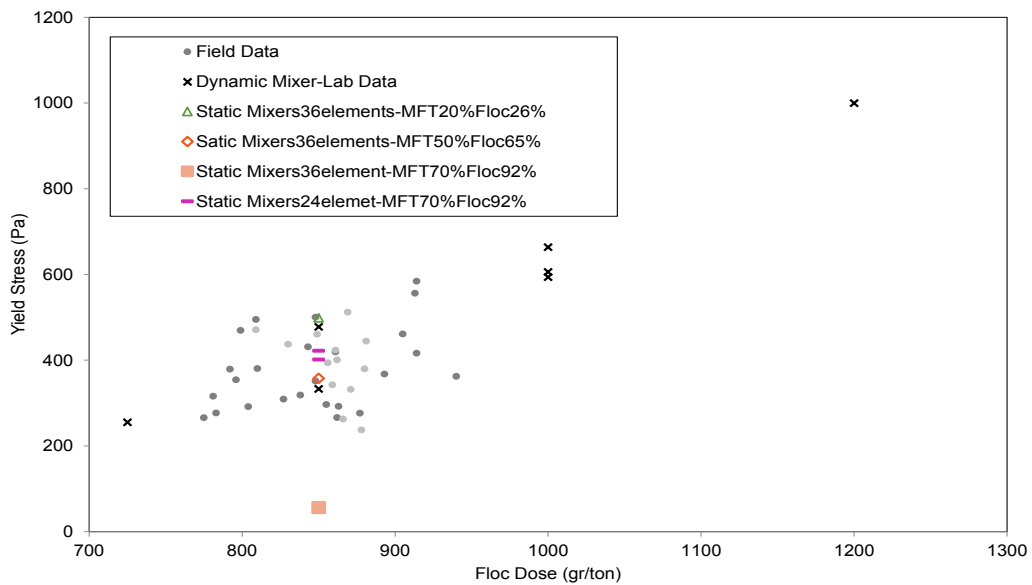


Figure 6.3-7 Yield stress values for various setup (please refer to Figure 6.3-9 for pump calibrations)

Figure 6.3-7 shows the yield stress values obtained at different depositional speeds and different number of static mixers. It can be seen that at higher speed (70% MFT pump corresponding to 31L/min and 92% Floc pump corresponding to 2.93L/min), less number of static elements is required as the longer setup resulted in over shearing of the mixture (yield stress value of 50Pa). This is consistent with the finding of Demoz, (2012) where the minimum CST (Capillary Suction Time) was obtained when higher number of static elements were used at lower velocities. Since mixing is achieved through both turbulence mixing and stretching along the elements of static mixers, the use of more elements at higher speeds would result in deterioration of the mixing process, which explains the observed behavior. A comparison of over sheared, and well flocculated tailings is shown in Figure 6.3-8 below.



Figure 6.3-8 a) Over sheared material-poor mixing (at highest flow rate using 3 static mixers) (b) Well flocculated material at same speed using 2 static mixers.

Two flume tests were performed (using lowest and highest capacity of the Flex pro pump) to investigate tailings flow behavior under different pumping rates on a flat bed. In addition, the test was used to find the point at which spreading flow changes to channel flow.

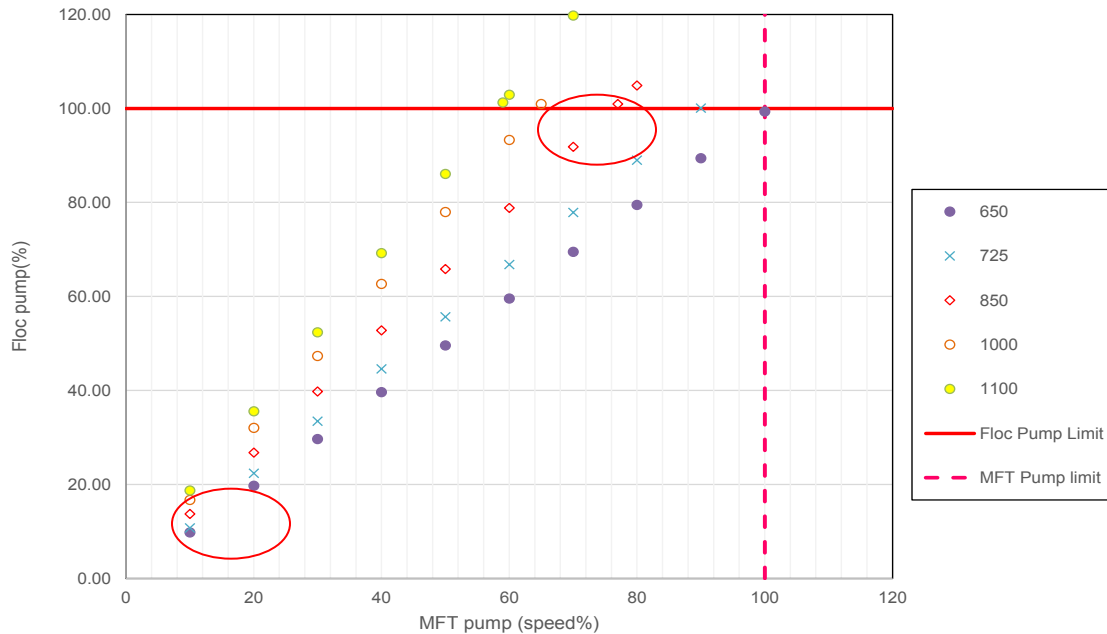


Figure 6.3-9 Flume test operational pump speed for various floc dosages (the following conversions were used: Floc pump speed (L/min) =32.465x-3.1371 and MFT Pump speed (L/min)=0.4261x+1.2594, where x is percent pump speed).

6.3.4 Flume test Results

6.3.4.1 Fast Pour

This test was performed using a speed of 36L/min (75% pump speed for MFT and 98% Floc solution), which was the highest possible speed using this setup. The total deposition

time was 21 minutes and 17 seconds. Pressure drops across the static mixers are illustrated in Figure 6.3-10 . A total of 773L of tailings were deposited and a total of 14.74 kg release water was collected at the end of deposition. Transient profile (5min interval) are illustrated in Figure 6.3-11 along with corresponding pictures.

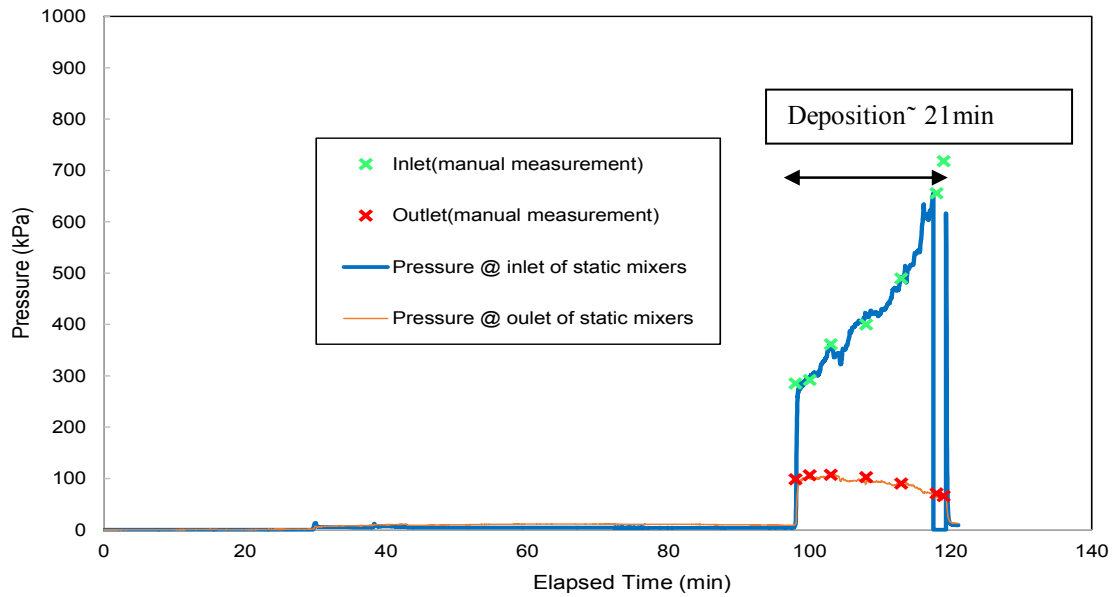


Figure 6.3-10 Pressure drop across static mixers during fast pour.

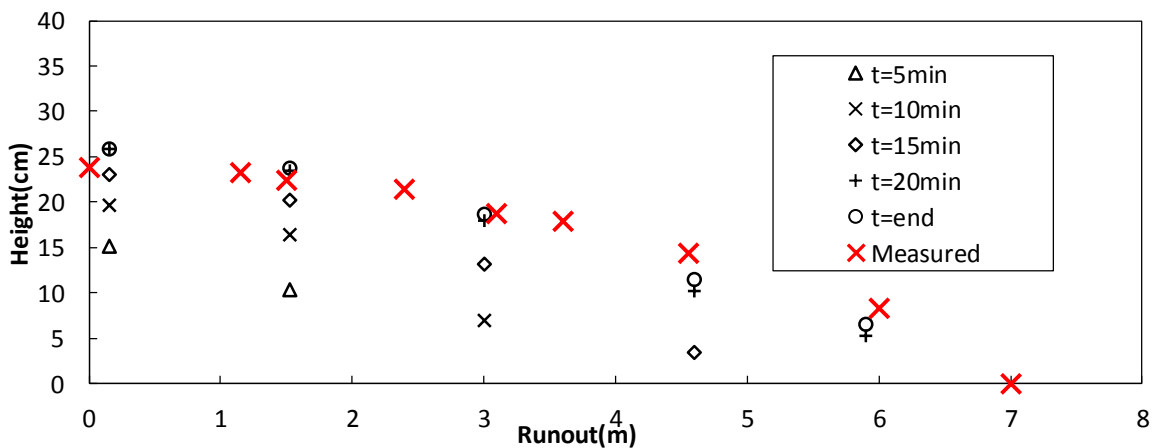
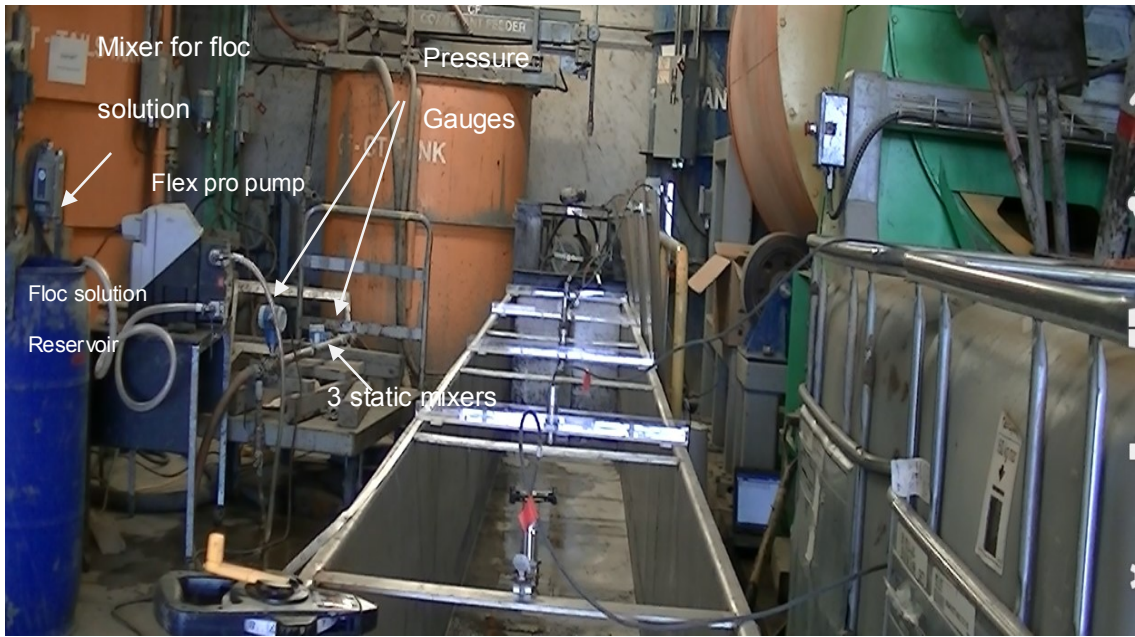


Figure 6.3-11 Transient profile in the flume for a single layer, at floc dosage of 850g/tonne (MFT pump speed of 75% and Floc pump speed of 98%).



(a)Initial



(b)After 5min



(c) After 10min



(d) After 15min



(e) End of deposition

Figure 6.3-12 Photos corresponding to transient profile in the flume for a single layer, at floc dosage of 850g/tonne (fast pour).

The following figure presents the yield stress (peak of each stress growth curve) of the tailings collected at various distances along the path of the tailings along with their solid content. Measurements were conducted after the tailings stack reached steady state and upon completion of deposition. The yield stress (and solid content) value recorded for the sample collected close to deposition point were higher than the yield stress of samples collected at a distance from discharge point, due to shearing of material and destructuring during deposition process.

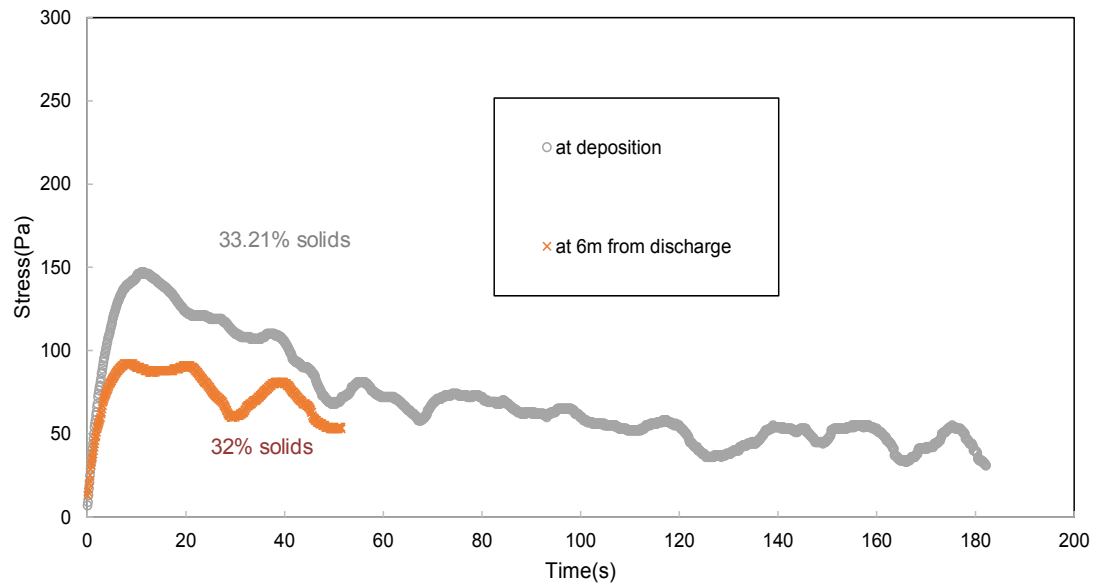


Figure 6.3-13 Yield stress values measured at the end of the flume test ($t=25$ minutes) at surface of the deposit and at 0 and 6m from deposition point.

6.3.4.2 Slow Pour

This test was performed using a speed of 10 L/min (20% pump speed for MFT and 26% floc solution), lowest possible speed using this setup. The total deposition time was 62 minutes. Pressure drops across the static mixers are illustrated in Figure 6.3-14. Transient profile (10min interval) are illustrated in Figure 6.3-15 along with some picture taken during deposition.

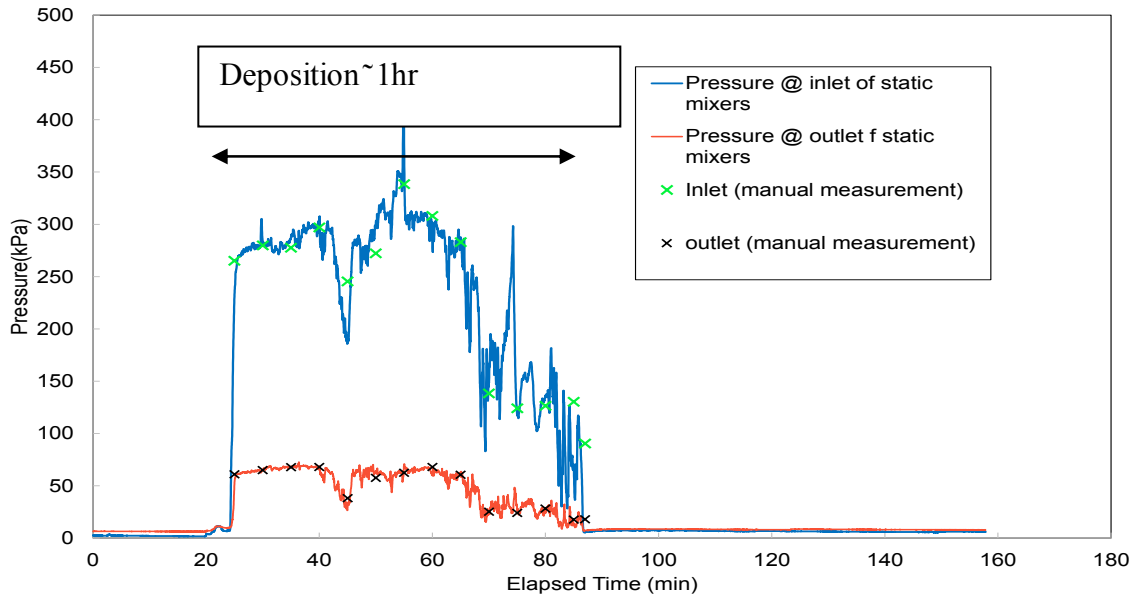


Figure 6.3-14 Pressure drop across static mixers during slow pour.

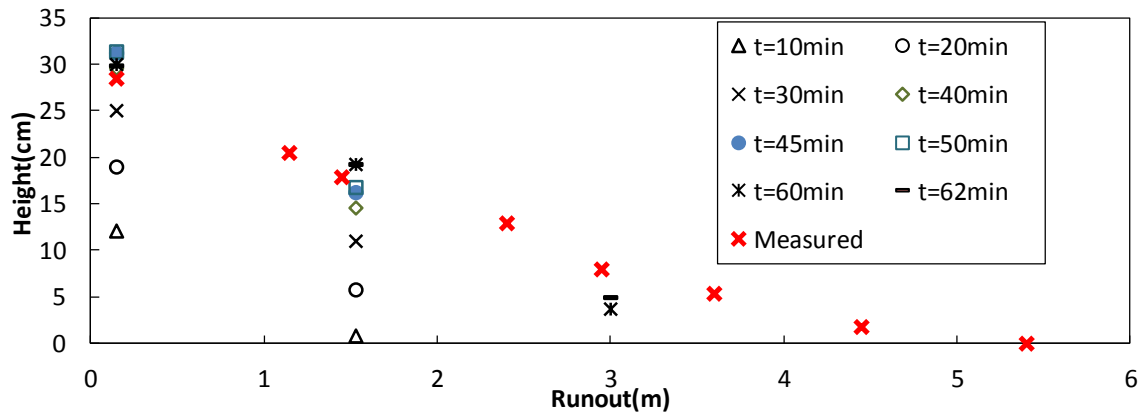


Figure 6.3-15 Transient profile in the flume for a single layer, at floc dosage of 850g/tonne (MFT pump speed of 20% and Floc pump speed of 26%)



(a)Initial



(b) After 10min



(c) After 20min



(d) After 30min



(e) After 45 min



(f) After 50 min



(g) After 60 min

Figure 6.3-16 Photos corresponding to transient profile in the flume for a single layer, at floc dosage of 850g/tonne (slow pour).

A total of 663L of tailings were deposited and a total of 52.56 kg of release water was collected at the end of deposition. The following figure (Figure 6.3-17) shows the yield stress of the tailings collected at various distances along the path of the tailings along with their solid content. As expected the yield stress (and solid content) value recorded for the sample collected at deposition point was higher than the yield stress for samples collected at a distance from discharge point due to shearing of material. Also, the yield stress values obtained for this test were higher than the values obtained from the faster pour probably because material had more time to recover the structural disturbance during shearing.

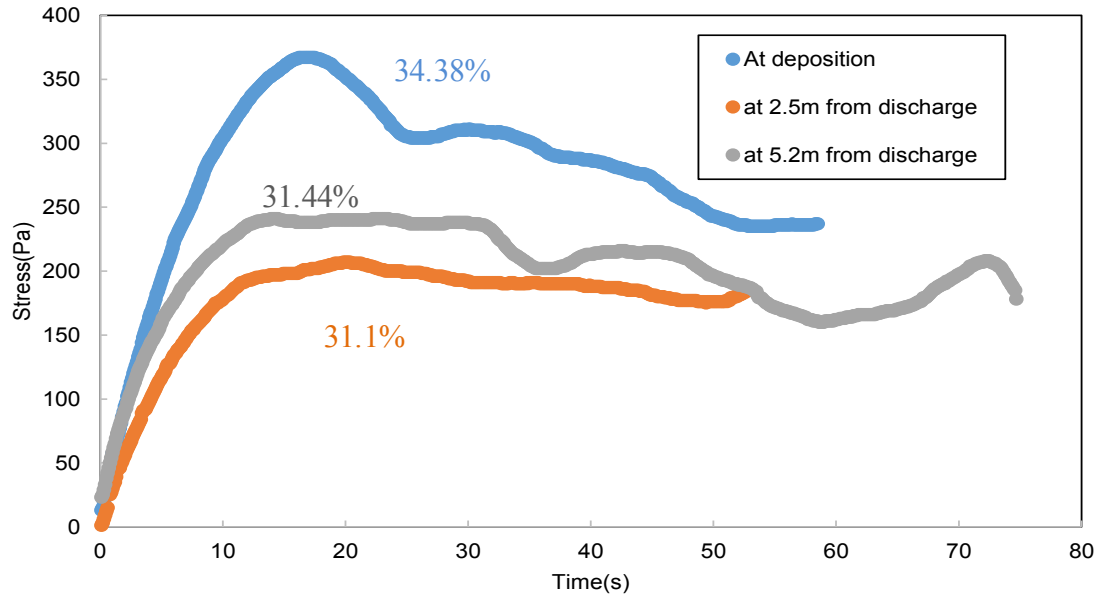


Figure 6.3-17 Yield stress values measured at the end of the flume test ($t=65$ minutes) at surface of the deposit and at 0, 2.5 and 5.2m from deposition point.

Figure 6.3-18 shows that despite local variation in the mixing energy a more or less consistent mixing energy was applied during both tests. The mixing energy density per swept static mixer (as defined by Demoz, 2012) was calculated using Equation 6.3-1.

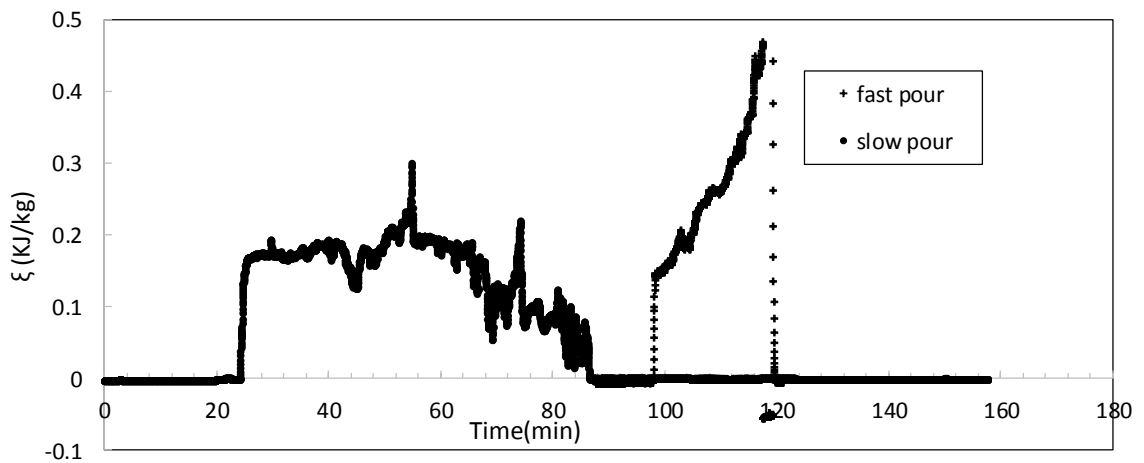


Figure 6.3-18 Mixing energy density of static mixers for fast and slow pour

While there exist some variability in the mixing energy, based on the yield stress results and observation based on trial, the pour quality appears to be more or less consistence. The pressure drop observed during the slow pour could be due an increase in the cross sectional area of the line (i.e constrictions due to deposits are cleared and plugging debris is removed).

6.4 Discussion on flume test results

The final profile of the faster deposition (36 L/ min) test can be fitted with lubrication theory based equation (Henriquez and Simms, 2009; Mizani and Simms, 2013a,b) for resting profiles of a Bingham fluid, using a yield stress value of 60Pa. This value is very close to the lower value of yield from the Hewitt interpretation of the rheology.

By contrast, the final profile of the slower deposition test cannot be fitted with a simple 1D LT equation. However, the progression of the geometry during this test is of interest to both those working in thixotropic fluids in general, and in surface deposition of tailings. Up until 45 minutes, the transient profiles evolve as observed in the shorter duration tests. However, at this point, tailings no longer accumulate on the upper part of the slope, but rather flow down to near the toe. Indeed, height somewhat decreases on the upper part of the slope due to consolidation. The 45 minute profile itself can be fitted with the LT equation, but with the yield stress value for an initially structured material (400 Pa). This suggests that at least part of the tailings near the bottom of the flume have come to a state equivalent to an initially fully structured state at rest.

This is important with respect to the ability of current modelling technique to represent surface deposition processes. For example, Hewitt and Balmforth, (2013) employ a rapid

transit simplification of viscosity bifurcation theory into modelling thixotropic fluids. However, the rapid transit theory allows for progression from a initially fully structured state, to a fully sheared state, and back to a new rest state, the latter defined by the lower yield stress (60 Pa), but not to the initial yield stress (Mizani and Simms 2016b).

A final note of interest is the formation of channel flow observed at about 45 minutes, seen in Figure 6.3-16. This type of behaviour is regularly seen in most dewatered tailings deposits (Mizani et al. 2013a). The channel flow mechanism persisted until the end of deposition and appears to have conveyed the bulk of the tailings to the toe-end of the deposit between 45 minutes and 62 minutes.

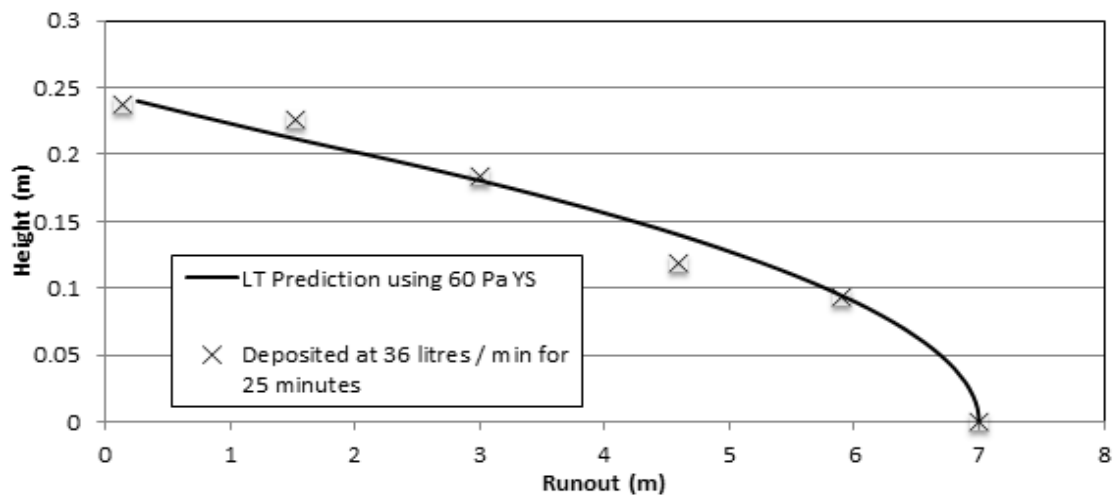


Figure 6.4-1 Flume deposition of 850gr/tonne tailings in a long flume (0.65 m wide) at 36 L/ min, fitted using 1D lubrication theory, yield stress of 60 Pa.

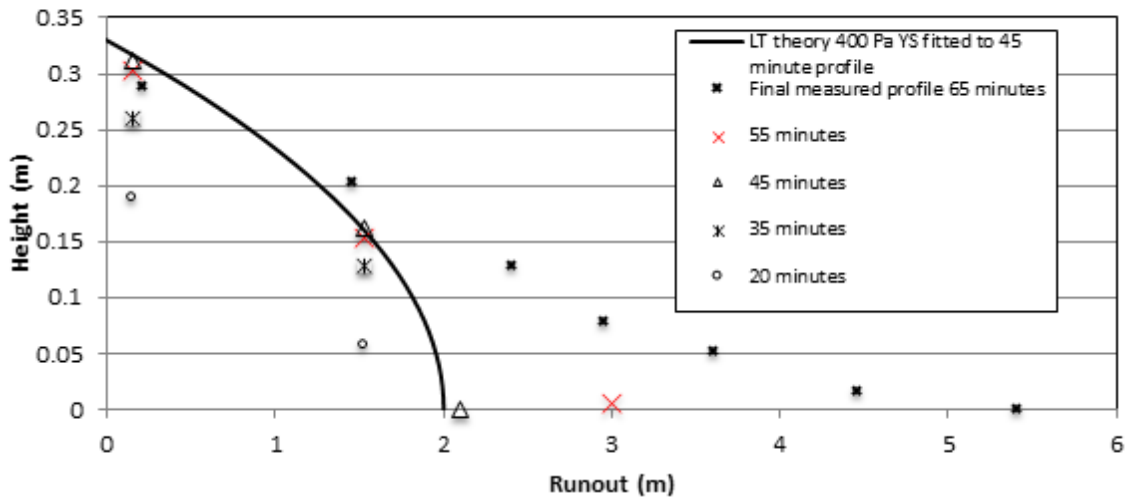


Figure 6.4-2 Flume deposition of 850 g/tonne tailings in a long flume (0.65 m wide) at 10 L/ min, the 45 minute profile fitted with 1D lubrication theory using yield stress of 400 Pa.

This is also the type of progression often observed during large scale depositions (Williams and Meynink, 1986; Fitton, 2007) in the field. It is of interest to define the slope when the flow changes from spreading to channel flow (in this case around 10.9%), as this point was identified as the limitation of the LT approach (by Simms et al. 2011), It is also believed that this point can be used by engineer as the point at which flow becomes less manageable, with respect to controlling every lift thickness. This type of behavior is often blamed for the uncontrolled part of tailings deposition making the control of deposit rather difficult.

7 Chapter: Numerical Simulation of Tailings Flow

7.1 ANSYS

In this work simulations were carried out using an available commercial computational fluid dynamics (CFD) software ANSYS CFX. CFD simulations have become very popular among researches for modelling the free-surface flow like dam-break flow and solitary waves. ANSYS CFX is a finite volume based method where the free surface is tracked using the VOF (Volume of Fluids) method.

7.1.1 Basic definitions

i) Volume fraction

The volume of fraction of the i^{th} phase denoted by α_i , represents the fraction of the cell occupied by that phase. The sum of the volume fractions in each cell is unity. In CFX volume fractions are defined as the volume of phase i over the total volume of the cell as illustrated in Figure 7.1-1:

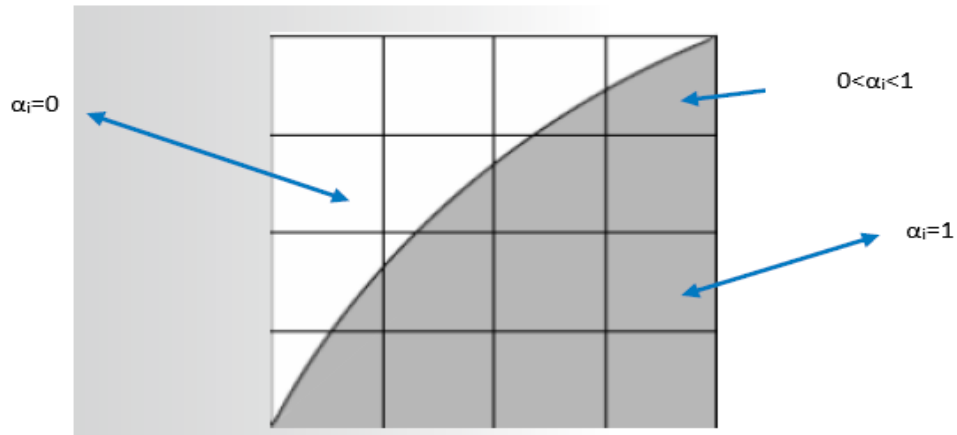


Figure 7.1-1 Volume of Fluid for an arc over a structured grid (ANSYS CFX 2015 Multiphase flow workshop).

ii) Phase Velocity

In case of two phase flow, where the cell is partially occupied by both phases the velocity of each phase is formulated as follow:

$$u_i = \frac{\dot{m}_i}{\rho_i A_i} \quad u_i = \frac{\dot{m}_i}{\alpha_i \rho_i A} \quad 7.1-1$$

$$\sum \alpha_i = 1 \quad 7.1-2$$

The superficial velocity for each phase is defined as if the phase of interest is the only flowing phase through the cross section:

$$(u_s)_i = \alpha_i u_i \quad 7.1-3$$

iii) Buoyancy

In case of multiphase flows involving gas-liquid flows (such as in our case), buoyancy plays an important role thus in buoyancy calculation a source term is added to the momentum equations as follow (ANSYS CFX 2015 Multiphase flow workshop):

$$S=(\rho-\rho_{ref})g \quad 7.1-4$$

$$P'=p-\rho_{ref}g(r-r_{ref}) \quad 7.1-5$$

Where,

ρ_{ref} is the buoyancy reference density (for free surface flows it is the density of the lightest fluid),

r_{ref} is reference location and

P' is the modified pressure (is the pressure field minus hydrostatic head due to ρ_{ref}).

Modelling of the multiphase flow can be very complex, thus depending on the available information or the required level of accuracy different approaches can be used in CFX (Stenmark, 2013; ANSYS CFX Theory Guide, 2015): the Euler-Lagrange approach and the Euler-Euler approach.

7.1.2 Euler-Lagrangian

In this approach the particles are tracked using Lagrangian description while an Eulerian description is used for the fluid (ANSYS CFX, 2015). Particles may represent a solid particle or gas bubbles or fluid droplets. The conservation equations are solved for the continuous media and the following equations for the particle phase:

$$\frac{\partial \alpha_f \rho_f}{\partial t} + \nabla \cdot (\alpha_f \rho_f \mathbf{u}_f) = S_{mass} \quad 7.1-6$$

$$\frac{\partial \alpha_f \rho_f}{\partial t} + \nabla \cdot [\alpha_f \rho_f (\mathbf{u}_f \mathbf{u}_f)] = \alpha_f \nabla P - \alpha_f \nabla \cdot \boldsymbol{\tau} + \alpha_f \rho_f \mathbf{g} - S_p = 0 \quad 7.1-7$$

$$\frac{\partial \mathbf{u}_p}{\partial t} = \sum F \quad 7.1-8$$

Where α is volume fraction and S_{mass} and S_p source term in case of mass and momentum exchange between the two phases. Above, F stands for force and f and p refer to fluid and particle respectively. Generally the coupling between the different phases happens through the source term. Location of each particle is determined by integrating the last equation. Since the equations are solved for each particle in this approach, it can become computationally expensive. This approach is thus more suitable for dilute dispersed flows.

7.1.3 Euler-Euler

In this method, which is mainly used for separated flows, the phases are modeled as a continuous phase. This approach can be also used for dense flow or when the overall motion of the particles are of interest.

In this approach one set of conservation equations is solved for each phase while coupling between different phases is done through the shared pressure. Moreover, a set of transport equation must be solved for each phase as shown below:

$$\frac{\partial \alpha_i \rho_i}{\partial t} + \nabla \cdot (\alpha_i \rho_i U_i) = 0 \quad 7.1-9$$

$$\frac{\partial \alpha_i \rho_i U_i}{\partial t} + \nabla \cdot [\alpha_i \rho_i (U_i U_i)] = -\alpha_i \nabla P - \alpha_i \nabla \cdot \tau_i + \alpha_i \rho_i g_i + S_i = 0 \quad 7.1-10$$

$$\frac{\partial \alpha_i}{\partial t} + \nabla \cdot (\alpha_i U_i) = 0 \quad 7.1-11$$

Here i refers to i^{th} phase and U is the mean velocity field.

7.1.4 Volume of Fluid

Volume of fluids is an (Euler-Euler) based method where the various phases are not allowed to interpenetrate. Also, in this method each phase is treated as a continuous fluid; where the fluid forms a continuous connected region (ANSYS CFX, 2015). In this method the ratio of the volume of the heavier phase to the total volume of the cell is defined as the volume fraction. In case of two phase flow, the cells containing both phases (interface), volume fraction will have a value between 0 and 1.

Volume of fraction (VOF) has been used for several decades and it will be used in this study for two reasons: i) preservation of mass, and ii) and relatively simple process of extending from 2D to 3D domains. Also, these algorithms can be applied in parallel, since only the neighboring values are required to update any cell. Moreover, using VOF method the cost of modelling may be significantly reduced since in each cell the volume of fraction of each phase will be tracked rather than individual particle (Yang, 2009). In other words, the total mass of each phase (summation of all particles in each cell), will be treated as a new variable, in each control volume (Figure 7.1-2) and thus eliminates the use of several

points to define a region of a fluid. In summary, using the VOF method the amount of stored information is minimized and therefore can be used as an economical technique to track free surfaces (Hirt and Nicholas, 1981).

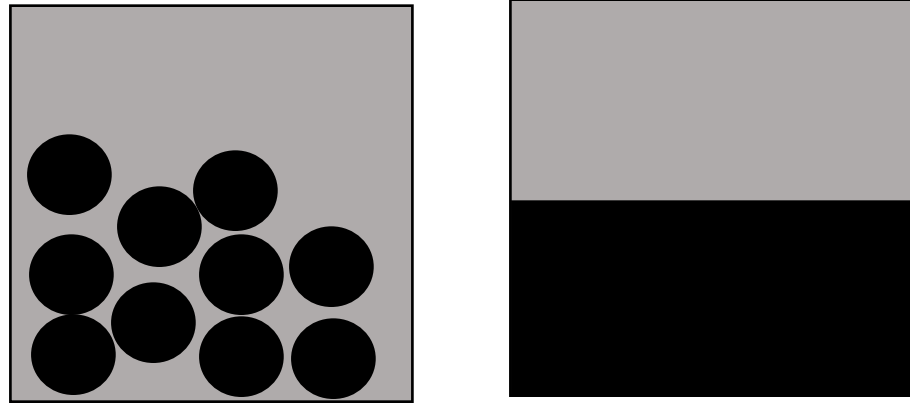


Figure 7.1-2 Schematic illustration of volume fraction for two phase flow.

The equations solved for the VOF method are as follow:

$$\frac{\partial \rho_m}{\partial t} + \nabla \cdot (\rho_m U) = 0 \quad 7.1-12$$

$$\frac{\partial \rho_m U}{\partial t} + \nabla \cdot [\rho_m (U \otimes U)] = -\nabla P + \nabla \tau + \rho_m g + S = 0 \quad 7.1-13$$

$$\frac{\partial \alpha}{\partial t} + \nabla \cdot (\alpha U) = 0 \quad 7.1-14$$

Where S is the source term, U is the velocity vector and viscosity (η) and density (ρ) correspond to the average value in the control volume and are calculated through:

$$\rho_m = \sum_{i=1, N} (\alpha_i \rho_i) \quad 7.1-15$$

$$\eta_m = \sum_{i=1,N} (\alpha_i \eta_i)$$

7.1-16

Subscript m represents the mixture and, i represents each phase and N is the total number of phases.

The VOF can be implemented in two modes in CFX: segregated Vs Coupled. In the segregated mode the velocity and pressure equations are computed in a couple manner and then the continuity equation for volume fractions is solved. When the coupled setup is used the solver implicitly couples the velocity, pressure and volume fraction equations (ANSYS CFX users guide, 2015).

7.2 Coupled Versus Segregated Solvers

Discrete forms of the Equations 7.1-12 and 7.1-13 show the strong correlation between pressure and velocity. This causes some challenge for CFD codes as the velocity obtained from the momentum equations (by knowing the pressures) should also satisfy the continuity equations. There are two different ways to deal with this issue: segregated solver and coupled solver. In the first method, velocity field is solved using an assumed pressure field. The new values are then checked to see if the assumed velocity field satisfies the continuity equations. If not, the pressure field will be corrected and this procedure is repeated until both momentum and continuity equations are satisfied. In coupled solver, on the contrary, the momentum and continuity equations are solved simultaneously. In this case more memory is required to store the data however, in return fewer iterations are required for convergence compared to the segregated solver (ANSYS Theory Guide, 2014).

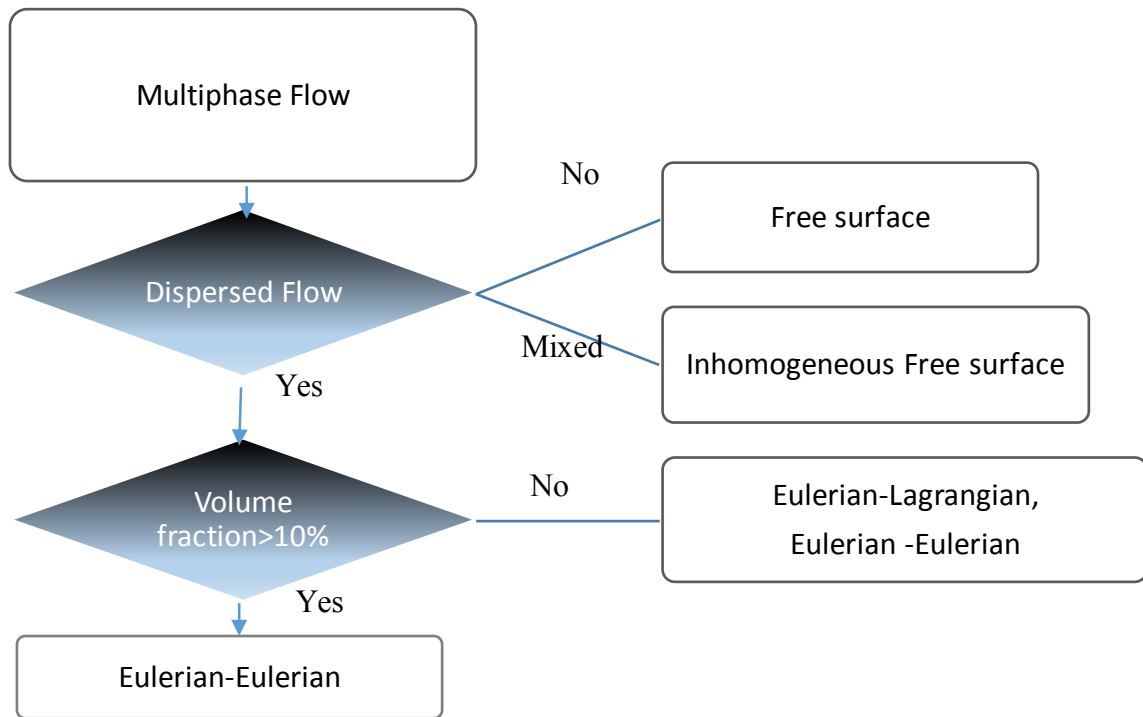
7.3 Advection and Transient Scheme

Commercial code CFX uses a coupled solver to resolve velocity and pressure field. The second order Backward Euler was used as the temporal discretization algorithm for the transient term (momentum equation). The second order Backward Euler scheme is an implicit, second order accurate which may be used for both constant and variable time step sizes (ANSYS CFX Modelling guide 2015).

The high resolution scheme was realized as the special discretization of the advection terms, which uses a blending factor depending on local variable gradient.

7.4 Free Surface Flow

Free surface flow is often used as a direct method for prediction of interface shape between immiscible (non penetrating) phases. In this method the interface is tracked through solving the phasic continuity equations. The homogeneous model (Eulerian-Eulerian based method where all fluids share the same velocity field except for volume fractions) with free surface model was used in all simulation. This is also known as the volume of fluids (VOF) model. The multiphase models were chosen based on the following flow chart as recommended in CFX handbook:



In the volume of fluid (VOF) method, originally developed by Hirt and Nicolas (1981), a scalar field (α) is introduced to quantify the volume fractions of a fluid in each cell. In cells located in interface the α value may vary anywhere between 0 and 1, where it jumps from 0 to 1 at the interface of the two fluids. Advecting this discontinuous function and tracking the position of the interface is challenging (Darwish and Moukalled, 2006). Moreover, it is essential to keep the sharpness of the interface; thus, in order to reduce the smearing at the interface the transient and spatial discretization has to be done accurately.

Advection schemes for Eulerian meshes are often categorized in two groups in literature: interface-tracking or interface capturing methods. In the first method the position of the free surface is recorded i.e using markers (Chen et al. 1997) or through deformation of grid (Welch, 1995). This technique is often associated with higher

computational cost with the advection scheme highly dependent on the reconstruction of the interface. Using the second method, interface capturing method, a compressive scheme is used to minimize smearing of the interface often with the aid of a coefficient, which vary spatially based on the direction of the flow.

ANSYS CFX relies on interface capturing approach for VOF (ANSYS CFX 2015 Multiphase flow workshop) to keep interface sharp. For this purpose a compressive discretization scheme is used in both time and space (advection of volume fractions). In this method the fluid is lumped near the interface using a downwind interpolation.

7.4.1 Volume of fluid with interface compression

In case of two phase flow (air and tailing) the density and viscosity may be formulated as:

$$\mu = \mu_{tailings}\alpha + \mu_{air}(1 - \alpha)$$

$$\rho = \rho_{tailings}\alpha + \rho_{air}(1 - \alpha) \tag{7.4-1}$$

The following presents the volume fraction transport equation with compression term:

$$\frac{\partial \alpha}{\partial t} + \nabla \cdot (\alpha U) + \nabla \cdot (u_c \alpha (1 - \alpha)) = 0, 0 \leq \alpha \leq 1 \tag{7.4-2}$$

Interface smearing is minimized through the introduction of u_c (artificial velocity), which reduces interface smearing (Lee and Rhee, 2015). The $\alpha(1-\alpha)$ term ensures that the artificial velocity is only active near the interface, and it thus does not affect the solution outside this region (Rusche, 2002). The interface sharpness is controlled through the interface compression level in CFX where it was set to 2 (default value) to help improve interface sharpness.

7.5 Methodology

A set of 2-D and 3-D simulations were conducted to investigate the flow behaviour of flocculated MFT using the Eulerian-Eulerian based method (corresponding to VOF) model on a fixed mesh. First, 2D simulation were conducted using the simplest way to implement flows (using a dam break initial conditions) as shown in Figure 7.5-1 using various rheological models (i.e Bingham, Coussot,). Figure 7.5-1 shows the initial condition of the simulations, where x and y define the arbitrary initial position of the tailings . In general, CFX 2-D simulations are computationally less expensive compared to 3D simulations and can be performed in a more timely manner.

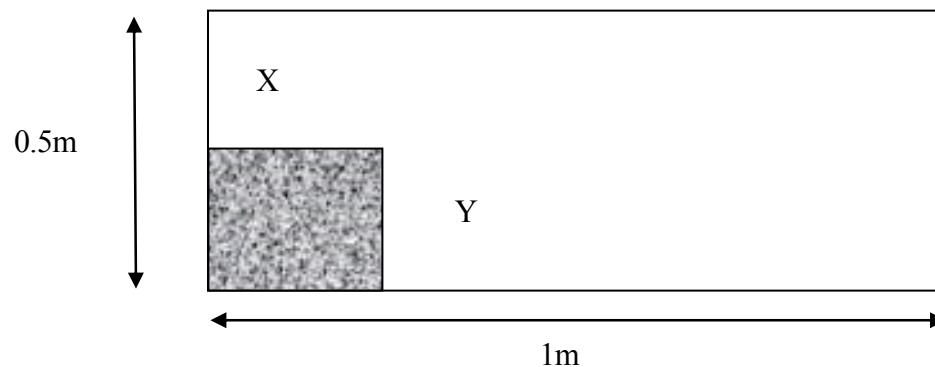


Figure 7.5-1 Schematic of initial position of tailings for 2D simulations.

In this setup, tailings are stored behind a barrier of various height (variable y). With the initiation of the flow, the paste will flow, due to gravity, and stop once the equilibrium condition is reached. Flow stoppage was confirmed by comparing the profile at various times and checking the velocities at the toe (Gao and Fourie, 2014).

In the first step, the effects of various terms such as potential energy, volume and yield stress on the final beach profile were investigated:

7.5.1 Boundary Conditions

The domain and the meshes were created using ANSYS CFX. The three sides were modelled using a wall with no slip boundary conditions while the top was modelled as entrainment with relative pressure set to zero. This boundary condition maintains atmospheric pressure at the top where air may enter or be forced out of the model domain. The tracking of interface is accomplished by solution of phasic continuity equations.

7.5.2 Computational Setup

CFX uses a finite volume method via the coupled solver to solve the Navier-Stokes equations. The equations solved for the VOF method are as follow:

$$\nabla \cdot (\rho U) = 0 \tag{7.5-1}$$

$$\nabla \cdot (\rho U \otimes U) = -\nabla p + \nabla \cdot \tau \tag{7.5-2}$$

$$\tau = \eta(\nabla U + (\nabla U)^T - \frac{2}{3} \delta \nabla \cdot U) \tag{7.5-3}$$

Where,

U is the velocity vector,

ρ is density,

P is the pressure and

τ is the viscous stress tensor

δ is unity tensor (dimensionless)

The stress tensor for an incompressible Newtonian fluid with a shear dependent viscosity is defined as follow:

$$\tau = 2\eta(D_{II})D \quad 7.5-4$$

$$D = \frac{1}{2}[\nabla U + (\nabla U)^T] \quad 7.5-5$$

D is the strain tensor, with 3 scalar invariant. The second invariant is called shear strain rate and is defined as $D_{II} = -1/2trD^2$.

For Non-Newtonian fluids, viscosity is expressed as a function of this scalar strain rate (Ansys Theory Guide, 2014).

7.5.3 Bingham Model

The Bingham model (a Non-Newtonian model used for describing the behaviour of viscoplastic fluid) was used in these simulations to describe the material rheological properties where:

$$\mu = \frac{\tau_y}{\dot{\gamma}} + K \quad 7.5-6$$

For the range of yield stress values used in this study it was found that a minimum value of $1*10^{-3}$ (s⁻¹) for the strain rate was small enough to reproduce the flow behaviour of ideal Bingham fluid and at the same time avoid numerical instabilities. Although this model only supports a single-value yield stress, values that vary over time or iterations can be defined in simulation using the CEL (cfx expression language) expressions.

7.5.4 2D Simulation using Thixotropic Models

Rheological measurement presented in chapter 4 illustrates the thixotropic nature of flocculated MFT. Thus a set of simulation were conducted to investigate the effects of

various rheological models on the final shape of deposits using similar setup as explained in previous section.

Thixotropic fluids may be modelled in CFX using two equations: one relating the evolution of the structure term (λ) to ageing and shear flow and the second equation flow to the structure term or the viscosity function.

$$\frac{d\lambda}{dt} = f(\lambda, \dot{\gamma}) = \frac{1-x\lambda}{T} - \alpha \dot{\gamma}^m \lambda \quad 7.5-7$$

Where T is the characteristic time of ageing, μ is viscosity at infinite shearing. X here relates the ageing term to structure term. Coussot et al. (2002) model uses the following relation to relate viscosity to structure.

$$x = 0, m = 1, \mu = \mu_0(1 + \lambda^n) \quad 7.5-8$$

Assuming that the flow reaches steady state in each time step we have

$$\frac{d\lambda}{dt} = f(\lambda, \dot{\gamma}) = 0 \quad 7.5-9$$

$$\lambda_{eq} = \frac{1}{\alpha T \dot{\gamma}} \quad 7.5-10$$

A numerical approximation was required in the shear free regions where the viscosity term becomes infinite. There are currently different models to avoid this problem i.e biviscosity model by O'Donovan and Tanner, (1984) or by introducing a penalty like factor to the shear rate as in the model as developed by Bercovier and Engleman, (1980). Papanastasiou, (1987) introduced a correction factor to avoid the problem of tracking surface between yielded and unyielded region in case of a Bingham fluid. The idea of Papanastasiou, (1987) was used in this study to bound the viscosity and overcome this problem the Coussot model may be expressed as (Couerbe et al. 2008):

$$\tau = 2\left(\mu_0 + \frac{\mu_0(1 - \exp(-M \dot{\gamma}^n))}{(\alpha T \dot{\gamma})^n}\right)D \quad 7.5-11$$

Couerbe et al. (2008), using a shear thinning thixotropy fluid, showed that for $M > 500s^n$ results were independent of the values assigned to M.

In case of the modified Coussot model, where the original model is modified with a maximum value of structure, and the rate of aging is proportional to difference between the current structure value and the maximum value, the structural term at steady state may be obtained through:

$$\frac{d\lambda}{dt} = \frac{(1 - \lambda)}{T} - \alpha\lambda\dot{\gamma} \quad 7.5-12$$

$$\lambda_{eq} = \frac{1}{\alpha T \dot{\gamma} + 1} \quad 7.5-13$$

Hewitt and Balmforth 2013, defined viscosity as a function of structure in the following form:

$$\mu = \frac{\mu_0}{(1 - \lambda)(1 - \beta\lambda)} \quad 7.5-14$$

Thus the stress term may obtained:

$$\tau = 2 \left(\frac{\mu_0}{\left(1 - \frac{1}{1 + T\alpha\dot{\gamma}}\right) \left(1 - \frac{\beta}{1 + T\alpha\dot{\gamma}}\right)} \right) D \quad 7.5-15$$

$d\lambda/dt$ will now become zero at two different points:

$$\lambda_{1,2} = \frac{1}{2\beta} \left[1 \pm \left(1 - \frac{4\beta\mu_0}{\alpha T \tau}\right)^{1/2} \right] \quad 7.5-16$$

For stress level in between τ_{aH} and τ_{cH} the behavior of the material is dependent on the shear history of the material (Hewitt, 2012). While λ_2 corresponds to an unstable equilibrium, the choice between $\lambda=1$ and λ_1 is function of shear history of the material as explained in chapter 4.

7.5.5 2D Simulation Results

7.5.5.1 Comparison with an analytical solution

First the capability of the numerical model for transient simulations was examined. This was done by comparing numerical results from a dam break in a 0.5m long channel (involving a Bingham fluid) with analytical solutions derived from lubrication theory, as per Henriquez and Simms (2009); Mizani et al. (2013a) and Balmforth et al. (2007). It should be noted that the analytical solution from lubrication theory and that of Balmforth et al. 2007 coincide and thus appear as one curve in this figure. As one lowers the initial height, inertia effects become less important and thus a better agreement with the theoretical values could be obtained. Figure 7.5-3 presents the comparison between numerical and analytical solution by Balmforth et al. (2007) for a Bingham number of 0.1.

This confirms the capability of the numerical model in capturing the front wave propagation.

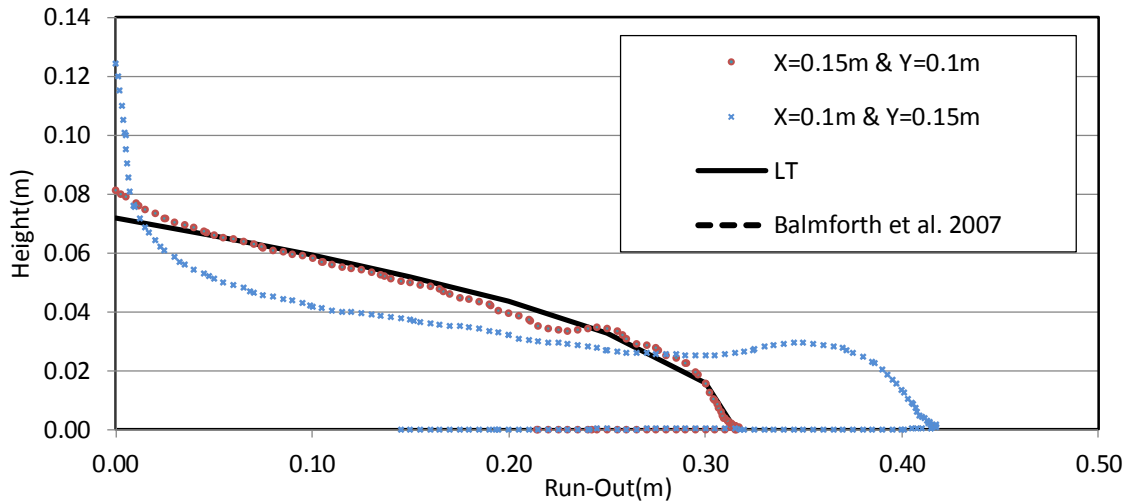


Figure 7.5-2 2D simulation: Effect of height of initial configuration on shape of final profile for a 100 Pa yield stress material.

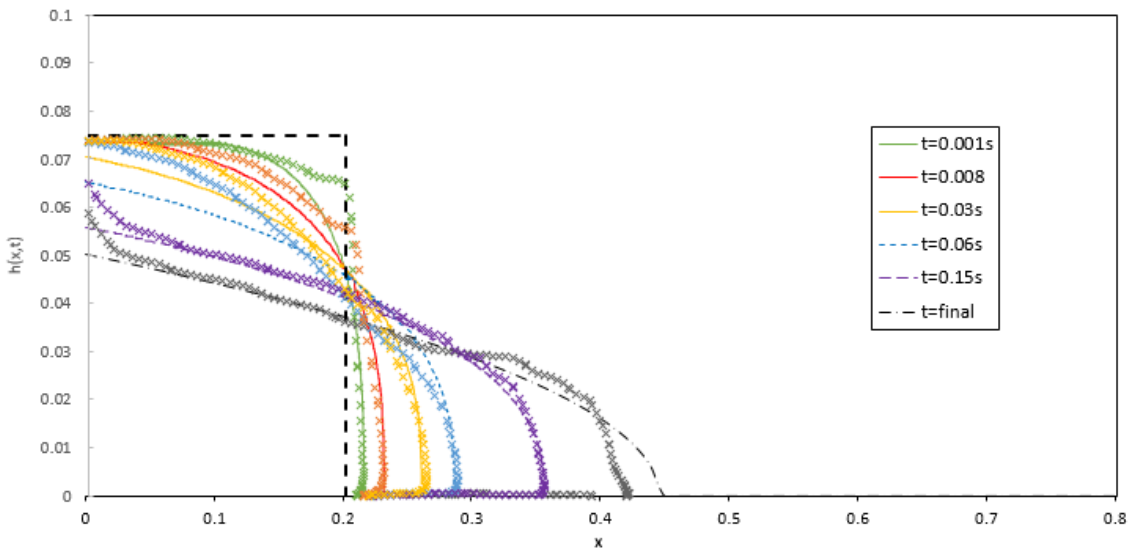


Figure 7.5-3 Comparison between simulated and 2D analytical solution of Balmforth et al. 2007 using a Bingham number of 0.1. Here lines show the results for analytical solution and dots are obtained from numerical simulation.

Figure 7.5-4 summarizes the run-out and slope at various yield stresses for the same volume of tailings. As expected the runout decreases and slopes increase with an increase in the yield stress of the material.

Also presented in this figure are the analytical solution of Balmforth et al. (2007) for dam break flows on horizontal surface. The discrepancies between the complete numerical solutions and Balmforth et al. (2007) are due to the shallow water approximation and small aspect ratio assumption ($H/L \ll 1$) in the theory. These assumptions are not reasonable at the beginning of the flow (in initial stages where the flow is dominated by inertial effects) and result in errors that propagate. Moreover, inclusion of the vertical velocities and all stress components results in an increased shearing (thinning) of the material.

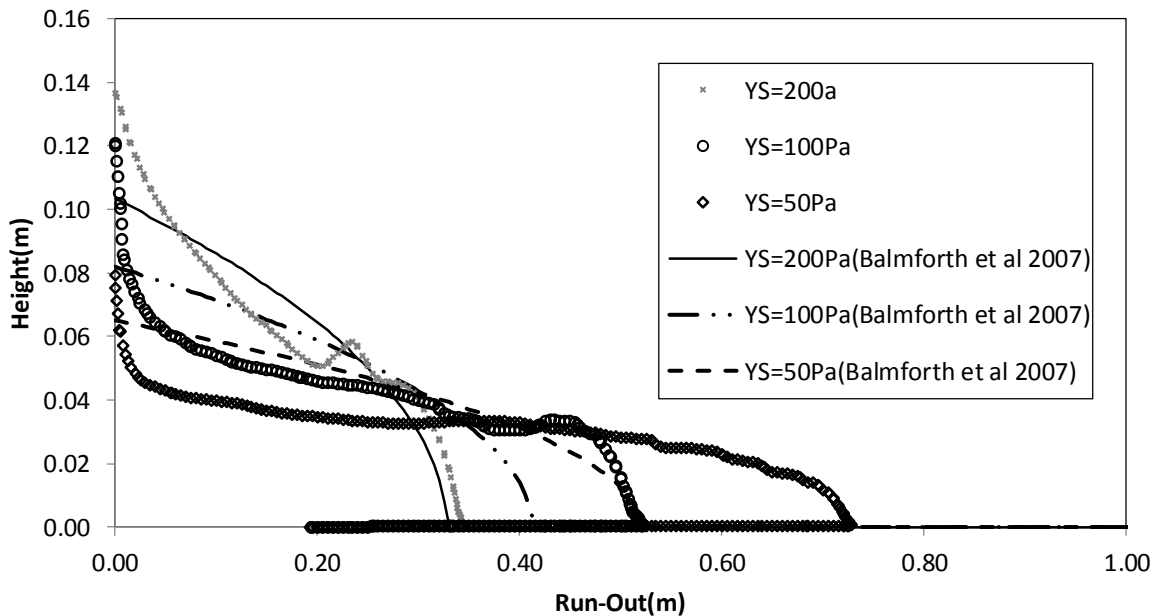


Figure 7.5-4 2D simulation: Effect of yield stress on shape of final profile of flocculated MFT at a viscosity of 0.5Pa.s where x and y=0.15m.

In all cases (Figure 7.5-2 and Figure 7.5-4) it can be observed that while the shape of the flow near the toe shows an increasing slope, the shape of the profile near the deposition point shows a decreasing slope from left to right. The former is the same as would be generated by predictions using lubrication theory (Mizani et al. 2013a; Henriquez and Simms 2009), and is similar to what is seen in low-inertia flume tests. The latter conforms more closely to the shape of mature field deposits close to the deposition point.

In all these cases, inertia was produced by the potential energy of a high initial deposit rather than by the pour flow rate. In the next section the final profiles obtained from using flow boundary conditions (inlet) will be presented and compared with values from flume tests.

7.5.5.2 2D Simulation Results of various Thixotropy Models

Figure 7.5-5 presents the final profile of a 3s simulation using various thixotropy models for the tailings. In these simulations tailings were released from a barrier of 15cm height and 15cm wide. Results obtained using the Bingham model and the analytical solution of Balmforth et al. (2007), are also illustrated on the same graph for the purpose of comparison.

Simulations were conducted using the values obtained through fitting the rheology of flocculated MFT at (dosage of 850g/tonne) to different thixotropy models as explained in chapter 4. For the Coussot model the best fit was obtained using the following values $T=0.01$, $\alpha=0.36$, $\mu_0=1$ Pa.s and $n=1.075$, while for Hewitt model the following values were used for each term in the model: $T=10$, $\alpha=0.01275$, $\beta=0.97$ and $\mu_0=1.5$.

Figure 7.5-5 shows a non slumping behavior when the Coussot model is used. The main discrepancy between the Coussot model and Hewitt is that in the Hewitt model the structure term (λ) may be selected such that the stress history of the tailings is taken into account (in this case λ_1 was used); however, when the Coussot model is used the material only flows once the critical shear stress is exceeded. It could thus be concluded that the Hewitt model could be used as a better representative of the behavior of tailings as they flow out of the pipe (taking into account the shear history)

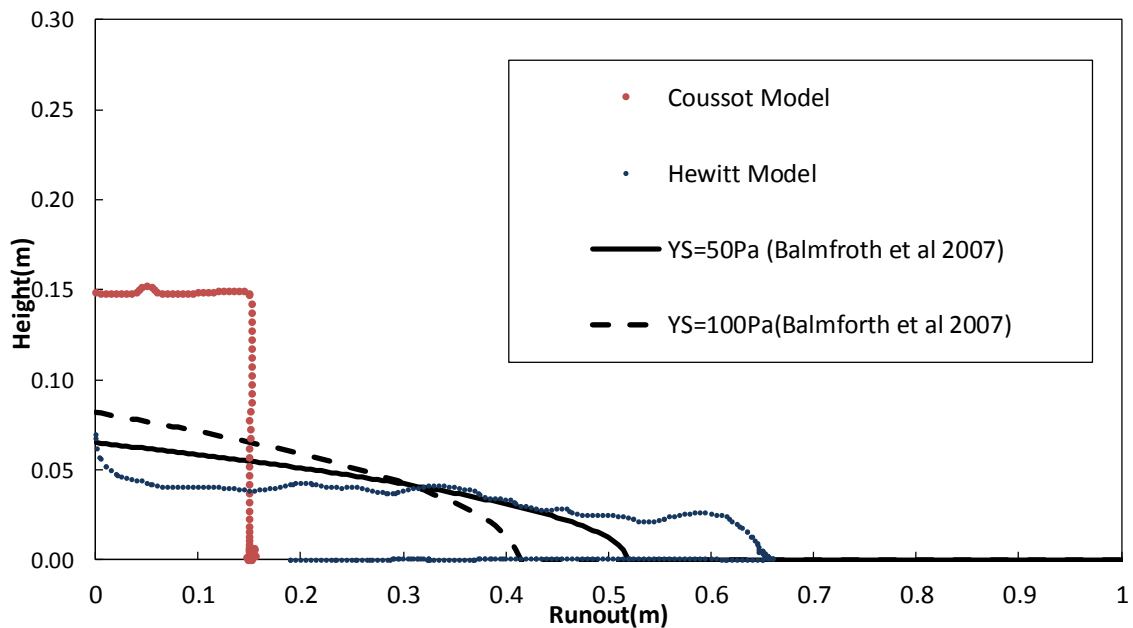


Figure 7.5-5 2D simulation: Effect of various rheological models on shape of final profile for dam break problem (0.15m by 0.15m).

Figure 7.5-6 shows the influence of initial height of tailings mass and variations in ageing and shearing terms at a constant volume. Increasing the height increased the run-out, while reduction in height resulted in non-slumping behaviour. The final profiles significantly changed when different values were used for T , β and α terms in the

thixotropic model, corresponding to different values of $\dot{\gamma}_c$. Figure 7.5-7 illustrates the effects of variation in ageing and shearing term on the final profile. Again, the material illustrated nonslumping behavior when a higher values were used for the ageing term or a lower values for the shearing term.

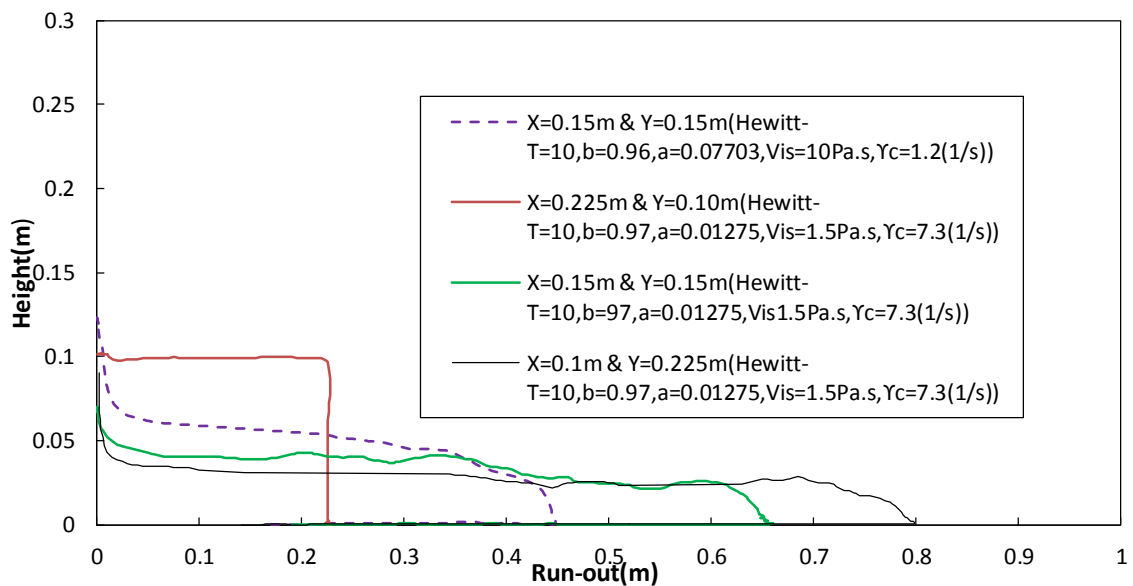


Figure 7.5-6 2D simulation: Effect of initial geometry and $\dot{\gamma}_c$ on shape of final profile using the Hewitt model.

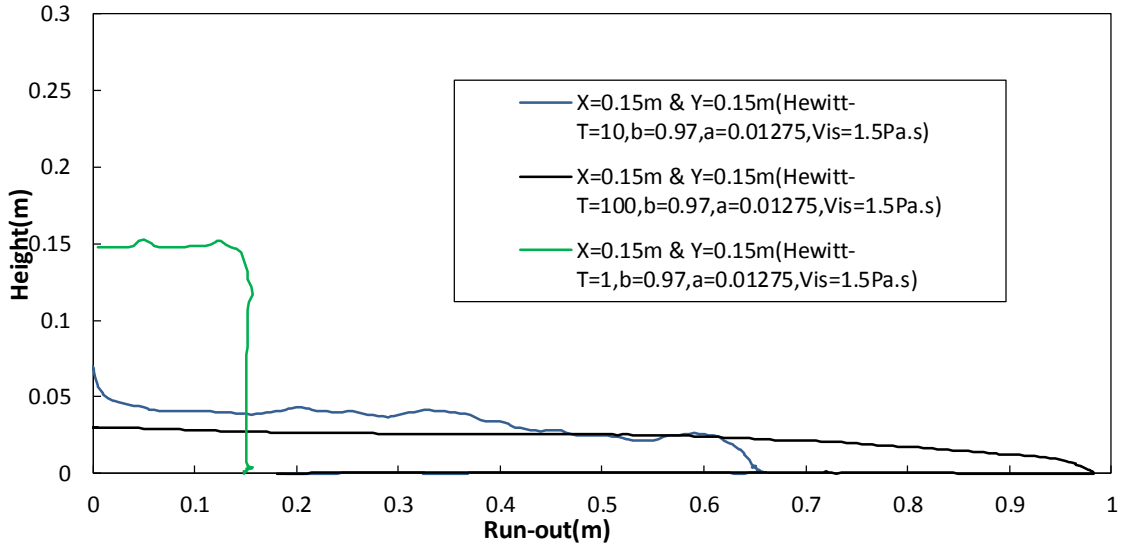


Figure 7.5-7 2D simulation: Effect ageing term on shape of final profile using the Hewitt Model.

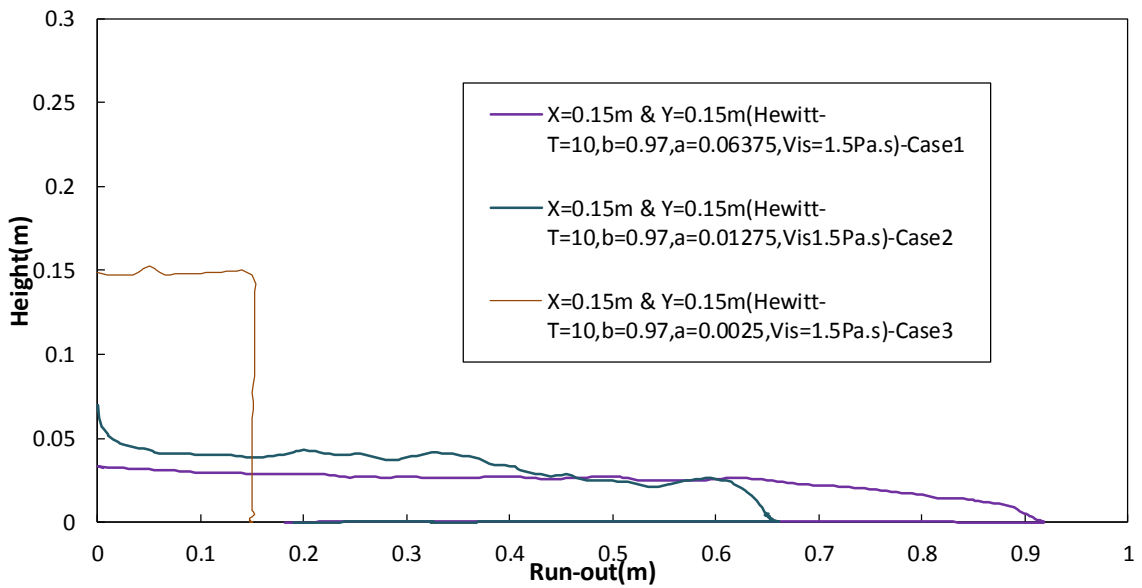
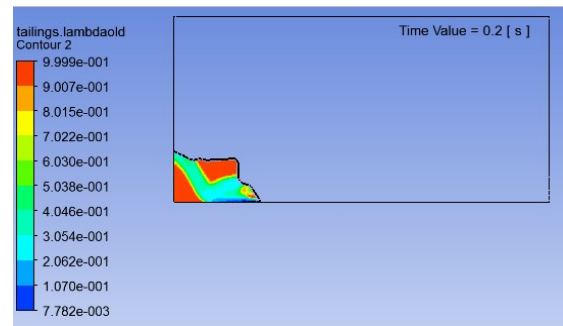
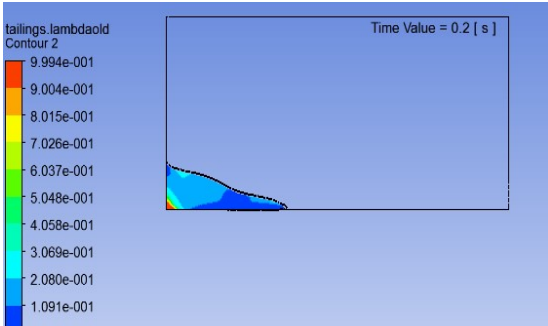
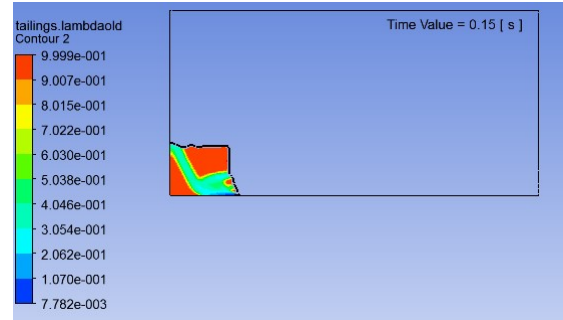
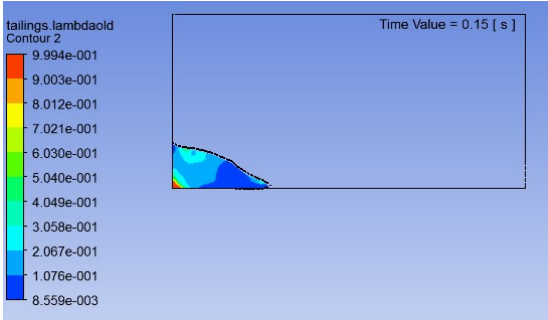
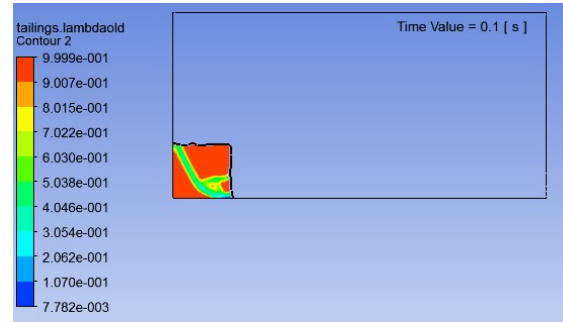
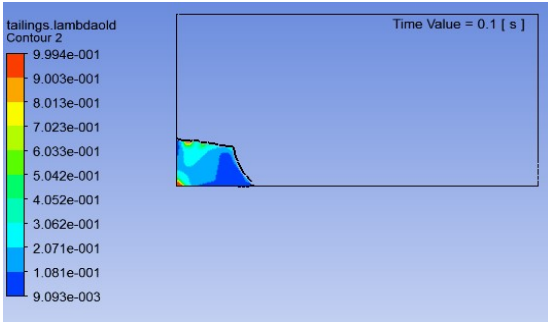
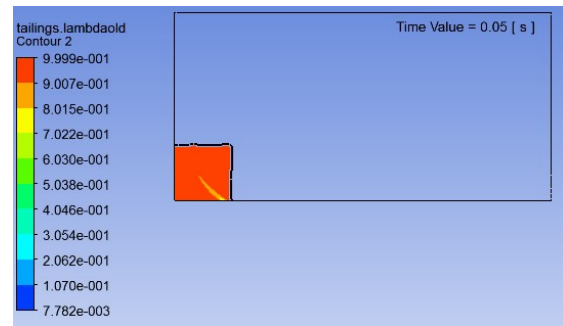
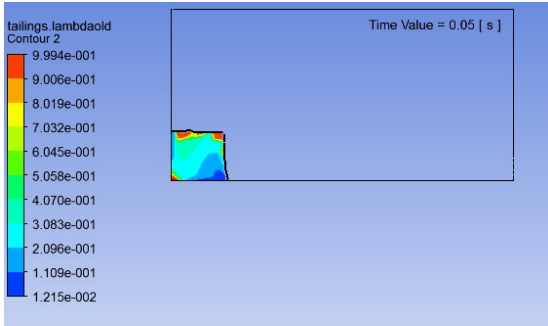


Figure 7.5-8 2D simulation: Effect shearing term on shape of final profile using the Hewitt Model.

The following figure illustrates the spatial variation of the structure term for cases 1(left) and 2(right) presented in the last figure at various times.

Case#1

Case#2



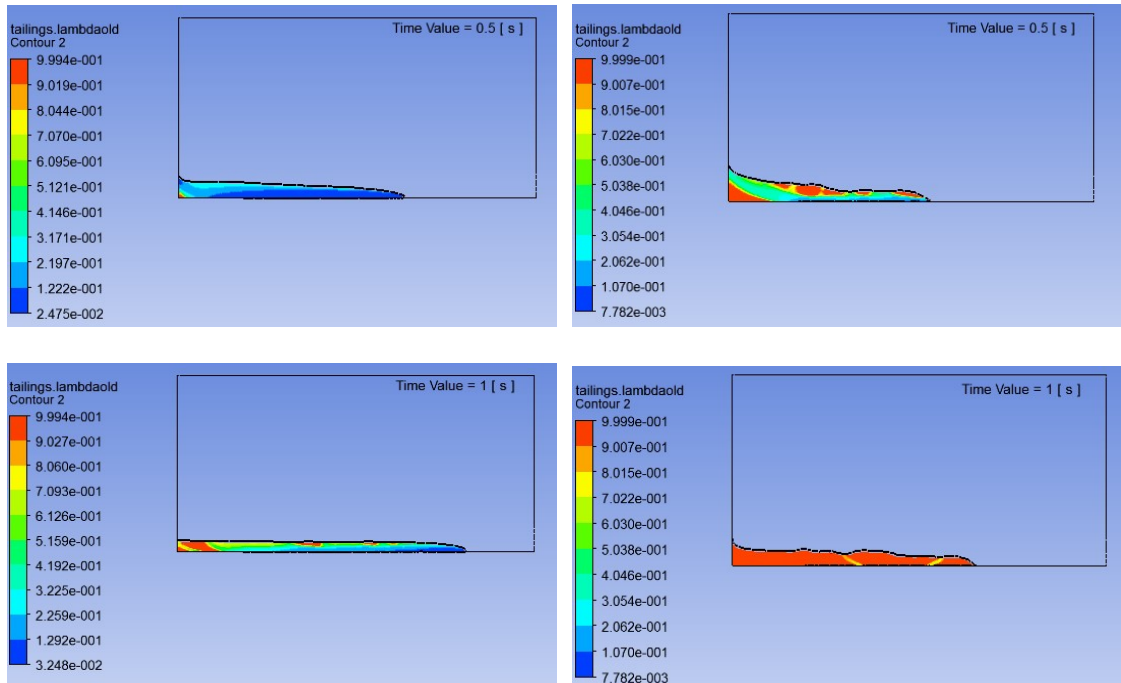


Figure 7.5-9 Variation of structure term with space for case#1 and 2 presented in Figure 7.5-8.

7.6 CFD Simulation of Flume Test on Flocculated MFT

In this section an attempt will be made to model the flume test presented in Chapter 7.

The summary of the test result is presented in Table 7.6-1 as per section 6.2.

Table 7.6-1 Summary of Flume Tests

Test No	Floc dosage (g/ton)	Total Mass(kg)	Time(s)	Flow (Kg/s)	Deposition method
1	650	5.711	104	0.055	Funnel
2	725				Funnel
3	850	5.807	221	0.026	Funnel
4	1000	5.879	323	0.018	Funnel
5	850	829	3720	0.22	Static Mixers and Pump
6	850	966	1277	0.75	Static Mixers and Pump

7.6.1 Model Set-Up (Bench scale)

3D simulations of flume tests were conducted using a block domain 1.5 m long, 0.15 m wide, and 0.30 m high. A total of 5.8 kg of tailings were deposited through a circular inlet located 15 cm above the bottom of the flume (similar to the experimental set up in Figure 6.2-2), where tailings were deposited through a funnel.

For these sets of tests, the Free Surface Model, an Eulerian based method, was applied in CFX, through which the interface between tailings and air was tracked. The two phase used in these simulations were air at temperature of 25C⁰ and tailings with an assigned density of 1250kg/m³, constant viscosity of 0.5Pa.s and Bingham rheological model was adapted. Yield stress values were chosen such that the best fit with experimental data were obtained. In addition, the interface between tailings and air were identified with isosurface where volume fraction of tailings was 0.5. The profiles at the end of the simulation were recorded at the centerline of the flume.

Both geometry and meshing were created using the CFX package. Several meshes were examined to investigate the mesh convergence, where the number of nodes were gradually

increased. Figure 7.6-1 illustrates an example of the mesh used. All meshes used in the simulation were inflated towards the bottom to adequately capture the changes in velocity profile in this region.

Flocculated MFT is pumped through the 2.5 cm diameter pipe at various velocities (as indicated in Table 7.6-1). Transient process were used for the deposition process and adaptable time step were found to be ideal where the courant number was set to a maximum value of 1.

7.6.2 Boundary conditions

The end of the pipe is assigned as velocity inlet boundary condition and the three sides were modelled using a wall with no slip boundary conditions while the top was modelled as entrainment with relative pressure set to zero. The no slip boundary condition was chosen base on the observation during the flume tests: In all test a tongue shape front with rippled surfaces were observed. Both of these observations are an indication of side wall friction. Moreover, the use of no slip boundary condition for viscous flows with homogeneous and uniform properties is widely acceptable in literature (Gao and Fourie, 2015; Whetham, 1890; Day, 1990; Prabhakara and Deshpande, 2004).

7.6.3 3D Simulation Results (Bench scale)

7.6.3.1 Validation

The grid sensitivity analysis was initially performed using the meshes with coarse, medium and fine grid density (Figure 7.6-2). The coarse mesh contains 157,465 nodes and the medium mesh 878,043 nodes. The fine mesh has 926,464 nodes. The meshes are generated by reducing the body sizing and inflammation size. Results becomes insensitive to the number of nodes as the mesh becomes finer. Also, after examining different number of inflation layers it was concluded that 10 inflation layers are adequate for this problem.

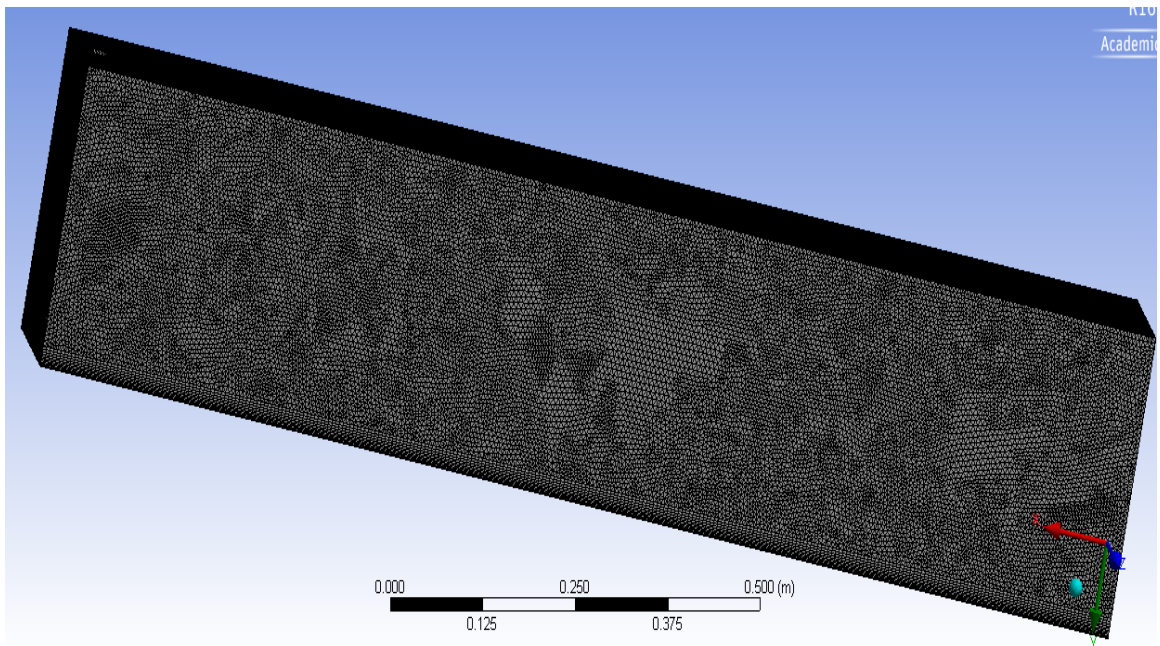


Figure 7.6-1 Medium mesh used for simulation of flume tests.

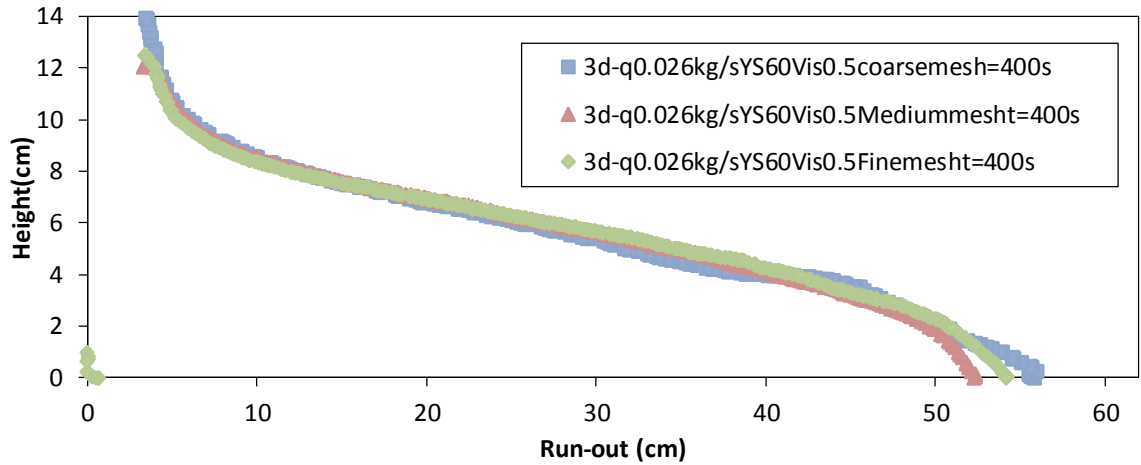


Figure 7.6-2 Final geometry for different mesh sizing for deposition velocity of 0.026kg/s and at t=400s employing a yield stress value of 60Pa and viscosity of 0.5Pa.s.

7.6.3.2 Results

The following figures illustrate the final geometry of the simulated profiles at various flow rates, the best fit were obtained using a values of 40, 60 and 70 Pa for test numbers 1, 3 and 4 respectively. Results of the numerical simulation at various times are illustrated in Figure 7.6-3 to Figure 7.6-8.

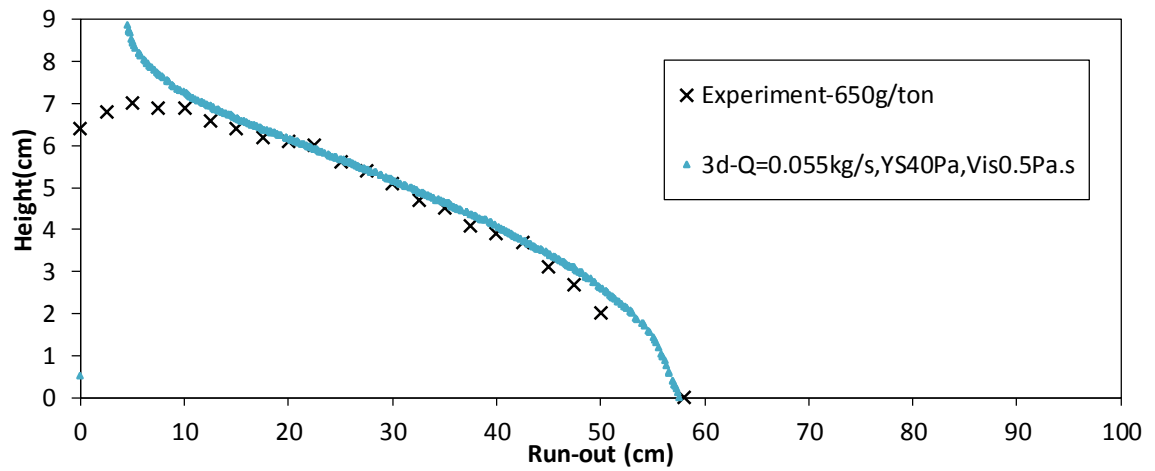
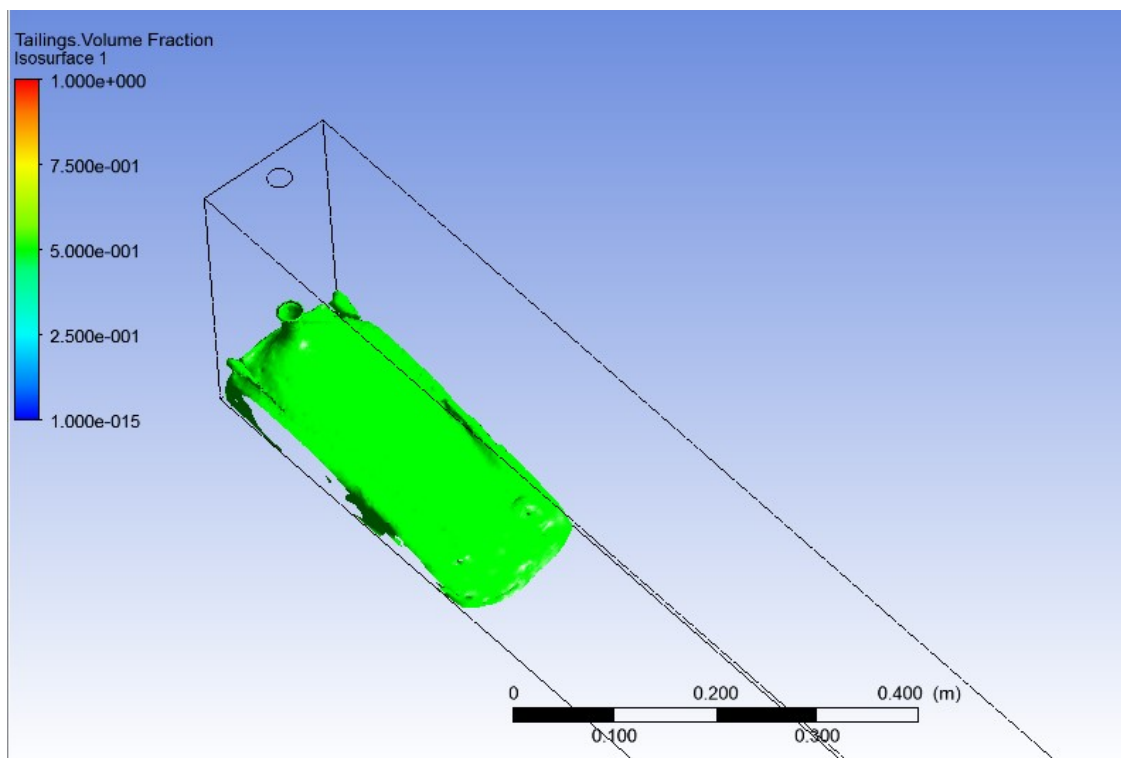


Figure 7.6-3 3D Numerical-experimental comparison of deposition of 5.7 kg of flocculated MFT (650g/tonne) into the flume using a yield stress value of 40Pa (Flume Test #1).



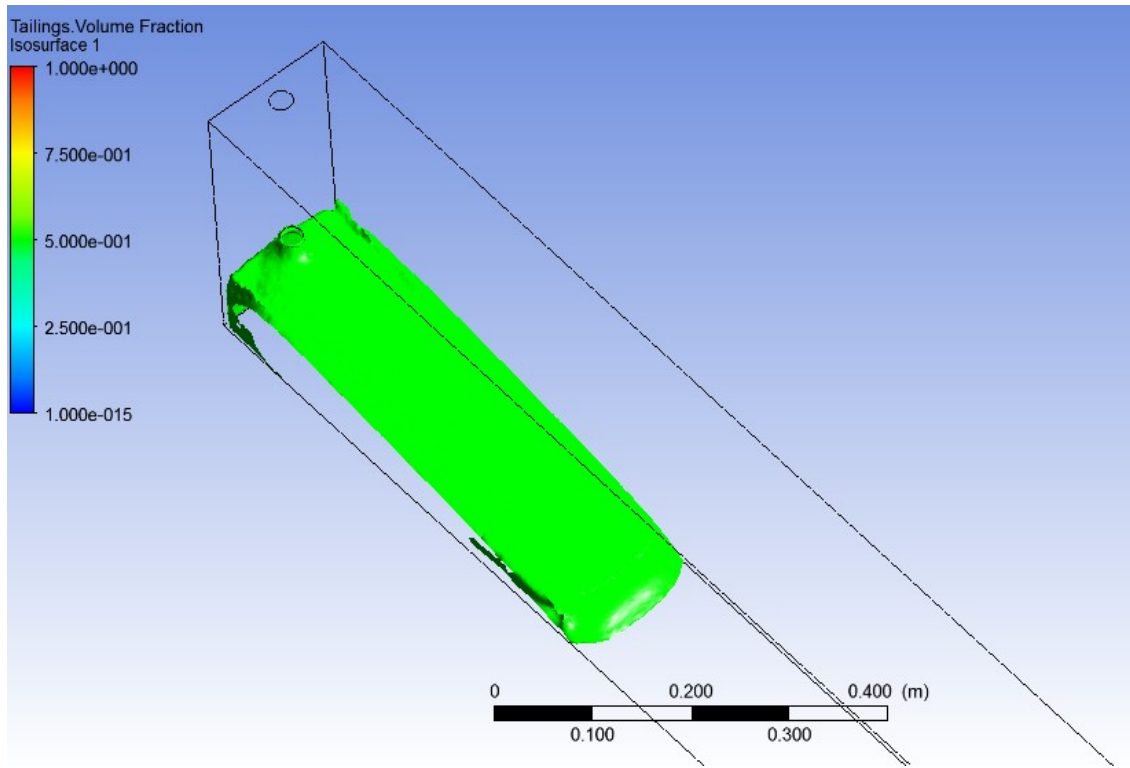


Figure 7.6-4 Tailings deposition simulation at $t=50s$, and $200 s$, employing a yield stress of $40 Pa$ and viscosity of $0.5 Pa.s$ (Flume Test #1).

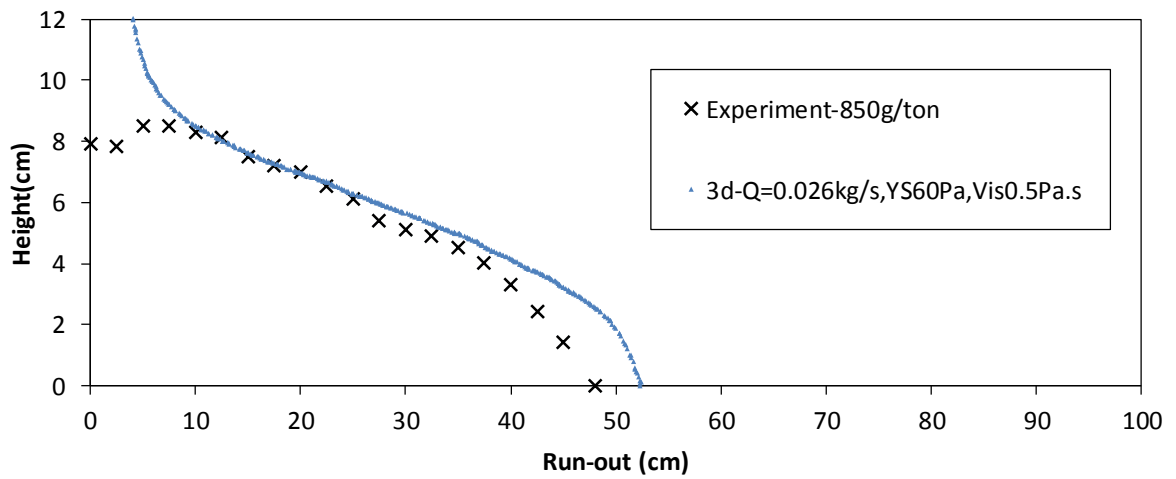


Figure 7.6-5 3D Numerical-experimental comparison of deposition of $5.8 kg$ of flocculated MFT($850g/tonne$) into the flume using a yield stress value of $60Pa$ (Flume Test #2).

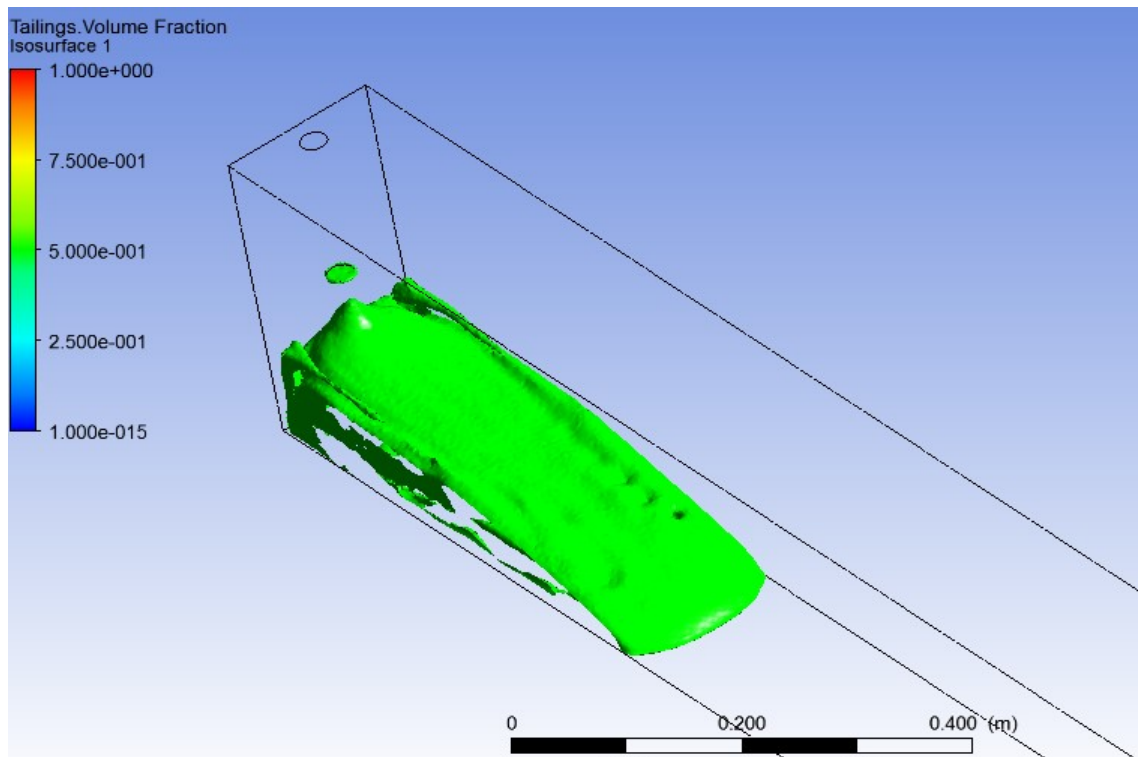
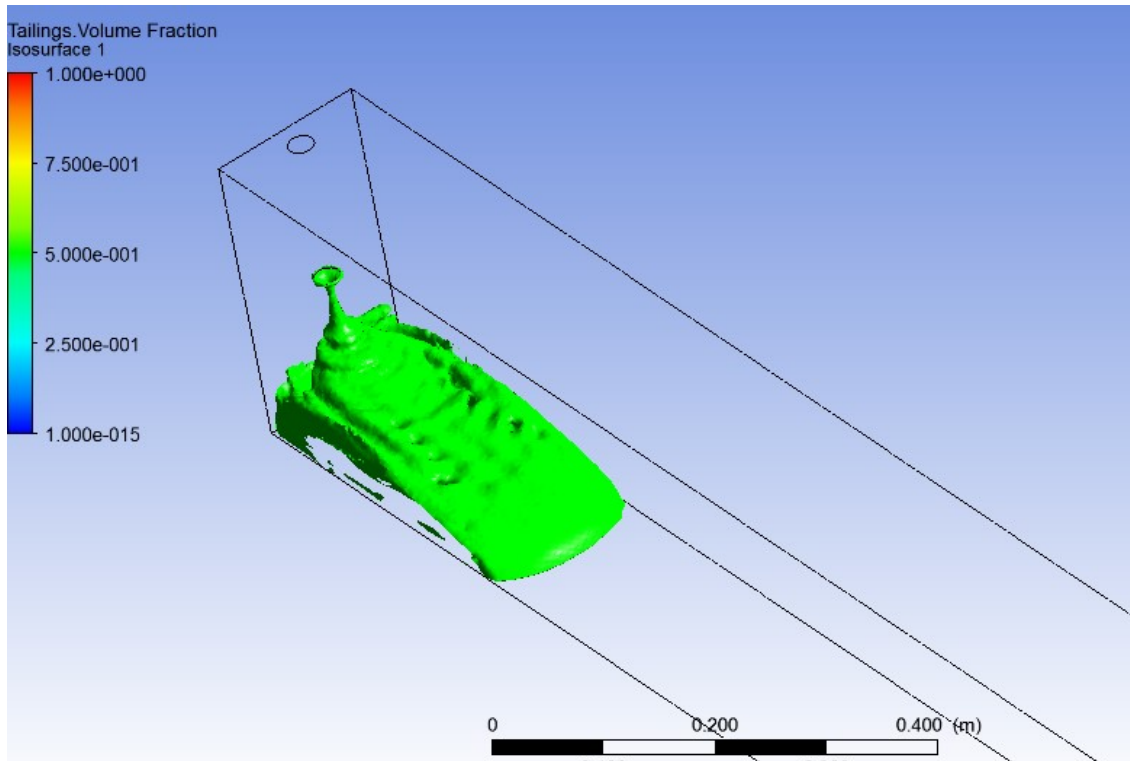


Figure 7.6-6 Tailings deposition simulation at $t=110s$, and $400 s$, employing a yield stress of $60 Pa$ and viscosity of $0.5 Pa.s$ (Flume Test #2).

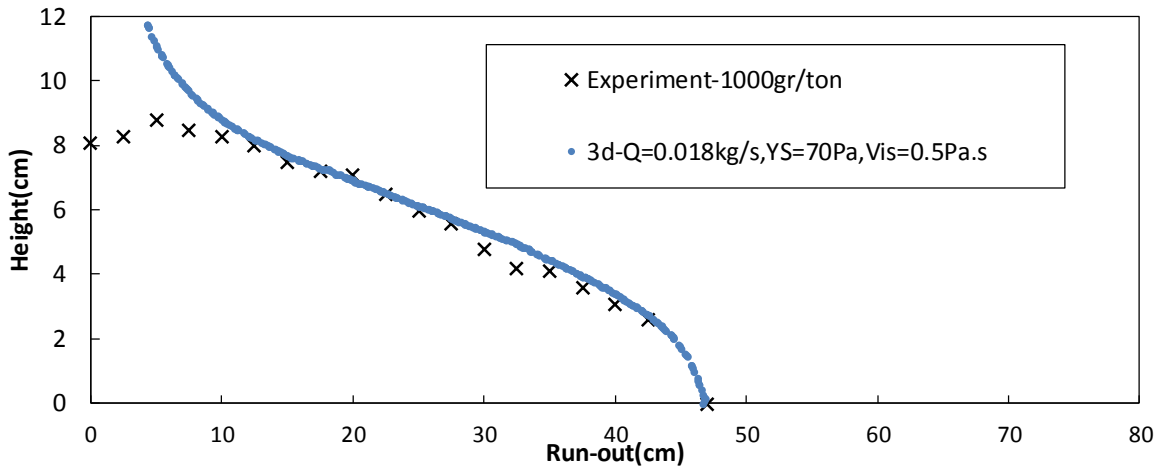
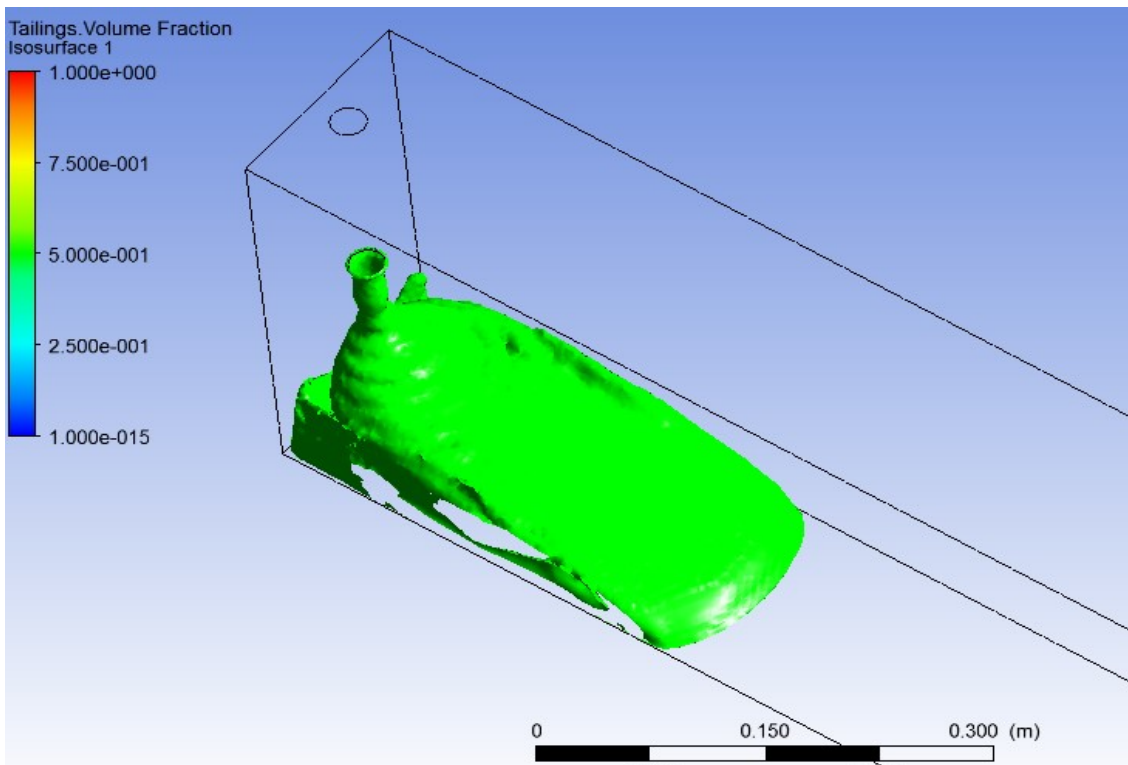


Figure 7.6-7 3D Numerical-experimental comparison of deposition of 5.88 kg of flocculated MFT(1000gr/ton) into the flume using a yield stress value of 70Pa (Flume Test #3).



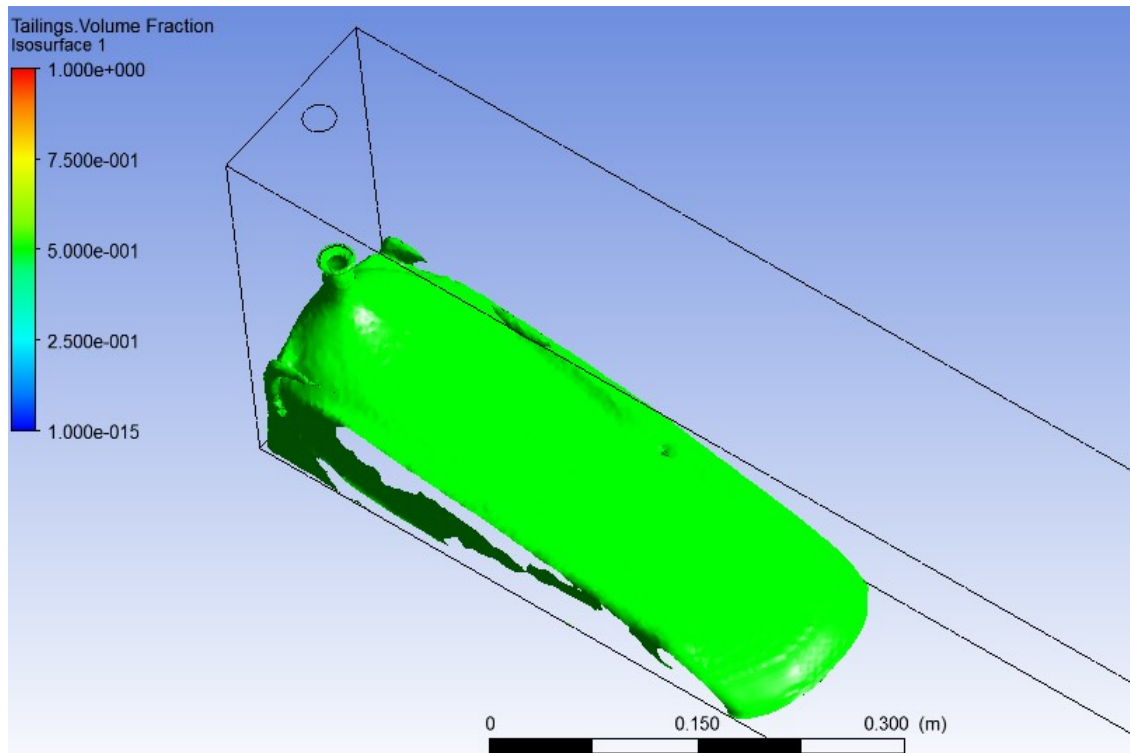


Figure 7.6-8 Tailings deposition simulation at $t=170s$, and $400 s$, employing a yield stress of $70 Pa$ and viscosity of $0.5 Pa.s$ (Flume Test #3).

Discrepancy between the measured and simulated profiles may be partially attributed to ongoing dewatering and consolidation. The yield stress values obtained using Equation 2.5-11 and cfx model which provided the best fit to the final geometry of the experiment are compared in Table 7.6-2. Generally the yield stress values obtained from the LT (Lubrication Theory) lie above the yield stress used in CFD simulations. The discrepancies may be explained by the fact that LT theory, which is based on theoretical solution of slow sheet flow, assumes a free slip sidewalls; therefore, it is not surprising to obtain higher values for yield stress using this theory.

Table 7.6-2 Yield stress obtained from flume test, predicted Eq. 2.5-11 and using cfx (Bingham model)

Dosage (g/ton)	Yield stress (Pa)LT	Yield stress (Pa) CFX-3D	Yield stress (Pa) CFX-2D
650	60	40	60
725	95	-	-
850	107	60	90
1,000	130	70	110

7.6.4 Model Set-Up (pilot scale flume tests)

3D simulations of flume tests were conducted using a block domain 8.00 m long, 0.66 m wide, and 0.59 m high. Tailings were pumped at a constant flow rate through a circular inlet with a diameter of 1 inch located 30 cm above the bottom of the flume (similar to the experimental set up in 6.3.1).

Free surface model was also applied in CFX, through which the interface between tailings and air was tracked. The two phase used in these simulations were air at temperature of 25C⁰ and tailings with an assigned density of 1250kg/m³. Simulation were done using two different rheological models i) Bingham constant viscosity of 0.5Pa.s and variable yield stress values ii) using the modified Coussot model (Hewitt, 2012) and using the following expression and using the values obtained from section ($T=10, \alpha=0.01275, \beta=0.97$).

Both geometry and meshing were created using the CFX package. Several meshes were examined to investigate the mesh convergence, where the number of nodes were gradually increased.

Flocculated MFT is pumped through the 1 inch diameter pipe at various velocities (as indicated in Table 7.6-1). Transient process were used for the deposition process and adaptable time step were found to be ideal where the courant number was set to a maximum value of 1 with a set minimum value of 1×10^{-6} and maximum value of 100s for the time step. The end of the pipe is assigned as velocity inlet boundary condition and the three sides were modelled using a wall with no slip boundary conditions while the top was modelled as entrainment with relative pressure set to zero.

After performing a grid sensitivity analysis it was concluded that a mesh with 327,483 nodes, 1,627,089 elements and 5 inflation layers are adequate for this problem (Figure 7.6-9).

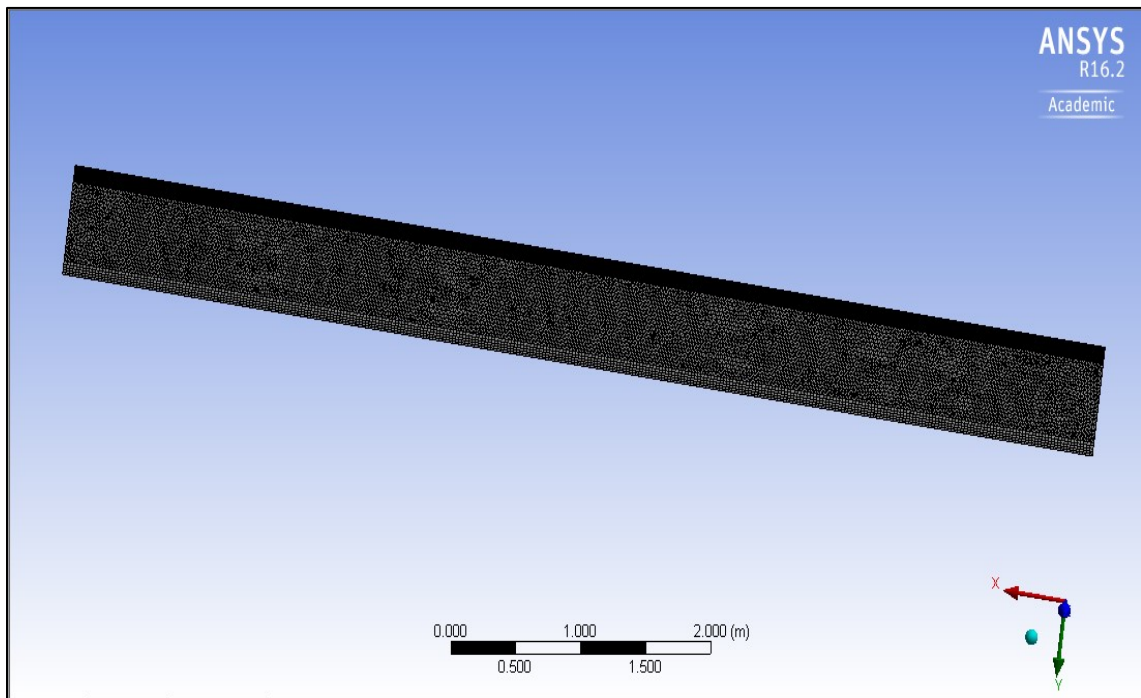
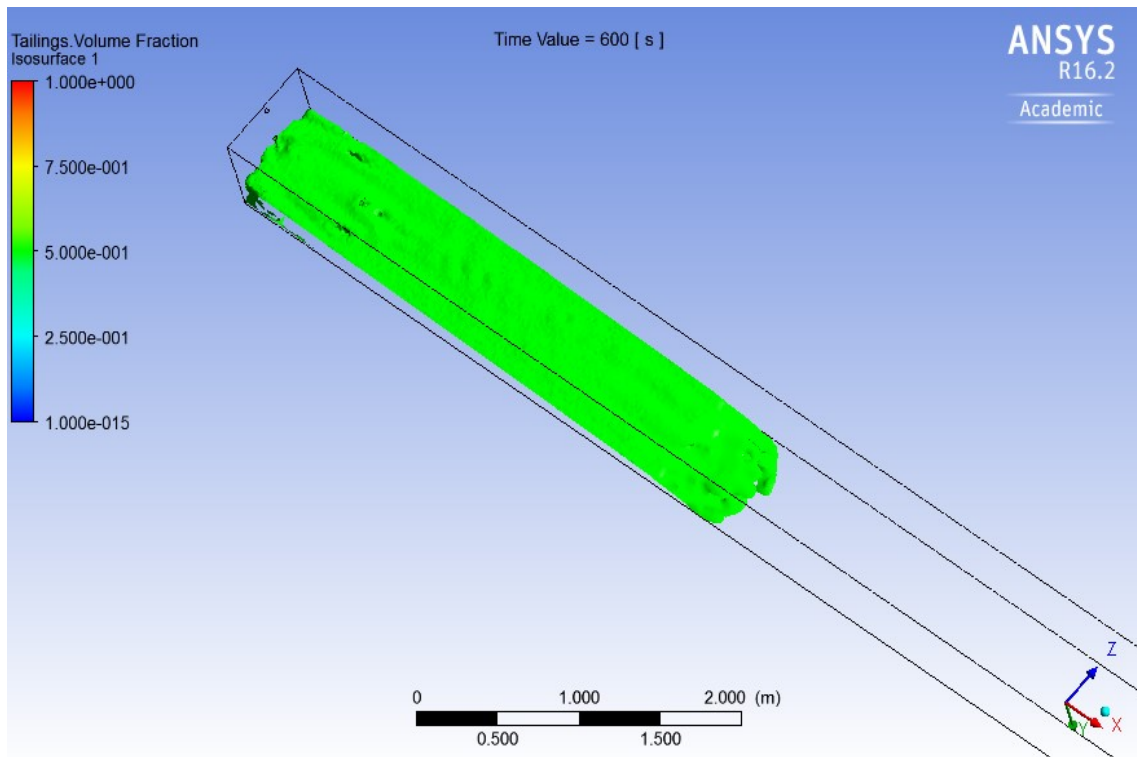


Figure 7.6-9 Mesh used for simulation of pilot scale testing at OSTRF.

Two different rheological models were used, the Bingham model and the Hewitt model. Simulation were performed in 3D for the Bingham model, and 2D using both models. In the 3D simulations, a good prediction for the fast pour could be obtained using the Bingham model, however not so good for the slow pour.



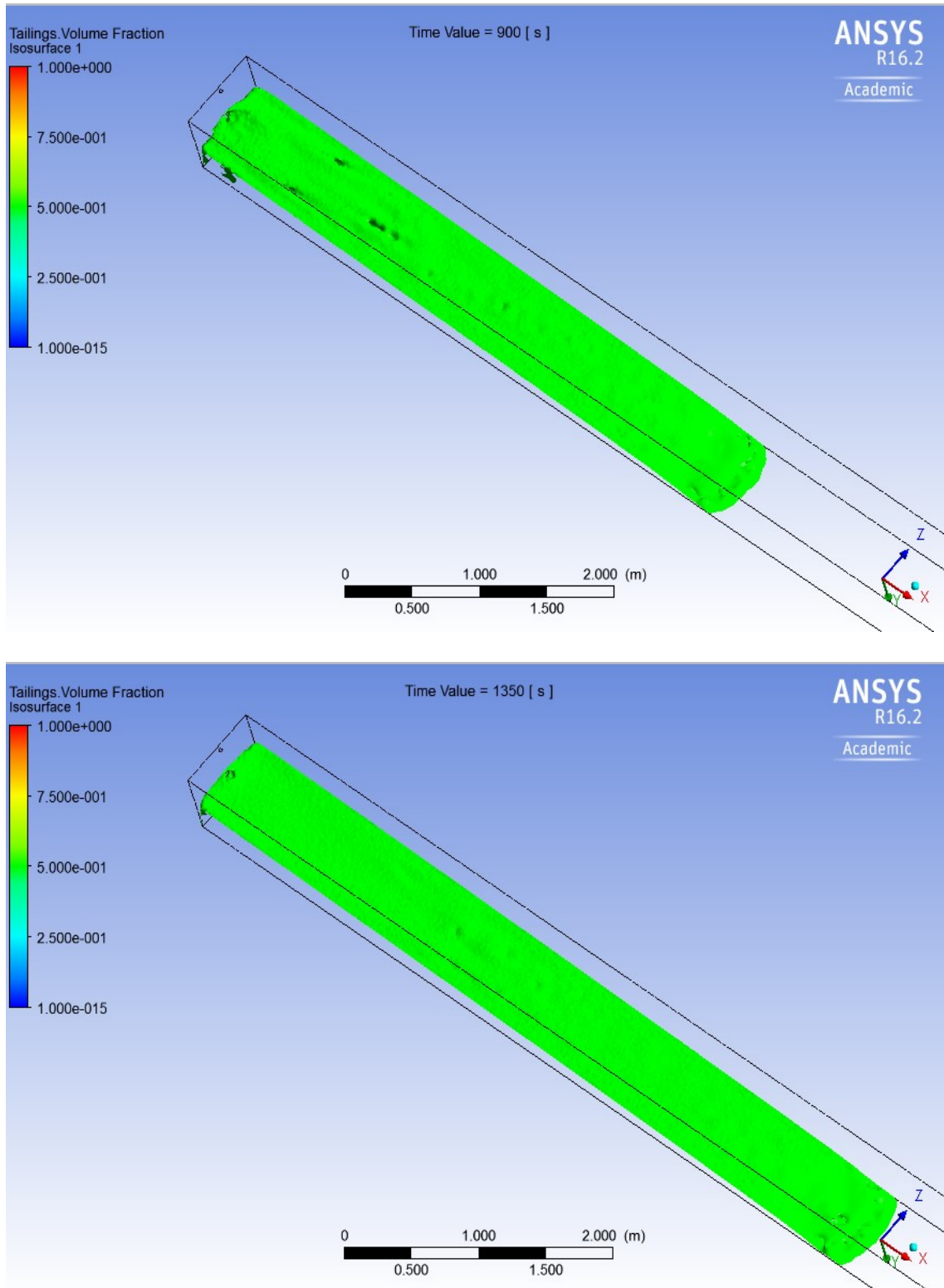


Figure 7.6-10 Tailings deposition simulation at $t=10\text{min}$, 15min and end of simulation, employing a yield stress of 40 Pa and viscosity of $0.5\text{ Pa}\cdot\text{s}$ (Flume Test #6).

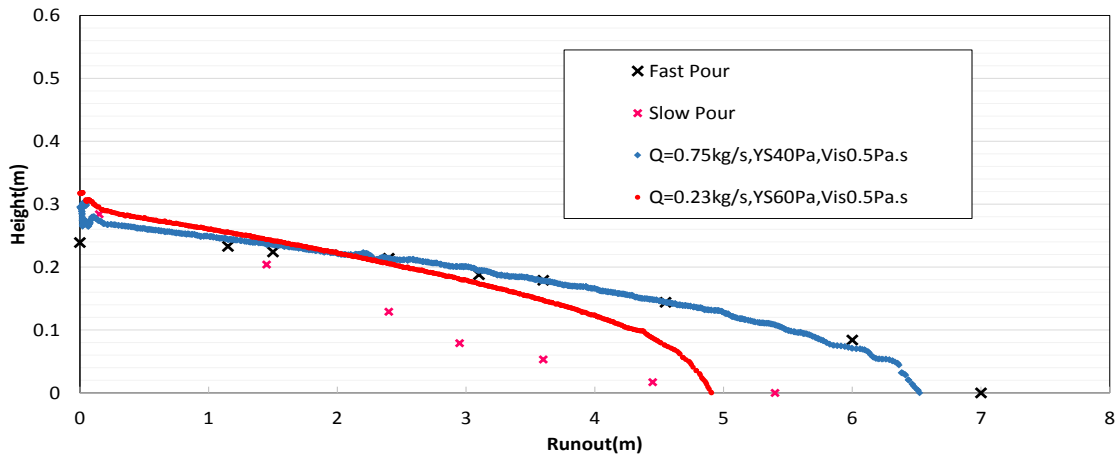


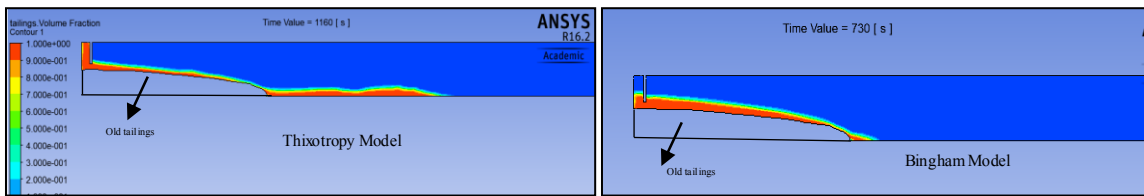
Figure 7.6-11 3D Numerical-experimental comparison of pilot scale flume test using Bingham model.

In 2D, several modelling simulations of the slow pour were attempted. The Hewitt model by itself is unable to provide an improved prediction. This is because while the Hewitt model considers the shear sensitive and ageing effects, using an Euler-Euler based method the identity of individual fluid elements is not conserved; thus, one cannot include the rapid increase in yield stress when the material comes to rest. That is, the rapid transit theory used here allows for progression from an initially fully structured state, to a fully sheared state, and back to a new rest state, the latter defined by the lower yield stress. However, rapid transit theory cannot describe recovery by ageing to the initial yield stress. Simulating this recovery could only be done with models with memory, probably using a lagrangian framework, or some mass tracking algorithm (such as through the use of virtual particles in an Eulerian framework).

The authors have accounted for this effects by considering an arbitrary volume of previously deposited tailings as “frozen”, and modelling them as a separate material. In

order to incorporate the effects of consolidation, and improve predictions for the slow pour, deposition was split in two steps: The geometry after 30 min was used as the new topography for the second half of deposition. Figure 7.6-12 illustrate the numerical simulation using two different rheological models presented.

(a)



(b)

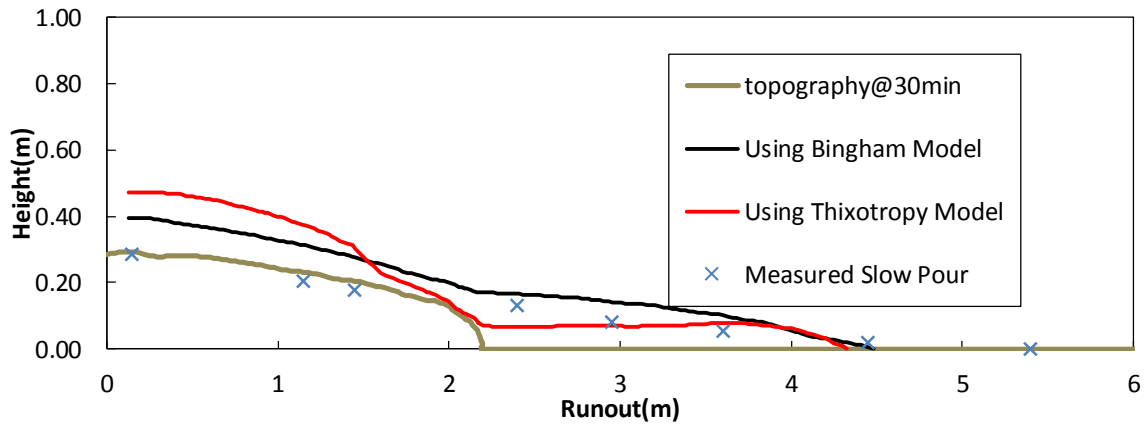


Figure 7.6-12 2D Numerical-experimental comparison of slow pour (~ 60 minute test) where the measured tailings profile at 30 minutes was used as the new topography. Figure (a) illustrates the profile in the Hewitt model at the time when channel flow was first observed in the experiment (~49 minutes using thixotropy model and 42min using Bingham model).

The predictions of both the Bingham model and Hewitt model improved when a section of the tailings is considered frozen. They still suffer from over-prediction of height as

substantial water loss still occurs during the 30 minutes of this simulation (52.56 kg of release water was collected at the end of deposition). Note that the volume of the measurements are considerably less than the volume of the predictions. However, when an earlier time (45 minutes) corresponding to a similar volume of predictions to measurements are used, shown in Figure 7.6-12(a), the agreement of the Hewitt model is much better.

Several 3D simulations of the slow pour were attempted, employing Hewitt thixotropy model, where the underlying slope was gradually increased. This was done to investigate the point at which spreading flow changes to channelize flow. Channelized flow was observed once the slope of underlying layer was set to 38%. Figure 7.6-3 presents snapshots of this simulation over an inclined bed of 38%. The channelized flow initiated at around 50 seconds into deposition. This slope, however, is larger the slope at which channelized flow was observed in the flume test (slow pour).

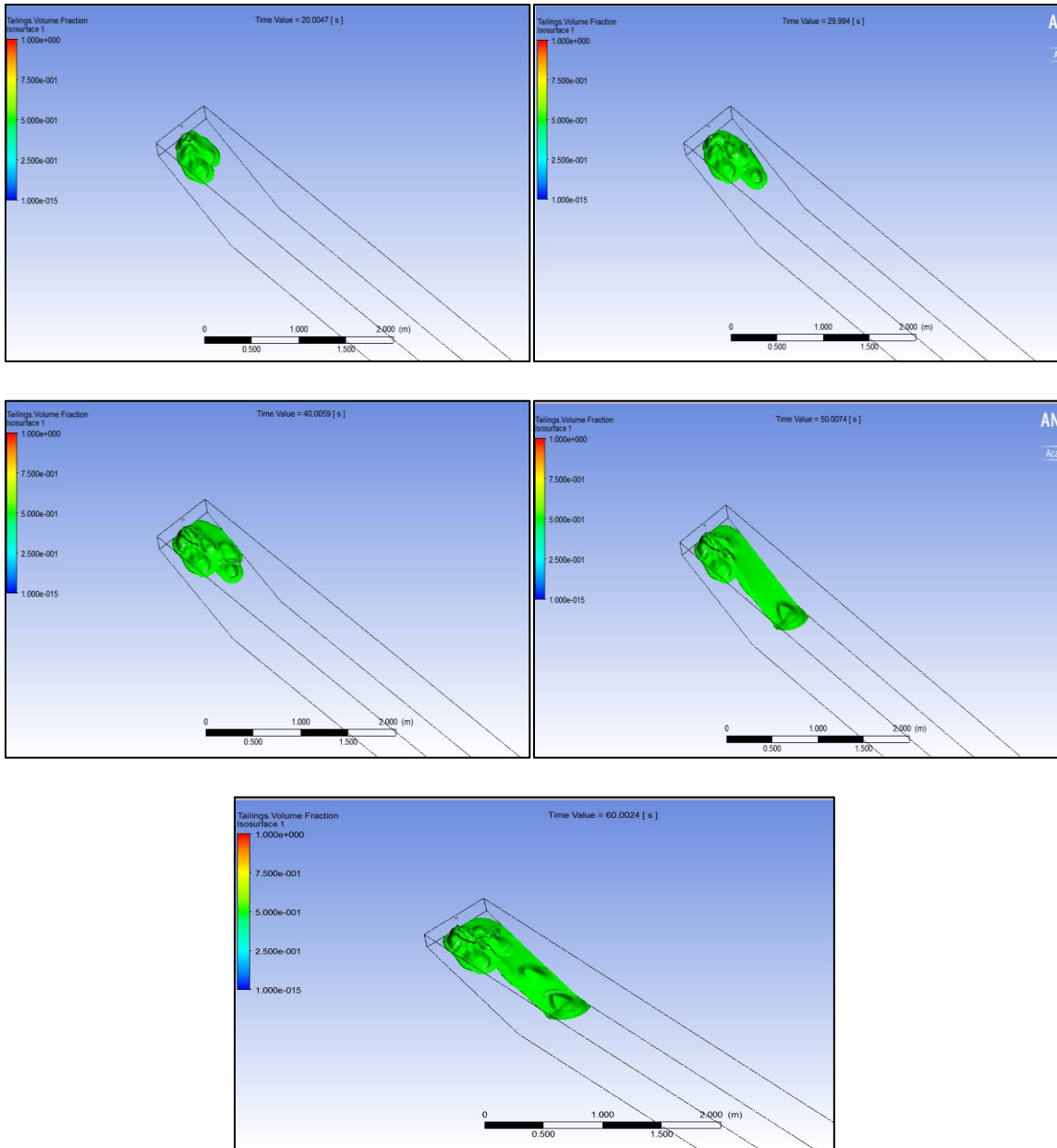


Figure 7.6-13 Snapshots of 3D simulation of tailings on inclined plane at 38%.

7.7 Simulation of Deposits at Field Scale

As previously mentioned in chapter 2, AFD (Air Fine Drying) technique relies on immediate water release (MFT flocculation) and atmospheric drying of deposits by climate forcing upon deposition on sloped cells. Field monitoring of flow conditions over a period

of two deposition seasons (2010-PhaseI and 2011-PhasII) at several locations at Shell Muskeg River Mine Fort McMurray, Alberta were conducted by Barr Engineering and were made available to Carleton University.

7.7.1 Deposition Cell

Phase I cells (2010) were generally built triangular in shape, with 300m length, with the discharge points located upstream at a central staging area (Shell 2011 technical report). The initial bed slope for cell 4 was around 1.5%, where it sloped down from the discharge point to facilitate tailing distribution and dewatering potential. The boundaries of the cell at the downstream is supplied by the constructed berm or standing pool of water resulting from drainage (Figure 7.7-1).

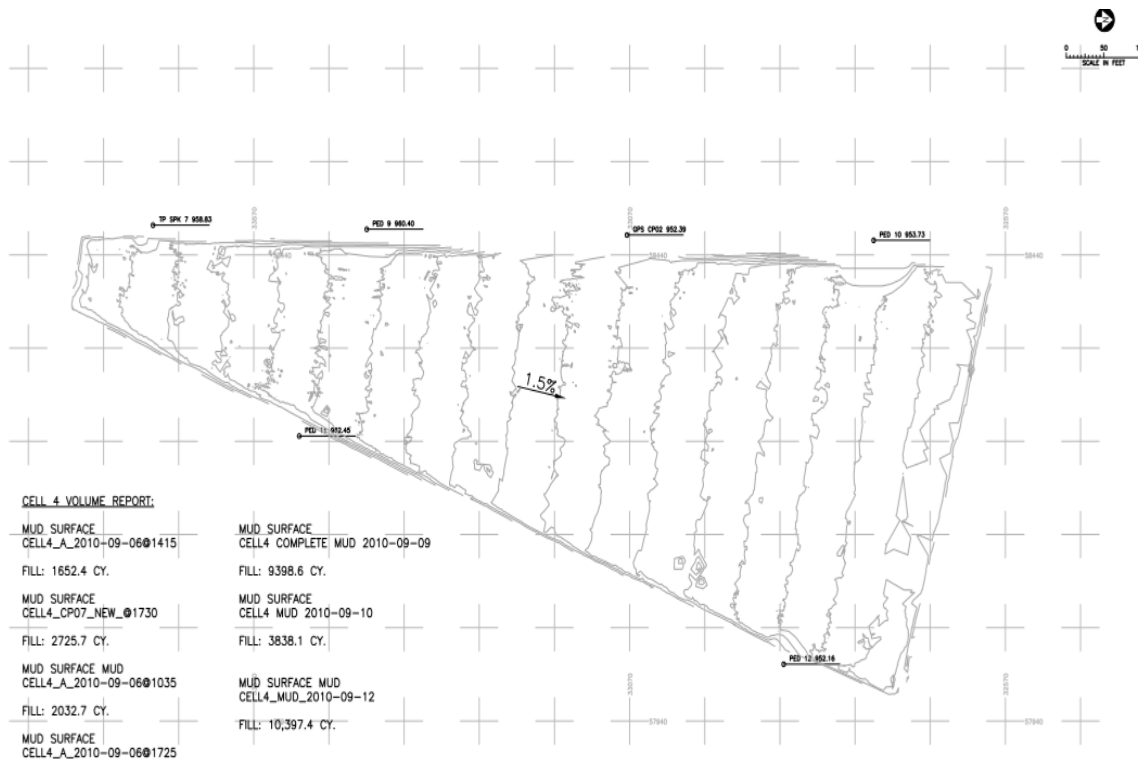


Figure 7.7-1 Schematic plan of cell 4 deposition cell.

Table 7.7-1 summarizes the timeline of operation of the commercial scale production of flocculated MFT at cell 4 along with some other information during the deposition in this cell.

Table 7.7-1 Cell 4 timeline

	Date and Time	Discharge Density(kg/m ³)	P/T Underflow Flow meter(m ³ /h)	Volume to Cell 1(m ³)	Volume in Cell Based on Control Room Data(m ³)	Mass to Cell 1(kg)
Start	03-Sep-10 13:53	1091.63	354.29			
Stop	03-Sep-10 15:08	1278.56	234.94	370.72	370.72	439339.34
Start	03-Sep-10 15:17	1282.63	73.50			
Stop	03-Sep-10 16:36	1268.13	59.15	87.33	87.33	111375.81
Start	04-Sep-10 09:28	1174.75	301.00			
Stop	04-Sep-10 10:00	1283.56	108.59	110.93	110.93	136349.34
Start	05-Sep-10 16:31	1226.19	232.93			
Stop	05-Sep-10 18:11	1233.13	168.09	334.18	334.18	410922.62
Start	06-Sep-10 08:53	1237.56	32.73			
Stop	06-Sep-10 09:26	1230.56	360.59	108.16	108.16	133477.50
Start	06-Sep-10 10:08	1214.81	6.21			
Stop	06-Sep-10 11:08	1203.88	349.48	177.84	177.84	215074.13
Start	06-Sep-10 13:16	1201.19	241.94			
Stop	06-Sep-10 13:33	1229.19	64.14	528.08	705.93	639727.69
Start	06-Sep-10 14:00	1223.56	198.98			
Stop	06-Sep-10 15:35	1205.00	118.83	251.59	251.59	305502.95
Start	06-Sep-10 16:28	1212.38	34.48			
Stop	06-Sep-10 18:11	1222.19	132.48	143.30	143.30	174435.03
Start	07-Sep-10 08:03	1222.19	300.39			
Stop	07-Sep-10 10:31	1201.88	295.23	734.59	734.59	890344.75
Start	07-Sep-10 11:40	1201.31	213.06			
Stop	07-Sep-10 12:33	1215.13	58.80	120.07	120.07	145073.98
Start	07-Sep-10 16:40	1197.06	420.44			

Stop	07-Sep-10 18:12	1198.25	203.26	478.17	478.17	572683.43
Start	08-Sep-10 09:46	1098.31	94.50			
Stop	08-Sep-10 10:57	1194.00	206.76	178.25	178.25	204299.96
Start	08-Sep-10 12:11	1187.69	90.83			
Stop	08-Sep-10 16:10	1183.13	54.16	289.37	289.37	343022.02
Start	08-Sep-10 16:44	1174.56	305.03			
Stop	08-Sep-10 16:59	1186.75	6.13	37.60	37.60	44389.58

In order to perform simulation in a timely manner, 2D setups similar to the ones used for pilot scale flume tests, using both Bingham and Hewitt thixotropy model, were also employed here. Since no information was provided in regards to the flow rate and floc dosage during the deposition time an average value was assumed for all days based on the total volume of tailings deposited in this cell.

In the first attempt all the tailings were deposited at once and from a single deposition point, and employing different values of yield stress (Figure 7.7-2). As the yield stress was lowered the tailings travelled over a further distance reaching perimeter berms, forming a horizontal surface after filling the cells. As apparent from Figure 7.7-2, none of the simulation were able to adequately estimate the ultimate concave beach profile; however, predictions improved when deposition was conducted in steps (Figure 7.7-3). One possible reason is the increase in yield stress over the extended time of deposition, which was not accounted for in the first simulations.

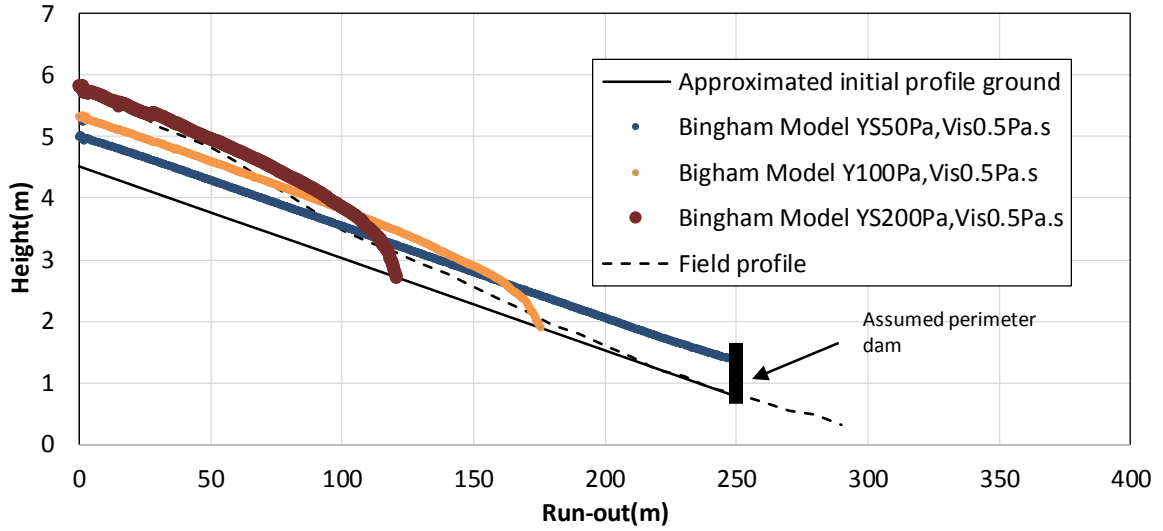


Figure 7.7-2 Measured and predicted beach profiles for Cell 4.

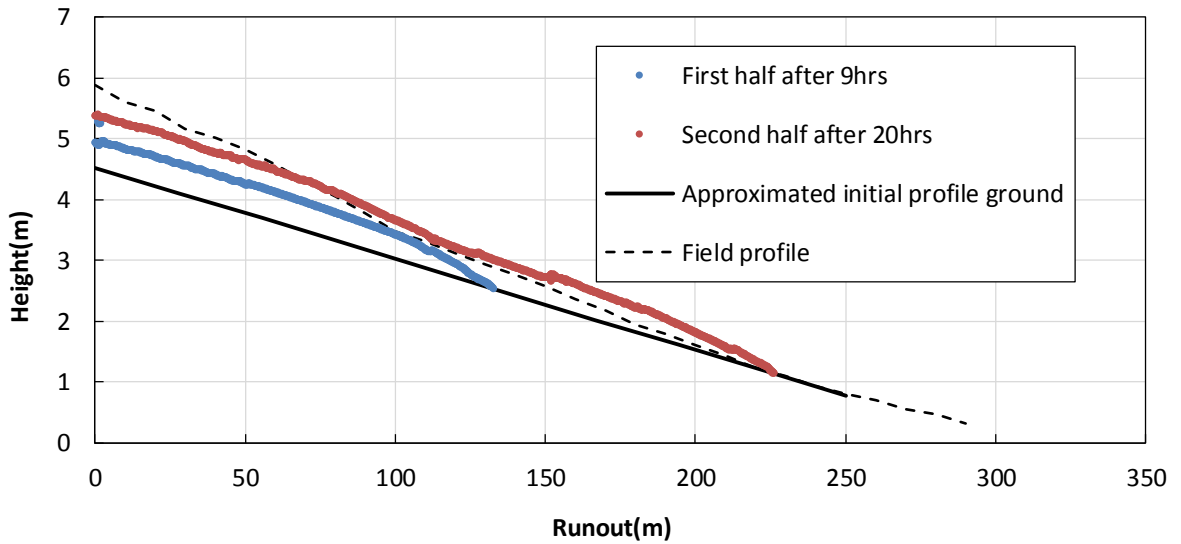


Figure 7.7-3 Measured and predicted beach profiles for Cell 4 conducted in 2 steps.

To account for rapid increase in yield stress when material come to rest at the end of each deposition period, all of the deposited tailings were “frozen” at the end of deposition on each day. For this purpose and in order to incorporate the effects of consolidation, and to improve predictions of the final profile, deposition was split in 6 steps (Figure 7.7-4):

The geometry after each day was used as the new topography for the deposition on the next day.

Figure 7.7-4 and Figure 7.7-5 illustrate the simulated tailings profile deposited at Shell Atmospheric Drying cell during the fall 2010 program using Bingham model and thixotropy model respectively.

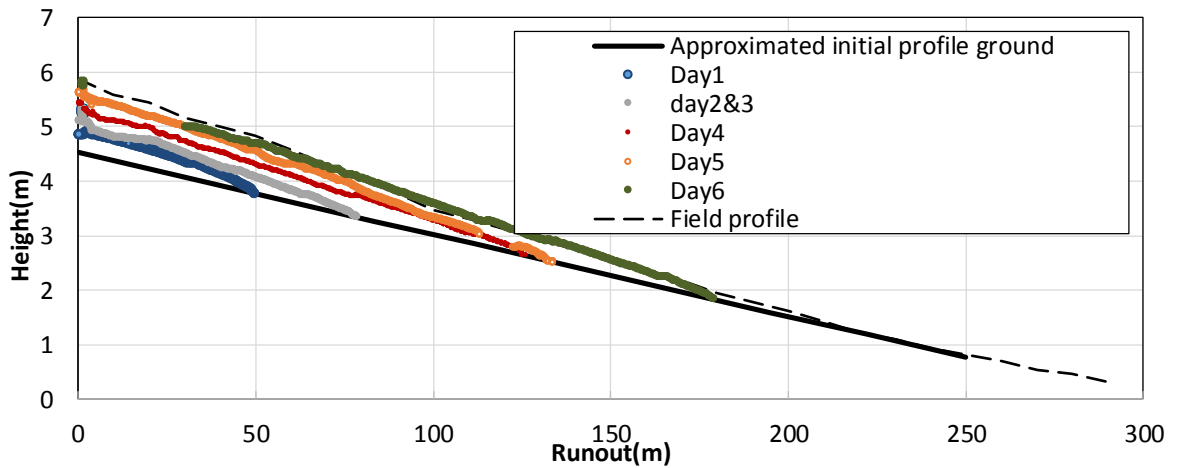


Figure 7.7-4 Measured and predicted beach profiles for Cell 4 using deposition periods as indicated in Table 7.7-1 employing yield stress of 50 Pa.

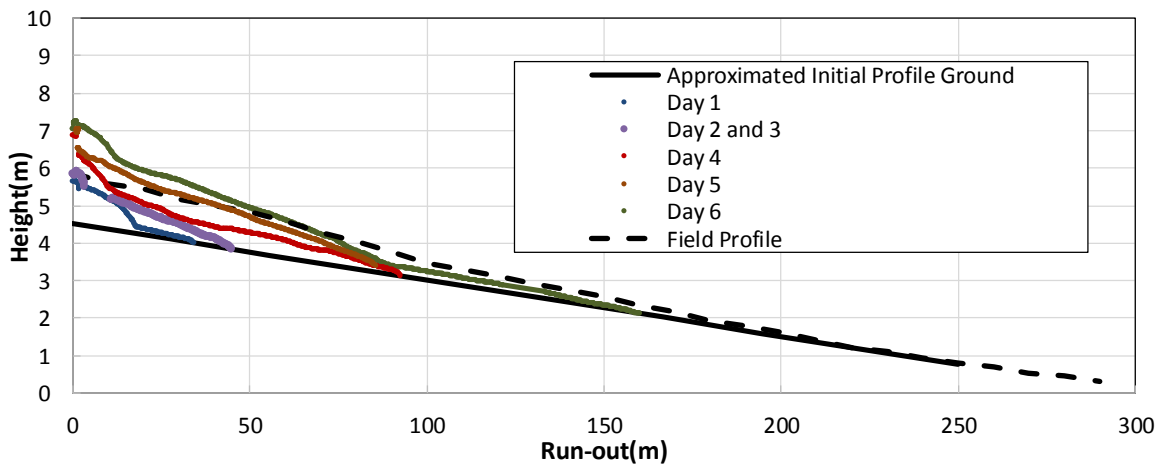


Figure 7.7-5 Measured and predicted beach profiles for Cell 4 using deposition periods as indicated in Table 7.7-1 employing thixotropy model.

7.8 Discussion

In this chapter flume test conducted at Carleton University and at the OSRF facility were modelled using the Volume of Fluid in CFX. Attempts were made to simulate the profile of the tailings at various deposition speed and floc dosages using CFD methods. Simulations in this study were conducted using the (Eulerian-Eulerian) method, which is suitable for dense flows (high volume fraction). Two rheological models were used for this purpose: Bingham model and thixotropy model of Hewitt. It was found that the final profile of the deposit was highly controlled by the deposition speed due to the thixotropic nature of the tailings, allowing the material more time to rebuild its structural damage under lower stress values. Generally the best fits (using the Bingham model) for the fast pour were obtained using the yield stress values of, 40-60Pa, which is within the lower value of yield stress from the Hewitt interpretation of the rheology (τ_{cH}). Gao and Fourie, (2015) also reported the yield stress value obtained from flume test may be used for field deposition, considering material shear history (experiencing shearing before and during deposition).

The slower pour, on the other hand, could not be simulated using a constant rheology, mainly due to the more pronounced dewatering and consolidation of the tailings over longer deposition times. Moreover, the material rearrangement and restructuring under lower stress levels lead to further strengthening of the material deposited at earlier time. Using the setup employed in this study (Euler-Euler), material ageing in later stages of deposition could not be considered. It is believed that this behavior is responsible for switching off the flow near the bottom the flume and the reason why a single value rheology could not be used along the path. This was also confirmed by fitting the profile before onset of channeling flow with the yield stress value for an initially structured material (400 Pa),

using the LT equation, suggests that at least part of the tailings near the bottom of the flume have come to a state equivalent to an initially fully structured state at rest.

In order to take these effects into account, for the slower pour, deposition was carried out in two stages: material deposited in earlier times were frozen before the fresh material were deposited. Similar approach was used for simulation of field deposition.

Another interesting note on the slower pour, was the development of a channelized flow which transport tailings to the bottom of the stack. A clear difference between the older tailings and the fresh tailings flowing in the channel could be observed. While the transient profiles evolve as observed in the shorter duration tests, fresh tailings started flowing down to near the toe 45minutes into deposition.

Generally the best fit yield stress value obtained using the 2D simulations were above the ones used in 3D simulation mainly due to absence of sidewall friction. However, 2D simulations may be performed in a timely manner reducing calculation costs. Though slopes near the boundaries may be effected by the perimeter dams (wall friction at field scale), quantitative effects of boundaries on the final profile was beyond the scope of this study and requires further investigation. Nevertheless, it was shown that 2D simulation may be used as a robust way to simulating field deposition, reducing unnecessary calculation costs. It is also conceivable that the CFD method employed here could be used to simulate surface deposition in 3D, using which a more accurate estimate of cell capacity could be obtained.

Finally, due to thixotropy nature of tailings, shear history of the tailings should be accounted for in any numerical modelling. Moreover, it was shown that ageing effects, or structural build up, in depositions of longer time frames (such as field scale deposition)

become more important to the point where time-based effects compensates the shearing effects. It was shown in this study that the modified Coussot model (Hewitt model) could be used. It is also believed that the use of Lagrangian method, may be more suitable for modeling the thixotropic tailing slurry flow, but require significant calculation effort.

8 Chapter: Discussion and Conclusion

8.1 Summary of the work

Several new fine tailings technologies in the oil sands generate polymer-amended materials that exhibit a yield stress upon deposition, and will therefore stack at a gentle slope. Poor spread-ability, underutilization of impoundment footprints, and overflowing of embankments, or accumulation of low yield stress material at deposit topographical lows are common challenges reported by operators of oil sands pilots or commercial trials. While these challenges can and have been dealt with by increasing the number of deposition points or increasing operational flexibility, or by rehandling the tailings, they are often associated with high costs.

In order to improve the sustainability of oil sands operations, such substantial costs should be reduced and costs associated with tailings rehandling should be minimized. This goal will be achieved by investigating the optimal lift thickness for maximum dewatering and by studying the sensitivity of dewatering to lift thickness. However, this all relies on the flow behavior of flocculated tailings post deposition and how the designed lift thickness can be achieved. The primary purpose of this study was to improve our understanding of

the flow behavior of tailings product, and to help improve operator's control of lift thickness and deposits geometry of flocculated MFT with the aid of numerical models.

In summary this study included the following tasks:

- I. Measuring the rheological properties of flocculated MFT under various loading conditions including increasing and decreasing stress/strain test. Conducting tests on laboratory prepared samples and those collected during field testing.
- II. Conducting microstructural testing to examine the microstructure and macroscopic behaviour of tailings for a wide range of polymer doses (650 – 1500g/ton). Structural investigation were used to characterize thixotropic behaviour of polymer amended tailings
- III. Observing and recording flow behavior of flocculated MFT in the field.
- IV. Conducting large flume test to investigate the effects of depositions duration on the flow behavior.
- V. Model said flows using ANSYS CFX using similar setup as explained in chapter 7.

The rheological parameters of polymer-amended MFT were examined using different rheometry techniques with a vane fixture in the range of 600 –1500 g/ton. Results revealed that the arresting stress – the yield stress that characterizes when the tailings stop flowing – is a function of shearing and ageing. This would mean that despite structural degradation under high stress levels, it can recover substantially under lower stress levels and over time. Recovery of the original structure of the polymer-amended tailings upon resting or as flowing under lower stress levels, was confirmed by a set of oscillatory rheometry.

In addition a set of controlled shear tests were designed to simulate the stress history of the tailings as they flow down the beach. Interestingly the results showed that, despite considerable shearing, residual yield stress always retained by the material, illustrating the ability of materials to recover a minimum level of yield stress upon shearing. The minimum yield stress manifested by the flocculated oil sands tailings appears not to vary with time of shearing, at least for the time scales examined. This was partly confirmed by the bench scale flume test.

In the course of investigating the rheology of these tailings, it became clear the material exhibited both thixotropy and hysteresis. Similar to what have been observed for pure clay suspensions; hysteresis is the dependency of the apparent yield stress on the stress history of the material. These effects were simulated using a viscosity bifurcation constitutive model of (Coussot et al. 2002 a,b; Hewitt and Balmforth, 2013): where viscosity variation are simulated by correlating viscosity to a structure parameter, which is affected by both destruction due to shear, and re-structuring due to ageing. Depending on the initial state of structure, the viscosity will either increase or decrease at a given shear rate or shear stress. Though the model prediction to experimental data isn't perfect, the ability of the model to simulate the differences between the initial yield stress and the apparent yield stress (or arresting stress) for decreases shear stresses was shown to be promising.

Comparing rheology test results on flocculated and raw MFT, showed significant difference in flow behaviour and yield stress values of the two different material. This showed that the flocculation process alters tailings structure significantly through bridging solid particle and formation of larger aggregates. Moreover, the elastic response was more

pronounced in case of flocculated MF and at the same density, as a result of stronger particle-particle interaction.

Similar rheometry test were also conducted on samples received from Shell's centrifuge cake trials, to investigate response of thickened tailings (raw MFT) to shearing and aging. In this case, however, the residual stress showed a more pronounced time dependent behavior.

The relevance of the rheology to surface deposition was then explored by analyzing two relatively large flume (8m long) deposition tests conducted at two different deposition rates at the Oil Sands Tailings Research Facility (OSTRF) in Devon, Alberta. To avoid over shearing of flocculated MFT at high pumping rate, a setup similar to the one utilized at field scale was used. Additional mixing (turbulence) was provided through the addition of several static mixers in lines to promote flocculation of MFT. Rheological changes of flocculated MFT dosed at 850g/tonne was tracked during deposition through the measurement of the yield stress (using the stress growth technique), at various distances along the path. Generally lower yield stress value were recorded for flume test of relatively shorter duration. In addition, the yield stress values of the fast pour were mainly found to be within the range of residual stress obtained from the constant decreasing stress test, as a result of greater shear that was imposed on the material. A higher yield stresses was measured closer to deposition point, for both cases, due to ongoing consolidation and possibly longer resting times. This was also confirmed by back calculating the yield stress using ANSYS CFX (yield stress of 40Pa) and those of lubrication theory (LT) based equation for resting profiles of a Bingham fluid (yield stress of 60Pa). Both values are within the lower value of yield stress from the Hewitt interpretation of the rheology (τ_{cH}).

Another interesting note on the slower pour, was the development of a channelized flow which transport tailings to the bottom of the stack. A clear difference between the older tailings and the fresh tailings flowing in the channel could be observed. While the transient profiles evolve as observed in the shorter duration tests, fresh tailings started flowing down to near the toe 45minutes into deposition. Fitting the profile before onset of channeling flow with the yield stress value for an initially structured material (400 Pa), using the LT equation, suggests that at least part of the tailings near the bottom of the flume have come to a state equivalent to an initially fully structured state at rest, if not higher.

The slow pour exhibits two behaviours seen in many different kinds of tailings deposits: channel flow, and a profile with flatter slopes near the toe and steeper slopes near the deposition point. This is a common issue often observed in most thickened tailings deposition making the deposition control challenging. This point is of particular interest to the engineer as to when the flow of individual lifts becomes less manageable, and thus can be avoided during deposition.

A final note on yield stress measurement is that while there exists a variety of methods to evaluate yield stress, performing a yield stress measurement on thixotropic material is still challenging. Variation in the results are often associated with the time scale of the technique and thus the use of other terms such as elastic modulus (in the LVE range), which is independent of time, may be used as a more reliable technique. Most importantly, however, is the choice of the representative technique which depending on its application: for instance, yield stress values used for surface deposition at which a flow stops is much different than that used for pipeline design (flow initiation). While methods such as stress growth technique, starting from zero stress, are more appropriate for determining the yield

stress for flow initiating (such as in a pipeline), they may not be applicable to deposition. The yield stress appropriate for modelling overland flow and beaching of high density tailings, may be obtained through the controlled decreasing shear stress test. These tests can simulate stress history during deposition and provides accurate values of the arresting stress.

In this study, it was shown that the yield stress is related to the elastic modulus, but it was shown that a linear correlation may be obtained between the slope of the linear elastic deformation and elastic modulus. This could be attributed to the fact that the yield stress measurement are made in the nonlinear (plastic flow) zone.

In the next step of research program, using a set of microstructural analysis, it was shown that small-strain oscillatory rheometry (through the measurement of elastic modulus) can be used as a sensitive measuring procedure for detection of microstructural changes. ImageJ analysis of SEM images showed that the tailings shifted towards pores of smaller diameter, to a greater degree, at the smaller dosages, which may also correlate with their increased dewatering.

In the final stage of this study, the mentioned flume test and field profiles were simulated using ANSYS CFX software as explained in chapter 7. Although the 3D simulations compare well with bench scale experiments, but they are computationally expensive and require considerable computer resources. As a result, 2D simulations were conducted using a flow boundary condition for simulations of longer deposition times.

Through the study of 2D simulations of the slow pour it was shown that the Hewitt model by itself is unable to provide an improved prediction. This is because while the Hewitt model considers the shear sensitivity and ageing effects, it does not consider the

third process – the rapid increase in yield stress when the material comes to rest. This suggested that for field scale deposition, where deposition of a particular layer of tailings may take hours or days, this increase in yield stress of the older material can influence the shape of the layer.

In order to incorporate the effects of this process and effects of consolidation during longer deposition, an arbitrary volume of previously deposited tailings was considered as “frozen”, and were modelled as a separate material. The predictions of both the Bingham model and Hewitt model improved when a section of the tailings was considered frozen. This illustrated the point that the properties of the older deposited material become highly different than that of the freshly deposited tailings and they cannot be modelled using a single flow curve.

Finally, using the developed model implemented in CFX, effects of various operational terms as such as deposition flow rate, underlying slope and materials properties (i.e. yield stress and viscosity) can be investigated on the final geometry. This model can be used as a tool to help engineers design pour quality deposition configuration, geometry of cell and underlying slope to ensure drying efficiency and maximize fines capture per unit footprint.

Specific conclusions include:

- Raw MFT presented much lower moduli and lower yield stress than the polymer amended material at same density, due to structural changes as a result of polymer addition.
- Using high polymer dosage showed the presence of free flocculant without attachment to any particles and thus no additional benefits in terms of long term dewatering and strength gain.
- The rheology of these polymer amended tailings is shown to be dependent not only on shear thinning behaviour but on ageing or thixotropic behaviour.
- The yield stress increases rapidly when the tailings come to rest, due to rapid dewatering/consolidation and thixotropic rheology of the material.
- The elastic shear modulus of the tailings could be almost completely recovered following high shear, even as the tailings were still flowing.
- The near full recovery of structure implied by the oscillatory rheometry tests showed that the de-structuration under high shear is reversible, and therefore the benefit of the polymer would be largely retained under most deposition scenarios
- Structural changes and thixotropic behavior of flocculant MFT of various dosages were confirmed by a set of microstructural analysis.
- Flume tests results showed that the test with a faster deposition rate could be modelled using Bingham rheology, employing the “coming to rest” yield stress.

- The flume test with the slower deposited rate showed evidence of thixotropic behaviour. The profile at 45 minutes could be modeled using Bingham rheology but only by using the “shearing from rest” yield stress. Past this point tailings began to be conveyed downslope by channel flow.
- Numerical modelling shows that at least qualitatively, the shape of the deposit is influenced by the time dependent behaviour. Thus, the rapid increase in yield stress due to dewatering is probably the more important factor to consider in deposition modelling.
- During the course of this study it became clear that the three different phenomenon are important to model deposition:
 - I. Destructuring by shear. Continuous shearing at relatively high rates results in reduction of the viscosity and apparent yield stress.
 - II. Recovery by rheology (increase of apparent yield stress) by ageing. At low rates of shear, the structure recovers.
 - III. Increase in yield stress required to remobilize the material once it comes to a stop. Once the material stops flowing, strength rapidly increases both due to thixotropy and consolidation (density increase). Practically this is important as the yield stress required to re-initiate flow becomes very much higher than the yield stress required to stop the flow.

In this study improvements were made in predictions of evolving geometry of deposited polymer amended tailings by including thixotropic effects, for the first time, in actual

deposition scenarios. The conclusions of this study might be used to predict flow behaviour more accurately, possibly by including density effects.

8.2 Implications for the Industry

In this study, the polymer dosage of 650 g/tonne was shown to provide the best dewatering behavior (in certain lift thicknesses considered here), over two week period. Even though higher yield stress values were measured at higher dosages, no considerable increase in dewatering was observed at dosages above 650g/tonne. It should be noted that the yield stress values measured, at this dosage, is still considered "On spec", as specified by Shell (having a yield stress greater than 150 Pa). However, this observation is based on MFT samples of certain characteristics (i.e. MBI values of 4meq/100g -clay content of around 30%), and over certain range of polymer dosages (650-1500g /tonne). It is thus recommended to further study the rheological and dewatering behaviour of flocculated MFT at lower dosages and over longer periods of time and using MFT samples of different characteristics. There are several other factors that limit the extension of dewatering results to the field as such as lift thickness and effects of thixotropy built up on long term dewatering. Both of which require further investigation.

8.3 Recommendations

While in this study a rapid transit simplification of viscosity bifurcation theory was employed, recovery of the material to the initial high yield stress cannot be simulated using an Eulerian frame work employed here. Thus, a much more physical realism may be conveyed if a modified version of the model, which can simulate this recovery and thixotropic buildup over time, is used. This may be done with models with memory, probably using a lagrangian framework, or some mass tracking algorithm (such as through the use of virtual particles in an Eulerian framework-i.e SPH)

Another source of uncertainty during field deposition modelling was the point at which the change in flow regime takes place. It is thus recommended to conduct field investigation to further study the point of conversion between spreading and channelized flow by installing cameras during field depositions. Moreover, more detailed information on field deposition (i.e actual flows) would be beneficial from the modelling perspective.

In this study and through a set of rheometry technique it was shown that flocculated MFT illustrate a thixotropic behavior. This phenomenon can slow or even reverse dissipation of pore-water pressures in oil sands mature fine tailings. Thus, the effects of thixotropic build up of particle structure should be studied on the consolidation behavior of tailings.

REFERENCES

Alagha, L., Wang, S., Yan, L., Xu, Z., and Masliyah, J. (2013). Probing Adsorption of Polyacrylamide-Based Polymers on Anisotropic Basal Planes of Kaolinite Using Quartz Crystal Microbalance. *Langmuir*, 29(12):3989-3998.

Alberta Energy Regulator. (2015). Bulletin 2015-11. Retrieved July 23, 2016 from <http://www.aer.ca/rules-and-regulations/bulletins/bulletin-2015-11>.

Alexandrou, A.N., Constantinou, N., and Georgiou, G. (2009). Shear rejuvenation, aging and shear banding in yield stress fluids, *Journal of Non-Newtonian Fluid Mechanics*. (158): 6–17.

Allen, E.W. (2008). Process water treatment in Canada's oil sands industry: I. Target pollutants and treatment objectives. *Journal of Environmental Engineering Science*, (7):123-138.

Aly, S. M., and J. Letey. (1988). Polymer and water quality effects on flocculation of montmorillonite. *Soil Science Society of America Journal*, 52:1453-1458.

Ancey, C. and Cochard, S., (2009). The dam break problem for Herschel-Bulkley viscoplastic fluids down steep flumes. *Journal of Non-Newtonian Fluid Mechanics*, 158: 18-35.

ANSYS CFX Solver Theory Guide (2015), 16th release, ANSYS Inc., Canonsburg, Pennsylvania.

ANSYS CFX Solver Modelling Guide (2015), 16th release, ANSYS Inc., Canonsburg, Pennsylvania.

ANSYS CFX-pre user's Guide (2015), 16th release, ANSYS Inc., Canonsburg, Pennsylvania.

ANSYS CFX Introduction to Multiphase Flow (2015), 16th release, ANSYS Inc., Canonsburg, Pennsylvania.

Babaoglu, Y., and Simms, P. (2013). The development of a non-Newtonian flow model for bounding the beach slope angle of high density tailings stacks. Tailings & Mine Waste Conference, Banff, Alberta, Canada.

Babaoglu, Y. (2014). Deposition Modelling of High Density Tailings using Smoothed Particle Hydrodynamics. M.S.c thesis, Carleton University, Ottawa, Canada.

Bajwa, T.M. (2015). Microstructure and macroscopic behaviour of polymer amended oil sands mature fine tailings". PhD thesis, Carleton University, Ottawa, Canada.

Balmforth, N.J., Craster, R.V., Perona, P., Rust, A.C. and Sassi, R. (2007). Viscoplastic dam breaks and the Bostwick consistometer. *Journal of Non-Newton Fluid Mechanics*, 142:63-78.

Banas, L. (1991). Thixotropic Behaviour of oil sands tailings sludge. M.S.c. thesis, University of Alberta, Edmonton, Alberta.

Barth, A., and Wirth, K. (n.d.). Geochemical Instrumentation and Analysis. Retrieved 20 09, 2016, from Carleton College:
http://serc.carleton.edu/research_education/geochemsheets/techniques/XRF.html.

Barr Engineering Report (2012). Atmospheric Fines Drying (AFD) Deposition Optimization: Multi-lift versus Deep Stacking. 2012 Program – Interim Project Report.

Barber, M. (2004). AST Dean Stark procedure: Determination of bitumen, water and solids. Devon: Natural Resources Canada, Canada Energy Technology Centre, Advanced Separation Technologies Tailings & Environment.

Barnes, H. (1997). Thixotropy — a review. *Journal of Non-Newtonian Fluid Mechanics*, 70: 1– 33.

Bayliss, P., and Levinson, A. A. (1976). Mineralogical review of the Athabasca oil sands deposits (Lower Cretaceous, Mannville Group), *Bulletin Canadian Petroleum Geology*. (24): 211-214.

Beier, N., Wilson, W., Dunmola, A., and Segó, D. (2013). Impact of flocculation-based dewatering on the shear strength of oil sands fine tailings. *Canadian Geotechnical Journal*, 50(9): 1001-1007.

Bercovier, M., and Engelman, M. (1980). A finite-element method for incompressible non-Newtonian flows. *Journal of Computational Physics*, 36(3): 313–326.

Boxill, L. (2011). Potential for Use of Methylene Blue Index testing to Enhance Geotechnical Characterization of Oil Sands Ores and Tailings. *Tailings and Mine Waste 2011*. Vancouver, BC.

Brenner, H. (1974). Rheology of a dilute suspension of axisymmetric Brownian particles. *International Journal of Multiphase Flow*, 1:195–341.

Bulmer, J.T., and Starr, J. (1979). Syncrude analytical methods for oil sands and bitumen processing. Edmonton Alberta: Syncrude Canada Limited.

Calgary Herald. (2015). Strong oil sands growth still forecast despite low oil prices. Retrieved September 5, 2016 from <http://calgaryherald.com/business/energy/strongoilsands-growth-still-forecast-despite-low-oil-prices>.

Chalaturnyk, R.J., Scott, J.D., and Ozum, B. (2002). Management of oil sands tailings. *Petroleum Science and Technology*. 20(9): 1025-1046.

Chanson, H., Jarny, S., and Coussot, P. (2006). Dam break wave of thixotropic fluid. *Journal of Hydraulic Engineering*, 132(3):280-293.

Charlebois, L. E. (2012). On the Flow and Beaching Behaviour of Sub-Aerially Deposited, Polymer-Flocculated Oil Sands Tailings: A Conceptual and Energy -based Model. M.S.c. thesis, University of British Columbia, Vancouver, BC.

Chen, S., Johnson, D. B., Raad, P. E., and Fadda, D. (1997). The surface marker and micro cell method. *International Journal for Numerical Methods in Fluids*, 25(7):749–778.

Cheng, D.C.H. (1986). Yield stress: a time-dependent property and how to measure it. *Rheologica Acta*. 25(5): 542–554

Couerbe, G., Fletcherb, D.F., Xuereba, C., and Poux, M. (2008). Impact of thixotropy on flow patterns induced in a stirred tank: Numerical and experimental studies. *Chemical Engineering Research and Design*. 86(6): 545–553.

Chhabra, R.P., and Richardson, J.F. (2008). Non-Newtonian flow and applied rheology –engineering applications, 2nd edition, Oxford, Great Britain: Butterworth-Heinemann.

Clark, K.A., and Pasternack, D.S. (1932). Hot water separation of bitumen from Alberta bitumenous sand. *Industrial & Engineering Chemistry*, 24(12): 1410–1416.

Coussot, P., Leonov A.I., and Piau, J.M. (1993). Rheology of concentrated dispersed systems in a low molecular weight matrix. *Journal of Non-Newtonian Fluid Mechanics*.46(2–3): 179–217.

Coussot, P., and Ancey, C. (1999). *Reophysics of Paste and Suspensions*. EDP Sciences, Paris.

Coussot, P., Nguyen, H.T., Huynh, H.T., and Bonn, D. (2002a). Avalanche behaviour in yield stress fluids. *Physical Review Letters*, 88, Number 17: 175501-1-175501-4

Coussot, P., Nguyen H.T., Huynh, H.T., and Bonn, D. (2002b). Viscosity bifurcation in thixotropic, yielding fluid. *Journal of Rheology*. 46 (3):573-589.

Cuddy, G., Farwell, K., and Wright, B. (2000). Empirical studies on the relationship between process water chemistry and oil sands processability. *Problem Ores, 1st Extraction Fundamentals Seminar, Canadian Oil Sands Network for Research and Development (CONRAD)*. Fort McMurray, AB.

Das, B. M. (2008). *Advance soil mechanics*, Third edition. Taylor & Francis, New York, USA.

Day, M.A. (1990). The no-slip condition of fluid dynamics. *Erkenntnis*, 33(3): 285–296.

Darwish, M., and Moukalled, F. (2006). Convective Schemes for Capturing Interfaces of Free-Surface Flows on Unstructured Grids. *Numerical Heat Transfer Part B*. 49: 19–42

Danilatos, G.D. (1993). Introduction to the ESEM instrument. *Microscopy Research Techique*, 25(5-6):354–361.

Dean, E.J, Glowinski, R., Guidoboni, G. (2007). On the numerical simulation of Bingham visco-plastic flow: old and new results. *Journal of Non-Newtonian Fluid Mechanics*, 142(1):36-6.

Delage, P. (2010). A microstructure approach to the sensitivity and compressibility of some Eastern Canada sensitive clays. *Geotechnique*, 60(5): 353 – 368.

Delage, P., Marcial, D., Cui, Y.J. and Ruiz, X. (2006). Ageing effects in a compacted bentonite: a microstructure approach. *Geotechnique*, 56(5): 291–304.

Demoz, A. (2012). Mixing Energy Density Criterion for Peak Dewatering Flocculation by Static Mixer. 3rd International Oil Sands Tailings Conference, Edmonton, Alberta.

Demoz, A., and Mikula, R.J (2012). Role of Mixing Energy in Flocculation of Mature Fine Tailings. *Journal of Environmental Engineering*, 138(2):129-136.

Devenny, D.W. (2010). A screening study of oil sands tailings technologies and practices. Prepared for Alberta Energy Research Institute, Edmonton, Alberta.

Diep, J., Weiss, M., Revington, A., Moyls, B., and Mittal, K. (2014). In-line mixing of mature fine tailings and polymers. In *Proceedings of the 17th International Seminar on Paste and Thickened Tailings*, Vancouver, BC.

Directive 074- Energy Resources Conservation Board of Alberta (ERCB). (2009). *Tailings Performance Criteria and Requirements for Oil Sands Mining*.

Dummola, A., Côté, C., Freeman, G. Kolstad, D., Song J., and Masala, S. (2013). Dewatering and Shear Strength Performance of In-Line Flocculated Mature Fine Tailings Under Different Depositional Schemes. *Tailings and Mine Waste Conference*. Banff, AB.

Dunmola, A. (2011). 2011 Atmospheric Fines Drying (AFD) Deposit Performance Report.

Dusseault, M. B., Scafe, D. W., and Scott, J. D. (1989). Oil sands mine waste management: Clay mineralogy, moisture transfer and disposal technology. *AOSTRA Journal of Research*, (5):303–320.

EUB (Alberta Energy and Utilities Board) Statistical Series (ST) 2004-98, (2004). *Alberta's Reserves 2003 and Supply/Demand Outlook 2004-2013*. Available from www.eub.gov.ab.ca (cited Sep 2016).

Energy Resource Conservation Board. (2011). *EnerFAQs Oil Sands*. Retrieved June 2016, from Energy Resources Conservation Board: <http://www.ercb.ca/enerfaqs/EnerFAQs 12-OilSands.pdf>

Farmer, V. C. (1971). The characterization of adsorption bonds in clays by infrared spectroscopy. *Soil Science*, 112:62-68.

Ferreira, T., and Rasband, W. (2012). *Image J/Fiji 1.46 User Guide*, available from (<http://imagej.nih.gov/ij/docs/guide/user-guide.pdf>)

Fitton, T.G. (2007). *Tailings beach slope prediction*, PhD thesis, RMIT University, Australia.

FTFC. (1995). Clark hot water extraction for fine tailings. In *Advances in oil sands tailings research*. Fine Tailings Fundamentals Consortium (FTFC), Oil Sands and Research Division, Alberta Department of Energy, Edmonton, Alberta. 1:79–84.

Garciano, L., Torisu, R., Takeda, J., and Yoshida, J. (2001). Resonance identification and mode shape analysis of tractor vibrations. *Journal of the Japanese Society of Agricultural Machinery*, 63:45-50.

Gandhi, K., and Salvoley, R. (1988). Dynamic mechanical behavior of polymers containing carbon black. *Polymer Engineering and Science*, 28(14): 877–887.

Gao, J.L., and Fourie, A.B. (2014). Studies on flume tests for predicting beach slope of paste using the computational fluid dynamic method. 17th international Seminar on Paste and Thickened Tailings. Vancouver, Canada.

Gao, J.L., and Fourie, A.B. (2015). Using the flume test for yield stress measurement of thickened tailings. *Minerals Engineering*, 81: 116–127.

Glowinski, R., and Wachs, A. (2011). On the numerical simulation of viscoplastic fluid flow. *Handbook of Numerical Analysis*, 16:483-717.

Government of Alberta, Canada. (2009). Environmental management of Alberta's oil sands. Available from <http://environment.gov.ab.ca/info/library/8042.pdf>

Griffiths, F.J., and Joshi, R.C. (1989). Change in pore size distribution due to consolidation of clays. *Geotechnique*, 39(1): 159 -167.

Guerrier, K., Boisson, D., Thimus, J., Schroeder, C. (2015). A Rheological approach to the mechanical behavior of some marls samples in Haiti. 68th Canadian Geotechnical Conference and the 7th Canadian Permafrost Conference. Quebec City, QC.

Hein, F.J., Langenberg, C.W., Kidson, C., Berhane, H., and Berezniuk, T. (2001). A comprehensive field guide for facies characterization of the Athabasca oil sands Northern Alberta. Special Report 13, May 2001.

Henriquez, J., and Simms, P. (2009). Dynamic imaging and modeling of multilayer deposition of gold paste tailings. *Minerals Engineering*, 22(2):128–139.

Hewitt, D.R. 2012. Report on thixotropic gravity currents, Proceedings of the Geophysical Fluid Dynamics program, WHOI (168-198).

Hewitt, D.R., and Balmforth N.J. (2013). Thixotropic gravity currents. *Journal of Fluid Mechanics*. 727:56–82.

Hirt, C. W., and Nichols, B. D. (1981). Volume of Fluid (VOF) Method for the Dynamics of Free Boundaries. *Journal of Computational Physics*, 39:201-225.

Hogg, R. (1999). The role of polymer adsorption kinetics in flocculation. *Colloids and Surfaces A: Physicochemical and Engineering Aspects*, 146:253–263.

Hogg, R. (2000). Flocculation and dewatering. *International Journal of Mineral Processing*, 58:223-236.

Houlihan, R., and Haneef, M. (2008). Oil Sands Tailings: Regulatory Perspective. 1st International Oil Sands Tailing Conference, Edmonton, Alberta.

Ignasiak, T. M., Kotlyar, L., Longstaffe, F. J., Strausz, O. P., and Montgomery, D. S. (1983). Separation and characterization of clay from Athabasca asphaltene. *Fuel*, 62(3): 353–362.

Ignasiak, T.M., Zhang, Q., Kratochvil, C., Montgomery, D.S., and Strausz, O.P., (1985). Chemical and mineral characterization of the bitumen-free Athabasca oil sands related to the bitumen concentration in sand tailings from the syncrude batch extraction test. *AOSTRA Journal of Research*, 2: 21–34.

Innocent-Bernard, T. (2013). Evaporation, cracking, and salinity in a thickened oil sands tailings. M.A.Sc. thesis, Carleton University, Ottawa, Canada.

Jardine, R.J. (1992). Some observations on the kinematic nature of soil stiffness. *Soils and Foundations*, 32:11-124.

Jardine, R.J., Potts, D.M., and Higgins, K.G. (2004). *Advances in Geotechnical Engineering: The Skempton Conference*. Thomas Telford Ltd, London, United Kingdom.

Jasmund, K., und G. Lagaly, (1993). *Tonminerale und Tone: Struktur, Eigenschaften, Anwendungen und Einsatz in Industrie und Umwelt*. 490 pp. Steinkopff-Verlag, Darmstadt.

Jeeravipoolvarn, S. (2005). Compressive Behaviour of Thixotropic Oil Sands Tailings. M.S.c. thesis, University of Alberta, Edmonton, Alberta.

Jeeravipoolvarn, S. (2010). Geotechnical behavior of in-line thickened oil sands tailings. Ph.D. thesis, University of Alberta, Edmonton, Alberta

Jeeravipoolvarn, S., Miller, W., and Scott, J.D. (2014). Modelling effect of bitumen extraction processes on oil sands tailings ponds. 67th Canadian Geotechnical Conference Regina, SK.

Jin, B., Wilén, B. M., and Lant, P. (2004). Impacts of morphological, physical and chemical properties of sludge flocs on dewaterability of activated sludge. *Chemical Engineering Journal*, 98(1): 115-126.

Kaminsky, H. A. (2008). *Characterization of an Athabasca Oil Sands Ore and Process Streams*. University of Alberta, Alberta, Canada.

Kaminsky, H. A. (2014). Demystifying the Methylene Blue Index. *International Conference on Oil Sands Tailings*, Lake Louis, Alberta.

Keslerova R., and Kozel, K. (2010). Numerical modelling of incompressible flows for Newtonian and non-Newtonian fluids. *Mathematics and Computers in simulation*, 80(8):1783-1794.

Kézdi, Á. (1974). *Handbook of soil mechanics - Volume 1: Soil Physics*. 1st edition. 294 pp. Akadémiai Kiadó, Budapest. ISBN 963-05-0088-4.

Khaldoun, A., Moller, P., Fall, A., Wegdam, G., De Leeuw, B., M'ehoust, Y., Fossum, J. O., and Bonn, D. (2009). Quick clay and landslides of clayey soils. *Physical Review Letters*, 103:188301-1-188301-4.

Klein, C.G. (2014). *Effect of Residual Bitumen on Polymer-assisted Flocculation of Fluid Fine Tailings*. University of Alberta, Alberta, Canada.

Kochmanova, N., and Tanaka, H. (2010). Role of microstructure in the mechanical behaviour of clay. *Geotechnical Special Publication*, 200: 166 -171.

Kotlyar, L.S., Sparks, B.D., and Kodama, H. (1984). Some chemical and mineralogical properties of fine solids derived from oil sands. *AOSTRA Journal of Research*. (1):99–106.

Kramer, S.L. (1996). *Geotechnical Earthquake Engineering*, Publisher: Prentice Hall.

Lambe, T.W. (1958). The structure of compacted clays. *Journal of Soil Mechanics and Foundation Division, ASCE*, 84(2):1–34.

Langford, J. I. & Louër, D. (1996). Powder diffraction. *Reports on Progress in Physics*, 59 (2), 131–234.

Lee, H., and Rhee, S.H. (2015). A dynamic interface compression method for VOF simulations of high-speed planing watercraft. *Journal of Mechanical Science and Technology*, 29 (5):1849-1857.

Liddell, P.V., and Boger, D.V. (1996). Yield stress measurement with the vane. *Journal of Non-Newtonian Fluid Mechanics*, 63(2-3):235-261.

Macosko, C. W. (1994). *Rheology: principles, measurements, and applications*. Willey-VCH.

Mahaut, F., Chateau, X., Coussot, P., and Ovarlez, G. (2008). Yield stress and elastic modulus of suspensions of noncolloidal particles in yield stress fluids. *Journal of Rheology*, 52(1): 287-313.

Markgraf, W. (2006). Microstructural changes in soils rheological investigations in soils mechanics. Ph.D Thesis, Christian-Albrechts-Universität, Germany.

Markgraf, W., Horn, R., and Peth, S. (2006). An approach to rheometry in soil mechanics – Structural changes in bentonite, clayey and silty soils. *Applied Clay Science*, 91:1 – 14.

Markgraf, W., Watts, C. W., Whalley, W. R., Hrkac, T., and Horn, R. (2012). Influence of organic matter on rheological properties of soil. *Applied Clay Science*, 64: 25 – 33.

Matthews, J., Dhadli, N., House, P., Simms, P. (2011). In *Proceedings of the 14th International Seminar on Paste and Thickened Tailings*, Perth, Australia.

Masliyah, J., Zhou, Z., Xu, Z., Czarnecki, J., and Hamza, H. (2004). Understanding water based bitumen extraction from Athabasca Oil Sands. *The Canadian Journal of Chemical Engineering*, 82: 628 - 654

Mcdougall, S. (2006). A new continuum Dynamic model for the analysis of extremely rapid landslide motion across complex 3d terrain. PhD Thesis. University of British Columbia. BC.

McPhail, G. (1995). Prediction of the beaching characteristics of hydraulically placed tailings, PhD thesis, University of the Witwatersrand, Johannesburg, South Africa.

Mewis, J. and Spaul, A. J. B (1976). Rheology of concentrated dispersions. *Advances in Colloid and Interface Science*, 6(3):173–200.

Mewis J. (1979). Thixotropy-A General Review. *Journal of Non-Newtonian Fluid Mechanics*, 6(1):1-20.

Mewis, J. and Wagner, N. J. (2009). Thixotropy, *Advances in Colloid and Interface Science*, 147-148:214–227.

Mezger, T. (2006). *The Rheology-Handbook: For users of rotational and oscillatory rheometers*. 2nd edition. Vincentz, Hannover.

Miller, W. G. (2010). Comparison of geoenvironmental properties of caustic and noncaustic oil sands fine tailings. PhD thesis, University of Alberta.

Minussi, R.B., and Maciel, G.F. (2012). Numerical experimental comparison of dam break flows with non-Newtonian fluids, *Journal of the Brazilian Society of Mechanical Sciences and Engineering*, 34(2):167–178.

Mitchell, J.K., and Soga, K (2005). *Fundamentals of Soil Behavior* (3rd Edition) John Wiley & Sons.

Mitchell J.K. (1960). Fundamental Aspects of Thixotropy in Soils. *Journal of Soil Mechanics and Foundation Division, ASCE*, 86 (SM 3):19-52.

Mizani, S., He, L., and Simms, P. (2010). “Out of pipe“ dewatering of thickened tailings during deposition. In proceedings of the 13th International Conference on Paste and Thickened Tailings, Toronto, Canada.

Mizani, S., He, X., and Simms, P. (2013a). Application of lubrication theory to modeling stack geometry of high density mine tailings. *Journal of Non-Newtonian Fluid Mechanics*, (198):59–70.

Mizani, S., Soleimani, S., and Simms, P. (2013b). Effects of polymer dosage on dewaterability, rheology, and spreadability of polymer-amended MFT. In *Proceedings 16th International Seminar on Paste and Thickened Tailings*. Belo Horizonte, Brazil.

Mizani, S., and Simms, P. (2014a). Geometry of polymer-amended fine tailings deposits: yield stress measurement and numerical modelling. *International Conference on Oil Sands Tailings*, Lake Louis, AB.

Mizani, S., and Simms, P. (2014b). Rheology for surface deposition of polymer-amended fine tailings. In *Proceedings of the 17th International Conference on Paste and Thickened Tailings*, Vancouver, BC.

Mizani, S., and Simms, P. (2016a). Method-dependent variation of yield stress in a thickened gold tailings explained using a structure based viscosity model. *Minerals Engineering*. (98):40–48.

Mizani, S., and Simms, P. (2016b) .Rheology for deposition control of polymer amended oil sands tailings. Submitted to *Journal of Rheologica Acta*. Recommended for publishing pending revision, December 2016.

Moller, P., Fall, A., Chikkadi, V., Derks D., and Bonn D. (2009) An attempt to categorize yield stress fluid behavior. *Philosophical Transactions of the Royal Society A*. 367:5139– 5155.

Monroy, R., Zdravkovic, L., and Ridley, A. (2010). Evolution of microstructure in compacted London clay during wetting and loading. *Geotechnique*, 60(2): 105 –119.

Nadeau, P. H., Wilson, M. J., McHardy, W. J., and Tait, J. M. (1984). Interstratified clays as fundamental particles. *Science*, (225):923–935.

Naef, D., Rickenmann, D., Rutschmann, P., and McArdell, B (2006). Comparison of flow resistance relations for debris flows using a one-dimensional finite element simulation model. *Natural Hazards and Earth System Science*, 6(1):155-165.

Najafi, A., Mian, H., Salehi, R., Lacoste-Bouchet, P., Friedrich, K., Keele, H., McWhan, C., Romero, J., Daliri, F., Jeeravipoolvarn, S., Boswell, J., and Moore, T. (2014). Flooding of in-line flocculated tailings after thin lift drying. *International Conference on Oil Sands Tailings*, Lake Louis, AB.

Nasser, M.S., and James, A.E. (2006). The effect of polyacrylamide charge density and molecular weight on the flocculation and sedimentation behaviour of kaolinite suspensions Original Research Article. *Separation and Purification Technology*, 52: 241-252.

Nielsen, B.D., (2004). Non destructive soil testing using x-ray computed tomography. M.S.c. thesis, Montana State University Bozeman, Montana.

Nguyen, Q.D., and Boger, D.V. (1992). Measuring the flow properties of yield stress fluids. *Annual Review of Fluid Mechanics*, 24: 47–88.

Nguyen, Q.D., Akroyd, T., De Kee, D.C., and Zhu, L. (2006). Yield stress measurements in suspensions: an inter-laboratory study. *Korea-Australia Rheology Journal*. 18 (1): 15–24.

O'Donovan, E.J., and Tanner, R.I. (1984). Numerical study of the Bingham squeeze film problem. *Journal of Non-Newtonian Fluid Mechanics*, 15(1): 75–83

Osipov, V.I., Nikolaeva, S. K., and Sokolov, V.N. (1984). Microstructural changes associated with thixotropic phenomena in clay soils. *Geotechnique*, 34 (2): 293-303.

Omotoso, O., Mikula, R. J., and Stephens, P. W. (2002). Surface area of interstratified phyllosilicates in Athabasca oil sands from Synchrotron XRD. *Advances in X-ray Analysis*, 45:391-396.

Omotoso, O., and Melanson, A. (2014). Influence of clay minerals on the storage and treatment of oil sands tailings. In Proceedings of the 17th International Seminar on Paste and Thickened Tailings, Vancouver, Canada.

Papanastasiou, T.C, (1987). Flows of materials with yield. *Journal of Rheology*, 31(5): 385–404.

Pashias, N., Boger D.V., Summers J., and Glenister, D.J. (1996). A fifty cent rheometer for yield stress measurement. *Journal of Geophysical Research*, 40(6):1179-1189.

Peng, F.F., and Di, P. (1994). Effect of multivalent salts, calcium and aluminum on the flocculation of kaolin suspensions with anionic polyacrylamide. *Journal of Colloid and Interface Science*, 164:229-237.

Prabhakara, S., Deshpande, M., (2004). The no-slip boundary condition in fluid mechanics. *Resonance*, 9: 61–71.

Quemada, D. (1999). Rheological modelling of complex fluids: IV: Thixotropic and “thixoelastic” behaviour. Start-up and stress relaxation, creep tests and hysteresis cycles. *The European Physical Journal Applied Physics*, 5(2): 191-207.

Read, P. (2014). Broad suite of practice and technology key to success in tailings management. International Conference on Oil Sands Tailings, Lake Louis, AB.

Rietveld, H. M. (1969). A profile refinement method for nuclear and magnetic structures. *Journal of Applied Crystallography*, (2): 65-71.

Romero E., and Simms, P. (2008). Microstructure investigation in unsaturated soil: A review with special attention to contribution of mercury intrusion porosimetry and environmental scanning electron microscopy. *Geotechnical and Geological*, 26: 705 – 727.

Rosenqvist, I.T. (1959). Physico-chemical properties of soils; soil-water systems. *Journal of Soil Mechanics and Foundation Division, ASCE*, 85:285-312.

Rosenqvist, I.T. (1962). The influence of physico-chemical factors upon the mechanical properties of clays. *Clays and Clay Minerals*, 9:12-27.

Roussel, W. B., Saville, D. A., and Schowalter, W. R. (1989). *Colloidal Dispersions* Cambridge University Press, Cambridge.

Roussel, N (2006). A thixotropy model for fresh fluid concretes: Theory, validation and application. *Cement and Concrete Research*, 36:1797-1806.

Roussel, N. (2005). Steady and transient flow behaviour of fresh cement pastes. *Cement and Concrete Research*, 35:1656-1664.

Roussel, N., Le Roy, R., and Coussot, P (2004). Thixotropy modelling at local and macroscopic scales. *Journal of Non-Newtonian Fluid Mechanics*. (117):85-95.

Rozina, L., Mizani, S., Malek, M., Sanchen-Sardon, M., and Simms, P. (2015). The effects of desiccation and consolidation on surface deposited thickened oil sands tailings. In *Proceedings of the 18th International Seminar on Paste and Thickened Tailings*, Perth, Western Australia.

Rusche, H. (2002). Computational fluid dynamics of dispersed two-phase flows at high phase fractions. PhD thesis, Imperial College, London.

Saak A. W., Jennings H. M., Shah S. P “The influence of wall slip on yield stress and viscoelastic measurements of cement paste”, *Cement and Concrete Research*, vol. 31, no. 2, pp. 205 - 212, 2001.

Scott, D. J., Dusseault, M.B, and Carrier, W. D (1985). Behaviour of the clay/bitumen/water sludge system from oil sands extraction plants. *Applied Clay Science*, 1 (1-2): 207-218.

Scott, J.D., Jeeravipoolvarn, S., Kabwe, L., Wilson G.W. (2013). Properties Which Affect the Consolidation Behaviour of Mature Fine Tailings. In *Proceedings of the 17th International conference on Tailings and Mine Waste*, Banff, Alberta.

Scintag, I. (1999). Chapter 7: Basics of X-Ray Diffraction.

Seed, H.B., and Chan, C.K., (1957). Thixotropic characteristics of compacted clays. *Journal of soil mechanics and Foundation Division*, ASCE, 83(SM 4): 1-35.

Sethi, A. (1995). Methylene Blue Test for Clay Activity Determination in Fine Tails. *MRRT Procedures*.

Simms, P., and Yanful, E.K. (2004). A discussion of the application of mercury intrusion porosimetry for the investigation of soils, including an evaluation of its use to estimate volume change in compacted clayey soils. *Géotechnique*, 54 (6): 421-426.

Simms, P., and Yanful, E.K. (2005). A pore-network model for hydro-mechanical coupling in unsaturated compacted clayey soils. *Canadian Geotechnical Journal*, 42 (2): 499 - 514.

Simms, P. (2007). On the relation between laboratory flume tests and deposition angles of high density tailings, In Proceedings 10th International Seminar on Paste and Thickened Tailings, Australia Centre for Geomechanics, Perth, Australia.

Skempton, A.W., and Northley, R.D. (1952). The sensitivity of clays, *Geotechnique*, 3(1):203-208.

Simms, P., William, M.P.A, Fitton, T.G, Mcphail, G. (2011). Beaching angles and evolution of stack geometry for thickened tailings — a review”. In proceedings of the 14th International Conference on Paste and Thickened Tailings, Perth, Australia.

Smith, R., and Ng, S. (1993). Towards a model for the prediction of fine tails volume. In J. L. Liu (Ed.). pp. F3-1 – F3-33. Edmonton, AB: Environment Canada.

Spelay R.B. (2007). Solids transport in laminar open channel flow of non-Newtonian slurries. PhD thesis, The University of Saskatchewan, Saskatchewan, Canada.

Stenmark, E. (2013). On Multiphase Flow Models in Asys CFD Software. Master Thesis, Chalmers University of Technology, Göteborg, Sweden.

Sworska, A., Laskowski, J.S., and Cymerman, G. (2000). Flocculation of the Syncrude fine tailings, part I, effect of pH, polymer dosage and Mg²⁺ and Ca²⁺ cations. *International Journal of Minerals Processing*, 60(2):143-152.

Tang, J., Biggar, K. W., Scott, J. D., and Segó, D. C. (1997). Examination of mature fine tailings using a scanning electron microscope. 50th Canadian Geotechnical Conference, Ottawa, Ontario.

Thakur, R.K., Vial, Ch., Nigam, K.D.P., Nauman, E.B., and Djelveh, G. (2003). Static mixers in the process industries. *Trans. IChemeE*, 81(Part A):787-825.

Theng, B. K. G. (1979). Formation and properties of clay-polymer complexes. Elsevier, Amsterdam.

Van Olphen, H. (1977). *An Introduction to Clay Colloid Chemistry* 2nd edition. John Wiley & Sons, New York, London, Sydney, Toronto.

Watson P., Fenderson, T., Mahmoudkhani A., Nair, M. Patel A., and Roberts, G. (2011). Breakage and Reformation of Floccs in Oil Sands Tailings. *Proceeding of Tailings and Mine Waste 2011*. Vancouver, BC.

Watson, P., Stewart K., Sanders L., Wu Y., Mahmoudkhani A., and Fenderson T. (2012). MFT chemical additives and the "Goldilocks zone" of mixing. *Proceedings of the 3rd International Oil Sands Tailings Conference*. Edmonton, Alberta.

Welch, S.W.J. (1995). Local simulation of two-phase flows including interface tracking with mass transfer. *Journal of Computational Physics*, 121(1):142 – 154.

Wells, P. S. (2011). Long term in-situ behaviour of oil sands fine tailings in Suncor's Pond 1A. *Proceeding Tailings and Mine Waste 2011*. Vancouver, BC

Whetham, W.D. (1890). On the alleged slipping at the boundary of a liquid in motion. *Philosophical Transactions of the Royal Society of London. A*, 181:559-582.

Williams, M.P.A., and Meynink, W.J.C. (1986). Tailings beach slopes, paper presented to Workshop on Mine Tailings Disposal, The University of Queensland.

Xu, Y., and Hamza, H. (2003). Thickening and disposal of oil sands tailings. *Mining Engineering*, 55(11): 19 – 25.

Yang, J. (2009). Computational Fluid Dynamics Modeling of Deposition of Oil Sands Slurry into Mature Fine Tailings. PhD thesis, University of Alberta.

Yilmaz, E., Belem, T., Bussière, B., and Benzaazoua, M. 2011. Relationships between micro structural properties and compressive strength of consolidated and unconsolidated cemented paste backfills. *Cement and Concrete Composites*, 33: 702 – 715.

Yong, R.N., and Sethi, A.J. (1983). Method for determining clay content in tailings and sludge, Canadian Patent No CA 1150610, Ottawa, Industry Canada.

Zbik, M.S., Smart, R.C., and Morris, G.C. (2008). Kaolinite flocculation structure. *Journal of Colloid and Interface Science*, 328: 73–80.

Zhu, Q. (2013). Understanding the role of caustic addition in oil sands processing. M.S.c. thesis, University of Alberta, Edmonton, Alberta.

Zhu, Y. (2015). Cationic and Anionic Dual Polymer Pairs for Mature Fine Tailings Flocculation and Dewatering. M.S.c. thesis, University of Alberta, Edmonton, Alberta.

Zhu, L., N. Sun, K. Papadopoulos and De Kee, D. (2001). A slotted plate device for measuring static yield stress. *Journal of Rheology*, 45:1105-1122.

APPENDICES

Appendix A Diffraction patterns of bulk samples

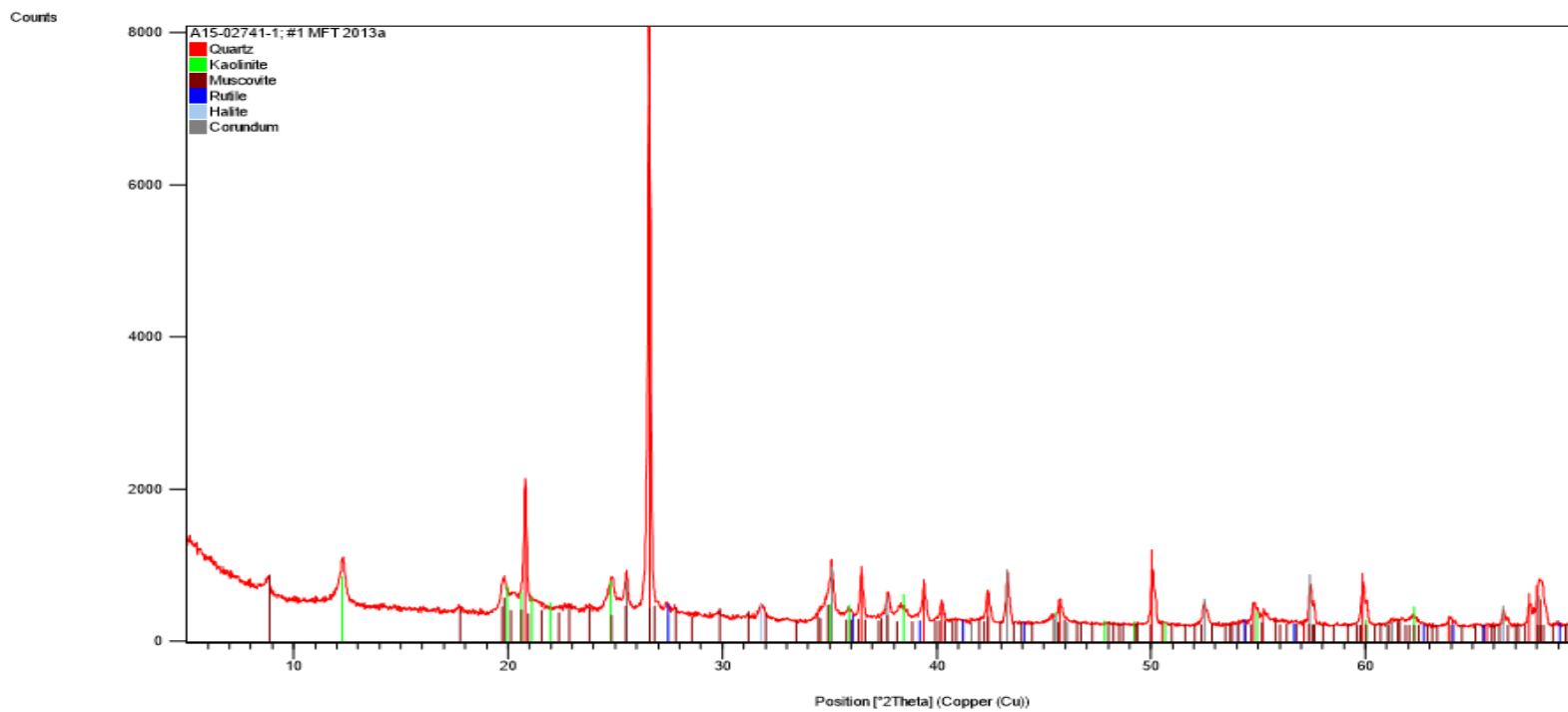


Figure A-1 Bulk Sample Diffraction Pattern 2013a.

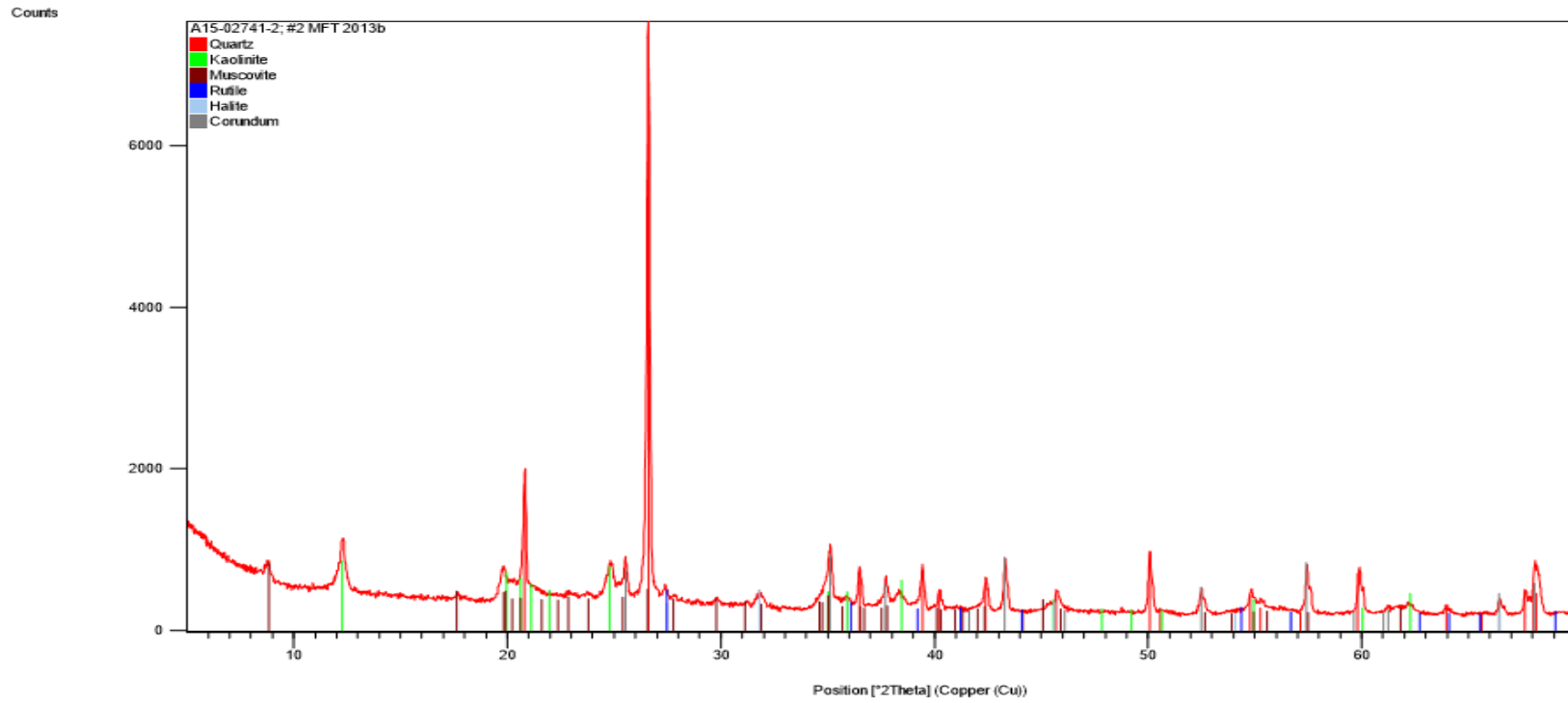


Figure A-2 Bulk Sample Diffraction Pattern 2013b.

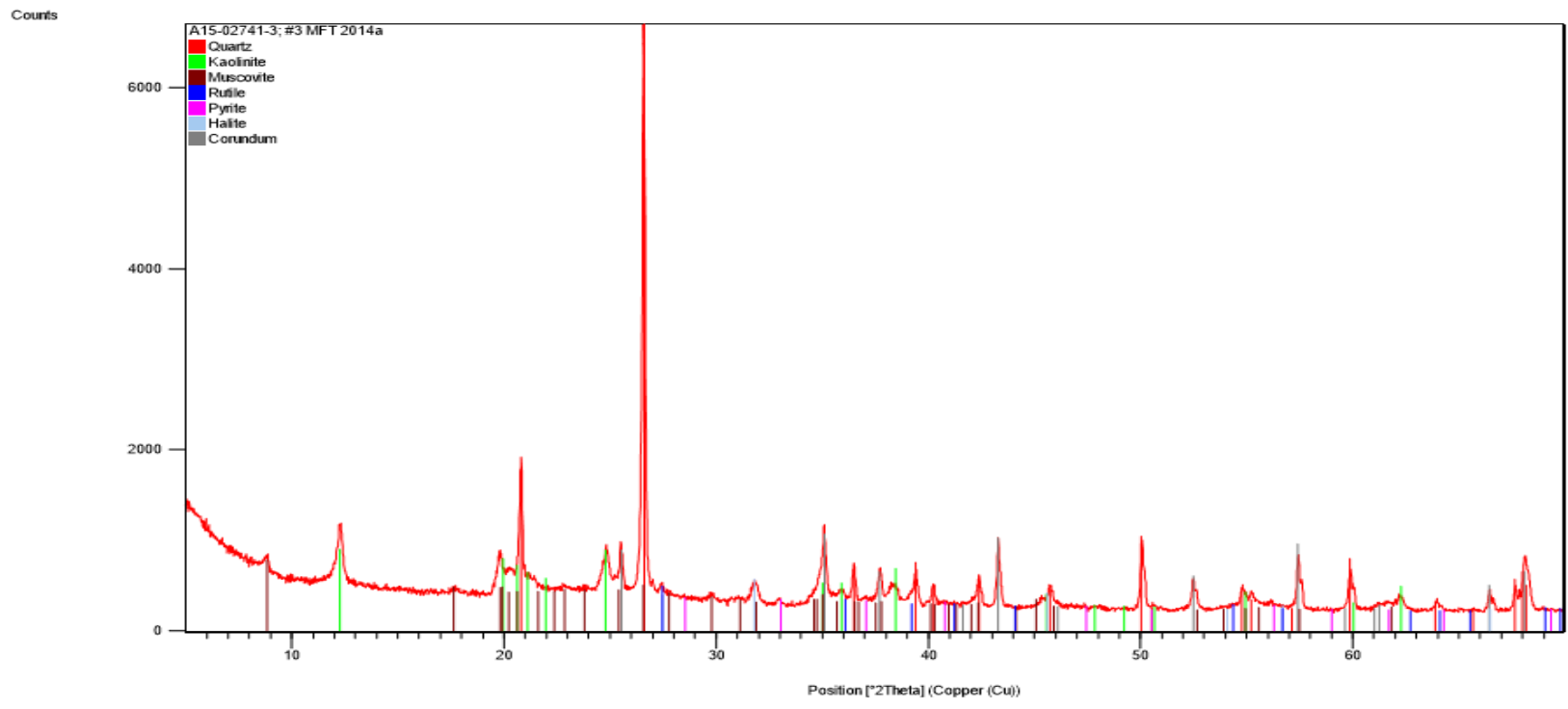


Figure A-3 Bulk Sample Diffraction Pattern 2014a.

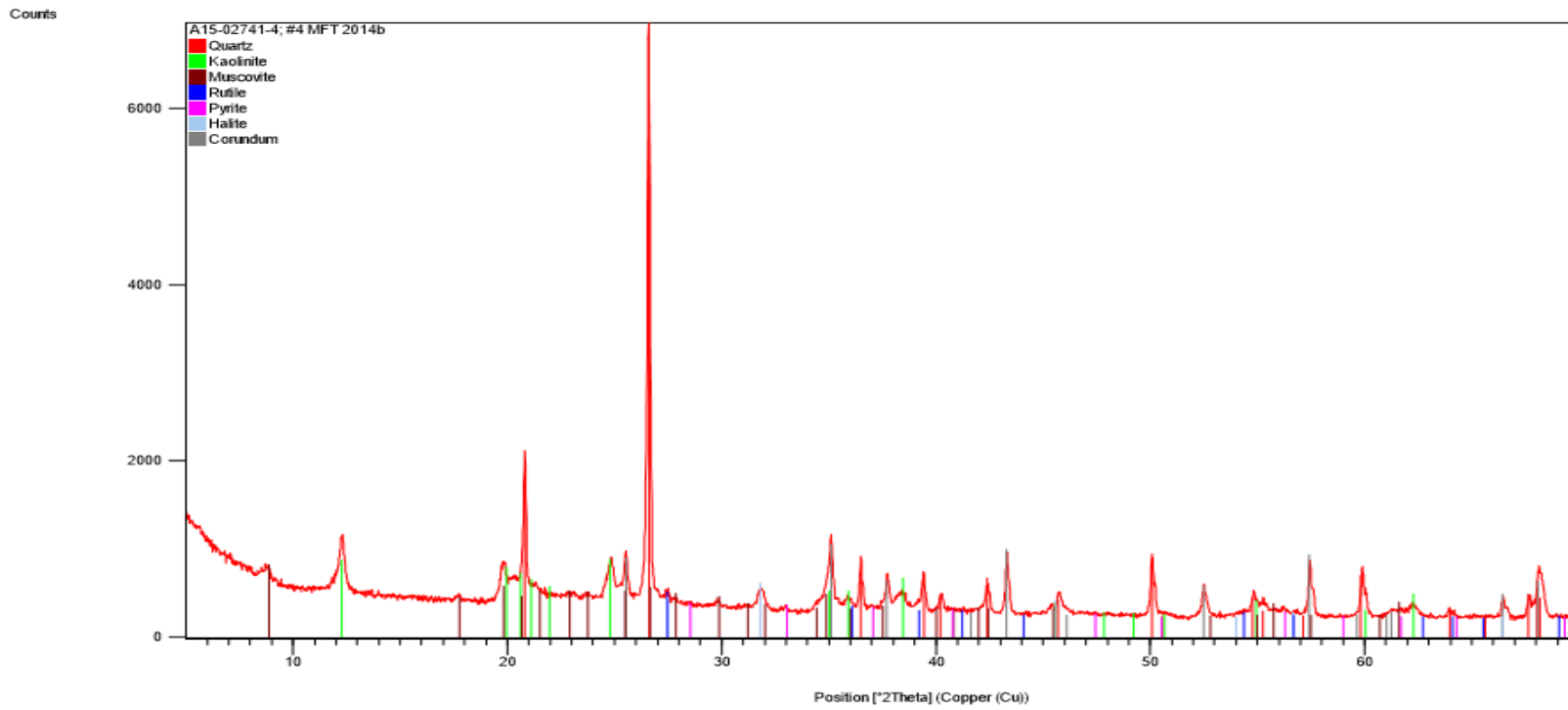


Figure A-4 Bulk Sample Diffraction Pattern 2014b.

Appendix B Diffraction patterns of the < 2 μm size fraction

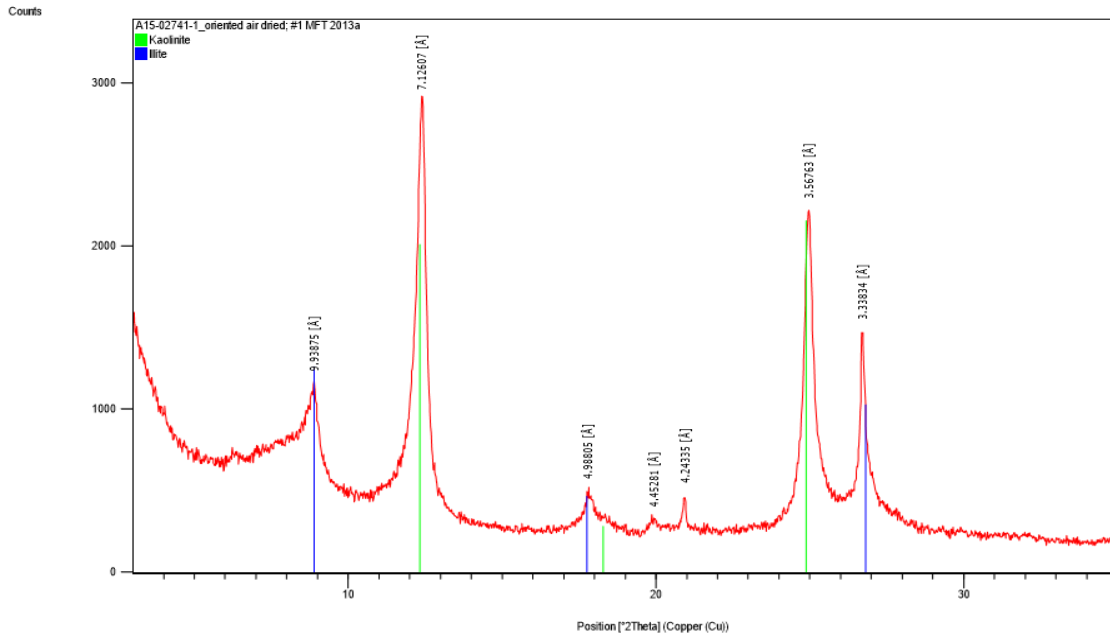


Figure B-5 XRD - Clay speciation (Air Dry) -2013a.

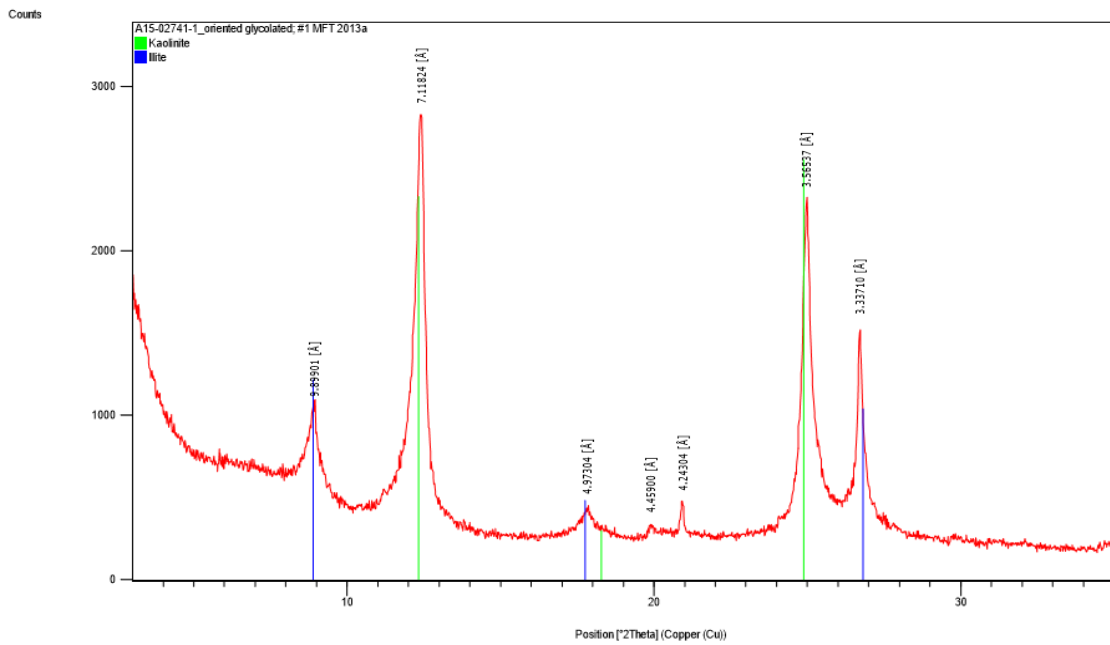


Figure B-6 XRD - Clay speciation (Glycolated) -2013a.

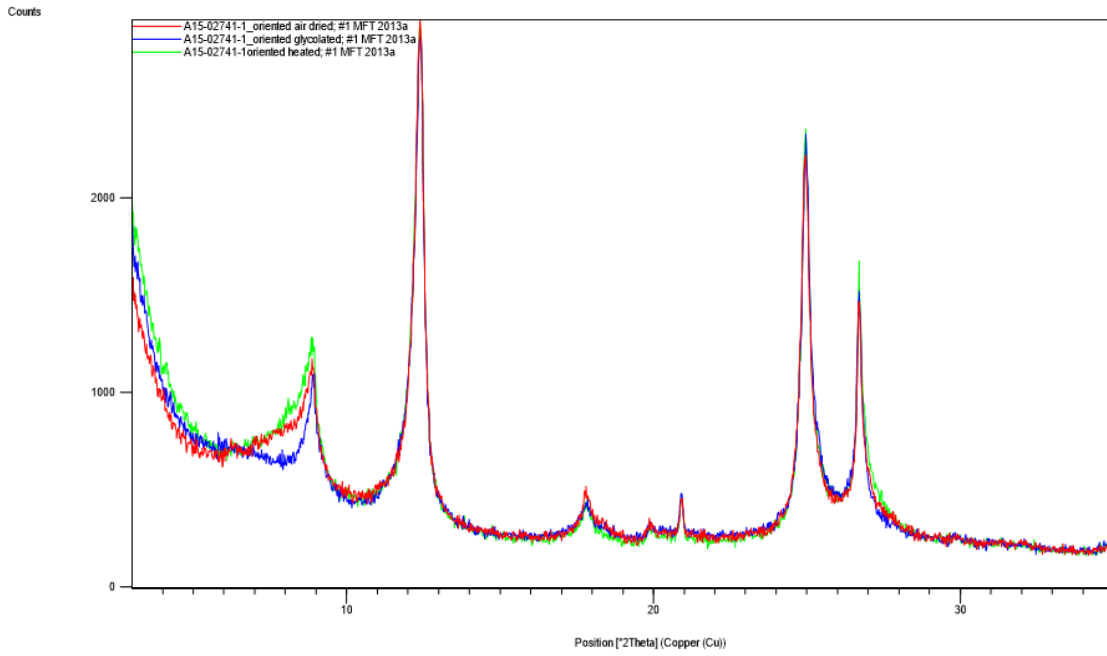


Figure B-7 XRD - Clay speciation Superimpositions -2013a

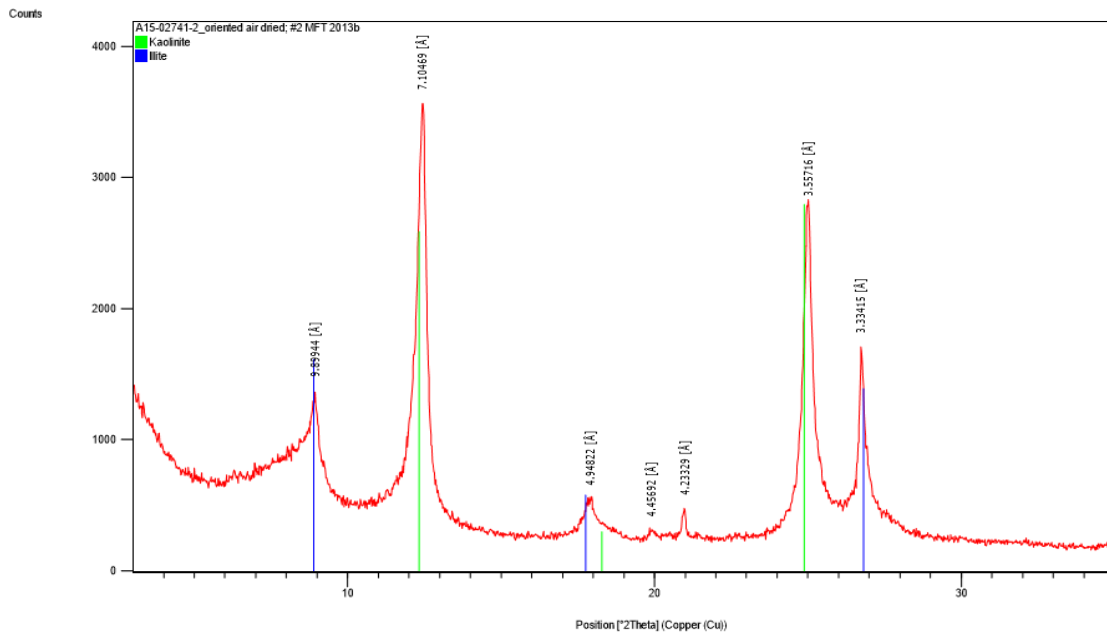


Figure B-8 XRD - Clay speciation (Air Dry) -2013b

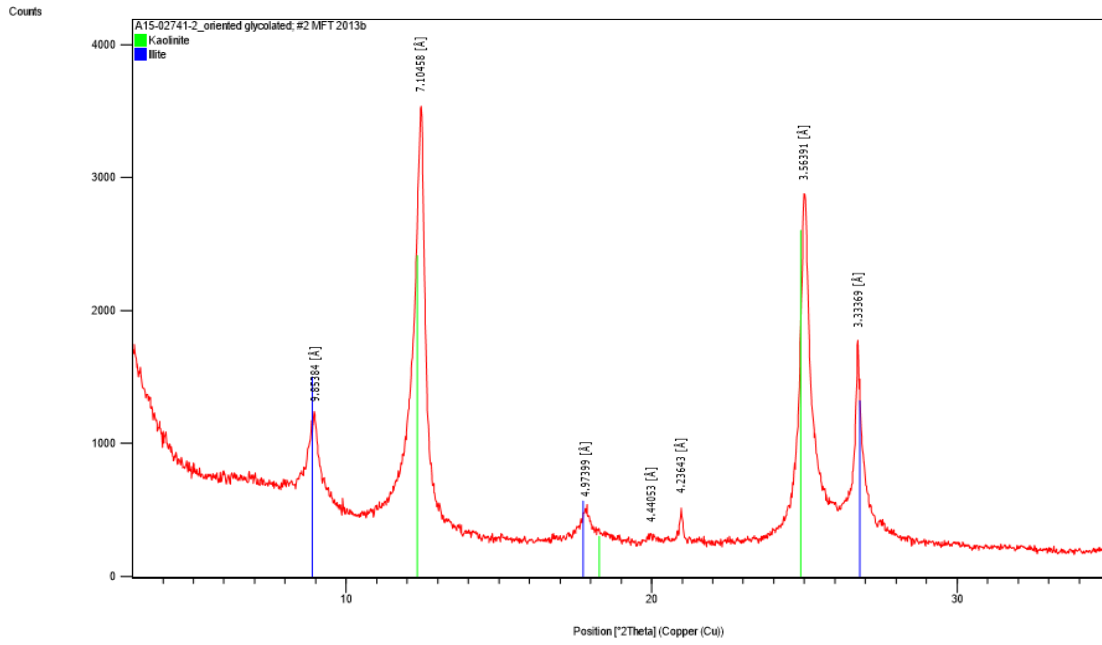


Figure B-9 XRD - Clay speciation (Glycolated) -2013b.

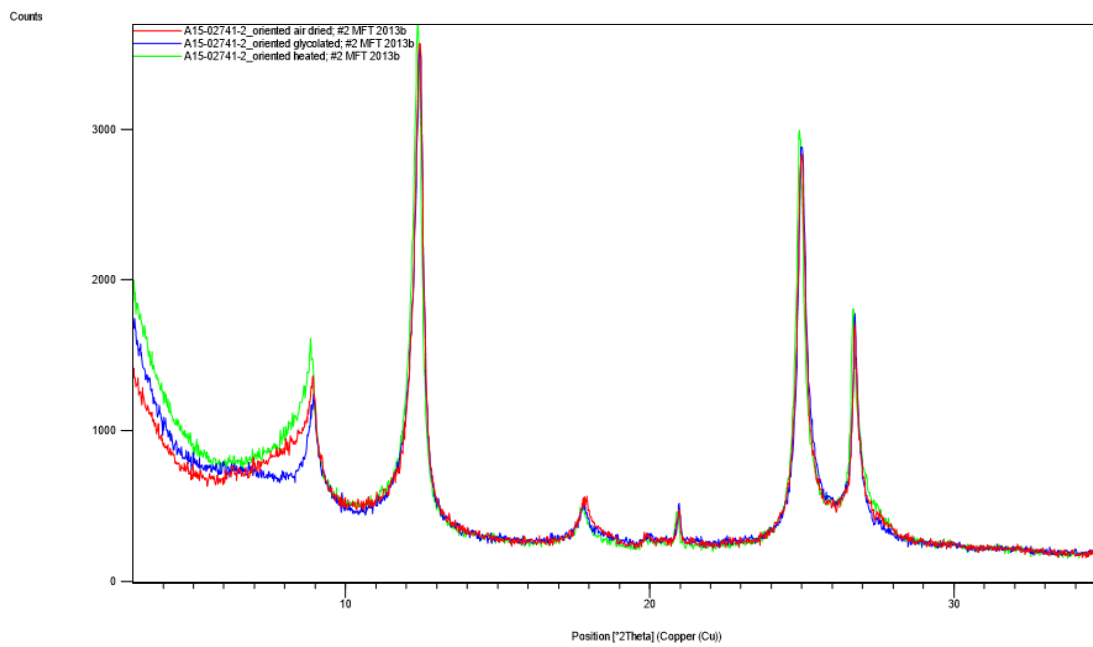


Figure B-10 XRD - Clay speciation Superimpositions -2013b.

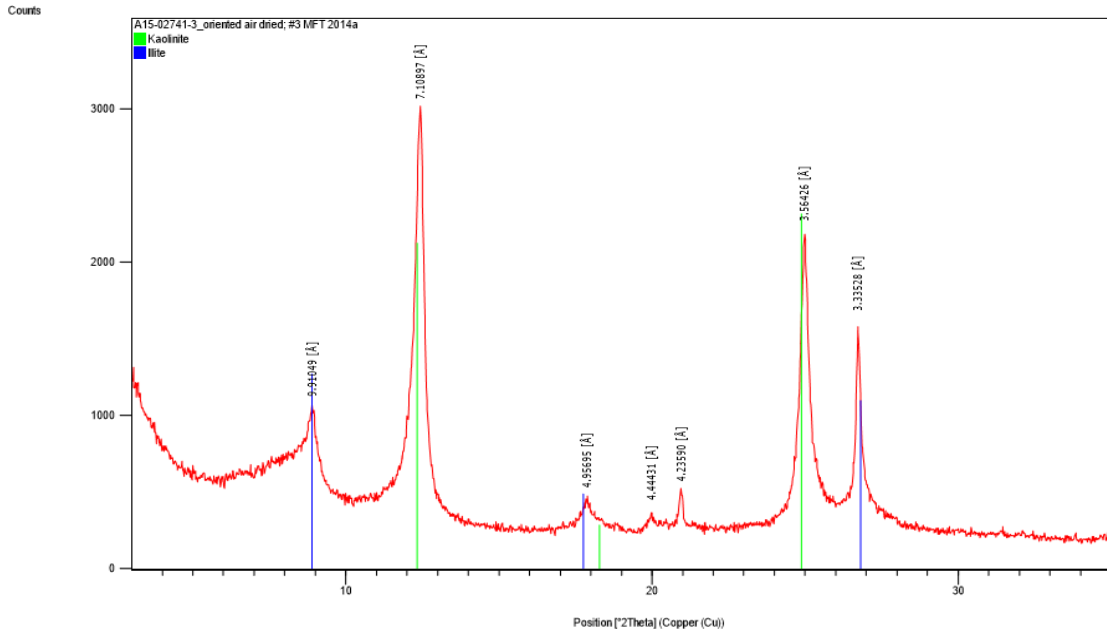


Figure B-11 XRD - Clay speciation (Air Dry) -2014a.

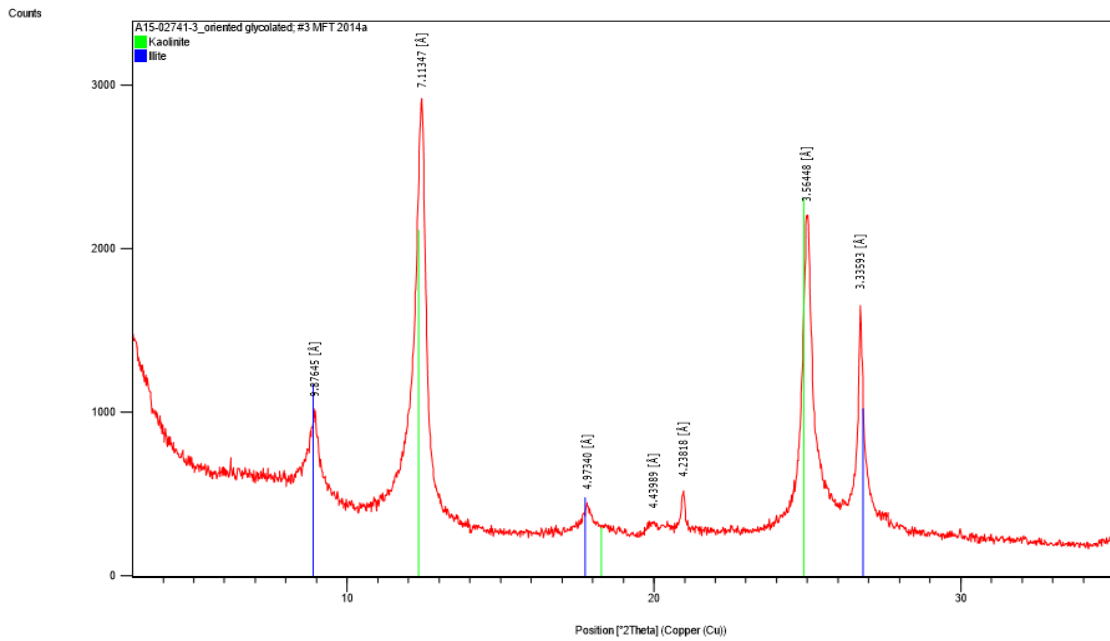


Figure B-12 XRD - Clay speciation (Glycolated) -2014a.

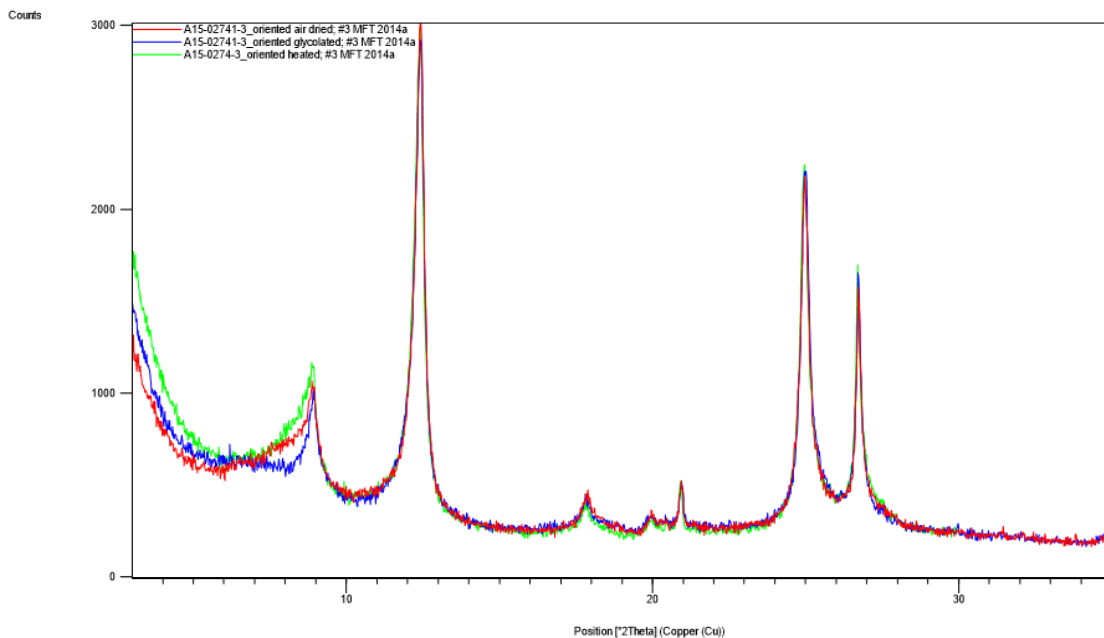


Figure B-13 XRD - Clay speciation Superimpositions -2014a.

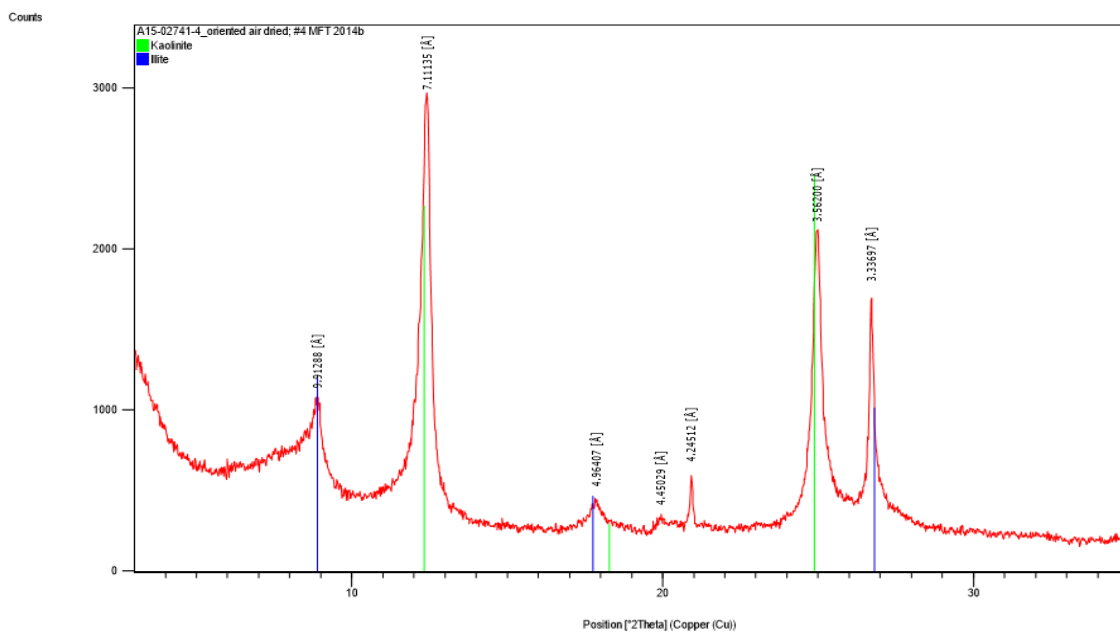


Figure B-14 XRD - Clay speciation (Air Dry) -2014b.

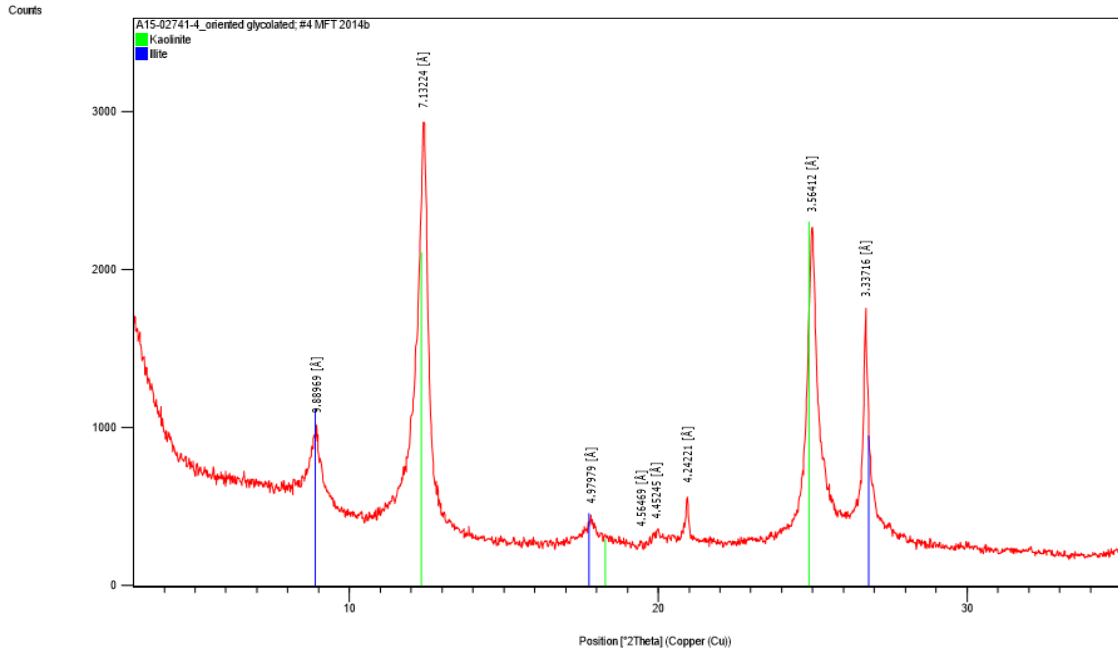


Figure B-15 XRD - Clay speciation (Glycolated) -2014b.

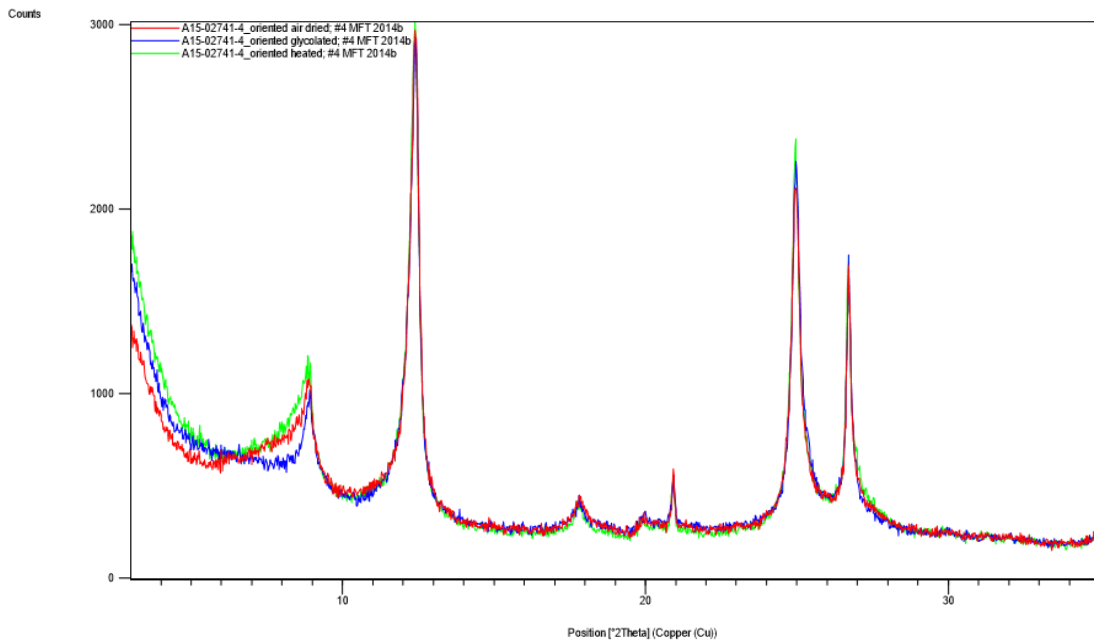


Figure B-16 XRD - Clay speciation Superimpositions -2014b.

Appendix C Centrifuge Cake Rheological Data

A total of nine (9) 250 L drums of oil sands thickened tailings were received from Shell's Pilot Plant. Of the 9, 1 was from the October 2014 batch and the remaining eight (8) from April 2015. Samples collected from each drum were assigned a number and its corresponding testing date can be found in Table C-1.

At the time the drums were received, a layer of supernatant water was collected at the top since the contents of the drum settled during transportation. The initial height of the sample in each drum was recorded, using which, compression for each core sample was calculated. Compression for Core #1, 2 and 3 were 64%, 75% and 70% respectively. The first drum received (October 2014 batch) was analyzed for variation in solids concentration, atterberg limit and Grain Size Distribution (GSD) with depth. Also a series of stress growth test were conducted on core samples collected at various depth.

Table C-1 Centrifuge cake sample identification and geotechnical properties

<i>Sample ID</i>	<i>Date Sample received</i>	<i>Sampling Procedure</i>	<i>Bottom(cm)</i>	<i>Top(cm)</i>	<i>Solid Content %</i>	<i>Density(gr/cm³)</i>	<i>PL</i>	<i>LL</i>	<i>Yield stress from stress growth(Pa)</i>	<i>Date tested</i>
1	22-Oct-14	Core# 1	0	6	46.63	1.11	-	-	-	
2	22-Oct-14	Core# 1	6	12	46.18	1.15	35.8	68.9	-	
3	22-Oct-14	Core# 1	12	18	46.19	1.06			-	
4	22-Oct-14	Core# 1	18	24	45.26	1.21			1410	12-Nov-2014
5	22-Oct-14	Core# 1	24	32	45.17	-	36.2	68.9		
6	22-Oct-14	Grab# 1	69	79	44.73	-	-	-	857	12-Nov-2014
7	22-Oct-14	Grab# 1	79	89	39.21	-	41.7	105.0	704	12-Nov-2014
8	22-Oct-14	Core# 2	12	21	45.17	-	37.6	84.5	1950	19-Feb-2015
9	21-Apr-15	Core# 3	0	12	57.54	-	-	-	2460	15-May-2015
10	21-Apr-15	Core# 3	12	24	60.60	-	-	-	1650	15-May-2015

Amplitude sweep tests were conducted on sample collected from core 1 (sample #7) to determine the LVE range (Figure C-17).

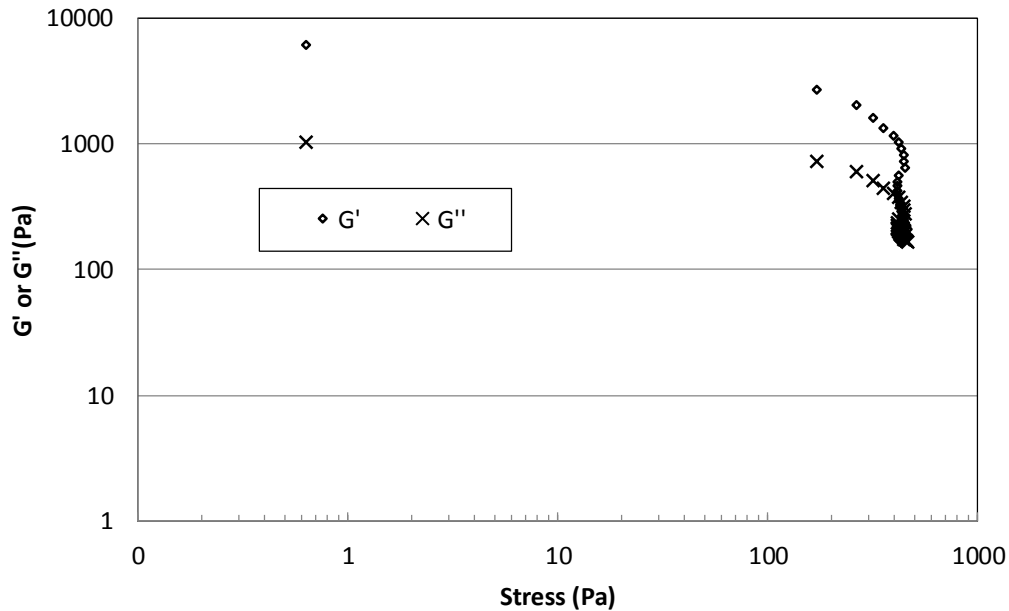


Figure C-17 Response to strain sweeps (0.01%-300%) for centrifuge cake (sample#7) showing the linear viscoelastic region of around 250Pa.

In order to investigate the effects of shearing on the percentage recovery of centrifuge cake, the three stage thixotropy test was used where an oscillatory stress of 10 Pa, at a constant frequency of 10 rad/s, was applied for five minutes in the first stage. High stress levels of (500Pa and 700Pa) were then applied for 240s and the elastic modulus was measured again under oscillatory stress of 10Pa to investigate percentage recovery of the sample. Figure C-18 illustrates recovery of the centrifuge test sample, along with a plot of G' before and after applying a high stress level.

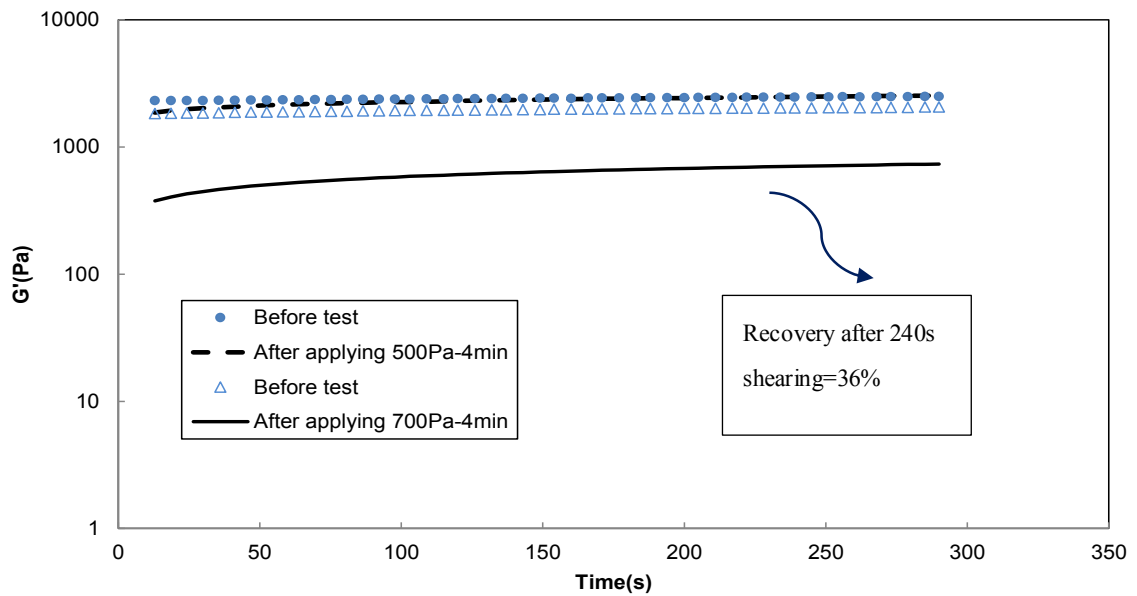


Figure C-18 Postshear recovery for sample #7 after applying a shear stress of 500 Pa and 700Pa for 240s.

Figure C-18 illustrates that centrifuge cake tailings also illustrated partial reformation of structure over time, however, a higher shear stress level resulted in a lower recovery rate.

In the second test, after applying an oscillating shear stress of 10 Pa, the material was sheared at 3000 Pa for 10 seconds. The stress was then gradually decreased in steps (2000 Pa, 1000 Pa, 500 Pa, 250Pa and 100 Pa), and each stress level was applied for only 10 seconds, giving a total time spent in stage 2 of 60 seconds.

The test was then repeated on another sample, but this time, all stress levels were held for five minute (Figure 4.5-9). Unlike flocculated MFT, a higher recovery rate was recorded in the first case, where the structure was not able to restore its original state.

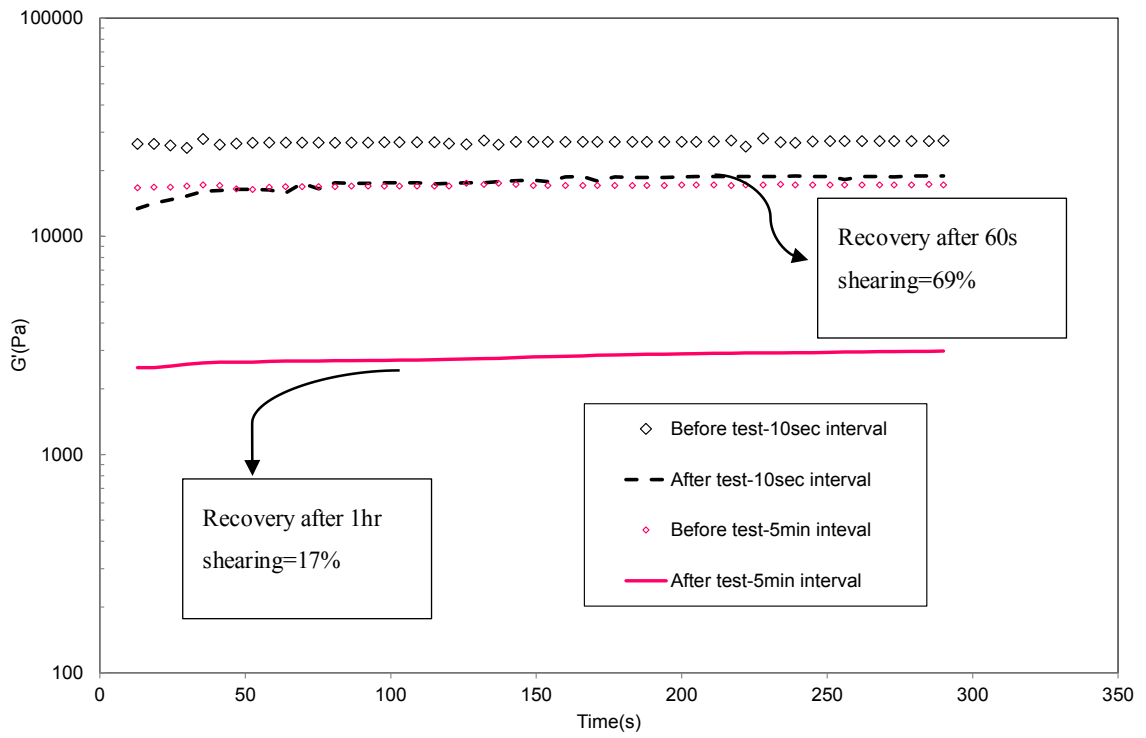


Figure C-19 Post shear recovery for sample #9&10 under constant decreasing shear stresses